GENERALISED PERIODIC GREEN'S FUNCTION ANALYSIS OF MICROSTRIP DIPOLE ARRAYS

BY

Stephen K.N. Yeo

A thesis submitted in fulfilment of the requirement for the degree of

Doctor of Philosophy

in

The University of Adelaide

Department of Electrical and Electronic Engineering

Faculty of Engineering

August, 1996

To my wife

and

two children

Contents

Abstract

The development of phased array antennas is an area of considerable current interest, driven by the demand for high performance electronic systems for personal communication systems, mobile satellite communications, wireless local networks and vehicular radar systems. With the increasingly congested frequency usage in the traditional lower frequency bands, attention is becoming focused on high frequency systems which make use of the millimetre and sub-millimetre wavelength parts of the spectrum. Where commercial interest is involved, issues such as low development and production cost assume a key significance with regard to the viability of any technology used to realise the systems described above. This thesis presents techniques that may be used to evaluate the performance of a wide variety of practical microstrip phased arrays in an efficient and insightful manner.

Microstrip phased arrays form a class of antennas suitable for operation at millimeter wavelengths. In order to meet modern system specifications, practical microstrip antennas have become increasingly more complex, comprising metallic radiators and feedlines as well as dielectric substrates and superstrates which may be continuous or discontinuous in the aperture plane. Moreover, for small to medium size arrays, the correct design of elements on the periphery of the array is important, precluding the use of traditional infinite array analyses without appropriate modification. Additional factors influencing the analytical and numerical techniques used in the design of microstrip arrays include the need to compute the scanning performance to a degree of accuracy sufficient to avoid costly experimental optimisation of the element design, and the need for realistic computing requirements in the numerical implementation. The objective of this work is to demonstrate that a generalised periodic Green's function integral-equation approach to practical phased arrays can achieve sufficient flexibility to model a variety of geometries, computational efficiency such that a desktop computer implementation is feasible, and accuracy sufficient for engineering design purposes.

This thesis presents a brief overview of microstrip antenna analysis, and describes the connections between spectral and spatial domain periodic Green's functions in integral equation methods. These ideas are developed into an efficient hybrid formulation which combines the benefits of both methods. The hybrid formulation is applied to a variety of problems from simple metal strip dipoles to more complicated microstrip geometries with different substrate and feed line configurations to demonstrate the performance of the technique. A further development to finite array analysis is described, in which spatial Fourier windowing is used to account for the effect of the array periphery. An improvement in the accuracy of this approximate technique is explored by an iterative technique to obtain a more accurate current window to be used in the convolution process.

The research described provides a unified view of the spatial and spectral periodic Green's functions and their application in a hybrid form to infinite and finite phased array analysis. The implementation of numerical analysis algorithms is shown to be highly efficient and accurate for modern microstrip array design.

Statement of Originality

This work contains no material which has been accepted for the award of any other degree or diploma in any university or other tertiary institution and, to the best of the author's knowledge and belief, contains no material previously published or written by another person, except where due reference has been made in the text.

The author gives consent to this copy of his thesis, when deposited in the University Library, being available for loan and photocopying.

Stephen K.N. Yeo 21/8/96

Acknowledgements

The author would like to express his sincere gratitude to his supervisor, Dr. Andrew J. Parfitt for his guidance and support throughout the course of this research, and for the time and effort that he devoted to many aspects of the work.

List of Author's Related Publications

The following is a list of the author's publications which are related to the research reported in this thesis.

K.N. Yeo and A.J. Parfitt, "Generalised spectral domain analysis of an infinite array of dielectric supported metal strip antennas", IEEE International Symposium on Antennas and Propagation, Newport Beach, California, pp. 972-975, June 1995.

K.N. Yeo and A.J. Parfitt, "Numerical analysis of arrays of finite lateral extent", Workshop on Applications of Radio Science, Canberra, June 1995.

K.N. Yeo and A.J. Parfitt, "Spectral domain analysis of infinite arrays of metal strip antennas in various configurations", Fifth Australian Symposium on Antennas, Sydney, pp. 23-24, February 1996.

K.N. Yeo and A.J. Parfitt, "Generalised Green's function analysis of infinite arrays of microstrip antennas with various configurations", IEEE International Symposium on Antennas and Propagation, Baltimore, Maryland, pp. 400-403, July 1996.

K.N. Yeo and A.J. Parfitt, "Finite array analysis using iterative spatial Fourier windowing of the generalised periodic Green's function", IEEE International Symposium on Antennas and Propagation, Baltimore, Maryland, pp. 392-395, July 1996.

List of Principal Symbols

Symbol	Description
a	ratio of currents on the two arms of a folded dipole
$\mathbf{A}$	magnetic vector potential
b	inter-element lattice spacing in the x dimension of a planar array
c	speed of light in vacuum
$c(x,y)$	two dimensional comb function
C, E, I, M	corner, edge, interior and center elements of a finite array
d	inter-element lattice spacing in the y dimension of a planar array
$\vec{E}^{i}$	incident electric field
$\vec{E}^{s}$	scattered electric field
$\vec{E}^{total}$	total electric field in the dielectric substrate
$\mathbf{E}$	vector of electric field excitations
E_0	electric field due to feedpoint voltage of one volt
E_j	elements of excitation vector $\mathbf{E}$
E_{rel}	relative error
$\tilde{F}$	Fourier transform
H	magnetic field
$G(r,r')$	Green's function
G_u	unit cell Green's function
$G_{isolated}$	Green's function for an isolated element

G_{∞}	infinite array Green's function
$G_{\infty}^{spatial}$	Spatial periodic Green's function for a rectangular grid
$G_{\infty,t}^{spatial}$	Spatial periodic Green's function for a triangular grid
$G_{\infty}^{spectral}$	Spectral periodic Green's function for a rectangular grid
$G_{\infty,t}^{spectral}$	Spectral periodic Green's function for a triangular grid
G_{∞}^{hybrid}	Hybrid periodic Green's function for a rectangular grid
$G_{finite}^{kl,MN}$	Periodic Green's function for the $(k,l)^{th}$ cell of a M x N finite array
h	height of metal strip dipole above the ground plane
J	electric current density
I	current
I_d	current on metal strip dipole
I_r , I_t	radiation and transmission line mode currents on coplanar strip feedline
$\mathbf{J}$	vector of current densities
J_c , J_d	current density on metal strip and in the dielectric
$J_{mn,kl}$	current density in the $(m,n)^{th}$ cell normalised to that in the $(k,l)^{th}$ cell
k_0	wave propagation vector in free space
k_{x_m}	wave propagation vector in the x dimension for the m^{th} Floquet mode
k_{y_n}	wave propagation vector in the y dimension for the n^{th} Floquet mode
$k_{z_{mn}}$	wave propagation vector in the z dimension for the $(m,n)^{th}$ Floquet mode
l	length of metal strip dipole
L_c , L_d	operators for scattered electric field

m, n	$(m,n)^{th}$ Floquet mode
m', n'	$(m',n')^{th}$ element of a planar array
M, N	number of elements in a finite array
n_x, n_y, n_z	number of segments in the x, y and z dimension
$\hat{n}$	outward pointing unit normal vector
N_f	number of samples used in Fast Fourier Transform
$P_j(x',y')$	two dimensional pulse basis function
$Q_j(x',y',z')$	three dimensional pulse basis function
R	active resistance
S	sum of a doubly infinite series
S_c	surface of metal strip conductor
S_d	surface of the dielectric substrate
t	thickness of substrate
T	vector transpose
T_x , T_y	direction cosines in the x and y dimensions
u	smoothing parameter
V	voltage
V_d	volume of dielectric region
w	width of metal strip
W	spectral window function
W_i	weighting function
X	active reactance
$\mathbf{Z}$	moment matrix

$\mathbf{Z_{xx}}$, $\mathbf{Z_{yy}}$	submatrices of moment matrix
$\mathbf{Z_{xy}}$, $\mathbf{Z_{yx}}$	submatrices of moment matrix
Z_{xx}^{spat}, Z_{xx}^{spec}	spatial and spectral components of moment matrix element
Z_{act}	active impedance
Z_b	active impedance at boresight angle
Z_d , Z_t	impedance of equivalent dipole and transmission line mode
Z_{in}	input resistance
Z_{kl}^{MN}	moment matrix element for the $(k,l)^{th}$ cell of a M x N array
Z^{∞}	moment matrix element for an infinite array
α, β, γ	unit normal terms
α_m , β_n	discrete variables used in Fast Fourier Transform
Ω	ohm
$\frac{\partial}{\partial x}$	partial derivative with respect to x dimension
λ	free space wavelength
ρ_c	charge density on metal strip
ρ_d	charge density in dielectric substrate
Δ	size of segment
ϕ	plane of scan
θ	beam steer angle
$\delta(x)$	Dirac delta function
∇	divergence
π	pi

$*$	convolution
μ_0	permeability of free space
ε_0	permittivity of free space
ε_r	relative permittivity
ω	angular frequency

List of Abbreviations

CAD	computer aided design
CPU	central processor unit
DBS	direct broadcast system
FDTD	finite difference time domain
FEM	finite element method
IVHS	intelligent vehicle highway systems
LITA	longitudinal integration and transverse assembly
MMIC	monolithic microwave integrated circuit
MoM	method of moments
PCS	personal communications systems
PWEMM	plane wave expansion moment method
TILA	transverse integration and longitudinal assembly
WLAN	wireless local area network

CHAPTER 1

Introduction

1.1 Microstrip Phased Arrays

In recent years, considerable effort in antennas research has been directed towards the realization of different types of arrays, ranging from the large and highly complex electronically-steered arrays in military surveillance systems, to the much simpler printed dipole antenna array. The emphasis in antenna array research has been driven by the demand for new, higher performance electronic systems, mainly in the fields of radar, communications and navigation. With increasing congestion in the frequency spectrum, attention is currently focussed on creating higher-frequency systems embracing millimetre, sub-millimetre and quasi-optical radiators [1].

Microstrip arrays form a major class of antennas that are useful for operation at millimetre wave frequencies. The basic configuration of the *microstrip antenna* is a metallic strip or patch printed on a grounded dielectric substrate. A *microstrip phased array* is a collection of such

substrate supported metal strips or patches together with their feed network, which are designed to provide a beam that is formed in the required direction by controlling the phase of excitation of the array elements.

Because of their high cost and thin profile, microstrip phased arrays had largely been used in military aircraft, missiles, rockets and satellites in earlier applications. However in the last decade, development and manufacturing costs of microstrip antennas have come down with increasing maturity of the technology, reduced cost of substrate material and manufacturing process, and the simplified computer aided design (CAD) tools that have become available. Cost reduction and new demands in areas such as civilian satellite communications have led to wider commercial applications of microstrip phased arrays [2]. Some of the recent commercial applications are in the areas of personal communications systems (PCS), mobile satellite communications, direct broadcast system television (DBS), wireless local area networks (WLANs), and intelligent vehicle highway systems (IVHS). Other applications include the use of microstrip arrays in synthetic aperture radars for remote sensing and in hyperthermia applications in the medical field.

In order to meet the modern specifications of the above applications, practical microstrip antennas have become increasingly more complex, comprising metallic radiators and feedlines as well as dielectric substrates and superstrates which may be continuous or discontinuous in the aperture plane. Appropriate modelling techniques are therefore required for the analysis and design of such complex antennas operating in an array environment. Compared to the scattering problem, the requirement for a well defined feedpoint and an accurate model of the feed region in the analysis of the antenna radiation problem poses a more stringent modelling requirement. Moreover, for small to medium size arrays, the correct design of elements on the periphery of the array is important, precluding the use of traditional infinite array analyses without appropriate modifications. A major challenge facing the array designer is to apply the known circuit and antenna modelling concepts to the design of an integrated assembly which not only achieves the scanning specifications, but is also robust and affordable. Additional factors influencing the analytical and numerical techniques used in the design of microstrip phased arrays include the need to compute the scanning performance to a degree of accuracy

sufficient to avoid costly experimental optimisation of the element design [3], and the need for realistic computing requirements in the numerical implementation.

The research reported in this thesis is concerned with numerical modelling of microstrip dipole arrays for purposes of analysis and engineering design. This thesis first presents a brief survey of the methods found in the literature which may be used for the analysis of microstrip antenna elements and arrays. Based on the considerations given in the survey, a new numerical technique which may be described as the *Generalised Periodic Green's Function Technique*, is developed, and then applied to the analysis of infinite arrays of metal strip and microstrip dipoles. Finally, the technique is extended into a *Generalised Periodic Green's Function - Spectral Windowing* technique which is used for the analysis of finite metal strip and microstrip dipole arrays.

1.2 Generalised Periodic Green's Function - Spectral Windowing Technique

The *Generalised Periodic Green's Function - Spectral Windowing technique* presented in this thesis falls under a general class of methods for analysis of microstrip antennas commonly known as full-wave analysis methods. The technique uses the *Integral Equation method* as the basis for formulating the problem, adopts the *Periodic Structure approach* which explicitly incorporates the periodicity of the array into the formulation, and implements the analysis numerically using the *Method of Moments*. As a first step, the technique is used for the analysis of an infinite array in which the current distributions on the elements are assumed to be identical. As a subsequent step, a *Spectral Windowing* technique is developed which transforms the periodic Green's function for the infinite array into a form that approximately describes the behavior of the elements in a finite array environment. The output of the two-step analysis is the set of equivalent currents representing each element of the array from which all the other parameters needed for understanding the behavior of the array may be obtained. One of the key advantages of the technique is that by modelling the equivalent currents making up the whole array structure,

no constraints are placed on the element geometry being modelled. In this thesis, the technique has been applied to the analysis of microstrip dipole arrays because of the interest in studying finite substrate, feedline and impedance matching effects on the scanning performance of such array elements. However in general, the technique can also be applied to the analysis of microstrip patch arrays and array elements with substrate inhomogeneities.

At millimetre wavelengths, the substrates used in typical Gallium Arsenide MMICs are electrically thick, and are therefore expected to have a significant effect on the design and performance of the elements and the phased array. In the past, considerable research into the radiation problem for dipole antennas on electrically thick substrates of infinite lateral extent has been published [4,5,6]. However, little has been published in the way of printed dipoles on finite size substrates until recently [7,8,9,10]. The work presented in thesis is an extension to these more recent investigations in that it develops a more computationally efficient technique for modelling infinite microstrip arrays with finite substrate geometries and extends the analysis to finite size arrays. Some work has been reported on the analysis of finite microstrip arrays [11,12,13,14], however in all these cases, the substrate is again modelled as an infinite slab. Therefore these techniques cannot be used to model finite microstrip arrays which have finite substrates. In the work reported in this thesis, the substrate which may be finite or infinite in dimensions, is explicitly modelled using basis functions in the infinite array technique. The application of the Spectral Windowing technique to the infinite array data would result in a finite array of elements in which the substrate would also be finite in extent.

Because of their small size and complex integration with the electronics, microstrip antennas fabricated using the MMIC process are difficult to tune and adjust. The accuracy of the numerical model is therefore crucial in the design process, and models which are able to analyse the whole physical structure of the array with a minimum of idealisations are highly desirable. The technique proposed in this thesis makes no assumptions about the current distributions on the radiating elements and about the nature of the fields in the dielectric regions. Furthermore, the entire structure of radiating elements with more

complicated geometries like folded-dipoles as well as the feedlines have been modelled with minimum idealisations. Because of its high computational efficiency, the technique can in principle be extended to the analysis of larger cells comprising sub-arrays of multiple elements and quasi-periodic structures such as those found in the literature [15].

Validation of numerical models is an essential requirement to establish confidence in their accuracy. Validation may be achieved using practical measurements, comparison with results of analysis published in the literature, comparison with calculations using alternative methods, or by testing the model under known conditions where the results are well established. In most cases, the infinite and finite array models presented in this thesis are compared either with results documented in the literature or with an analysis using an alternative method. Furthermore, the results of the infinite array models are also validated at known conditions such as scan angles at which a grating lobe is expected, and at scan angles along the array plane where no real power is expected to propagate away from the array. In the case of the finite array models, predictions for the centre element of a large but finite array are validated against an infinite array model with the same structure and geometry, where similar results are expected. Therefore, no reliance has been place on practical measurements for purposes of validation in this research.

In the numerical analysis of a microstrip array, the results reflect the total contribution of all the elements. The complexity of the array elements makes it difficult to isolate the cause of some of the effects. For example, an observed scan blindness might be due predominantly to the mutual coupling of the radiating element with either the feedline or the substrate. To solve this problem, a modular and stage-by-stage modelling approach has been adopted in this research. The simpler array models have been developed as self-contained modules so that they can form a part of a more complex array model. For instance, the model of an infinite array of substrate supported, coplanar stripline fed folded-dipoles was developed from the basic model of an infinite array of horizontal metal strips; the various other components such as the feedlines, substrates and folded arms were then added in stages. This has potential significance if it is required to develop the models into design software packages for general usage.

In this thesis, the numerical models are presented in three stages. In the first stage, metal strip dipoles in various configurations which operate in the central region of a large phased array, are analysed using an infinite array model. In the second stage, infinite array models are presented for microstrip dipole arrays with various substrate configurations. In the final stage, models are presented for metal strip and microstrip antennas operating both in the central region and periphery of a finite phased array. At each stage, the accuracy of the models are confirmed by validation against well established results from other sources. The models are also used to obtain results for various array parameters, so that the characteristics of the physical array represented by these models can be established before proceeding to the next stage. In certain cases, a component of the array element such as the feedlines may be omitted from the model when the substrates are included in the analysis, so that the effects due to the feedlines and the substrates could be separately observed and isolated.

One of the major research goals in this work is to develop a technique of analysis leading to numerical models which are computationally efficient so as to enable their implementation on a desktop computer. All the computer models have been developed with the view to minimise the computation time, computer memory and storage requirements. For purposes of standardisation, the numerical results presented in this thesis are all based on FORTRAN 77 programs which have been run on a single desktop computer in which the specifications which are given in Appendix A.

The numerical analysis using the proposed technique has revealed effects on metal strip and microstrip arrays associated with the geometry of the radiating elements, feedlines and substrate, as well as effects associated with the array lattice structure and the finite size of the array. For purposes of engineering design, some of these effects like grating lobes and scan blindnesses need to be avoided, whilst others could be exploited for reasons of impedance matching and optimization of the array's radiation and impedance characteristics. In this thesis, the implications of these effects have been illustrated using a number of design examples. Therefore, the demonstrated accuracy, flexibility and computational efficiency of the Generalised Periodic Green's Function - Spectral

Windowing technique makes it highly attractive for application to the analysis and design of practical microstrip phased array systems.

1.3 Outline of Thesis

This thesis is concerned with the development and application of a numerical technique for the analysis and design of various conventional and novel microstrip dipole arrays. The proposed technique is relevant for the analysis of arrays with both large and small number of elements, and where the substrate component of each array element may be infinite, semi-infinite or completely finite in its lateral extent.

Chapter 2 describes the main considerations leading to the development of the Generalised Periodic Green's Function technique for the numerical modelling of microstrip phased arrays. The demands of new applications are reflected in the requirement for more complex microstrip antenna element geometries which may involve discontinuous, multi-layered or inhomogeneous substrates. The complexity of the antenna element, coupled with the high cost of post-fabrication testing and adjustments, have created the necessity for accurate and flexible models to be used in the design process. The more widespread use and the availability of advanced software for engineering design on desktop computers, as well as the need to minimise design costs also make it very attractive for a numerical technique to be implementable on such computers. A survey of various methods to meet this requirement is presented, leading to the conclusion that the Integral Equation method using an appropriate form of Green's function may provide the best results. After examining the options on the approaches and types of Green's function that may be employed, it is proposed that the new technique should be based on a generalised periodic Green's function.

Chapter 3 develops the theoretical basis for the Generalised Periodic Green's Function technique and identifies the key properties of this Green's function that relate to the

computationally efficient modelling of phased arrays in general. The spatial form of the generalised periodic Green's function of an infinite array of point sources is first derived for a rectangular grid lattice, and then extended to the case of a triangular grid lattice. Using the Fourier transform, the point sources representation of the infinite array is transformed into a planar current sheet representation, leading to the derivation of the spectral form of the generalised periodic Green's function for both the rectangular and triangular grid lattices. The key properties of the periodic Green's function are then described and related to phased array modelling as applicable to the work reported here. Compared with the spatial form, the spectral form of the periodic Green's function enables the integration over the sources to be evaluated analytically. This property is highlighted as a major computational advantage of working in the spectral domain and the main reason for selecting the *Spectral Periodic Green's Function* to be used in this research. The numerical convergence property is highlighted as being critical to the computational efficiency of the technique, and the singularity and convergence properties of the spatial and spectral forms of the periodic Green's function are derived and discussed. The number of lobes in the radiation pattern is identified to correspond to the number of propagation Floquet modes of the spectral periodic Green's function. The emergence of grating lobes is shown to be dependent on the inter-element spacings of the array and the direction at which the beam is scanned. Out of an analysis of the spectral periodic Green's function is derived the well known condition that to avoid grating lobes for all scan angles, the inter-element spacings should not exceed half a wavelength for rectangular grid lattices and one wavelength for triangular grid lattices. Finally, the contribution of the Floquet modes to the active impedance is described, leading to the expected condition that at the grazing scan angle, no real power is propagated away from the infinite array.

Chapter 4 describes the procedure for applying the Generalised Periodic Green's function technique to the modelling of an infinite arrays. The technique is illustrated by modelling an infinite array of horizontal metal strips orientated with their faces parallel to the array plane. The problem is formulated in terms of equivalent two-dimensional currents on the surface of the metal strips, and the electric field integral equations are then solved using the Method of Moments. Various ways to maximise the computational efficiency of the technique are then described. In the problem formulation stage, one way is to use the

spectral form of the periodic Green's function in which the integration over the sources may be evaluated analytically. Numerical results from the model using this technique are shown. The issue of slow numerical convergence of the results and various approaches to overcome this problem are discussed. A technique of accelerating the convergence of the spectral periodic Green's function for on-plane interactions is described, leading to the development of a *Generalised Hybrid Periodic Green's Function* having *a spatial and a spectral component* both of which are rapidly convergent in their respective domains. An improvement in the computational speed by a factor of 40 to obtain a converged value of the hybrid Green's function over either the spatial or spectral forms is illustrated with numerical results.

In the numerical implementation stage, computational efficiency in the filling of the Moment Matrix by taking advantage of Toeplitz-like symmetries in the spectral periodic Green's function, use of look-up tables and by a grid segmentation scheme to minimise numerical evaluation of the spatial component of the hybrid periodic Green's function are adopted. In preparation for the modelling of three-dimensional element geometries, a new technique of integrating the Green's function over the sources distributed in the z dimension is described. The technique is then applied to the case where the horizontal dipoles are modelled as thin metal strips orientated with their faces perpendicular to the array plane. The accuracy of the models is validated using results obtained from other sources in the literature.

Chapter 5 describes some practical issues of modelling arrays of metal strip structures which may be utilised as the radiating elements and feedlines of microstrip phased arrays. The first issue relates to the efficient modelling of array elements with three-dimensional geometries. The technique for accelerating the convergence of the spectral periodic Green's function described in Chapter 4 is applied to the case where the source segments are distributed in the z dimension. A numerical experiment is used to demonstrate the computational efficiency achieved by this convergence acceleration technique. Based on this technique, an infinite array of vertical metal strip monopoles is developed. The issue of metal strip junctions is introduced, and various approaches for junction modelling found

in the literature are discussed. A new metal strip junction model is described and applied to the modelling of the metal strip folded-dipole infinite array. The next issue is the modelling of feedlines; this is done using the junction modelling technique described above and applied to the analysis of an infinite array of horizontal metal strips with coplanar strip feedlines. Finally, impedance matching considerations are discussed and the modelling of an infinite array of folded dipoles with feedlines, is described. In every case, the accuracy of the models is validated either using published data from another source or at specific conditions where the behavior of the array is well established. The numerical efficiency of the technique is demonstrated by the short computation time taken by the models using a desktop computer, and the flexibility of the technique can be seen in the variety of models used for illustration.

In Chapter 6, the Generalised Periodic Green's Function technique is applied to the analysis of infinite arrays of microstrip dipoles with conventional and novel substrate configurations. Two basic architectures of MMIC phased arrays are described in which the antenna elements, module electronics and distribution networks may be integrated either in the transverse direction of the array plane or longitudinal to the array plane. In these two architectures, the substrate is usually a continuous slab in the first case and finite in at least one of the lateral dimensions in the second case. A model is developed for an infinite array of metal strip dipoles supported on an infinite slab of grounded dielectric substrate, which corresponds to the transverse integration architecture. The problem is formulated in terms of surface currents on the metal strips and volume polarisation currents in the dielectric substrate; the rest of the solution procedure is similar to that for the infinite array of horizontal metal strip dipoles. Numerical results obtained from the model are compared with data for a similar structure published in the literature [33] and excellent agreement is found, especially in the detection of the substrate-induced scan blindness angles of the array. Using the same technique, a metal strip dipole infinite array model is developed where the substrates are in the form of semi-infinite sheets. Again, the numerical results of the model compare very well with published data of a similar structure using a different technique of analysis [7]. A third metal strip dipole infinite array model is then developed in which the substrates are finite in both the lateral dimensions, and the results agree very well with an analysis using the spatial form of the generalised periodic Green's function

[10]. The superior computational efficiency of the spectral periodic Green's function over the spatial form is demonstrated by a comparison of the results using both techniques. For all the three models developed, computer CPU times of less than a minute to calculate a converged value of active impedance using a desktop computer demonstrates the numerical efficiency of the technique. Finally, models of infinite arrays of substrate supported metal strip dipoles and metal strip folded dipoles with coplanar strip feedlines are developed to explore the relative significance of feedline and substrate induced scan blindness, and for impedance matching considerations.

Chapter 7 develops a *Spectral Windowing* technique which, when applied to the results of the infinite array models described in Chapter 4 to 6, enables the finite array behavior to be predicted. This technique is based on a *Generalised Periodic Green's Function for a finite array* which is derived from first principles using an Element-by-Element approach. An iterative variant of the technique is also developed which is able to improve the accuracy of the technique and indicate the likely accuracy of the results. The technique is illustrated using the analysis of a finite array of horizontal metal strip dipoles. The results compare well to those obtained by an accurate but less numerically efficient full analysis of the array using the Element-by-Element method. The technique is then applied to the analysis of a finite array of horizontal metal strips having coplanar strip feedlines in the first case and a substrate in the second case, where feedline and substrate induced scan blindness effects for the respective infinite arrays have been observed from the models described earlier. In both cases, near unity active reflection coefficient values for all the elements and negative active resistances in some of the elements are predicted by the model in the vicinity of the substrate-induced scan blindness angle of the infinite array. Therefore, it is clear that the technique has yielded information regarding the edge effects of a finite array not otherwise available from an infinite array analysis, and which is very computationally demanding to obtain using a full Element-by-Element approach analysis. This information would be very useful for purposes of practical engineering design of finite microstrip arrays.

From the theoretical derivations and extensive applications discussed in this thesis, conclusions regarding the capability of the Generalised Periodic Green's Function

technique are drawn in Chapter 8. The relevance of this research to the accurate, flexible and computationally efficient analysis and design of microstrip arrays in general is highlighted and certain areas for further research are identified.

In summary, the major contributions presented in this thesis are as follows:

- A survey of the current methods useful for analysis and design of microstrip antennas and phased arrays together an indication of their relative merits, is provided.
- A new infinite array technique for the analysis of metal strip and microstrip dipole arrays is developed, and which is characterised by:
    - Problem formulation using Electric Field Integral Equations.
    - A generalised periodic Green's function which is not constrained by the element geometry and which explicitly models the array's periodicity.
    - Numerical implementation using the Method of Moments.
    - Accurate prediction of the array behavior as testified by validated results.
    - High computational efficiency to be able to model with minimum idealisations and to implement on a desktop computer, a microstrip array with a complex three-dimensional element geometry comprising as an example, a folded-dipole radiating element and coplanar strip feedlines on a finite substrate.
    - Flexibility to model discontinuities in the substrate of the microstrip antenna element, and array elements arranged in both rectangular or triangular grid lattices.
- A technique for accelerating the convergence of the spectral periodic Green's function has been further developed, together with a technique for integrating this Green's function over sources distributed in the direction perpendicular to the array plane, so that three-dimensional phased array geometries can be efficiently analysed.
- A simple and accurate technique for modelling metal strip junctions is presented.

- A spectral windowing technique based on the Finite Array Generalised Periodic Green's Function is developed which is able to predict the behavior of the finite array by operating on the results of the infinite array model.
- The phenomenon of feedline-induced and substrate-induced scan blindnesses in the scanning performance of microstrip phased arrays is described, and various ways to minimise the scan blindness effect are identified.
- The effects of the dielectric substrate on the performance of microstrip arrays is described and ways to exploit the beneficial effects to optimise the antenna's performance are also described.
- Extensive practical design examples are used to illustrate the application of the above modelling techniques, and solutions to design problems for both infinite (representing very large) and small finite arrays are described.

The key features of accuracy, flexibility and computational efficiency of the Generalised Periodic Green's Function - Spectral Windowing technique demonstrate its potential for modelling microstrip arrays in general.

CHAPTER 2

Methods for Analysis and Design of Microstrip Arrays

2.1 Introduction and Overview

In Chapter 1, microstrip phased arrays were introduced as a class of antennas suitable for operation at millimetre wavelengths and for use in a wide variety of military and commercial applications. Since the invention of the microstrip antenna over 40 years ago [16,17] , the demand for its application has been increasing rapidly, especially in the last two decades. The early models used for analysing such antennas were sufficiently adequate to meet the simpler design needs of the applications at that time. However, in order to meet the demands of modern system specifications, practical microstrip antennas have become increasingly more complex and hence require more complex and accurate

analysis. In line with advances in the technology, the techniques for numerical analysis need to be sufficiently *flexible* to deal with more complex structures and yet be able to yield accurate results with a minimum of computational resources. Numerical techniques for such applications which can be implemented on personal computers or workstations widely available in industry and R&D establishments are desirable. Based on these considerations, a numerical technique suitable for the analysis of microstrip arrays should desirably have the following characteristics:

- Prediction Capability - It should be able to predict the main parameters describing the characteristics of the elements in an array including the input impedance, radiation patterns, directivity, gain, efficiency and polarization pattern. This is a primary requirement of the numerical tool.

- Flexibility - It should be sufficiently general to be able to model a variety of array configurations which may include:

    - Arrays with different numbers of elements, ranging from large arrays with thousands of elements, to small arrays with only a few elements.

    - Various lattice arrangement of the elements, including rectangular and triangular grid lattices.

    - Metallic part of the elements, including striplines and patches, located either on top or at the side of the substrate.

    - Substrate or superstrate continuity and homogeneity.

    - Feed mechanism which may be direct feedlines or electromagnetic coupling.

- Accuracy - It should have adequate accuracy for purposes of engineering analysis and design.

- Computational efficiency - It should place a realistic demand on the computational resources required for its numerical implementation.

Having surveyed various methods found in the literature which may be used for the analysis of microstrip antennas and phased arrays, it has been concluded that although each

of these methods has certain unique advantages, none of the methods has all of the above characteristics to a high degree. Therefore, a new technique for the analysis of microstrip dipole arrays is proposed. The purpose of this chapter is to briefly describe the methods of analysis found in the literature and to evaluate their suitability for modelling of microstrip antennas and arrays based on the characteristics listed above. The reasons for the selection of the Integral Equation method and the development of a new *Generalised Periodic Green's Function and Spectral Windowing technique* based on this method is also provided.

2.2 Methods of Analysis for Microstrip Arrays

The development of flexible and numerically efficient techniques for analysis and design of microstrip antennas and arrays is currently still an active area of research. Some of these techniques have already been developed into Computer-aided Design (CAD) software for general usage and marketed commercially for applications in industry, defence and academia. Examples of such software include Ensemble, Micropatch, PCAAD, em and PATVU. As surveyed by Pozar and James [18], the various techniques can be broadly divided into two groups: *reduced analysis* methods, and *full-wave analysis* methods. Some of the techniques can be used for the analysis of microstrip antennas only whilst others can be used for analysing both microstrip antennas and arrays; the distinction will be made in the description to follow. In Figure 2.1, a chart is given which provides an overview of the various methods which fall under these two classes, as well the relationship to the choice of a specific method as the basis for developing a new technique to be derived in Chapter 3. The details of the chart are elaborated below. In this section, each method will be briefly described and evaluated in terms of its suitability for modelling microstrip phased arrays based on the characteristics of a desirable technique provided in Section 2.1. The survey will also identify the key issues for the selection of the *Integral Equation method* as the basis for developing the new *Generalised Periodic Green's Function technique*, whose theoretical basis will be presented in Chapter 3 and whose application to metal strip and microstrip dipole arrays will be discussed in the following chapters.

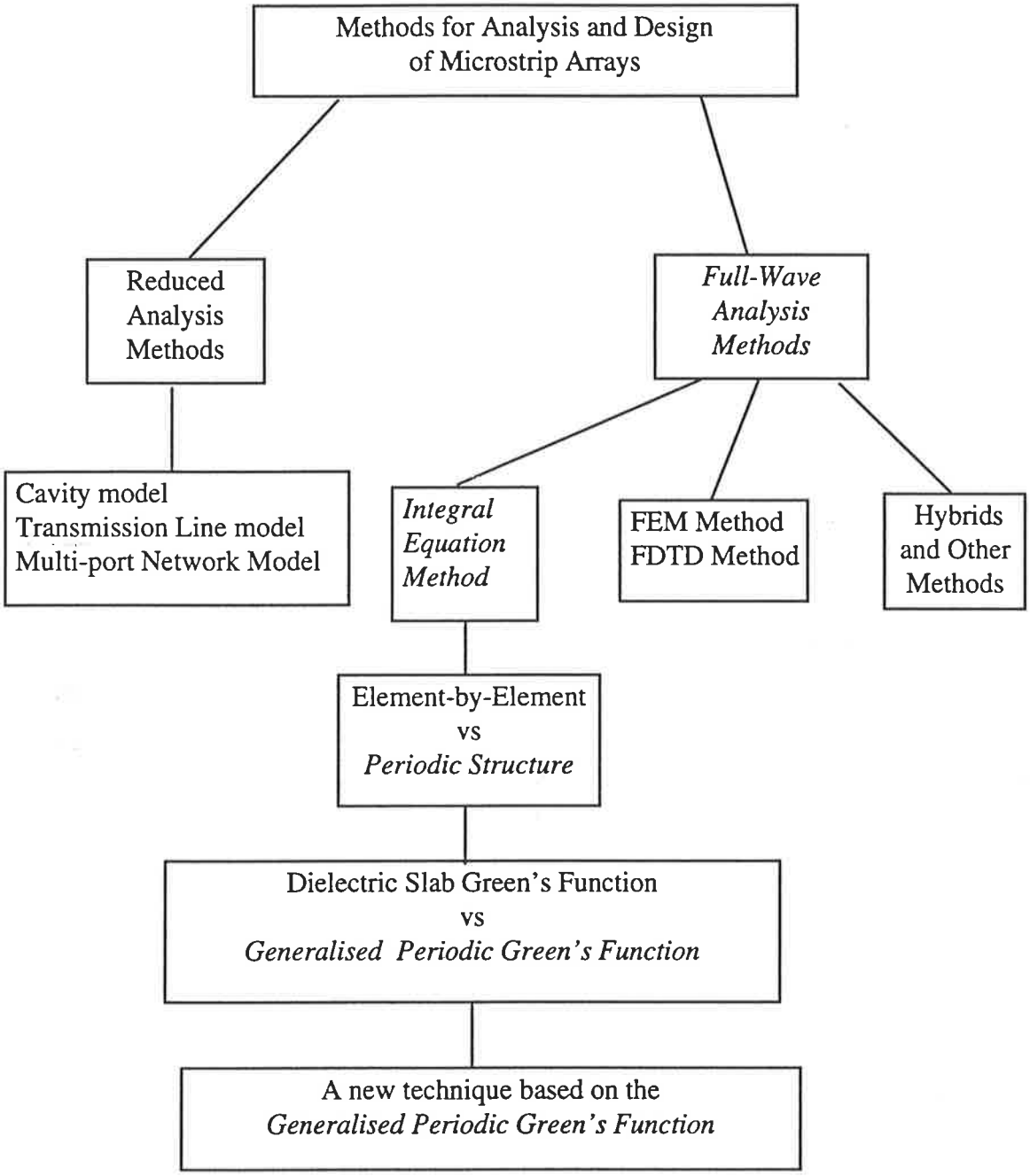

Figure 2.1 : Chart showing methods suitable for the analysis and design of microstrip antennas and arrays

2.2.1 Reduced Analysis Methods

Reduced analysis methods generally introduce one or more approximations to simplify the microstrip antenna problem. They are often accurate enough for first cut designs, and have a clear advantage in terms of computational simplicity and speed. Examples of these methods include the transmission line technique which models the antenna as a transmission line section with lumped loads; the cavity model which uses a magnetic wall boundary condition approximation for the periphery of the patch; and the multi-port network model which is a generalisation of the cavity model. These models were the first to be developed for microstrip antennas and have been useful for practical design as well as providing a good intuitive explanation of the operation of such antennas.

Transmission Line Model

Transmission line models treat the microstrip antenna as a loaded transmission line resonator, and models the patch as two identical resonant slots. Each slot is formed by the radiating edge of the patch and the ground plane, and has a depth of approximately a quarter wavelength in the dielectric substrate. The advantage of this model lies in its simplicity as the resonant frequency and input resistance are given by simple formulas based on transmission line theory. However its disadvantages [19] include unsuitability for modelling of arrays and of patches with other than rectangular shape, a need for an empirically determined correction factor to account for the fringing fields at the radiating edges, and difficulty in modelling the feed mechanism. More recent work has attempted to improved the accuracy of this type of model by various methods such as taking into account the mutual coupling between the slots and introducing simple analytic expressions for parameters such as the input admittance [20].

Cavity Model

In the *cavity model*, the microstrip patch antenna is modelled as a thin TM_z - mode cavity surrounded by magnetic walls. The electric and magnetic fields between the patch and ground plane are then expanded in terms of a series of cavity resonant modes [21,22]. As with the transmission line model, the effect of fringing fields at the edges of the patch is not modelled, but compensated for by means of a correction factor to the resonant patch length. An effective dielectric loss tangent is used to account for the power lost to radiation. A variation of the cavity model known as the *multi-port network model*, divides the cavity into segments, expands the fields in these segments in terms of eigenfunctions, and combines the multi-port Z-matrices corresponding to the segments to form an overall Z-matrix for the structure [23]. This technique is an improvement over the cavity model in that the feed reactance is built into the theory, but its main limitations are unsuitability for modelling arrays and the effect of thick substrates.

Despite some notable advances that have been made to overcome some of their limitations, the inherent drawbacks of reduced analysis methods have been:

- Limited accuracy in determining the resonant frequency and input impedance, especially when dealing with thick substrates
- Limited capacity to handle mutual coupling, large arrays, feed network effects and multi-layer substrate configurations.

Therefore these methods have not been considered here as candidates to develop a comprehensive tool for the analysis and design of microstrip arrays.

2.2.2 Full-wave Analysis Methods

Full-wave analysis refers to an electromagnetic solution that includes all relevant wave mechanisms, allowing the enforcement of boundary conditions to an accuracy limited only by the numerical implementation of the solution. Hence a full-wave analysis method

accounts for the dielectric substrate more rigorously than reduced analysis methods in the analysis of the microstrip antenna problem. Such models include the Integral Equation, Finite Element (FEM), Finite Difference Time Domain (FDTD) methods. The methods in this category are accurate and capable of calculating all the relevant electrical parameters of the microstrip array for a wide range of array geometries including feed networks and multi-layer configurations. However, their disadvantages are their greater computational requirement compared with reduced analysis methods and lower level of user confidence when experimental or other independent validation is absent.

Integral Equation Method

The Integral Equation method is among the most commonly used full-wave analysis methods, and a large number of solutions have been developed for specific classes of antennas. The problem is formulated using the integral form of Maxwell's equations and usually with a Green's function to account for the mutual coupling. The different types of Green's functions that may be used has led to the development of a number of different techniques for formulating the problem within this general method. The integral equations are discretised to convert them to matrix equations using the Method of Moments. The last step in this method is the numerical solution of a set of linear equations, which is usually done with a computer subroutine based on a method such as Gaussian elimination [24]. The solution is a set of equivalent currents from which all the other parameters such as radiation pattern and reflection coefficient may be obtained. Being a full-wave analysis method, mutual coupling between the sources and all the field effects of the antenna are explicitly modelled, so that no correction factors need to be applied to the results. The Integral Equation method has the advantage of being able to predict the behavior of microstrip antennas and arrays with high accuracy, and is suitable for modelling of microstrip arrays. However despite the demonstrated versatility and accuracy, most of the techniques based on the Integral Equation method suffer from the drawback of requiring extensive computer time, and from the fact that any change in the geometry such as the patch shape, configuration of substrate or method of feeding, would require the development of a new solution.

Finite Element Method

The Finite Element Method has been used for accurately simulating scattered or radiated fields from complex three-dimensional objects whose geometry varies on a scale of a fraction of a wavelength. A region to be analysed is enclosed by bounding walls and divided into a finite-element mesh, so that electromagnetic fields can be simulated in the waveguides and cavities formed in the bounded region. The difficulty in applying this method to radiation problems involving large arrays is that the finite-element mesh has to be truncated at some large but finite size. Recent extension of this method [25,26] has coupled the three-dimensional Finite Element (FE) solutions interior to the bounding surface with an efficient Integral Equation (IE) solution that enforces the Sommerfeld radiation condition either exactly or approximately. The main advantage of this method is in modelling objects that do not allow an analytic solution. However, the number of elements making up the mesh is usually very large, thus making the technique more suitable for implementation on a parallel processing supercomputer.

Finite Difference Time Domain Method

Like the FEM, FDTD solutions model the entire antenna, including substrate and metal components, and some of the surrounding volume. The FDTD method is formulated using a central difference technique for discretizing Maxwell's curl equations in both time and space, in order to calculate the fields on the nodal points of the discretized finite volume which surrounds the antenna [27].

The FEM and FDTD methods are both extremely versatile for handling arbitrary geometries, including discontinuous, multi-layer and inhomogeneous dielectrics. However, they often also require considerably more computing power than the Reduced Analysis methods and the Integral Equation solution for the analysis of a comparable array element geometry. In most cases, supercomputer implementation is required by these methods to produce results within a reasonable time. Hence these two methods are not preferred for modelling the radiation of microstrip arrays.

Hybrid and Other Methods

The methods listed in this chapter are not exhaustive, but only represent the more common numerical methods encountered in the literature. There are a number of other techniques which may be either a variation of one of the methods discussed above, or represent a hybrid of two or more of these methods. One of these methods is the Plane Wave Expansion Moment Method (PWEMM) [28], which is a form of Integral Equation solution but which does not make use of the Green's function. It has been successfully used in the modelling of infinite arrays of thin-wire radiating elements with feedlines [28]. However, without a Green's function, it is difficult to adapt this method to model the substrate part of microstrip antennas and to model finite size arrays.

Summary

Of the two broad classes of modelling techniques outlined above, it may be concluded that reduced analysis can offer quick and simplified solutions with minimal computational requirements; but these solutions are inherently less accurate and limited to simple antenna structures. Hence the approach used in reduced analysis methods are considered to be unsuitable as a basis for developing a highly accurate and flexible, but computationally efficient numerical technique for the analysis and design of microstrip arrays. Full-wave analysis methods offer much better solution accuracy and flexibility, but generally require large computing resources in their numerical implementation. In many cases, a supercomputer is required to evaluate the solutions within a reasonable amount of time. Among the full-wave analysis methods, the Integral Equation method offers good accuracy for purposes of engineering design and allows the problem to be formulated such as to require less computational resources for their implementation than FE and FDTD methods. Hence, the Integral Equation method is adopted to develop a new numerical technique which offers good accuracy and flexibility to handle a wide range of microstrip antenna structures, but at the same time, avoid the high demand on computing resources normally associated with full-wave analysis methods. A brief description of the important features of this technique is provided in the next section.

2.3 The Generalised Periodic Green's Function Technique

Integral Equation analysis implemented using the Method of Moments (MoM), is one of the most commonly used full-wave methods for the analysis of microstrip antennas and arrays. Whilst the MoM implementation technique is already well established, there is considerable scope within the Integral Equation analysis method for formulating the antenna problem in such a manner as to optimise both the accuracy and efficiency of the numerical solution. Some techniques produce extremely accurate results, but they usually also require large computing resources which can often only be met by a supercomputer. The two factors which determine computational efficiency of the technique to a large degree are the way that mutual coupling between the array elements is modelled, and the way that the source elements are modelled by the Green's function.

2.3.1 Modelling of Mutual Coupling

It is widely known that *electromagnetic coupling* between elements has an influence on array performance, and that these effects are often significant, particularly if the radiators are closely spaced. The *active impedance* is the impedance at the feed port of an antenna element under conditions where all of the elements of the array are excited to produce a given radiation pattern. Because of mutual coupling, the active impedance of a phased array element changes as the elements are excited to scan the beam through different angles. In the case of finite arrays, the active impedance also depends on the relative position of the particular element with respect to other elements in the array. Hence, mutual coupling effects produce a number of practical difficulties in the design and operation of a scanning array, and must accordingly be taken into account in any numerical technique employed to model the array's behavior. There are in general, two approaches to account for mutual coupling in phased arrays.

Element-by-Element Approach

The *Element-by-Element Approach* accounts for the cumulative effect of mutual coupling between all the elements. The active impedance of an element in an array is therefore obtained from a knowledge of the self-impedance of the element and the mutual impedance between neighbouring elements. The advantage of the Element-by-Element approach is that it may be used to analyse either an isolated element or an array of elements. Although it does not by itself, yield any insight into the characteristics associated with the periodicity of an array, the numerical results using this approach serve as a useful check on those of other approaches. The main drawback of this approach is that the computational resources required is proportional to the square of the number of elements making up the array. If the array has many elements, or if the complexity of the element geometry requires the currents to be represented by a large number of basis functions, a numerical analysis using this approach would almost certainly require excessive computer resources.

Periodic Structure / Infinite Array Approach

If a phased array consists of a large number of elements, it is convenient to view it as consisting of two components: a central region and a peripheral region near the edges. The elements in the central region appear to operate in the same environment, and thus may be analysed as if they are located within an infinite array environment. This method, which has been described by Oliner and Malech among others as the *Periodic Structure Approach* [30], incorporates the array's periodicity into the model. A description of the application of this approach to the derivation of the generalised periodic Green's function is given in Chapter 3.

In summary, analysis based on the Element-by-Element approach offers potentially accurate results and flexibility by progressing from the single isolated element to an element operating in a array which may be of any size. However, its main disadvantage is the prohibitively high requirement for computational resources to model microstrip arrays. The Periodic Structure approach enables the direct analysis of an element operating in an infinite array environment, and is computationally more efficient for predicting the

behavior of elements in the central region of large arrays. Chapter 7 will describe a *Spectral Windowing* technique which uses the information yielded by a Periodic Structure analysis of an infinite array to predict the behavior of elements at the periphery of a finite array having the same element and lattice structure. It has been found that compared with the Element-by-Element approach, this two-stage analysis still offers significantly greater computational efficiency for the analysis of finite microstrip arrays. For the above reasons, the new technique to be introduced in this section is based on the Periodic Structure approach.

2.3.2 Green's Function Modelling of Sources

In most Integral Equation solutions for microstrip antenna arrays the dielectric substrate is accounted for in a rigorous manner by means of the Green's function. The Green's function is essentially the vector potential response to the current sources in the antenna. A form of Green's function which has been frequently used by Pozar [31] and others for the analysis of microstrip antennas is known as the Dielectric Slab Green's Function whose geometry is given in Figure 2.1.

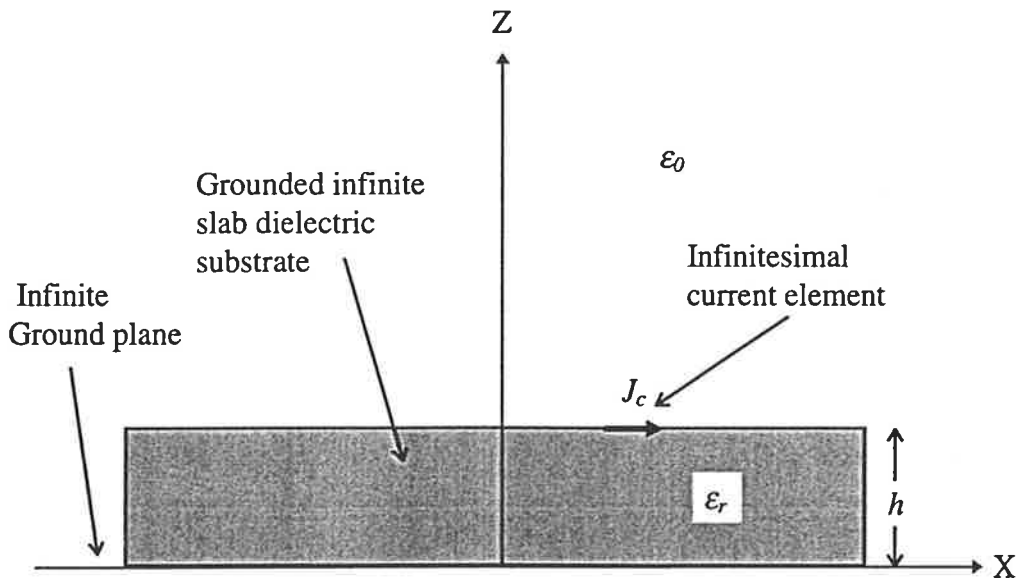

Figure 2.1 : Geometry for an infinitesimal current element on an infinite slab of grounded dielectric substrate

Figure 2.1 shows an infinitesimal current element located on the top face of a grounded dielectric substrate which is infinitely large in extent in the *xy* plane. The Green's function has been developed for this single current element on the infinite dielectric substrate. It has been shown [32] that this Green's function can also be configured to model an infinite array of sources; in this form, it is may be described as a Green's function of a periodic structure. Examples of full-wave analysis models using the Dielectric Slab Green's function for modelling of infinite arrays of printed dipoles and microstrip patches [33,34] are widely available in the literature.

An alternative Green's function for a periodic structure is the *Generalised Periodic Green's Function* of an infinite planar array of regularly spaced sources with uniform amplitude and linear progressive phase shift. A formal derivation of this Green's function will be presented in Chapter 3. Although both types of Green's functions are capable of modelling an infinite array, the distinct differences between them are summarised in Table 2.1 below.

Dielectric Slab Green's Function	Generalised Periodic Green's Function
Dielectric substrate automatically accounted for by the Green's function - hence, no basis functions required for the substrate	Green's function is independent of substrate geometry; substrate is modelled by volume polarisation currents and expanded using basis functions
Not suitable for modelling discontinuities of the substrate	Able to model both finite and infinite geometry substrates
Assumption of infinite slab substrate is retained when modelling a finite size array of radiating elements	Able to model a truly finite array where the radiating element, substrate and ground plane are all finite in extent
More difficult for modelling layered or inhomogeneous substrate.	Not inherently constrained by substrate inhomogeneity

Table 2.1 : Comparison between Dielectric Slab Green's function and Generalised Periodic Green's function

Of the two types of Green's functions, numerical evaluation of the Dielectric Slab Green's function appears to be more computationally efficient as basis functions are not required for modelling the substrate. However, it offers less flexibility for modelling microstrip arrays with finite substrate geometries. It has been found that the computational efficiency for the numerical evaluation of the Generalised Periodic Green's function can be significantly improved by other means; a detailed discussion of this will be given in Chapter 4. Hence it was decided to base the new technique on the Generalised Periodic Green's function which will be derived in Chapter 3.

2.4 Summary

From the considerations outlined in this chapter, it is apparent that the choice of the method of analysis has considerable impact on the overall characteristics of a numerical technique for the analysis of microstrip arrays. In this chapter, various methods have been briefly described and evaluated against the desirable characteristics enumerated in Section 2.1. It is concluded that there is scope for developing a new technique with overall improvement over the existing techniques in terms of accuracy, flexibility and numerical efficiency. This new technique is proposed as the *Generalised Periodic Green's Function technique* which makes use of the Integral Equation method of analysis, the periodic structure approach and a generalised Green's function which because it is not constrained by the element geometry offers better modelling flexibility than the Dielectric Slab Green's function. This chapter has therefore provided the context for the development and application of the Generalised Periodic Green's function technique in the chapters to follow. Over the last four decades, a proliferation of many innovative microstrip antenna designs have emerged to meet a wide variety of applications. The models presented in the thesis are not intended to be exhaustive, but to demonstrate the technique's potential for flexible, accurate and numerically efficient modelling of a wide variety of microstrip arrays to meet the requirements of engineering design. Therefore, the proposed technique widens the options currently available for the analysis and design of the new generation of microstrip phased array antennas to meet the demands of modern applications.

CHAPTER 3

The Generalised Periodic Green's Function: Derivation and Properties

3.1 Introduction and Overview

In the last chapter, a brief survey was presented of various methods that may be used for the analysis of microstrip antennas and arrays. It was concluded that a full-wave analysis using a *Generalised Periodic Green's Function Technique* based on the Integral Equation Method offers the advantages of good engineering accuracy, flexibility to handle array elements with substrate discontinuities, and potential computational efficiency to enable implementation on a desktop computer. The kernel of the technique developed in this thesis is the *Generalised Periodic Green's Function.* An in-depth understanding of this

Green's function and its properties enables the technique to be efficiently applied to the analysis of both infinite and finite arrays. In its basic form, the Green's function refers to infinite arrays; hence the technique using this Green's function by implication adopts an *infinite array approach* to the solution of the problem. However in Chapter 7, a form of the *Generalised Periodic Green's Function for a Finite Array* is derived and developed into a technique to solve the finite array problem.

A description of some of the properties of the periodic Green's function can be found in a number of references in the literature [35,36,37,38]. However, the discussion in these references is focused on the mathematical properties of the Green's function rather than the implications for analysis of antenna arrays. Furthermore, the Green's function described in the literature applies only to structures where the sources are spaced at regular intervals in the aperture plane to form a rectangular grid lattice. In practice, it is also possible to arrange the sources at regular intervals into other types of lattices such as a skewed [39] or triangular grid [40].

In this chapter, a method of deriving the *Spatial and Spectral forms of the Generalised Periodic Green's Function* for a *rectangular grid lattice* will be presented. The analysis will be extended to the derivation of these two forms of the periodic Green's function for a *triangular grid lattice*, which will be used in Chapter 5 for the analysis of phased arrays arranged in a triangular grid. Some of the properties of the Generalised Periodic Green's Function will then be described in relation to practical phased array modelling. Based on the theoretical concepts developed in this chapter, the Generalised Periodic Green's Function Technique is described in Chapter 4 and applied to the analysis of infinite arrays of metal strip structures and microstrip dipoles in Chapters 5 and 6, respectively.

3.2 The Spatial Periodic Green's Function

Figure 3.1 shows an infinite planar array where the elements are scalar point sources arranged in a rectangular grid lattice and spaced at regular intervals b and d apart in the x and y directions, respectively. The point sources have identical magnitudes and a linear progressive inter-element phase shift in the xy plane such that a plane wave is propagated away from the array in the (θ, ϕ) direction.

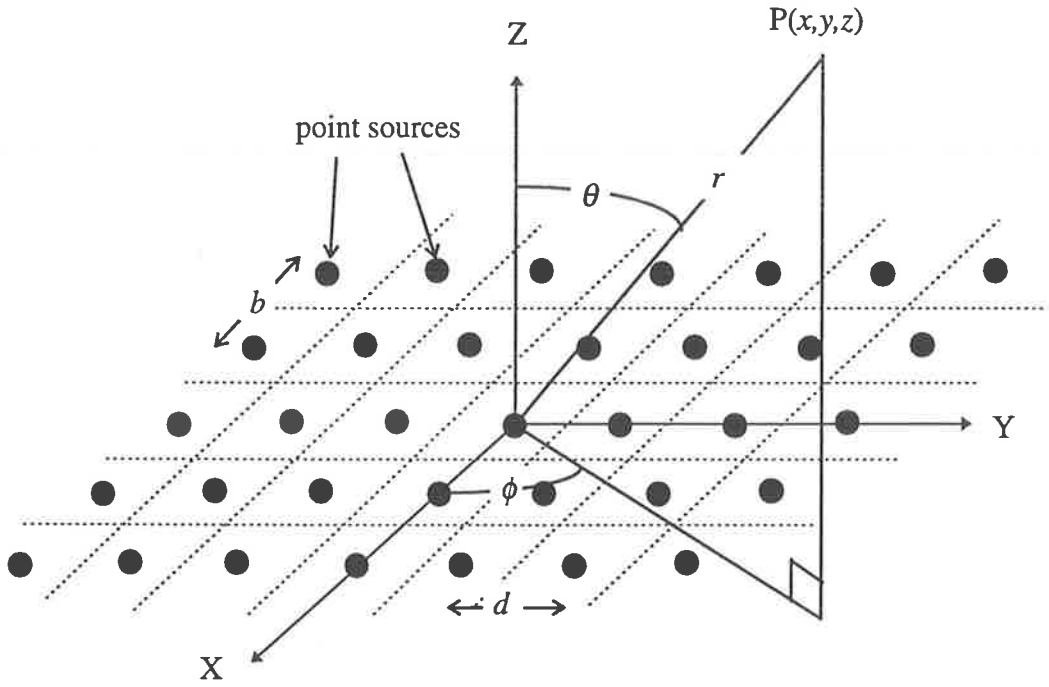

Figure 3.1 : An infinite planar array of point sources arranged in a rectangular grid lattice

Each point source is located within a unit cell which is enclosed by the cell boundaries represented by the dashed lines in the diagram. As described by Jorgenson and Mittra [37], the spatial periodic Green's function is defined as the vector potential response at a point $P(x,y,z)$ due to the infinite array of sources J, each of which is located at (x',y',z') in the (m,n)th unit cell. The array of unit amplitude phase-shifted sources may be represented mathematically as a product of phase-shifted Dirac delta functions as follows:

$$J(x,y,z) = \sum_{m=-\infty}^{\infty} \sum_{n=-\infty}^{\infty} \delta(x-x'-mb)\,\delta(y-y'-nd)\,\delta(z-z')\,e^{-jk_x mb}\,e^{-jk_y nd} \qquad (3.1)$$

where $k_x = k_0 \sin\theta\cos\phi$ and $k_y = k_0 \sin\theta\sin\phi$ are the components of the free-space wave propagation vector, k_0, in the x and y directions respectively; and the exponentials represent the linear phase shifts. The Dirac delta functions are used to denote locations where the currents exist, and do not imply infinite currents at these locations. The spatial form of the periodic Green's function for a rectangular grid lattice is then given by the integral of the 3-dimensional free-space scalar Green's function over the sources:

$$\begin{aligned} G_{\infty}^{spatial} &= \int_{-\infty}^{\infty}\int_{-\infty}^{\infty}\int_{-\infty}^{\infty} \frac{e^{-jk_0 r}}{4\pi r} J(x,y,z)\, dx\, dy\, dz \\ &= \sum_{m=-\infty}^{\infty}\sum_{n=-\infty}^{\infty} \frac{e^{-jk_0 r_{mn}}}{4\pi r_{mn}} e^{-jk_x mb}\, e^{-jk_y nd} \end{aligned} \tag{3.2}$$

where $r_{mn} = \sqrt{(x-x'-mb)^2 + (y-y'-nd)^2 + (z-z')^2}$, and each term in the double summation refers to the contribution of the point source in the (m,n)th cell to the periodic Green's function. The superscript and subscript of the symbol G refers to the spatial form of Green's function, and the fact that it is an infinite array Green's function, respectively. Unless otherwise stated, the Green's function should be taken as referring to an infinite array in a rectangular grid lattice.

It should be noted that the infinite array Green's function defined in (3.2) describes only one point source in each unit cell. If the radiating element in each unit cell consists of distributed sources, then the Green's function may be integrated over all the sources making up the element. Hence (3.2) describes a generalised periodic Green's function in the sense that it is not constrained by the geometry of the array element. An important implication of this is that when this Green's function is applied to the modelling of practical phased arrays, the technique is also not constrained by the geometry of the array elements.

3.2.1 Spatial Periodic Green's Function for a Triangular Grid Lattice

The periodic Green's function derived in Section 3.2 applies only to an infinite array in which the elements are arranged in a rectangular grid lattice. Although the rectangular grid lattice is probably the simplest to analyse, it is not optimum in terms of avoiding a grating lobe which is the scan angle at which a second main lobe emerges in the radiation pattern of the array. In general, it is possible to arrange the elements of the array in an alternative grid shape such as a skewed grid of which a special case is the triangular grid. The ability to modify a chosen grating lobe is extremely useful in array design, and certain types of grid lattices allow substantially wider inter-element spacings and consequently the use of fewer elements to achieve the same scanning effect. Sharp [40] has found that by arranging the elements of a phased array in a triangular pattern, the number of elements needed is reduced by as much as 13.4% compared with the rectangular grid lattice, for no grating lobes at the same scan angle of the main beam. Hence it is useful to extend the periodic Green's function analysis of infinite arrays to include a triangular lattice because of its practical design advantages. It is also noted that a number of infinite array analyses given in the literature that are useful of comparison of results, are based on triangular grid lattices. It is therefore important to develop models which can be configured for the triangular grid lattice, so as to be able to validate their accuracy by comparison with these results.

Figure 3.2 depicts a triangular grid lattice where the rectangles and circles both represent the point sources of the infinite array. In this lattice, the columns of sources are separated by a distance b, and the rows of sources are separated by a distance d. In order for a plane wave to be propagated away from the array in the direction (θ,ϕ), a linear phase shift of bk_x is imposed on the sources between adjacent columns, and dk_y is imposed on the sources between adjacent rows, where $k_x = k_0 sin\theta cos\phi$ and $k_y = k_0 sin\theta sin\phi$.

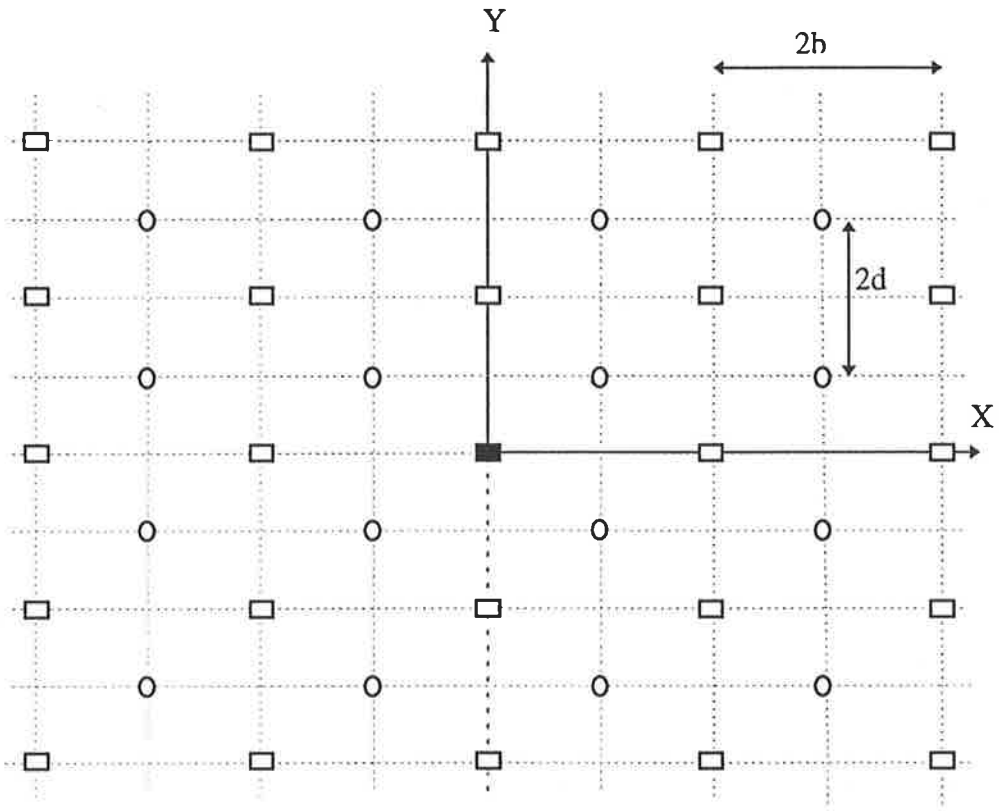

Figure 3.2 : An infinite planar array of point sources arranged in a triangular grid lattice

The derivation of the triangular grid lattice recognises two superimposed rectangular sub-lattices in the grid, one sub-lattice represented by the rectangles and the other represented by the circles in Figure 3.2. In each of these sub-lattices, the point sources are arranged with inter-element spacings of *2b* and *2d*, respectively in the *x* and *y* directions. One of these sub-arrays is centred on the reference element shown by the black rectangle in Figure 3.2, whilst the other is offset by a distance *b* and *d* away from this element in the *x* and *y* directions, respectively. The sources in the triangular grid lattice may be represented as the sum of these two rectangular grid sub-arrays as follows:

$$J(x,y,z) = J_1(x,y,z) + J_2(x,y,z) \tag{3.3}$$

where,

$$J_1(x,y,z) = \sum_{m=-\infty}^{\infty} \sum_{n=-\infty}^{\infty} \delta(x-x'-2mb)\,\delta(y-y'-2nd)\,e^{-jk_x 2mb}\,e^{-jk_y 2nd}\,\delta(z-z') \tag{3.3a}$$

$$J_2(x,y,z) = \sum_{m=-\infty}^{\infty}\sum_{n=-\infty}^{\infty}\delta(x-x'-[2m-1]b)\,\delta(y-y'-[2n-1]d)\,e^{-jk_x(2m-1)b}\cdot e^{-jk_y(2n-1)d}\,\delta(z-z') \tag{3.3b}$$

The sources shown as rectangles in Figure 3.2 are represented by (3.3a), whilst the sources shown as circles are represented by (3.3b). The spatial form of the periodic Green's function for a triangular grid lattice is then obtained by integrating the free space Green's function over the sources, as follows:

$$\begin{aligned} G_{\infty,t}^{spatial} &= \int_{-\infty}^{\infty}\int_{-\infty}^{\infty}\int_{-\infty}^{\infty}\frac{e^{-jk_0 r}}{4\pi r}J(x,y,z)\,dx\,dy\,dz \\ &= \sum_{m=-\infty}^{\infty}\sum_{n=-\infty}^{\infty}\frac{e^{-jk_0 r_{1mn}}}{4\pi r_{1mn}}e^{-j(2k_x mb+2k_y nd)} \\ &\quad+\sum_{m=-\infty}^{\infty}\sum_{n=-\infty}^{\infty}\frac{e^{-jk_0 r_{2mn}}}{4\pi r_{2mn}}e^{-j[k_x(2m-1)b+k_y(2n-1)d]} \end{aligned} \tag{3.4}$$

where $r_{1mn} = \sqrt{(x-x'-2mb)^2+(y-y'-2nd)^2+(z-z')^2}$

and $r_{2mn} = \sqrt{(x-x'-[2m-1]b)^2+(y-y'-[2n-1]d)^2+(z-z')^2}$

The symbol for the Green's function, G has a superscript denoting the spatial form of the Green's function, a subscript with symbols ∞ implying that it is for an infinite array, and t in the subscript implying that it is for a triangular grid lattice. The derivation can also be extended to a skewed grid lattice, if required. The spatial form of the periodic Green's function is related to the spectral form by a Fourier transform. The next section will derive this spectral form for both the rectangular and triangular grid lattices.

3.3 The Spectral Periodic Green's Function

In Section 3.2, the concept of a phased array was represented by an infinite planar array of point sources with periodic spacing and imposed with a progressive linear phase shift. The periodicity of the array is described by the regular spatial separation of the elements.

Hence the Green's function derived is known as the spatial form of the periodic Green's function. Consequently, the use of the generalised spatial periodic Green's function in the analysis of practical phased arrays is commonly known as spatial domain analysis. However, Wheeler has shown [41,42,43] that it is also possible to idealise a phased array as a planar electric current sheet which is the limiting case of many small electric dipoles, closely spaced, and backed by an open-circuit boundary, as shown in Figure 3.3.

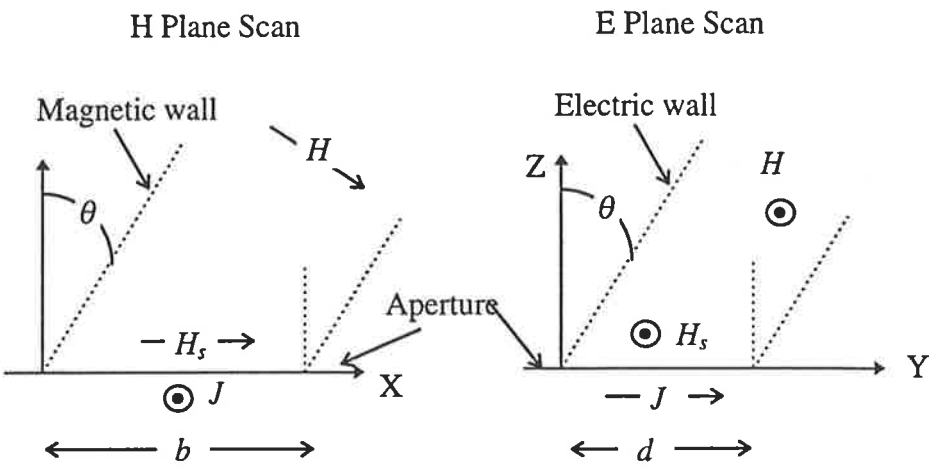

(a) Plane of scan showing the current sheet and magnetic field

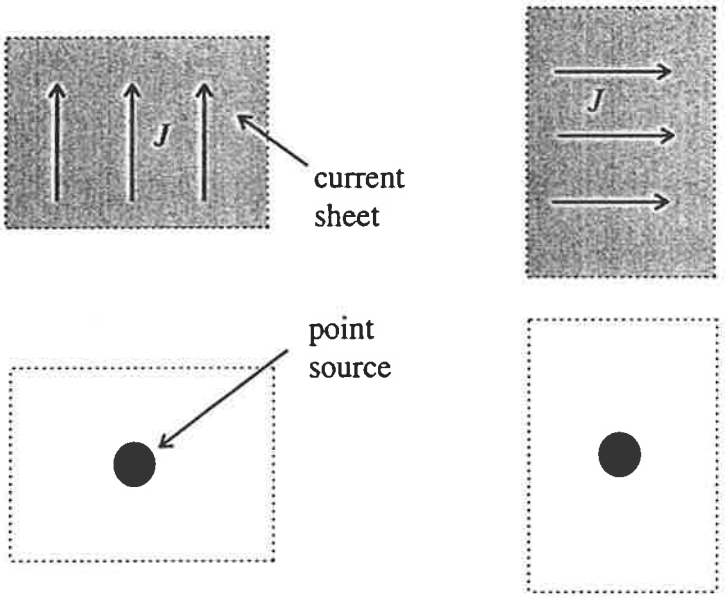

(b) Plane of array, showing a unit cell of current sheet and the equivalent point source

Figure 3.3 : An idealised model of a planar array, made of an electric current sheet

The infinite array of point sources in Figure 3.1 is idealised as an electric current sheet located at the aperture plane of the array, as shown in Figure 3.3. The region above the aperture plane is the radiation region. The region below the aperture plane is assumed to be an *open circuit* reflector which is characterised by permittivity given by $\varepsilon = 0$ and permeability given by $\mu = \infty$. The current sheet has a current density J of uniform amplitude, but phased for radiating a plane wave in a direction at an angle θ from boresight, where boresight is defined as the direction normal to the aperture plane. The current density is associated with a magnetic intensity H_s of equal amplitude and phase, but perpendicular to the direction of the current. Owing to the imposed phase shift and the symmetry of the array, the unit cell of dimensions b and d can be assumed to be bounded by electric and magnetic walls which have no effect on the field distribution. However, once the walls are present, the field outside the unit cell may be ignored because all mutual coupling effects of the neighbouring elements are inherently taken into account. Hence the current sheet in a unit cell which is bounded by the electric and magnetic walls, radiates in the direction of the *tube* formed by these walls. The current sheet representation of the infinite array of point sources enables a different form of the periodic Green's function to be derived, as described below.

The mathematical representation of the infinite array of point sources given in (3.1) may be converted into the current sheet representation of Figure 3.3 by means of the Fourier transform. In this section, extensive use will be made of the two dimensional Fourier transform pair, which is given by:

$$\tilde{F}(\beta_x, \beta_y) = \int_{-\infty}^{\infty}\int_{-\infty}^{\infty} f(x,y)\, e^{-j(\beta_x x + \beta_y y)}\, dx\, dy \tag{3.5a}$$

$$f(x,y) = \frac{1}{(2\pi)^2}\int_{-\infty}^{\infty}\int_{-\infty}^{\infty} \tilde{F}(\beta_x,\beta_y)\, e^{+j(\beta_x x + \beta_y y)}\, d\beta_x\, d\beta_y \tag{3.5b}$$

where $f(x,y)$ is a function in the spatial domain and $\tilde{F}(\beta_x,\beta_y)$ is the Fourier transform of $f(x,y)$. Applying the Fourier transform in (3.5a) to (3.1), the current expression becomes:

$$\tilde{J}(\beta_x,\beta_y,z)=\int_{-\infty}^{\infty}\int_{-\infty}^{\infty} J(x,y,z)\,e^{-j(\beta_x x+\beta_y y)}\,dx\,dy$$

$$=\frac{(2\pi)^2}{bd}\sum_{m=-\infty}^{\infty}\sum_{n=-\infty}^{\infty}\delta(\beta_x-\frac{2\pi m}{b})\,\delta(\beta_y-\frac{2\pi n}{d}) \qquad (3.6)$$

$$e^{-jk_x(x-x')}\,e^{-j\beta_x x'}\,e^{-jk_y(y-y')}\,e^{-j\beta_y y'}\,\delta(z-z')$$

The inverse Fourier transform in (3.5b) returns the expression to the spatial domain:

$$J(x,y,z)=\frac{1}{(2\pi)^2}\int_{-\infty}^{\infty}\int_{-\infty}^{\infty}\tilde{J}(\beta_x,\beta_y,z)\,e^{+j(\beta_x x+\beta_y y)}\,d\beta_x\,d\beta_y$$

$$=\frac{1}{bd}\sum_{m=-\infty}^{\infty}\int_{-\infty}^{\infty}\delta(\beta_x-\frac{2m\pi}{b})\,e^{j\beta_x(x-x')}d\beta_x\,e^{-jk_x(x-x')} \qquad (3.7)$$

$$\sum_{n=-\infty}^{\infty}\int_{-\infty}^{\infty}\delta(\beta_y-\frac{2n\pi}{d})\,e^{j\beta_y(y-y')}d\beta_y\,e^{-jk_y(y-y')}\,\delta(z-z')$$

$$=\frac{1}{bd}\sum_{m=-\infty}^{\infty}\sum_{n=-\infty}^{\infty}e^{j\beta_{x_m}(x-x')}\,e^{j\beta_{y_n}(y-y')}\,\delta(z-z')$$

where $\beta_{x_m}=2m\pi/b-k_x$ and $\beta_{y_n}=2n\pi/d-k_y$. It can be seen from (3.7) that the sources are represented as an infinite sheet of current located at the aperture plane $z = z'$ of the array, and described by the integer values of m and n. Since the summations over m and n are infinite, it is possible to re-express the above current expression in a more convenient form:

$$J(x,y,z)=\frac{1}{bd}\sum_{m=-\infty}^{\infty}\sum_{n=-\infty}^{\infty}e^{-jk_{x_m}(x-x')}\,e^{-jk_{y_n}(y-y')}\,\delta(z-z') \qquad (3.7a)$$

where $k_{x_m}=2m\pi/b+k_x$ and $k_{y_n}=2n\pi/d+k_y$ (3.7b)

For a point on the current sheet representing the infinite array, the Green's function satisfies the inhomogeneous scalar Helmholtz equation. Sommerfeld [44] has shown that separation of variables in rectangular coordinates yields the one dimensional Green's function in the z dimension for a unit source at a point z':

$$G(z,z')=\frac{1}{2jk_z}\,e^{-jk_z|z-z'|} \qquad (3.8)$$

where k_z is the wave propagation vector in the z direction. Summing the response at a point (x,y,z) due to all the point sources in the current sheet by combining (3.7a) and (3.8) yields the spectral form of the periodic Green's function:

$$G_{\infty}^{spectral} = \frac{1}{bd} \sum_{m=-\infty}^{\infty} \sum_{n=-\infty}^{\infty} \frac{1}{2jk_{z_{mn}}} e^{-jk_{x_m}(x-x')} e^{-jk_{y_n}(y-y')} e^{-jk_{z_{mn}}|z-z'|} \tag{3.9}$$

where the wave propagation vector in the z direction, $k_{z_{mn}} = \sqrt{k_0^2 - k_{x_m}^2 - k_{y_n}^2}$ for the propagating wave condition $k_0^2 \geq k_{x_m}^2 + k_{y_n}^2$, and $k_{z_{mn}} = -j\sqrt{k_{x_m}^2 + k_{y_n}^2 - k_0^2}$ for the evanescent wave condition $k_0^2 < k_{x_m}^2 + k_{y_n}^2$. The Green's function in (3.9), and consequently the plane waves propagating away from the infinite array exist only for discrete values of m and n. Hence, the set of integer values for m and n corresponds to what is commonly referred to as the (m,n)th Floquet mode of the array. The generality of the Green's function in (3.9) is the same as for that in (3.2) since it is not constrained by the array element geometry. As (3.9) is periodic for a set of discrete wave propagation vectors described by (3.7b) rather than in the lattice spacings, it is known as the generalised spectral periodic Green's function. Consequently, the use of this Green's function in practical array analysis is referred to as spectral domain analysis.

The above derivations of the spatial and spectral forms of the periodic Green's function have been obtained by using either an infinite array of point sources (*spatial domain*) or an infinite current sheet (*spectral domain*) representation of the periodic structure. It is also possible to transform the spatial form of the periodic Green's function directly into its spectral form by using the Poisson Transformation as suggested in [38]. A full derivation of the Poisson transform method is given in Appendix B for completeness.

3.3.1 Spectral Periodic Green's Function for a Triangular Grid Lattice

The procedure for transforming the spatial form of the periodic Green's function for the triangular grid lattice into its spectral form is similar to that for the rectangular grid lattice shown in Section 3.3. By applying the Fourier transform to (3.3) which is the point source representation of the infinite array for the triangular grid, and then applying the inverse transform to return to the spatial domain, the current sheet representation of the array is obtained. It is noted that the triangular grid lattice is made up of two rectangular sub-lattices in which the source representations are given by (3.3a) and (3.3b), respectively. Application of this analysis procedure for the first sub-lattice represented by (3.3a) is straight forward, and the result is given below.

$$J_1(x,y,z) = \frac{1}{(2b)(2d)} \sum_{m=-\infty}^{\infty} \sum_{n=-\infty}^{\infty} e^{-jk_{x_m}(x-x')} e^{-jk_{y_n}(y-y')} \delta(z-z') \tag{3.10}$$

where $k_{x_m} = 2m\pi/(2b) + k_x$ and $k_{y_n} = 2n\pi/(2d) + k_y$

The form of (3.10) is evident because the rectangular sub-lattice represented by the small rectangles in Figure 3.2 has inter-element spacings of $2b$ and $2d$, respectively in the x and y dimensions; and the reference element is located at the origin of the coordinate axes. The derivation of the current sheet representation of the sources for the second rectangular sub-lattice given in (3.3b) is not as straight forward, and a more detailed description is given below. Application of the Fourier transform to the point sources representation of the array in (3.3b) leads to the following:

$$\tilde{J}_2(\beta_x,\beta_y,z) = \sum_{m=-\infty}^{\infty} \sum_{m=-\infty}^{\infty} \int_{-\infty}^{\infty} \int_{-\infty}^{\infty} \delta(x-x'-[2m-1]b)\,\delta(y-y'-[2n-1]d) \cdot \delta(z-z') e^{-j\beta_x x} e^{-jk_x(2m-1)b} e^{-j\beta_y y} e^{-jk_y(2n-1)d} dxdy \tag{3.11}$$

The above expression needs to be simplified and arranged into a form suitable for an inverse transformation to be applied. By using a change of variable $u = x\text{-}x'+b$ and $v = y\text{-}y'+d$, (3.11) becomes:

$$\tilde{J}_2(\beta_x,\beta_y,z)=\tilde{J}_{2a}(\beta_x,\beta_y,z).\tilde{J}_{2b}(\beta_x,\beta_y,z)\delta(z-z') \tag{3.12}$$

where,

$$\begin{aligned}\tilde{J}_{2a}(\beta_x,\beta_y,z) &= \sum_{m=-\infty}^{\infty}\sum_{n=-\infty}^{\infty}\int_{-\infty}^{\infty}\delta(u-2mb)e^{-j\beta_x u}du \\ &= \sum_{m=-\infty}^{\infty}\sum_{n=-\infty}^{\infty}\frac{\pi}{b}\delta\left(\beta_x-\frac{m\pi}{b}\right)e^{-j\beta_x(x'-b)}e^{-jk_x(2m-1)b}\end{aligned} \tag{3.12a}$$

$$\begin{aligned}\tilde{J}_{2b}(\beta_x,\beta_y,z) &= \sum_{m=-\infty}^{\infty}\sum_{n=-\infty}^{\infty}\int_{-\infty}^{\infty}\delta(v-2nd)e^{-j\beta_y v}dv \\ &= \sum_{m=-\infty}^{\infty}\sum_{n=-\infty}^{\infty}\frac{\pi}{d}\delta\left(\beta_y-\frac{n\pi}{d}\right)e^{-j\beta_y(y'-d)}e^{-jk_y(2n-1)d}\end{aligned} \tag{3.12b}$$

The regular spacings between elements in each dimension of the infinite array may be re-expressed as $(2m\text{-}1)b = x\text{-}x'$ and $(2n\text{-}1)d = y\text{-}y'$. Taking the inverse Fourier transform of (3.12) returns the expression to the spatial domain, but in a current sheet representation:

$$\begin{aligned}J_2(x,y,z) &= \frac{1}{4\pi^2}\int_{-\infty}^{\infty}\int_{-\infty}^{\infty}\tilde{J}_2(\beta_x,\beta_y,z)\,e^{j(\beta_x x+\beta_y y)}d\beta_x d\beta_y \\ &= \frac{1}{4bd}\sum_{m=-\infty}^{\infty}\sum_{n=-\infty}^{\infty}\int_{-\infty}^{\infty}\delta(\beta_x-\frac{m\pi}{b})\,e^{j\beta_x(x-x'+b)}d\beta_x\,e^{-jk_x(x-x')}\cdot \\ &\quad \int_{-\infty}^{\infty}\delta(\beta_y-\frac{n\pi}{d})\,e^{j\beta_y(y-y'+d)}d\beta_y\,e^{-jk_y(y-y')}\delta(z-z) \\ &= \sum_{m=-\infty}^{\infty}\sum_{n=-\infty}^{\infty}\frac{1}{4bd}e^{-jk_{x_m}(x-x')}\,e^{-jk_{y_n}(y-y')}\,e^{j(m+n)\pi}\,\delta(z-z')\end{aligned} \tag{3.13}$$

By summing the equations for the current sheet representation of the sources for the two rectangular sub-lattices given in (3.10) and (3.13), the sources of the entire triangular grid lattice may be represented by:

$$\begin{aligned}J(x,y,z) &= J_1(x,y,z)+J_2(x,y,z) \\ &\sum_{m=-\infty}^{\infty}\sum_{n=-\infty}^{\infty}\frac{1}{4bd}e^{-jk_{x_m}(x-x')}\,e^{-jk_{y_n}(y-y')}\left[1+e^{j(m+n)\pi}\right]\delta(z-z')\end{aligned} \tag{3.14}$$

The one-dimensional Green's function for a source point on the current sheet is given by (3.8). Summing the response at a point (x,y,z) due to all the source points in the current

sheet, the spectral form of the periodic Green's function for the infinite array in the triangular grid lattice shown in Figure 3.2 is given by:

$$G_{\infty,t}^{spectral} = \sum_{m=-\infty}^{\infty}\sum_{n=-\infty}^{\infty} \frac{1}{2jk_{z_{mn}}(2b)(2d)} e^{-jk_{x_m}(x-x')} e^{-jk_{y_n}(y-y')} e^{-jk_{z_{mn}}|z-z'|} \cdot \left[1+e^{j(m+n)\pi}\right] \tag{3.15}$$

The form of the periodic Green's function is similar to that for the rectangular lattice in (3.9), which is reproduced below for direct comparison:

$$G_{\infty}^{spectral} = \sum_{m=-\infty}^{\infty}\sum_{n=-\infty}^{\infty} \frac{1}{2jk_{z_{mn}}bd} e^{-jk_{x_m}(x-x')} e^{-jk_{y_n}(y-y')} e^{-jk_{z_{mn}}|z-z'|}$$

In comparison with the spectral periodic Green's function for the rectangular lattice, it is noted that the differences in (3.15) are the term within the square brackets representing the contribution of the two rectangular sub-lattices, the lattice parameters at the denominator of the first term now given by $2b$ and $2d$, and the wave propagation vectors given by $k_{x_m} = 2m\pi/2b + k_0 sin\theta cos\phi$ and $k_{y_n} = 2n\pi/2d + k_0 sin\theta sin\phi$. It should be noted that the term within the square bracket has a value of zero whenever $(m+n)$ is odd, and a value of 2 when $(m+n)$ is even. This result has implications in both the spatial and spectral domains. In the spatial domain, m and n represent the elements of the infinite array, and a zero value of the Green's function for odd values of $(m+n)$ corresponds to the absence of an element at that location in the spatial pattern. In the triangular lattice shown in Figure. 3.2, it can be seen that for an odd value of $(m+n)$, there is no element at a location corresponding to mb units of distance along the x axis and nd units of distance along the y axis from the reference element in either the positive or negative direction. The more important implication of this phenomenon is in the spectral domain in relation to grating lobes, and this is described in the next section.

3.4 Properties of the Periodic Green's Function

In Section 3.2 , the spatial form of the generalised periodic Green's function for both the rectangular and triangular grid lattices were derived. In Section 3.3, it was shown that the point sources representation of the infinite array may be idealised using a current sheet representation. It was also shown that by application of the Fourier transform, the spectral form of the periodic Green's function could be derived from its spatial form. In general, it is readily possible to transform the periodic Green's function of an infinite array from one domain into the other. The two forms of this Green's function, however, have uniquely different properties. In this section, and in the next chapter, some of the more useful properties of the periodic Green's function will be described and related to practical array analysis. The first two properties described below relate to the computational effort involved in the use of the Green's functions; they are briefly described in this section, and then illustrated using numerical modelling data in the next chapter to show the extent of computational efficiency that can be achieved. The other properties are fully discussed in this section.

3.4.1 Integration over the Sources

Integral equation method analysis of metal strips and microstrip phased arrays generally employ the Electric Field Integral Equation to solve for the unknown currents on the metal parts (radiating element and feedline) and dielectric part (substrate) of the array element. This is normally done by expanding the unknown currents as a set of basis functions to discretise the integral equation and satisfy boundary conditions on the electric field scattered by these currents. The solution of the integral equation so obtained involves an integration of the Green's function over the basis functions. The use of the spatial periodic Green's function requires the integration to be evaluated numerically. Numerical integration is computationally time consuming, especially if the array element is modelled

by a large number of basis functions. In contrast, the spectral periodic Green's function enables the integration to be evaluated in closed form provided that the basis functions used in the analysis are analytically integrable functions. In Chapter 4, this property of the spatial and spectral forms of the periodic Green's function will be illustrated by way of an analysis of an infinite array of horizontal metal strips. For this reason, a form of the generalised spectral periodic Green's function has been used in the all numerical models reported on this thesis.

3.4.2 Singularities and Numerical Convergence

Two important properties of the generalised periodic Green's function in relation to its application for phased array analysis, are its *singularities* and *numerical convergence* characteristics. The meaning of these two terms are explained below. For convenience, the two forms of the periodic Green's function given in (3.2) and (3.9) are reproduced here to illustrate their properties.

$$G_{\infty}^{spatial} = \sum_{m=-\infty}^{\infty} \sum_{n=-\infty}^{\infty} \frac{e^{-jk_0 r_{mn}}}{4\pi r_{mn}} e^{-jk_x mb} e^{-jk_y nd} \tag{3.16}$$

$$G_{\infty}^{spectral} = \frac{1}{bd} \sum_{m=-\infty}^{\infty} \sum_{n=-\infty}^{\infty} \frac{1}{2jk_{z_{mn}}} e^{-jk_{x_m}(x-x')} e^{-jk_{y_n}(y-y')} e^{-jk_{z_{mn}}|z-z'|} \tag{3.17}$$

where the parameters $r_{mn} = \sqrt{(x-x'-mb)^2 + (y-y'-nd)^2 + (z-z')^2}$, $k_x = k_0 \sin\theta\cos\phi$, $k_y = k_0 \sin\theta \sin\phi$, $k_{x_m} = 2m\pi/b + k_x$, $k_{y_n} = 2n\pi/d + k_y$; $k_{z_{mn}} = -j\sqrt{k_{x_m}^2 + k_{y_n}^2 - k_0^2}$ for the evanescent wave condition $k_0^2 < k_{x_m}^2 + k_{y_n}^2$. It should be noted that in the case of (3.16), the summation is over the point sources of the infinite array, whereas the summation in (3.17) is over the Floquet modes of the infinite current sheet representation of these sources. A *singularity* exists when the value of the Green's function tends to infinity and cannot be accurately stored by the computer. In the numerical implementation of either of these Green's functions for the modelling of practical phased arrays, there is a need to truncate the double infinite summation at a large but finite value. *Numerical convergence* refers to

the number of terms of the summation that must be used in order that the Green's function may be accurately evaluated in the numerical solution.

It may be seen from (3.16) that the spatial Green's function has a singularity when $r_{mn} = 0$. This can only happen when the field point is at the same location as the source, which requires the condition $z = z'$. This is known as the *on-plane* condition when the observation point lies in the array plane. Furthermore, when $\theta \rightarrow 0$, $k_x \rightarrow k_0 cos\phi$ and $k_y \rightarrow k_0 sin\phi$, so that for negative values of $m = -m'$ and $n = -n'$, the two exponential terms representing the phase shifts in (3.16) become $e^{jm'bk_0 cos\phi}$ and $e^{jn'dk_0 sin\phi}$, respectively. It is apparent that the contribution of these two exponentials do not decay with increasingly large but negative values of m and n. This explains the poor convergence of the Green's function for large scan angles. In summary, the generalised spatial periodic Green's function has a singularity for interactions which satisfy the on-plane case, and a poor convergence property for large scan angles.

In the case of the spectral periodic Green's function, it is apparent from (3.17) that the Green's function is singular when $k_{z_{mn}} = 0$, which occurs for Floquet mode (0,0) corresponding to grazing scan angle, $\theta = 90°$. In the on-plane case defined by $z = z'$, it may be shown that the summand in (3.17) varies as $\left(e^{-jm\Delta x}\, e^{-jn\Delta y}\right)\Big/\sqrt{m^2+n^2}$ which does not decay for Floquet modes corresponding to large but negative values of m and n. Hence, the Green's function is again slowly convergent. In summary, it has been shown that the generalised spectral periodic Green's function has poor convergence in the on-plane condition and has a singularity at the grazing scan angle.

The two forms of the periodic Green's function form a Fourier transform pair, and the dual nature of their singularity and convergence condition is well established [37]. The amount of computational effort required in the periodic Green's function technique is largely determined by the numerical convergence of the Green's function. It has been shown above that the periodic Green's function has very different numerical convergence

properties in the spatial and spectral domains. Hence, the flexibility to work in either or both domains makes it possible to use a particular form of the Green's function in a region where it does not exhibit poor convergence, so that a computationally efficient numerical solution can be obtained. A detailed discussion of how this is achieved will be presented in Chapter 4, in the context of modelling an infinite array of horizontal dipoles.

3.4.3 Propagation Floquet Modes and Grating Lobes

Under certain circumstances, a phased array may have a grating lobe which is an additional main beam appearing in the radiation pattern of the array. The existence and prediction of grating lobes for rectangular grid lattice arrays is well understood and may be found in the literature. However, a description of the spectral periodic Green's function's grating lobe prediction capability is useful for validating the results of the technique that will be discussed in the next chapter. The spectral periodic Green's function given in (3.9) is governed by the propagating wave and evanescent wave conditions, given respectively by:

$$k_0^2 \geq k_{x_m}^2 + k_{y_n}^2 \qquad \text{for the propagation condition} \tag{3.18a}$$

$$k_0^2 \leq k_{x_m}^2 + k_{y_n}^2 \qquad \text{for the evanescent condition} \tag{3.18b}$$

The numbers of the (m,n)th Floquet modes for which the integers m and n satisfy the propagating wave condition are referred to as the *propagation Floquet modes*. Each of these propagation Floquet modes corresponds to a lobe in the array's radiation pattern. If the expression for the wave propagation vectors in the x and y directions, $k_{x_m} = 2m\pi/b + k_0 sin\theta cos\phi$ and $k_{y_n} = 2n\pi/d + k_0 sin\theta sin\phi$ are substituted into (3.18a), the following inequality is obtained:

$$\left(\frac{m^2\lambda^2}{b^2} + \frac{n^2\lambda^2}{d^2}\right) + 2sin\theta\left(\frac{m\lambda}{b}cos\phi + \frac{n\lambda}{d}sin\phi\right) \leq cos^2\theta \tag{3.19}$$

The term on the right hand side of the inequality has a maximum value of 1 when $\theta = n\pi$ and a minimum value of 0 when $\theta = n\pi/2$. These two conditions correspond respectively

to the boresight scan angle, which is the scan angle normal to the array plane and the grazing scan angle, which is the scan angle along the plane of the array. At the boresight scan angle, the propagating wave condition reduces to:

$$\frac{m^2\lambda^2}{b^2}+\frac{n^2\lambda^2}{d^2}\leq 1 \tag{3.20}$$

It is evident from this expression that so long as the inter-element spacings b and d are both less than the wavelength λ, then m and n can each only take a value of 0 for the above condition to be satisfied. In this case, mode *(0,0)* is the only propagation Floquet mode and consequently, there is only one lobe in the radiation pattern of the array at this scan angle. All the other integer values of m and n in the spectral periodic Green's function satisfy (3.18b) and are referred to as the evanescent Floquet modes. Conversely, if either b or d is greater than one wavelength, then there would be more than one propagation Floquet mode, and the array would have grating lobes at the boresight scan angle. Of course in practice, a phased array is used for scanning to angles other than boresight, and the limitation on inter-element spacings for avoiding grating lobes is more stringent than one wavelength.

The prediction of grating lobes for all possible scan angles is achieved by setting θ to 90° (which is the grazing scan angle) in the propagating wave condition given by (3.19), so that:

$$\frac{m\lambda}{b}\left(\frac{m\lambda}{b}+2cos\phi\right)+\frac{n\lambda}{d}\left(\frac{n\lambda}{d}+2sin\phi\right)\leq 0 \tag{3.21}$$

This condition is fulfilled if the following more stringent inequalities are satisfied together:

$$\frac{m\lambda}{b}\left(\frac{m\lambda}{b}+2cos\phi\right)\leq 0 \tag{3.22a}$$

$$\frac{n\lambda}{d}\left(\frac{n\lambda}{d}+2sin\phi\right)\leq 0 \tag{3.22b}$$

It is evident that (3.22a) is satisfied for $m = 0$, and for negative values of m such that the term within the bracket is positive. This would lead to the condition:

$$b \geq (-m)\left(\frac{\lambda}{2cos\phi}\right) \tag{3.23a}$$

which is seen to be dependent on the integer m and the scan plane described by ϕ. The smallest non-zero value of b in (3.23a) is given by $\lambda/2$ when m = -1 and ϕ = 0. In the same way, (3.22b) is satisfied for n = 0, and for negative values of n such that the term within the bracket is positive, so that:

$$d \geq (-n)\left(\frac{\lambda}{2sin\phi}\right) \tag{3.23b}$$

Again, the smallest non-zero value of d in (3.23b) is given by $\lambda/2$ when n = -1 and $\phi = \pi/2$. The physical meaning of these results is that a second lobe (the first grating lobe) will propagate at the grazing scan angle if $b = d = \lambda/2$ which is the well known grating lobe condition [45,46]. The Floquet mode associated with this grating lobe is either mode $(-1,0)$ in the $\phi = 0$ plane, or mode $(0,-1)$ in the $\phi = \pi/2$ plane.

GRATING LOBES FOR THE TRIANGULAR GRID LATTICE

The analysis for predicting the grating lobes of the infinite array in a rectangular grid lattice can also be applied to that in a triangular grid lattice. In the case of triangular grid lattice, however, the wave propagation vectors in the x and y directions associated with the spectral periodic Green's function in (3.15) are given by $k_{x_m} = m\pi/b + k_0 sin\theta cos\phi$ and $k_{y_n} = n\pi/d + k_0 sin\theta sin\phi$. Using the same procedure of analysis as before, it can be shown that the propagating wave condition for the triangular grid lattice is given by:

$$\left(\frac{m^2\lambda^2}{4b^2} + \frac{n^2\lambda^2}{4d^2}\right) + sin\theta\left(\frac{m\lambda}{b}cos\phi + \frac{n\lambda}{d}sin\phi\right) \leq cos^2\theta \tag{3.24}$$

The prediction of grating lobes for all possible scan angles is achieved by setting θ to the grazing scan angle (ie, $\theta = 90°$), so that the above inequality reduces to:

$$\left(\frac{m\lambda}{2b}\right)\left\{\left(\frac{m\lambda}{2b}\right)+2cos\phi\right\}+\left(\frac{n\lambda}{2d}\right)\left\{\left(\frac{n\lambda}{2d}\right)+2sin\phi\right\}\leq 0 \tag{3.25}$$

The above condition is fulfilled if the following two inequalities are simultaneously satisfied:

$$\left(\frac{m\lambda}{2b}\right)\left\{\left(\frac{m\lambda}{2b}\right)+2cos\phi\right\}\leq 0 \tag{3.26a}$$

$$\left(\frac{n\lambda}{2d}\right)\left\{\left(\frac{n\lambda}{2d}\right)+2sin\phi\right\}\leq 0 \tag{3.26b}$$

where m and n can take integer values from $-\infty$ to $+\infty$. Considering the $\phi = 0$ plane for the moment, it is evident that (3.26b) is satisfied only by $n = 0$. Equation (3.26a) is satisfied by $m = 0$ and negative values of m which satisfy the following condition:

$$b\geq\frac{(-m)\lambda}{4} \tag{3.27}$$

which has as its solution all negative values of m. However, it is noted that the spectral periodic Green's function for the triangular lattice represented by (3.15) is zero for values of m and n such that $(m+n)$ is odd, and consequently an additional condition is that $(m+n)$ should be an even value. Since $n = 0$ is required to satisfy (3.26b), $m = -1$ cannot be used for this reason, and therefore, the next negative value of m which satisfies (3.27) is $m = -2$. The Floquet mode associated with this value of m is mode $(-2,0)$ and corresponds to the first grating lobe for the triangular lattice with $b = \lambda/2$. By considering the $\phi = \pi/2$ plane, it can be shown that the first grating lobe emerges with $d = \lambda/2$. Since the inter-element spacings for a triangular grid lattice are $2b$ and $2d$ in the x and y directions respectively, no grating lobes will emerge for inter-element spacings of λ or less.

The above discussion highlights the fact that the expression for the spectral periodic Green's function contains the information in the Floquet modes from which the grating lobe condition may be derived. This information is useful not only for prediction of grating lobes but also for design of periodic lattices in which grating lobes are avoided.

3.4.4 Contribution of Floquet Modes to Active Impedance

For a phased array, the active impedance is defined as the impedance at the feed port of an antenna element under conditions when all of the elements are excited to produce a given radiation pattern. In the periodic structure analysis of phased arrays, the contribution of the Floquet modes to the active impedance of the array is well documented in the literature [37]. The propagation Floquet mode (or modes, if grating lobes are present) contributes to the real part of the active impedance. The reactive component of the active impedance involves all the higher, non-propagating Floquet modes which satisfy the evanescent wave condition in (3.9). It was shown in Section 3.4.1 that when no grating lobes are present, the only contribution of the spectral periodic Green's function to the active resistance is from the term associated with Floquet mode *(0,0)*. The wave propagation vector in the z direction for this Floquet mode is given by:

$$k_{z_{00}} = \sqrt{k_0^2 - k_{x_0}^2 - k_{y_0}^2} = k_0 \cos\theta \tag{3.28}$$

As the scan angle $\theta \rightarrow \pi/2$, then by (3.28), $k_{z_{00}} \rightarrow 0$. This is the singularity condition of spectral form of the periodic Green's function described in Section 3.4.2. In the absence of grating lobes, an infinite value of Green's function would lead to a zero active resistance. This result is consistent with physical reality because when no grating lobes are present, the real part of an infinite array's active impedance must be zero at the grazing scan angle since no real power can propagate away from the array at this angle. This condition of zero active resistance at the grazing scan angle applies to all types of infinite arrays, and has been found to be very useful as a check against errors in both the analysis and numerical implementation of the various infinite array models discussed in the next three chapters.

3.5 Summary

In the course of developing the theoretical basis for the analysis and modelling of various types of phased arrays in the following chapters, the contributions of this chapter are in:

- Deriving the spatial form of the Generalised Periodic Green's Function for an infinite planar array in both a rectangular and a triangular grid lattice using a point sources representation, and the spectral form using a current sheet representation of the array.
- Describing the properties of the Generalised Periodic Green's Function and relating them to practical aspects of phased array modelling such as computational efficiency and avoidance of grating lobes.
- Deriving and describing the implications of the singularity and convergence properties of the two forms of the Generalised Periodic Green's Function.

The insight gained and the techniques developed in this chapter have been applied to the analysis and modelling of infinite arrays of metal strips and microstrip dipole antenna elements which will be discussed in the next three chapters. The theoretical work discussed in this chapter also forms the basis for the development of a technique for the analysis of finite arrays, using an infinite array approach; this technique will be presented in Chapter 7 and illustrated using numerical examples of metal strip and microstrip dipole finite arrays.

CHAPTER 4

Generalised Periodic Green's Function Analysis of Infinite Arrays

4.1 Introduction and Overview

In Chapter 3, the theoretical basis of the Generalised Periodic Green's Function technique for modelling microstrip arrays was established. The spatial and spectral forms of the generalised periodic Green's function were derived for an infinite array of point sources in rectangular and triangular grid lattices. The properties of this periodic Green's function which are relevant to practical phased array modelling, were also described. At this point the analytical tools necessary for the application of this technique to the analysis of an infinite phased array have been assembled. As described in Section 2.2.2, high accuracy

may be achieved with this technique subject to constraints on the discretisation of the geometry, because it is based on a full-wave solution of the problem. The relative merits of this technique as compared to the others in the same class of full-wave solutions would therefore depend largely on the numerical efficiency of the overall solution.

The purpose of this chapter is to describe how the technique is applied to the analysis of a phased array problem. The problem is analysed in two stages:

- Problem formulation using Electric Field Integral Equations.
- Numerical implementation using the Method of Moments.

In both of these stages, techniques to maximise the computational efficiency of the solution are described and illustrated with numerical data by using a relatively simple model of an infinite array of horizontal metal strip dipoles above an infinite ground plane. Apart from its simplicity, the dipole array model is also chosen because numerical results from other sources are available for validation, and because it forms a basic building block for modelling other more complex structures which will be described in the later chapters. In the first case, the horizontal dipoles are modelled as thin metal strips orientated with their faces parallel to the array plane. This orientation of the metal strip is simpler to model as the equivalent currents representing the array elements are not distributed in the direction perpendicular to the array plane.

Finally, as a prelude to the modelling of array elements with three-dimensional geometries, a second configuration consisting of horizontal metal strips orientated with their faces perpendicular to the array plane is also discussed. A new technique is prescribed for dealing with the equivalent current sources distributed in the plane of the metal strips in this orientation.

4.2 Analysis Procedure for the Generalised Periodic Green's Function Technique

The idealized structure of the planar infinite array is given in Figure 4.1. Each element of the array consists of a horizontal metal strip of length l and width w, orientated with its face parallel to the array plane, and positioned at a height h above an infinitely large, perfect electric conducting ground plane.

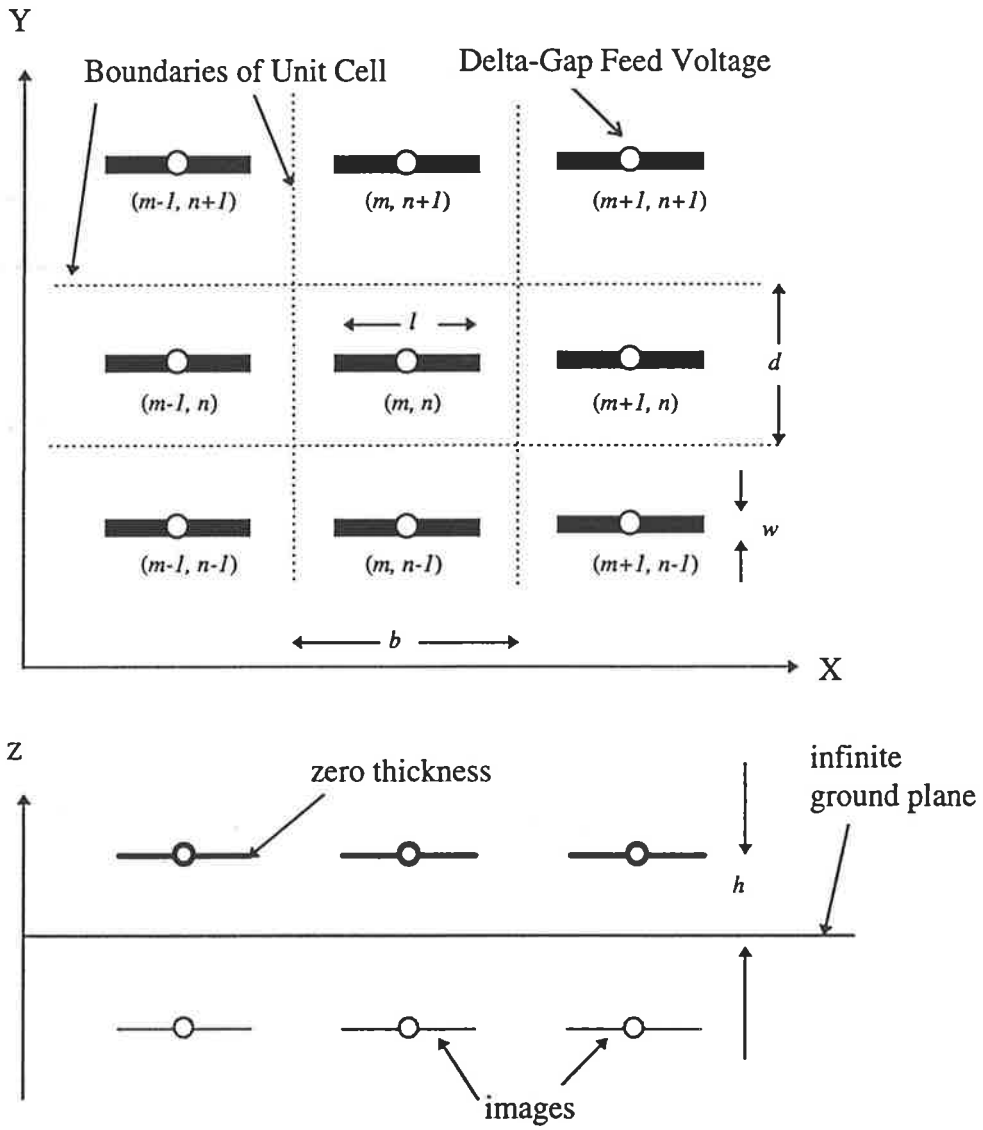

Figure 4.1: An infinite array of horizontal metal strips in a rectangular grid lattice, orientated with their faces parallel to the array plane and located above an infinite ground plane (top view and side view).

The width of the metal strip is narrow with respect to its length (ie, $w << l$). The metal strip is also assumed to be infinitesimally thin, such that the equivalent surface current $\vec{J}(\vec{r})$ represents the total current on the metal strip. The inter-element spacings are b and d in the x and y directions, respectively. Each metal strip is assumed to be excited by an ideal delta-gap voltage source at its centre [47], and no feedline is included in the model at this stage. The excitation is assumed to have a uniform magnitude and a linear progressive phase shift between successive elements across the aperture plane, such that a plane wave is propagated away from the array in the direction (θ, ϕ). The array is divided into identical unit cells as shown in the diagram, with each metal strip element being located in a unit cell. Because the array is infinite in extent across the xy plane, each element of the array operates in an identical electromagnetic environment as all the other elements. It is therefore sufficient to analyze only one unit cell of this periodic structure, which shall be denoted as the reference unit cell and whose centre lies at coordinates (m,n). All the other unit cells of the infinite array and their mutual interactions are then accounted for by the periodicity.

4.2.1 Integral Equation Formulation

Boundary conditions dictate that the sum of the tangential incident and scattered electric fields, $\vec{E}^i(\vec{r})$ and $\vec{E}^s(\vec{r})$ respectively, at location $\vec{r}$ on the surface S_c of each metal strip, must be zero. Thus the Electric Field Integral Equation (EFIE) associated with this geometry is given as follows:

$$\left[\vec{E}^i(\vec{r})\right]_{\tan} + \left[\vec{E}^s(\vec{r})\right]_{\tan} = 0 \qquad \text{for } \vec{r} \in S_c \tag{4.1}$$

The scattered electric fields $\vec{E}^s(\vec{r})$ can be expressed in terms of the associated magnetic vector potential, **A** as follows:

$$\vec{E}^s = -j\omega\mathbf{A} + \frac{\nabla\nabla' \cdot \mathbf{A}}{j\omega\varepsilon_0\mu_0} \tag{4.2}$$

It should be noted that the divergence of **A** with respect to the source coordinates is primed, whereas the divergence with respect to the field coordinates is not primed. As shown in Figure 4.1, the effect of the ground plane is accounted for by including the image of the infinite array of metal strips, located at the same distance below the ground plane. Using the equivalence principle, each metal strip and its image may be replaced by equivalent two-dimensional surface currents $\vec{J}(\vec{r})$ in the *xy* plane. In early infinite array models of such elements [48,49], each of the metal strips was assumed to have an idealised sinusoidal current distribution. In this model, no assumptions are made about the current distributions on the metal strips of the infinite array, except that they are identical. The magnetic vector potential **A** is related to $\vec{J}(\vec{r})$ through the infinite array generalised periodic Green's function G_∞, by the following equation:

$$\mathbf{A} = \mu_0 \iint_{S_c} \vec{J}(\vec{r})\, G_\infty \, dS \tag{4.3}$$

At this stage, it is noted that either the spatial form of the generalised periodic Green's function given in (3.2) or the spectral form given in (3.9) may be used in (4.3). The equations (4.1) to (4.3) are solved to obtain the equivalent currents on the metal strip of the reference unit cell. The active impedance at the feed point of the metal strip is then given by the ratio of the excitation voltage over the equivalent current at the segment. The solution of the equations (4.1) to (4.3) by the Method of Moments is outlined below.

4.2.2 Numerical Implementation

In the numerical solution of the integral equations using the Method of Moments, the element geometry is discretised so that the problem becomes a solution of a system of matrix equations. Because of the rectangular geometry of the element, a numerical implementation is developed here using the *Point Matching* method in which the currents are expanded as rectangular pulse basis functions and the testing points are Dirac delta functions. Higher order basis functions [50] and the Galerkin method are avoided in order

to minimise the associated computational overheads and complexity of the analysis, the aim being to apply a simple and efficient solution using the Method of Moments for the metal strip element geometry and for the more complex element geometries described in the following chapters.

Segmentation, Basis and Testing Functions

For solution by the Method of Moments using the procedure described by Harrington [51], the centre-fed metal strip is divided into n_x identical segments in the x direction, as shown in Figure 4.2.

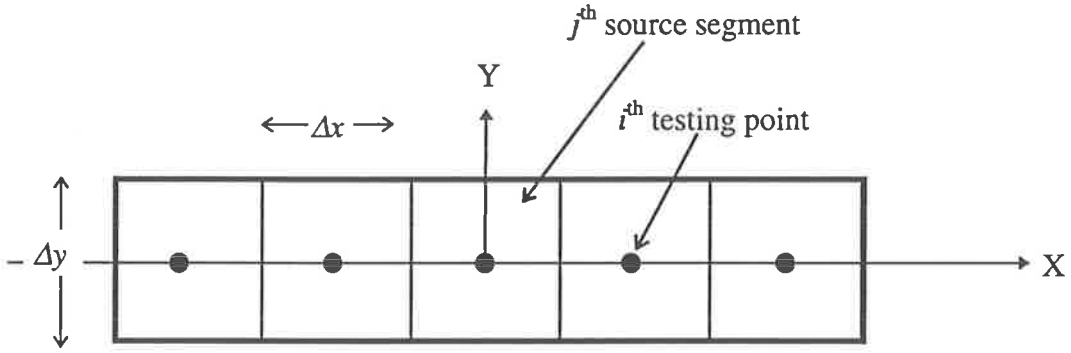

Figure 4.2 : Segmentation of metal strip and location of testing points for point matching to be applied.

Because the metal strip is narrow in its transverse dimension, it may be modelled as a single segment in this dimension. Each rectangular segment has dimensions Δx, Δy respectively, in the xy plane. Since the metal strip is assumed to be infinitesimally thin in the z dimension, the currents $\vec{J}(\vec{r})$ are expanded using two-dimensional pulse basis functions $P_j(x',y')$ in the xy plane, and a dirac-delta function $\delta(z'-z_j)$ in the z dimension, and may be represented as follows:

$$\vec{J}(\vec{r}) = \sum_{j=1}^{n_x} [J_{xj}\hat{x} + J_{yj}\hat{y}]\, P_j(x',y')\, \delta(z'-z_j) \tag{4.4}$$

where the pulse function are given by:

$$P_j(x',y') = \begin{cases} 1, & \text{if } x',y' \in j^{th} \text{ segment} \\ 0, & \text{otherwise} \end{cases} \tag{4.4a}$$

and the j^{th} term in the summation refers to the current expansion of the j^{th} source segment of the metal strip. Using the point matching method, the testing functions consist of Dirac-delta functions in all three dimensions and are given by:

$$W_i = \delta(x - x_i)\delta(y - y_i)\delta(z - z_i) \tag{4.5}$$

where the i refers to the testing point at the centre of the i^{th} segment, represented by the dots (•) in Figure 4.2; each source segment being tested once in both the x and y dimensions. J_{xj} and J_{yj} are the metal strip's equivalent current coefficients in the x and y directions, respectively, which may be ordered to give the current vector:

$$\mathbf{J} = \left[J_{x1}, \ldots, J_{xn_x}, \quad J_{y1}, \ldots, J_{yn_x} \right]^T \tag{4.6}$$

where the superscript T denotes the vector transpose.

Moment Matrix Elements

Having discretised the geometry of the array element, the currents are related to the excitation by the Moment Matrix equation:

$$[\mathbf{Z}]_{2n_x,2n_x} [\mathbf{J}]_{2n_x,1} = [\mathbf{E}]_{2n_x,1} \tag{4.7}$$

Here **E** is the vector corresponding to the impressed electric field. Since a delta-gap voltage is used at the feed point located at the centre segment of the metal strip antenna, the elements of the vector **E**, denoted by E_j are given by:

$$E_j = \begin{cases} E_0 & \text{for a feed point at } j = (n_x + 1)/2 \\ 0 & \text{otherwise} \end{cases} \tag{4.8}$$

where E_0 is the impressed electric field caused by a feed point voltage of one volt.

The Moment Matrix, $\mathbf{Z}$, which takes into account the mutual coupling between source segments on the antenna and its image, is may be expressed in the form:

$$[\mathbf{Z}]_{2n_x,2n_x} = \begin{bmatrix} [\mathbf{Z_{xx}}]_{n_x,n_x} & [\mathbf{Z_{xy}}]_{n_x,n_x} \\ [\mathbf{Z_{yx}}]_{n_x,n_x} & [\mathbf{Z_{yy}}]_{n_x,n_x} \end{bmatrix} \tag{4.9}$$

where in the evaluation of the matrix elements, the first subscript within the square brackets of each sub-matrix refers to the direction of the testing function and the second subscript refers to the direction of the source segment being tested. The derivation of a typical element of the moment matrix is given below.

The $(i,j)^{\text{th}}$ element in sub-matrix Z_{xx} in (4.9) denotes the action of the current sources with coefficients J_{xj} in the x direction, onto the i^{th} segment of the metal strip in the same direction. Based on equations (4.1) to (4.3), the tangential incident field $\left[\vec{E}^i(\vec{r})\right]_{\tan}$ at the point in space corresponding to this i^{th} segment where the equations are to be enforced, is given by:

$$\begin{aligned} E_x^i \hat{x} &= -E_x^s \hat{x} \\ &= j\omega\mu_0 \iint_{S_c} \vec{J}_{xj} G_\infty \, dS_c + \frac{j\nabla}{\omega\varepsilon_0}\left(\nabla' \cdot \iint_{S_c} \vec{J}_{xj} G_\infty \, dS_c\right) \end{aligned} \tag{4.10}$$

Taking the inner product of this expression for the field and the testing function [42], the corresponding element of the Z_{xx} sub-matrix is then given by:

$$\begin{aligned} Z_{xx} &= \left\langle W_i \hat{x} \cdot E_x^i \hat{x} \right\rangle \\ &= \left(j\omega\mu_0 + \frac{j}{\omega\varepsilon_0}\frac{\partial^2}{\partial x_i^2} \right) \iiint \iint \int_{-\infty}^{\infty} W_{xi} J_{xj} G_\infty dx\, dy\, dz\, dx'\, dy'\, dz' \end{aligned} \tag{4.11a}$$

Because pulse basis functions are used, and the problem is solved using the point matching method, the source point derivative has been taken outside the integral with no effect to the

computation. Furthermore, it is also permissible to compute both derivatives with respect to the field point, since the basis and testing functions are symmetrical. Using the same procedure, the other sub-matrices in (4.9) may be expressed as follows:

$$Z_{xy} = \left(j\omega\mu_0 + \frac{j}{\omega\varepsilon_0} \frac{\partial^2}{\partial x_i \partial y_i} \right) \iiint \iint \int_{-\infty}^{\infty} W_{xi} J_{yj} G_{\infty} dx\, dy\, dz\, dx'\, dy'\, dz' \qquad (4.11b)$$

$$Z_{yx} = \left(j\omega\mu_0 + \frac{j}{\omega\varepsilon_0} \frac{\partial^2}{\partial x_i \partial y_i} \right) \iiint \iint \int_{-\infty}^{\infty} W_{yi} J_{xj} G_{\infty} dx\, dy\, dz\, dx'\, dy'\, dz' \qquad (4.11c)$$

$$Z_{yy} = \left(j\omega\mu_0 + \frac{j}{\omega\varepsilon_0} \frac{\partial^2}{\partial y_i^2} \right) \iiint \iint \int_{-\infty}^{\infty} W_{yi} J_{yj} G_{\infty} dx\, dy\, dz\, dx'\, dy'\, dz' \qquad (4.11d)$$

Having derived the expressions for the elements of the Moment Matrix in (4.9), the moment equation in (4.7) may now be solved numerically on the computer to obtain the equivalent currents on the metal strip.

4.3 Maximising Computational Efficiency

The key to obtaining an efficient solution using the Generalised Periodic Green's Function technique lies in identifying areas where the computational load of the solution procedure may be reduced. The solution of the infinite array problem has two stages - problem formulation and numerical implementation. For each of these stages, a number of techniques to maximise the computational efficiency of the solution procedure are described below.

4.3.1 Integration of the Periodic Green's Function over the Sources

It is apparent from (4.11a) to (4.11d) that the elements of the Moment Matrix in (4.9) involve an integration of the product of the Green's function with the basis and testing functions over the source and field coordinates. Since the testing function given in (4.5) involves three Dirac-delta functions, the integral over the field coordinates will yield a value of unity at the location of each testing point. From (4.4), it can be seen that each basis function has two pulse functions corresponding to each segment of the metal strip. Hence, the Moment Matrix elements may be said to involve an integration of the periodic Green's function over the current sources representing each segment of the metal strip. Either one of the spatial and spectral forms of the periodic Green's function derived in Chapter 3 may be used in the evaluation of the integrals, but the computational efficiency of the solution associated with each of these two Green's functions is different.

The evaluation of the sub-matrix element Z_{xx} is considered as an illustration. If the spatial form of the periodic Green's function given by (3.2) is substituted into (4.11a), the following is obtained:

$$Z_{xx} = \sum_{m=-\infty}^{\infty} \sum_{n=-\infty}^{\infty} \left(j\omega\mu_0 + \frac{j}{\omega\varepsilon_0} \frac{\partial^2}{\partial x_i^2} \right) \int_{S_c} \frac{e^{-jk_0 r_{mn}}}{4\pi r_{mn}} e^{-jk_x mb} e^{-jk_y nd} \, dS_c \tag{4.12}$$

where S_c is the surface area of a segment of the metal strip, and the integrals are summed over all the $(m,n)^{th}$ elements of the infinite array. The implementation of (4.12) is known as a spatial domain solution, and the integrals have to be evaluated numerically. The computational load may be minimised by evaluating the integral numerically only for the self coupling terms which correspond to $m = n = 0$. For cross coupling terms, a stationary integrand approximation is used by multiplying the value of the integrand with the surface area of the metal strip segment. Nevertheless, numerical integration is computationally time consuming, especially if each array element must be represented by a large number of basis functions.

However, if the spectral form of the Green's function given by (3.9) is substituted into (4.11a), the procedure of analysis is known as a spectral domain solution, and (4.11a) may be expressed as follows:

$$Z_{xx} = \sum_{m=-\infty}^{\infty} \sum_{n=-\infty}^{\infty} \frac{1}{2bd} \left(j\omega\mu_0 + \frac{j}{\omega\varepsilon_0} \frac{\partial^2}{\partial x_i^2} \right) I_x \, I_y \, I_z \tag{4.13a}$$

where the summations are over the $(m,n)^{th}$ Floquet modes of the infinite array; and I_x, I_y, and I_z are the integrals given below. The integral I_x is evaluated by parts, so that:

$$\begin{aligned} I_x &= \int_{-\infty}^{\infty} \int_{-\infty}^{\infty} e^{-jk_{x_m}(x-x')} \delta(x-x_i) P(x'-x_j) \, dx \, dx' \\ &= \int_{-\infty}^{\infty} e^{-jk_{x_m}x} \delta(x-x_i) \, dx \quad \int_{-\infty}^{\infty} e^{jk_{x_m}x'} P(x'-x_j) \, dx' \\ &= \Delta x \, sinc\left(k_{x_m} \Delta x/2\right) e^{jk_{x_m}(x_j-x_i)} \end{aligned} \tag{4.13b}$$

where $sinc(x) = sin(x)/x$. I_y may be evaluated in the same way to yield:

$$I_y = \Delta y \, sinc\left(k_{y_n} \Delta y/2\right) e^{jk_{y_n}(y_j-y_i)} \tag{4.13c}$$

In the z direction, the integration must be evaluated over each source and its image:

$$\begin{aligned} I_z &= \int_{-\infty}^{\infty} \int_{-\infty}^{\infty} \left(\frac{e^{-jk_{z_{mn}}|z-z'|}}{jk_{z_{mn}}} - \frac{e^{-jk_{z_{mn}}(z+z')}}{jk_{z_{mn}}} \right) \delta(z-z_i) \, \delta(z'-z_j) \, dz \, dz' \\ &= \frac{1}{jk_{z_{mn}}} - \frac{e^{-jk_{z_{mn}}(z_i+z_j)}}{jk_{z_{mn}}} \quad = \frac{1}{jk_{z_{mn}}} - \frac{e^{-jk_{z_{mn}}2h}}{jk_{z_{mn}}} \end{aligned} \tag{4.13d}$$

Substituting (4.13b) to (4.13d) into (4.13a):

$$\begin{aligned} Z_{xx} = \sum_{m=-\infty}^{\infty} \sum_{n=-\infty}^{\infty} & \left(\frac{k_0^2 - k_{x_m}^2}{2k_{z_{mn}} bd\omega\varepsilon_0} \right) \Delta x \, sinc\left(\frac{k_{x_m} \Delta x}{2} \right) \Delta y \, sinc\left(\frac{k_{y_n} \Delta y}{2} \right) \\ & e^{jk_{x_m}(x_j-x_i)} \left(1 - e^{-jk_{z_{mn}}2h} \right) \end{aligned} \tag{4.14}$$

Hence, it is seen that by using the generalised spectral periodic Green's function and appropriate basis and testing functions, the integration over the sources can be evaluated in

closed-form. A similar analysis may be performed to obtain all the other sub-matrices in (4.9).

It should be noted however that integration of the Green's function over the sources is not the only factor that determines the overall numerical efficiency of the technique. As described in Section 3.4.2, the numerical convergence properties of the spatial and spectral forms of the periodic Green's function also have a significant effect [37] on their application to phased array analysis. This is illustrated in Table 4.1 which shows the active impedance of an infinite array of horizontal metal strips at boresight scan angle (viz., $\theta = 0°$), computed using both the spatial and spectral Green's function techniques. In the evaluation of the spatial periodic Green's function, m' and n' represent the total number of the elements used in the x and y directions, respectively. For the spectral periodic Green's function, m'' and n'' correspond to the total number of Floquet modes used in the respective directions. It was found that the results are converged when the metal strip is divided into $n_x = 21$ segments, and that the use of a greater number of segments did not change the values in the table by more than 1%.

Spatial Periodic Green's Function Model			Spectral Periodic Green's Function Model		
Elements in E-plane (m')	Elements in H-plane (n')	Active Impedance (Ω)	Floquet Modes in E-plane (m'')	Floquet Modes in H-plane (n'')	Active Impedance (Ω)
3	3	107.2 - j70.0	21	11	0.01 - j1.2
7	7	103.9 - j50.3	31	11	102.4 - j44.0
11	11	103.5 - j47.1	41	11	101.8 - j45.0
41	41	102.7 - j43.3	81	11	102.1 - j44.2

Table 4.1 : Active impedance for an infinite array of horizontal metal strips above an infinite ground plane in the boresight scan angle; $l = 0.44\lambda$, $b = 0.6\lambda$, $d = 0.5\lambda$, $h = 0.5l$. The metal strip is divided into $n_x = 21$ segments.

It is noted that numerical convergence does not necessarily correspond to absolute convergence towards the correct result [52]. In this case, numerical convergence of the results to approximately the same value using two techniques which employ different Green's functions provide a measure of confidence in the accuracy of the results. It is also clear from Table 4.1 that the results at the boresight angle using the spatial periodic Green's function model are well converged for a 7 x 7 element array. This result confirms the fact that the spatial Green's function is well converged at the boresight scan angle. For the spectral Green's function model, a well converged solution is only obtained when the number of Floquet modes corresponding to $m'' \geq 31$ is used; it is not dependent on the value of n''. This result is expected because it involves on-plane interactions where the spectral Green's function is slowly convergent. The CPU time to calculate a converged value of the active impedance is approximately 2 seconds in both models. Hence, for a simple element geometry such as a metal strip and at the boresight scan angle, there is no significant improvement in computation time gained by a technique using the spectral periodic Green's function in its conventional form, over one using the spatial periodic Green's function. Table 4.2 shows the data for a grazing scan angle in the H-plane where the inter-element spacing is 0.5λ and the active resistance is expected to be zero .

Spatial Periodic Green's Function Model			Spectral Periodic Green's Function Model		
Elements in E-plane (m')	Elements in H-plane (n')	Active Impedance (Ω)	Floquet Modes in E-plane (m'')	Floquet Modesin H-plane (n'')	Active Impedance (Ω)
3	3	140.4 + j116.0	21	11	0.0 + j0.0
15	15	100.0 + j248.9	31	11	0.0 + j590.0
31	31	77.3 + j288.9	41	11	0.0 + j512.2
61	61	58.6 + j315.8	71	11	0.0 + j457.5
101	101	47.0 + j330.8	91	11	0.0 + j419.2

Table 4.2 : Active impedance for an infinite array of horizontal metal strips above an infinite ground plane at the grazing scan angle in the H-plane; $l = 0.44\lambda$, $b = 0.6\lambda$, $d = 0.5\lambda$, $h = 0.5l$. The metal strip is divided into $n_x = 21$ segments.

The data in Table 4.2 shows that at the grazing scan angle, the results of the spatial periodic Green's function model are still not converged even after 101 x 101 elements have been used in the summation, with a corresponding CPU time of about 50 seconds required. In contrast, the spectral periodic Green's function model requires the same number of Floquet modes for convergence as for the case of boresight scan. Clearly, the spectral periodic Green's function model is superior in terms of accuracy and computational efficiency for large scan angles. The variation of active impedance with scan angle for the two techniques is given Figure 4.3.

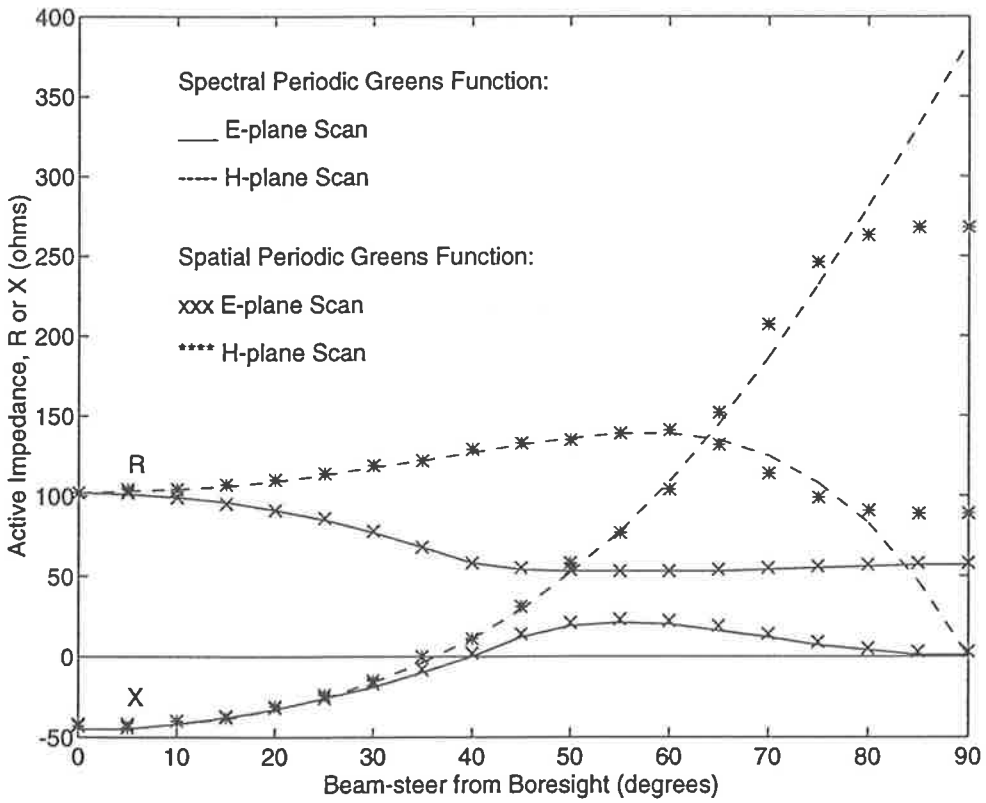

Figure 4.3 : Variation of active impedance with scan angle for an infinite array of horizontal metal strips above an infinite ground plane; $l = 0.44\lambda$, $b = 0.6\lambda$, $d = 0.5\lambda$, $h = 0.5l$, $n_x = 21$; for calculation of spatial periodic Green's function: $m' = n' = 21$; for calculation of spectral periodic Green's function: $m'' = 31$ and $n'' = 21$.

In Figure 4.3, the results of the spatial and spectral periodic Green's function models in the are similar in the E-plane scan. As expected, for an inter-element spacing of 0.6λ in this plane, a grating lobe appears at about 42° scan angle, and consequently the active resistance does not become zero at the grazing scan angle. The results in the H-plane are also similar except at large scan angles. As $\theta \rightarrow 90°$, the spectral periodic Green's function model correctly predicts the active resistance to tend to zero. The results of the spatial periodic Green's function model, as expected, are inaccurate because the Green's function is not well converged at this scan angle. The poor convergence property of the spatial periodic Green's function for large scan angles is a disadvantage when it is used to model more complex structures such as a microstrip array which may have a scan blindness condition occurring at a large scan angle.

In summary, the results show that when modelling infinite arrays with relatively simple element geometries like dipoles, the advantage of the spectral domain solution in accuracy and numerical efficiency is only marginal except at very large scan angles. When scanning near to the grazing angle, the spectral periodic Green's function model is clearly more accurate and numerically efficient because unlike the spatial periodic Green's function, it does not suffer from slow convergence in this region. The next section will describe a technique to accelerate the convergence of the spectral periodic Green's function for on-plane interactions, so that the overall computational efficiency of the technique using this Green's function may be further improved.

4.3.2 Convergence Acceleration of the Spectral Periodic Green's Function for the On-plane Case

The slow convergence of the spectral periodic Green's function can be overcome in one of two ways. The first way is to enhance the convergence of the overall solution by using higher order differentiable basis and testing functions such as triangular, piecewise sinusoidal or entire domain functions [53]. However, it is widely acknowledged that such higher order functions tend to increase the complexity of the analysis and the computation

time for the integration. Furthermore, it is often the case that the use of such higher order basis functions tends to rely on a specific knowledge of the geometry of the structure, and is therefore undesirable where a generalised approach is sought. The use of pulse basis functions and Dirac-delta testing functions for all the models described in this thesis has the advantages of simplicity in problem formulation and minimum computational overheads in numerical implementation. For comparison, the infinite dipole array used for illustration in this chapter was also modelled using a Galerkin method involving pulse basis and testing functions. The results showed neither an appreciable improvement in accuracy of the results nor a faster rate of convergence of the spectral periodic Green's function. In fact, the computation time was marginally longer than the model using the point matching technique. The results thus appear to confirm a recent finding [54] that in the numerical solution of electromagnetic radiation and scattering problems, the error in the equivalent currents obtained by discretizing the integral equations is mainly due to the basis functions and is largely insensitive to the choice of the testing function; and that the advantages of the Galerkin method may have been overstated. Based on the above considerations, the use of higher order differentiable basis and testing functions was not pursued.

A second approach that is independent of the geometry seeks to improve the convergence of the series representing the periodic Green's function. A number of techniques have been successfully developed and documented in the literature. All of them are based on an understanding of the numerical properties of the spatial and spectral forms of the periodic Green's function, and of how these properties may be exploited to accelerate the convergence of the Green's function [37]. The convergence properties of the spatial and spectral representations of the periodic Green's function have been described in Section 3.4.2. The spatial domain formulation is rapidly convergent everywhere except at large scan angles, whilst the spectral domain formulation is rapidly convergent except for the on-plane case. It is feasible to split the periodic Green's function into two parts and to evaluate each of these parts in the respective domain in which it is more rapidly convergent. The result is that a converged value of the periodic Green's function is evaluated more efficiently than evaluating it in either the spatial or spectral domains alone.

Jorgenson and Mittra [37] have developed a technique to accelerate the on-plane component of the spatial Green's function by evaluating it in the spectral domain, where it converges rapidly. Using a different approach, a technique reported by Singh [38] begins with the spectral periodic Green's function and translates the on-plane component to be evaluated in the spatial domain in which it converges more rapidly. Although the two approaches are expected to offer similar numerical efficiency in the evaluation of the periodic Green's function, the latter approach has been adopted here because the spectral formulation of the problem has been used. For completeness, an outline of Singh's technique is reproduced in Appendix C.

The expression for the spectral periodic Green's function which has accelerated convergence characteristics, referred to from here onwards as the *Generalised Hybrid Periodic Green's Function* , is given by:

$$G_{\infty}^{hybrid} = \frac{1}{2bd}\sum_{m=-\infty}^{\infty}\sum_{n=-\infty}^{\infty} e^{-jk_{x_m}(x-x')}\, e^{-jk_{y_n}(y-y')}\left[\frac{e^{-jk_{z_{mn}}|z-z'|}}{jk_{z_{mn}}} - \frac{e^{-k_{mn}|z-z'|}}{k_{mn}}\right] + \sum_{m=-\infty}^{\infty}\sum_{n=-\infty}^{\infty} e^{jk_x mb}\, e^{jk_y nd}\,\frac{e^{-ur_{mn}}}{4\pi r_{mn}} \tag{4.15}$$

It is apparent from (4.15) that the new hybrid periodic Green's function consists of two components. The first component is described as the spectral component and takes the form of the original spectral periodic Green's function, except that an asymptotic part is subtracted away from it. The asymptotic part, which causes the slow convergence of the Green's function, is the second term within the square brackets, and is described by the parameter:

$$k_{mn} = \sqrt{k_{x_m}^2 + k_{y_n}^2 + u^2} \tag{4.16}$$

where u is a finite, real variable which is called the smoothing parameter to be described later. The second component is described as the spatial component. It has a form similar in all respects to the spatial form of the periodic Green's function given in (3.16), except that the exponent of the exponential term has the smoothing parameter u which replaces the

term jk_0 in the expression. This spatial component is the Fourier transform of the asymptotic part of the spectral component. Hence the hybrid periodic Green's function is actually the spectral periodic Green's function in which the slowly convergent part has been subtracted away, and returned to the expression in the spatial domain form. As described in Appendix C, the two components of the hybrid periodic Green's function are both rapidly convergent, so that a significant improvement in computational efficiency is achieved by an evaluation of the Green's function in this form rather than in either of the spatial or spectral forms alone.

The procedure for implementing the Generalised Hybrid Periodic Green's Function technique to calculate the elements of the Moment Matrix is briefly outlined here. Each term in the Moment Matrix comprises two parts - the *direct* component being the effect of a source point on a testing point, and the *image* component being the effect of the image of this source (representing the reflection from the ground plane) on the same testing point. As the images for this geometry are located far away from the testing points on the metal strips, referred to as the *off-plane* condition, the spectral periodic Green's function is rapidly convergent in this case and is used for the image component. However, the mutual coupling between source and testing points on the metal strips are all in the on-plane condition, and hence the hybrid form of the periodic Green's function is used for the direct component. Since the metal strips are orientated parallel to the ground plane, every term of the Moment Matrix has a direct component, and thus every term requires convergence acceleration. Applying the convergence acceleration to the direct component of (4.13d) yields:

$$I_z = \int_{-\infty}^{\infty}\int_{-\infty}^{\infty}\left\{\left[\frac{e^{-jk_{z_{mn}}|z-z'|}}{jk_{z_{mn}}} - \frac{e^{-k_{mn}|z-z'|}}{k_{mn}}\right] - \frac{e^{-jk_{z_{mn}}(z+z')}}{jk_{z_{mn}}}\right\}\delta(z-z_k)\,\delta(z'-z_j)\,dz\,dz' \qquad (4.17)$$

$$= \left[\frac{1}{jk_{z_{mn}}} - \frac{1}{k_{mn}}\right] - \frac{e^{-jk_{z_{mn}}(z_k+z_j)}}{jk_{z_{mn}}} = \left[\frac{1}{jk_{z_{mn}}} - \frac{1}{k_{mn}}\right] - \frac{e^{-jk_{z_{mn}}2h}}{jk_{z_{mn}}}$$

Subtracting the asymptotic part of the spectral Green's function, transforming that part into the spatial domain and then adding it back, the expression for Z_{xx} in the impedance matrix then comprises a spectral and a spatial component described by:

$$Z_{xx} = Z_{xx}^{spec} + Z_{xx}^{spat} \tag{4.18}$$

where the accelerated spectral component is given by:

$$Z_{xx}^{spec} = \sum_{m=-\infty}^{\infty}\sum_{n=-\infty}^{\infty}\left(\frac{k_0^2 - k_{x_m}^2}{2bd\omega\varepsilon_0}\right)\Delta x\, sinc\left(\frac{k_{x_m}\Delta x}{2}\right)\Delta y\, sinc\left(\frac{k_{y_n}\Delta y}{2}\right) e^{jk_{x_m}(x_j - x_k)}\left(\left[\frac{1}{k_{z_{mn}}} - \frac{j}{k_{mn}}\right] - \frac{e^{-jk_{z_{mn}}2h}}{k_{z_{mn}}}\right) \tag{4.19}$$

The terms in the last bracket are made up of the accelerated direct component within the square bracket and the unaccelerated image component outside of it. From (4.15) and (4.19), the spatial component of Z_{xx} is given by:

$$Z_{xx}^{spat} = \frac{j}{4\pi\omega\varepsilon_0}\sum_{m'=-\infty}^{\infty}\sum_{n'=-\infty}^{\infty} e^{j(k_x m' b + k_y n' d)}\left(k_0^2 + \frac{\partial^2}{\partial x^2}\right)\iint_{S_c}\frac{e^{-ur_{m'n'}}}{r_{m'n'}}\,dS_c \tag{4.20}$$

where the integral is over the surface S_c of the metal strip. It should be noted that the double summations in the above two equations have entirely different, though related meanings. In (4.19), the summation is over the $(m,n)^{th}$ Floquet modes for the spectral component. In (4.20), and the summation is over the $(m',n')^{th}$ elements of the infinite array. The spectral and spatial components of the hybrid periodic Green's function need not be truncated with the same number of terms for their evaluation. For convenience, Singh [38] has proposed an optimum value for the smoothing parameter u such that both the spatial and spectral components are well converged when the summations in both cases are truncated at the same numerical value (viz., $m = m'$ and $n = n'$). This proposed optimum value of the smoothing parameter $u = \pi / b$, where b is one of the inter-element spacings, has been adopted by Shubair and others [55] for modelling of periodic sources in layered dielectric media. It has also been found that the results are not sensitive to the exact value of u provided that it stays within ±100% of the optimum value. Hence Singh's suggested value of $u = \pi / b$ is used in all the models described in this thesis. The surface integrals in the spatial component are evaluated numerically using the Fortran double precision IMSL™ [56] math library routine for multi-dimensional integration using iterated application of product Gauss formulas which has been found to be efficient and accurate. The surface of the metal strip is segmented by a grid as shown in Figure 4.4, and the spatial

Green's function integrals are evaluated for distances between the grid line intersections and the origin, and stored in a look-up table.

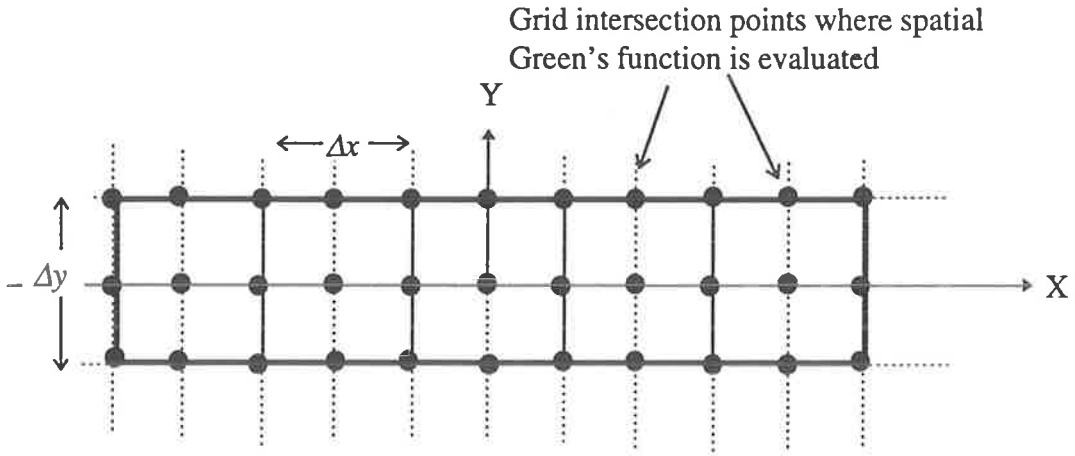

Figure 4.4 : Segmentation grid at half inter-element spacings apart, placed over the metal strip to compute the spatial component of the Hybrid Periodic Green's Function.

In all the cases, the Green's function singularity which occurs when the source and field point coincide, is integrable [57]. The integrand in (4.20) is symmetrical in the x and y directions. Hence if a testing point is located at the reference grid position (0,0,0), then the spatial Green's function involves an integrand $G_{xy}(p,q,0)$ for a source segment located at grid position ($p\Delta x$, $q\Delta y$, 0) which is given by:

$$G_{xy}(p,q,0) = \int_{q_1}^{q_2}\int_{p_1}^{p_2} \frac{e^{-ur_{mn}}}{r_{mn}}\,dx\,dy \tag{4.21}$$

where the limits of integration are from $p_1 = \Delta x\text{-}0.5\Delta x$ to $p_2 = \Delta x\text{+}0.5\Delta x$ in the x dimension and from $q_1 = \Delta y\text{-}0.5\Delta y$ to $q_2 = \Delta y\text{+}0.5\Delta y$ in the y dimension. The method of finite difference is used to evaluate the second order partial derivatives of the integrals, so that:

$$\frac{\partial^2}{\partial x^2}\int_{q_1}^{q_2}\int_{p_1}^{p_2} \frac{e^{-ur_{mn}}}{r_{mn}}\,dx\,dy = \frac{1}{\Delta x^2}\{G_{xy}(p+2,q,0) - 2G_{xy}(p,q,0) + G_{xy}(p-2,q,0)\} \tag{4.22}$$

and

$$\frac{\partial^2}{\partial x \partial y}\int_{q_1}^{q_2}\int_{p_1}^{p_2}\frac{e^{-ur_{mn}}}{r_{mn}}dxdy = \frac{1}{\Delta x\,\Delta y}\{G_{xy}(p+1,q+1,0) - G_{xy}(p+1,q-1,0) - G_{xy}(p-1,q+1,0) + G_{xy}(p-1,q-1,0)\} \quad (4.23)$$

The second partial derivative with respect to y is calculated in a similar way. The spectral and spatial components of the impedance matrix are then added together corresponding to the double summation. Finally, the moment matrix is solved using the Fortran double precision IMSL™ [56] math library routine for solving complex variable equations with iterative refinement to obtain the equivalent currents on the metal strip.

Computational Burden of Convergence Acceleration

In the Section 4.3.1, it was shown that the spectral form of the periodic Green's function has a desirable feature in that the integration over the sources can be evaluated analytically. However, this form of the periodic Green's function also has an undesirable feature in that it is poorly convergent for on-plane interactions. To overcome this undesirable feature, a hybrid form of the periodic Green's function has been developed. However, the hybrid form contains a spatial component in which the integration over the sources has to be evaluated numerically. Hence it appears that the requirement for numerical integration has become inevitable in the process. It is acknowledged that convergence acceleration of the spectral periodic Green's function imposes a computational burden on the solution. However, it should be noted that evaluation of the spatial component of the hybrid periodic Green's function is not as computationally demanding as that of the spatial periodic Green's function for the following reasons:

- Firstly, convergence acceleration of the spectral periodic Green's function is required only for the set of on-plane interactions. All the off-plane interactions, including interactions from the image sources, can be evaluated using the conventional spectral periodic Green's function which is rapidly convergent and which does not require numerical integrations.

- Secondly, the number of numerical integrations required to evaluate the spatial component which has the form given in (4.21), is only half the number required for evaluating the spatial periodic Green's function given by the integrand of (4.12). Because the integrand in the case of the spatial component has a real exponential, the numerical integration need only be evaluated once for each set of interaction. In the case of the spatial periodic Green's function, the integrand contains a complex exponential which is more conveniently split into a real and an imaginary part before evaluating the numerical integration. Each part is integrated separately as a real function, and the results are then recombined to obtain the final result. Hence for the same testing point and source segment, the integrand in (4.12) is twice as computationally intensive to evaluate as that in (4.21).

The computational efficiency of the Generalised Hybrid Periodic Green's Function technique is illustrated by in Table 4.3 below for an infinite array of horizontal metal strips.

Summation Terms in E-plane	Summation Terms in H-plane	Active Impedance at Boresight Scan Angle (Ω)	Active Impedance at Grazing Scan Angle in E-plane (Ω)
1	1	110.0 - j66.5	0.0001 - j3.1
3	1	117.2 - j56.7	0.0001 - j24.5
3	*3*	*122.8 - j44.7*	*0.0001 - j24.7*
5	5	122.1 - j43.9	0.0001 - j24.6
11	11	122.2 - j44.1	0.0001 - j26.5
21	21	121.8 - j45.1	0.0001 - j26.2
21*	21*	120.9 - j42.8	0.0001 - j26.0

Table 4.3 : Active impedance for an infinite array of horizontal metal strips above an infinite ground plane; $l = 0.44\lambda$, $b = 0.5\lambda$, $d = 0.5\lambda$, $h = 0.5l$. All the above results are obtained with a metal strip segmentation of $n_x = 5$, except the last row indicated by * in which the metal strip is divided into $n_x = 11$ segments.

In the evaluation of the hybrid periodic Green's function, both the spatial and spectral components are truncated after m and n terms, respectively in the E-plane and H-plane. In Table 4.3, it is apparent that the results are converged for values of m and n corresponding to $-1 \leq m \leq 1$ and $-1 \leq n \leq 1$, respectively. The results are converged at both boresight and grazing scan angles when the metal strip is divided into $n_x = 5$ segments. Compared to the results using $n_x = 21$ segments to obtain convergence for both the spatial and spectral periodic Green's function techniques, it is noted that the hybrid periodic Green's function technique requires a smaller number of basis functions to achieve convergence. The accuracy of the converged results as compared with those using the unaccelerated spectral periodic Green's function technique is shown in Figure 4.5.

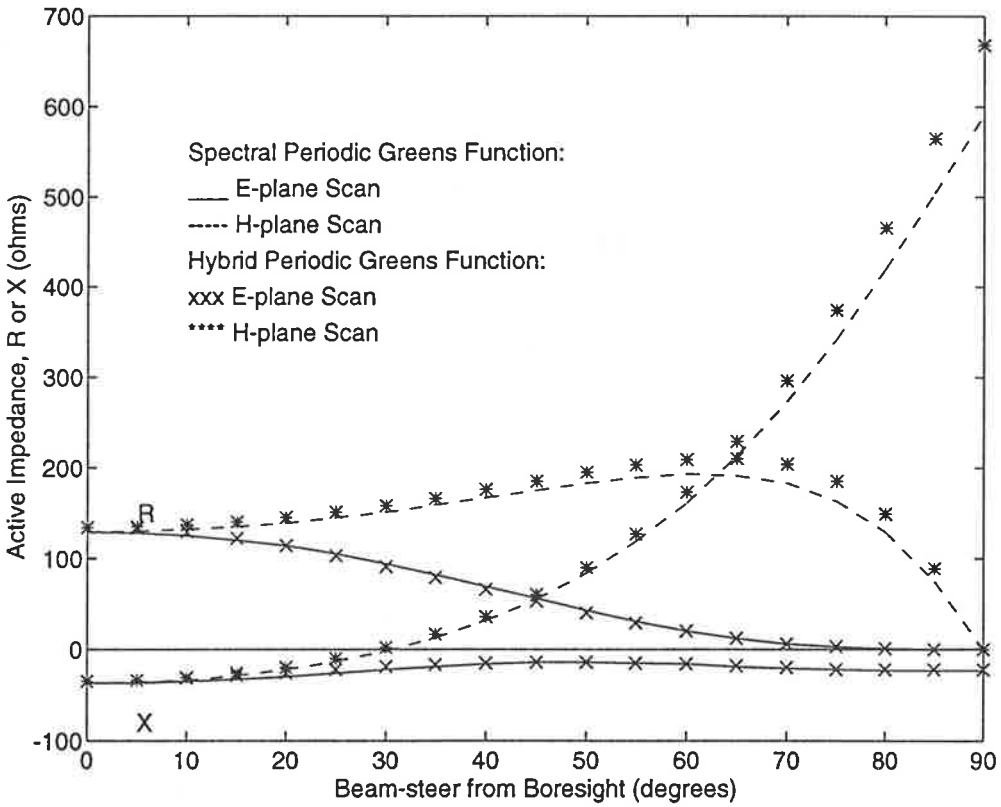

Figure 4.5: Comparison of Active Impedance obtained using the Spectral and Hybrid Periodic Green's Function techniques for various scan angles; $l = 0.44\lambda$, $b = 0.5\lambda$, $d = 0.5\lambda$, $h = 0.5l$. For the spectral periodic Green's function technique, the Floquet modes used are for $-15 \leq m \leq 15$ and $-10 \leq n \leq 10$ and the segmentation used is $n_x = 21$. For the hybrid periodic Green's function technique, the Floquet modes used are for $-1 \leq m \leq 1$ and $-1 \leq n \leq 1$ and the segmentation used is $n_x = 5$.

Figure 4.5 shows the active impedance as a function of scan angle in the principal scan planes for the infinite array of metal strips above an infinite ground plane. The results are shown for analysis using the spectral and hybrid periodic Green's functions. It can be seen that the converged results for the two cases are in very good agreement. However, in the case of the hybrid periodic Green's function, a much smaller number of Floquet modes and segments are required to obtained converged results. Consequently, the computation time of 0.05 seconds per scan angle is 40 times faster than that using the spectral or spatial periodic Green's function models. Hence, the computational efficiency of the Hybrid Periodic Green's Function technique is shown to be significantly superior. It should be noted that for the analysis of microstrip arrays described later in this thesis where the element geometry is far more complex than the horizontal metal strip, the computational advantage of the generalised hybrid periodic Green's technique is even more significant. It will be shown in Chapter 6 that a spatial periodic Green's function analysis of a typical microstrip infinite array would typically require supercomputing resources for its numerical implementation, whereas a hybrid periodic Green's function solution of the same problem can be implemented very efficiently on a desktop computer.

4.3.3 Exploiting Toeplitz-like Symmetries in the Moment Matrix

In Section 4.3.1, it was highlighted that the use of the generalised spectral periodic Green's function enables the integration over the sources to be evaluated analytically. Section 4.3.2 introduced the hybrid form of the periodic Green's function which has better numerical convergence characteristics than the spatial and spectral forms. Both of these techniques are applied at the formulation stage of the problem, and improve the computational efficiency of the overall solution. In the numerical implementation stage, one way to minimise computation time is to identify areas in the evaluation procedure in which repeated calculations may be avoided. This is achieved partly by identifying Toeplitz-like

symmetries [58] in the expression for spectral periodic Green's function which is restated below.

$$G_{\infty}^{spectral} = \frac{1}{2bd} \sum_{m=-\infty}^{\infty} \sum_{n=-\infty}^{\infty} e^{-jk_{x_m}(x-x')} \, e^{-jk_{y_n}(y-y')} \left[\frac{e^{-jk_{z_{mn}}|z-z'|} \pm e^{-jk_{z_{mn}}(z+z')}}{jk_{z_{mn}}} \right] \tag{4.24}$$

The terms in the square brackets account for the contribution from the primary sources and their image across the ground plane. It is apparent from the above equation that the value of the Green's function is identical for interactions which have the same displacements (x-x') , (y-y'), $|z-z'|$, and (z+z'). In the case of a metal strip whose axis lies in the x direction, only repeated calculations in the x dimension can be reduced, since $y = y'$ and $z = z'$. If for example, the metal strip is divided into 4 segments, then the elements of the moment matrix which need to be calculated are shown by the symbol **x** in (4.25).

$$\begin{bmatrix} [Z_{xx}] & [Z_{xy}] \\ [Z_{yx}] & [Z_{yy}] \end{bmatrix} = \begin{bmatrix} \begin{bmatrix} \mathbf{x} & \mathbf{y} & \mathbf{y} & \mathbf{x} \\ \mathbf{x} & \mathbf{y} & \mathbf{y} & \mathbf{x} \\ \mathbf{x} & \mathbf{y} & \mathbf{y} & \mathbf{x} \\ \mathbf{x} & \mathbf{y} & \mathbf{y} & \mathbf{y} \end{bmatrix} & \begin{bmatrix} \mathbf{x} & \mathbf{y} & \mathbf{y} & \mathbf{x} \\ \mathbf{x} & \mathbf{y} & \mathbf{y} & \mathbf{x} \\ \mathbf{x} & \mathbf{y} & \mathbf{y} & \mathbf{x} \\ \mathbf{x} & \mathbf{y} & \mathbf{y} & \mathbf{y} \end{bmatrix} \\ \begin{bmatrix} \mathbf{x} & \mathbf{y} & \mathbf{y} & \mathbf{x} \\ \mathbf{x} & \mathbf{y} & \mathbf{y} & \mathbf{x} \\ \mathbf{x} & \mathbf{y} & \mathbf{y} & \mathbf{x} \\ \mathbf{x} & \mathbf{y} & \mathbf{y} & \mathbf{y} \end{bmatrix} & \begin{bmatrix} \mathbf{x} & \mathbf{y} & \mathbf{y} & \mathbf{x} \\ \mathbf{x} & \mathbf{y} & \mathbf{y} & \mathbf{x} \\ \mathbf{x} & \mathbf{y} & \mathbf{y} & \mathbf{x} \\ \mathbf{x} & \mathbf{y} & \mathbf{y} & \mathbf{y} \end{bmatrix} \end{bmatrix} \tag{4.25}$$

In (4.25), the overall impedance matrix has 4 blocks of elements consistent with the 4 combinations of interactions between the x and y directed currents on the metal strip. If the metal strip were to be divided into n_x segments, then each block would be a square matrix of rank n_x , and the overall impedance matrix would have $4(n_x)^2$ elements. Based on the above considerations, it is sufficient to evaluate the Green's function only for coupling displacements from $-(n_x - 1)\Delta x$ to $(n_x - 1)\Delta x$ in the x dimension, so that a total of $4(2n_x - 1)$ unique interactions need to be evaluated for the whole matrix. This is depicted in the above matrix equation where **x** represent the elements in which the Green's function has to

be evaluated, and y represent those elements in which the Green's function can simply be copied over from a previous evaluation which has been stored in a look-up table.

4.3.4 Look-up Tables for Repeatedly Used Parameters

Another way to minimise computation time is to avoid repeated calculations of parameters with the same values which are used many times in the algorithm. The values of the wave propagation vectors, complex exponentials and sinc functions associated with the closed-form integration over the pulse basis functions, may be calculated and stored into look-up tables for each scan angle and Floquet mode, and then recalled when required. The improvement in computational efficiency from the use of look-up tables is not as significant as that obtained by working in the spectral domain and from the convergence acceleration for the spectral periodic Green's function; in fact, there is a marginal increase in storage requirements for the look-up tables. Nevertheless, the exploitation of Toeplitz-like symmetries and use of look-up tables have been implemented in all the models described in this thesis.

4.4 Modelling of Sources Distributed Perpendicular to the Array Plane

Up to this point, a procedure of analysis has been provided for an infinite array in which all the sources are distributed in two-dimensions on the array plane. In order to model three-dimensional element geometries, the analysis needs to be extended to the case where the sources are distributed perpendicular to the array plane (viz., in the z dimension). To illustrate this, the analysis is applied to the case where the horizontal metal strips of the infinite array depicted in Figure 4.1, are orientated with their faces perpendicular to the array plane as shown in Figure 4.6 below.

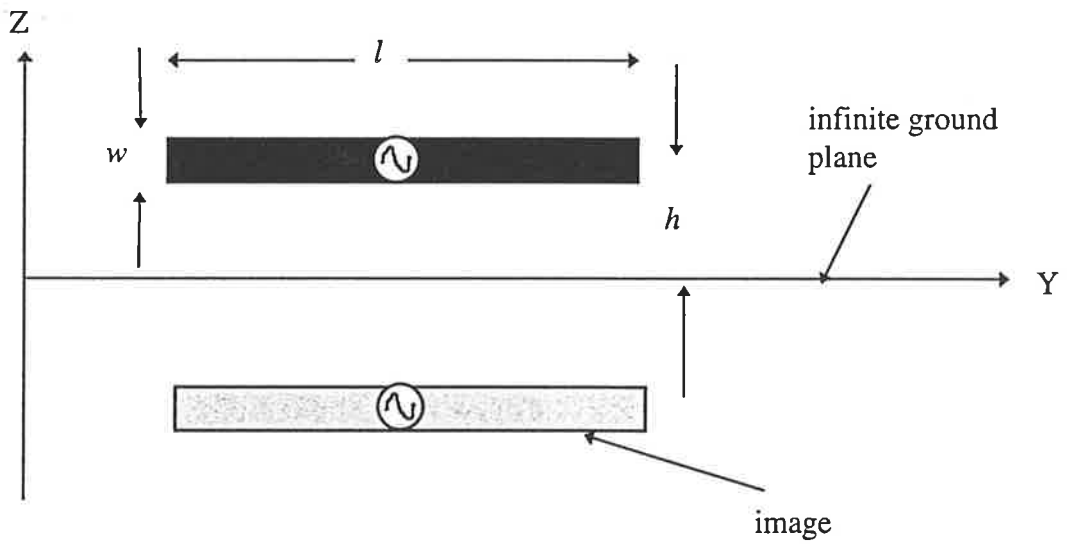

Figure 4.6 : Geometry of metal strip element orientated in the yz plane.

Figure 4.6 shows the geometry of an element in the infinite array. The metal strip of length l and width w , is located at a height h above the infinite ground plane. The Electric Field Integral Equations and expressions for the scattered electric field, magnetic vector potential and periodic Green's function in equations (4.1) - (4.3) still apply to this geometry, but have to be adapted to deal with the current sources which are distributed in the yz plane.

4.4.1 Integrating in the Z-Dimension

In the case of elements orientated parallel to the ground plane as in Section 4.2, the metal strips are assumed to be infinitesimally thin in the z-dimension. Hence there is no requirement to integrate over the sources in this direction. However, if the elements are metal strips orientated perpendicular to the ground plane, each of the sources is represented by a two-dimensional rectangular pulse segment in the yz plane. Here, the centre of each pulse segment is at the same height above the ground plane as the testing point which is located either at this same point in the case of self coupling, or at the centre of another segment of the metal strip in the case of mutual coupling. Hence the current distributed on each pulse segment will lie both above and below the testing point in the z dimension, as shown in Figure 4.7 below.

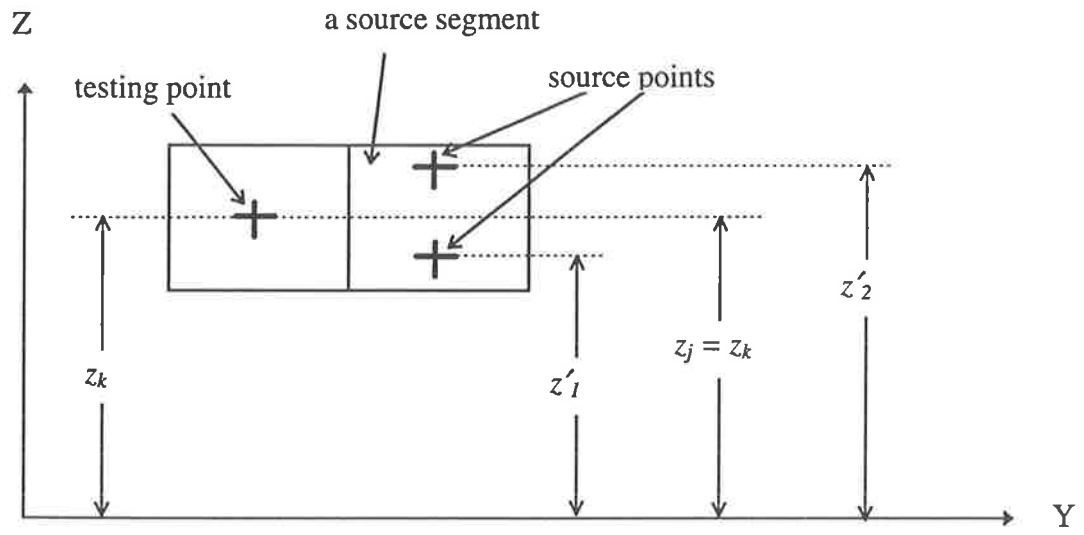

Figure 4.7 : Source points located above and below testing point in the z dimension.

Ignoring for the moment the image component, the integration over the sources in the z direction is the same as that given in (4.13d) but with the Dirac-delta function replaced by a pulse function. The term -|z-z1 in the exponential indicates the direction of wave propagation which needs to be accounted for when evaluating the integral. If the modulus sign is ignored and the integral is evaluated analytically using separation of variables, the result becomes:

$$I_z = \int_{-\infty}^{\infty}\int_{-\infty}^{\infty}\left(\frac{e^{-jk_{z_{mn}}|z-z'|}}{jk_{z_{mn}}}\right)\delta(z-z_k)\,P(z'-z_j)\,dz\,dz' \qquad (4.26)$$
$$= -\frac{1}{k_{z_{mn}}^2}\left(e^{jk_{z_{mn}}\Delta z/2} - e^{-jk_{z_{mn}}\Delta z/2}\right)$$

In the evanescent wave condition given in (3.18b), $k_{z_{mn}} = -j\sqrt{k_{x_m}^2 + k_{y_n}^2 - k_0^2}$ is a complex number which is negative and imaginary. Let $k_{z_{mn}} = -jk_{rz_{mn}}$ where $k_{rz_{mn}}$ is a real and positive number whose value increases with m and n. (4.26) then becomes:

$$I_z = \frac{1}{k_{rz_{mn}}^2}\left(e^{k_{rz_{mn}}\Delta z/2} - e^{-k_{rz_{mn}}\Delta z/2}\right) \qquad (4.27)$$

For increasing values of m and n, it can be seen that the first term within the brackets, and consequently the value of I_z increases exponentially without bound. Clearly, this is a divergent formulation and cannot be successfully implemented on the computer. The key to the solution of this problem is to take account of the correct direction of Floquet mode propagation in the z direction when evaluating the integral. The sources below the testing point should be integrated with an upward direction of Floquet mode propagation, and the sources above it should be integrated with a downward direction of Floquet mode propagation. The enforcing of this condition still allows the integration to be evaluated in closed form, provided it is performed by parts as follows:

$$I_z = \int_{-\infty}^{\infty}\int_{-\infty}^{\infty}\left(\frac{e^{-jk_{z_{mn}}|z-z'|}}{jk_{z_{mn}}}\right)\delta(z-z_k)\,P(z'-z_j)\,dz\,dz'$$
$$= \int_{-\infty}^{\infty}\left(\int_{z_j-\Delta z/2}^{z_j}\frac{e^{-jk_{z_{mn}}(z-z')}}{jk_{z_{mn}}}dz' + \int_{z_j}^{z_j+\Delta z/2}\frac{e^{-jk_{z_{mn}}(z'-z)}}{jk_{z_{mn}}}dz'\right)\delta(z-z_k)dz \qquad (4.28)$$
$$= -2\left(1-e^{-jk_{z_{mn}}\Delta z/2}\right)\Big/k_{z_{mn}}^2$$

As shown in (4.28), the double integral is evaluated over the sources first, and then over the testing points. The direction of Floquet mode propagation implicit in the exponential term within the bracket is taken into account by integrating by parts over the sources below

the testing point corresponding to the term $e^{-jk_{z_{mn}}(z-z')}$, and over the sources above the testing point corresponding to $e^{-jk_{z_{mn}}(z'-z)}$. It is evident that the result is convergent even for large values of m and n. It should be noted that this procedure is unnecessary when integrating over the sources in the xy plane. The significance of the technique is that it overcomes the problem of integrating in the z-dimension and enables the spectral periodic Green's function to be used for modelling infinite phased arrays with elements distributed in all three dimensions.

4.4.2 Convergence Acceleration for On-plane Points

For the geometry of Figure 4.7, the technique described in Section 4.4.1 explicitly enforces the direction of Floquet mode propagation from every source point to a given testing point, except for those source points which are exactly the same height above the ground plane as the testing point. These *on-plane points*, for which the direction of Floquet mode propagation is indeterminate, will cause the spectral periodic Green's function to be slowly converging. Therefore, it is important to use the rapidly convergent hybrid periodic Green's function, where the spectral component, after integration by parts, becomes:

$$\begin{aligned} I_z &= \int_{-\infty}^{\infty}\int_{-\infty}^{\infty}\left(\frac{e^{-jk_{z_{mn}}|z-z'|}}{jk_{z_{mn}}}-\frac{e^{-k_{mn}|z-z'|}}{k_{mn}}\right)\delta(z-z_k)\,P(z'-z_j)\,dz\,dz' \\ &= -2\left[\left(\frac{1-e^{-jk_{z_{mn}}\Delta z/2}}{k_{z_{mn}}^2}\right)+\left(\frac{1-e^{-k_{mn}\Delta z/2}}{k_{mn}^2}\right)\right] \end{aligned} \tag{4.29}$$

Although the analyses derived for the metal strips orientated parallel and perpendicular to the ground plane are different, the variation of active impedance with scan angle is expected to be almost identical in the two cases, provided the metal strip is relatively thin with respect to its length. However, the case of metal strips orientated perpendicular to the array plane has applications to element geometries where the currents are distributed in the z dimension as well as in the xy plane. The analyses for infinite arrays of horizontal metal

strips orientated parallel and perpendicular to the array plane, were applied to model the array of half-wave dipoles analysed by Chang [59]. The dimensions of the array parameters are given in Figure 4.8.

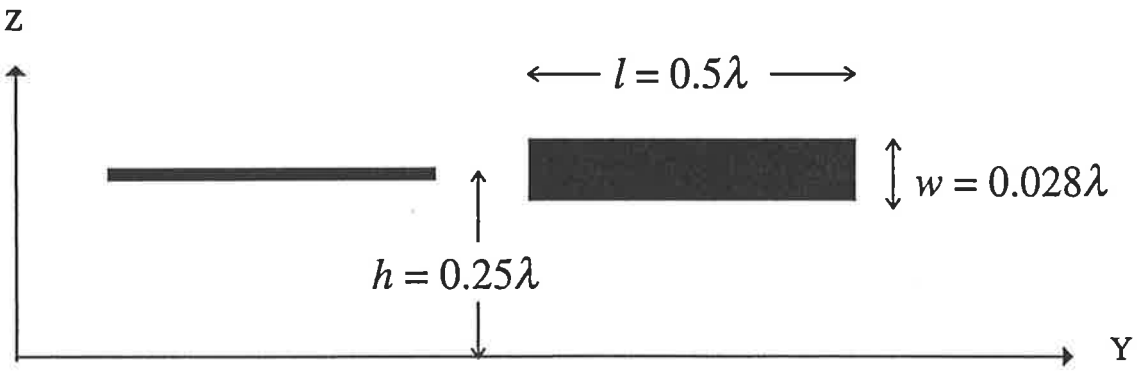

Figure 4.8 : Metal strip elements orientated with their faces parallel and perpendicular to the array plane; $b = 1.2\lambda$, $d = 0.25\lambda$, $h = 0.25\lambda$, $w = 0.028\lambda$.

This infinite array structure was analysed in [59] using a form of the Integral Equation method together with a Fourier series and a five-term approximate expansion of the equivalent currents on the dipoles which were modelled as thin wires with axial currents only. All the array dimensions used in [59] are also used in the analysis here, except that the width of each metal strip is modelled as 4 times the equivalent radius a of his wire dipole where $a = 0.007022\lambda$. It is noted that the inter-element spacing $b = 1.2\lambda$, has been specified such that there is a grating lobe appearing in the E-plane. Furthermore, the inter-element spacing $d = 0.25\lambda$ results in very strong mutual coupling in the H-plane. Therefore, this structure constitutes a rigorous validation of the accuracy of the results obtained using the Generalised Hybrid Periodic Green's Function technique. The variation of active admittance with scan angle in the principal planes of the array is given in Figure 4.9 below.

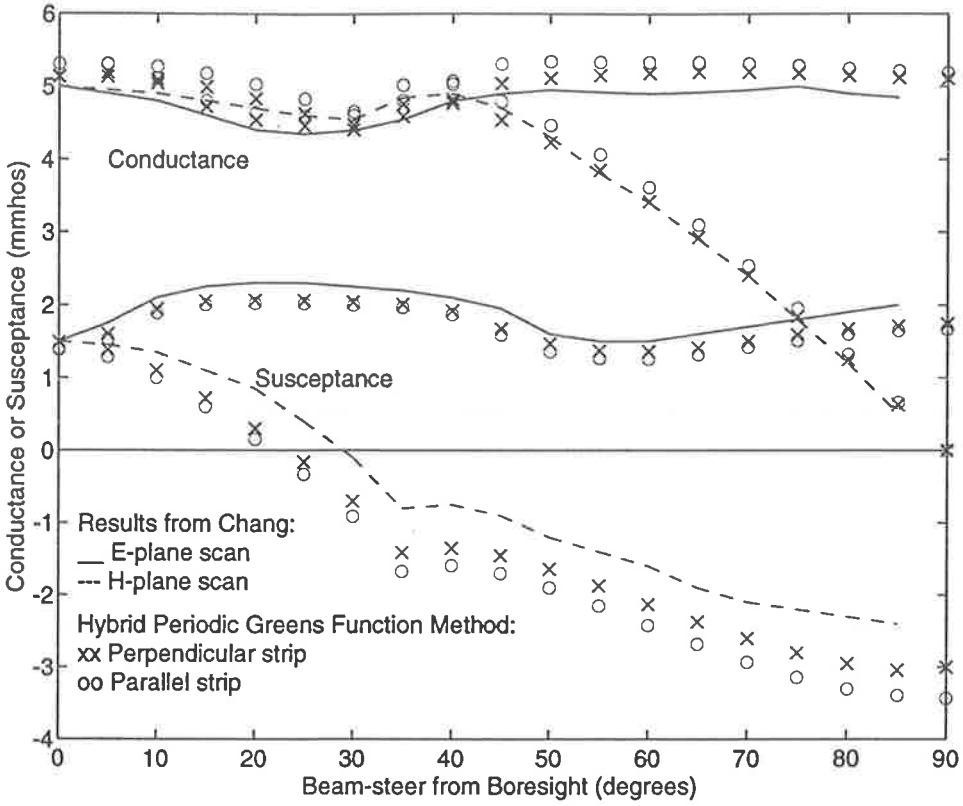

Figure 4.9 : Active Admittance as a function of scan angle for an infinite array of metal strips in the parallel and perpendicular orientations above an infinite ground plane; $b = 1.2\lambda$, $d = 0.25\lambda$, $h = 0.25\lambda$, $w = 0.028\lambda$, $n_y = 7$.

As expected, the active conductance becomes zero as the grazing scan angle in the H-plane, but not for the E-plane because of the grating lobe due to the inter-element spacing of 1.2λ. It can be seen that the results for the models in the two orientations are reasonably close to those of Chang's data for wire dipoles with a small equivalent radius. Of greater significance is the potential of this technique to be extended to model metal patches with two-dimensional currents. In both cases, converged results are obtained with Floquet modes corresponding to $-1 \leq m \leq 1$ and $-1 \leq n \leq 1$. In terms of segmentation, converged solutions were obtained when the metal strip was divided into 7 segments. All the 38 active impedance results in the two principal scan planes were obtained in about 2 seconds of CPU time, so that the average CPU time required was about 0.05 seconds per scan angle. Hence it may be said that this method allows accurate results to be obtained in a reasonably short time using a desktop computer.

4.5 Summary

In this chapter, the procedure of analysis using the Generalised Periodic Green's Function technique has been described and illustrated using the analysis of an infinite array with a relatively simple element geometry consisting of a horizontal dipole above an infinite ground plane. Apart from the description of the procedure, a major focus of this chapter has been to describe the methods to maximise the numerical efficiency of the technique. In the formulation stage of the solution, the possibility of evaluating the integrals over the sources in closed-form, points to the advantage of working in the spectral domain. The slow numerical convergence of the spectral periodic Green's function for on-plane interactions is overcome by the use of a convergence acceleration technique, which leads to the development of a *Generalised Hybrid Periodic Green's Function* having rapid numerical convergence characteristics. The implementation of this Green's function using a Moment Method solution is described, and the numerical data shows a 40 times improvement in computation speed to obtain a set of well converged results. Two techniques to improve computational efficiency in the numerical implementation stage by exploiting Toeplitz-like symmetries of the spectral periodic Green's function, and by the use of look-up tables, are described.

As a prelude to the modelling of three-dimensional element geometries, a new technique for integrating the Green's function over current sources distributed perpendicular to the array plane has been developed. Finally, the accuracy of the techniques described is validated by modelling an infinite array of half-wave dipoles which has been analysed by a different technique and in which the results are used for comparison. The good agreement with Chang's results and the high computational speed achieved has shown the potential for this technique to be used for modelling arrays having more complicated geometries such as microstrip antennas.

In the next chapter, the application of this technique to the modelling of practical metal strip arrays with different element geometries, metal strip junctions and feedlines will be described. As preparation for modelling of microstrip dipole arrays in chapter 6, Chapter 5 will demonstrate that the high numerical efficiency of the technique enables the geometry of a more complex metal strip element such as a metal strip folded dipole with coplanar strip feedlines to be modelled in its entirety with a minimum of idealisations.

The major contributions presented in this chapter are:

- An accurate and numerically efficient technique for the analysis of infinite arrays based on the Generalised Hybrid Periodic Green's Function has been developed, and the procedure for implementing this technique has been described.

- Four methods to maximise the computational efficiency of the technique have been described; some of these methods are also applicable to Integral Equation methods of analysis in general.

- A method of integrating the hybrid periodic Green's function over current sources distributed perpendicular to the array plane, which contributes to a more rapidly convergent solution, has been developed.

CHAPTER 5

Infinite Array Analysis of Metal Strip Structures in Various Configurations

5.1 Introduction and Overview

In Chapter 4, it was demonstrated how the Generalised Periodic Green's Function technique could be efficiently implemented using the Method of Moments to model an infinite array of horizontal metal strips above an infinite ground plane. In preparation for the analysis of three-dimensional element geometries, the element geometry of a horizontal metal strip with its face perpendicular to the array plane, was also analysed. It was shown that for current sources on these metal strips distributed perpendicular to the array plane, the direction of Floquet mode propagation from a source point the testing point needs to be correctly accounted for in the analysis. However, because the metal strips are of one

segment width, all the testing points and the centres of all the metal strip segments are located on the same horizontal plane, which implies that the interactions between the source and testing points result in the *on-plane* condition for all the interactions. The hybrid periodic Green's function was developed in Section 4.3.2 specifically to deal with on-plane interactions so that rapid convergence of the solution may be achieved. For the image sources located far away from the testing points on the metal strip, the interactions are said to be in the *off-plane* condition, and the associated spectral periodic Green's function representing these interactions is rapidly convergent. Therefore the spectral periodic Green's function is applied without convergence acceleration to these interactions. In this chapter, the Generalised Periodic Green's Function technique will be applied to infinite arrays of metal strip structures in which the element geometry extends over more than one segment in the z dimension, as well as in the xy plane. Successful modelling of such structures will mean that the technique can also be extended further to model full three-dimensional geometries in general.

With the requirement to model a feedline for each metal strip element, and a radiating element whose impedance is better matched to the feedline than the metal strip, there is also a need to develop a model for metal strip junctions, which does not appear to be well developed in the literature. The junction models more commonly encountered [60] are for thin wires, and between wires and surfaces. The thin wire model assumes only axial currents, and Kirchoff's current law is enforced at the wire junctions by the use of the one-dimensional continuity equation. This model has the drawback that the accuracy of the model is dependent on the correct specification of the thin wire's equivalent radius which has to be separately determined [61,62]. Furthermore, it has been found that the thin wire junction model cannot be adapted to model metal strip junctions in phased array problems which are formulated in the spectral domain. It will shown in this chapter that the current continuity condition can be implicitly enforced for metal strip junctions in a straight forward manner by using two-dimensional currents on the metal strip segments, and by taking special care in applying the convergence acceleration technique to the spectral periodic Green's function for interactions between adjacent junction segments. This concept will be described in the next section.

5.2 Convergence Acceleration for the Near On-Plane Case

In Section 4.3.2, a technique was developed to accelerate the convergence of the spectral periodic Green's function for the *on-plane* case where the testing point lies *on* the same plane as that of the source. The case when the testing point is located *away* from the plane of the sources, is referred to as the *off-plane* case. In this case, no convergence acceleration is necessary as the spectral periodic Green's function is rapidly convergent. It is found however, that the spectral periodic Green's function is slowly convergent whenever the testing point lies *near* the plane of the sources. Hence, there exists a third condition when the interaction between source and testing points may be described as being *near on-plane*. A quantitative judgement on how near the testing point should be to the plane of the source point for the near on-plane condition to be satisfied, will be made later. In preparation for modelling of three-dimensional element geometries, this section will demonstrate from the viewpoint of computational efficiency, the benefit to be gained by accelerating the convergence of the spectral periodic Green's function, not only for on-plane but also for near on-plane interactions.

5.2.1 Requirement for Convergence Acceleration

In Figure 4.1, the reference point source, S, of an infinite planar array on the xy plane, is located at the origin of the coordinate axes, and a testing point T is at coordinates (Δx, Δy, Δz). The periodic Green's function at T represents the effect of the infinite array of sources on the point T. For a given Δz and convergence criterion which is explained later, a numerical experiment is used to investigate the computational effort needed to obtain a converged value of the spectral and the hybrid periodic Green's functions.

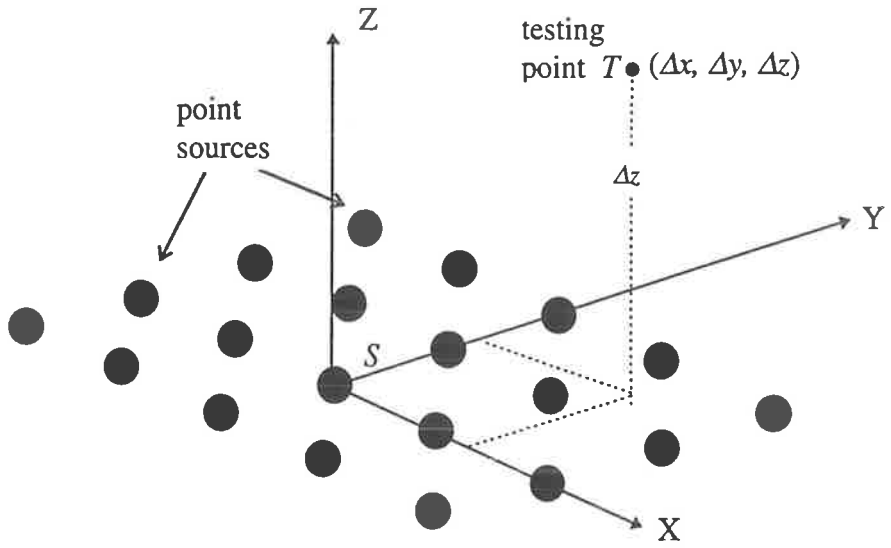

Figure 5.1 : A testing point T located at a distance Δz away from the plane of the infinite array of point sources in the xy plane.

Based on the above considerations, a computer program was written to calculate the spectral and hybrid periodic Green's functions, and to enable a fair comparison of the computation time taken in each of the calculations. The objective of the numerical experiment was to determine the minimum number of Floquet modes required by each of these two periodic Green's functions to satisfy the convergence criterion for a given vertical distance of the testing point away from the plane of the sources. Each of the series representing the spectral and hybrid periodic Green's function given by (3.9) and (4.15) is used in the first case to calculate a value of the respective Green's function when the series is truncated for values of (m,n) where $-M \le m \le M$ and $-N \le n \le N$. In the second case, the calculations are made for values of (m,n) where $-M-1 \le m \le M+1$ and $-N-1 \le n \le N+1$. The convergence criterion E_{rel} is the relative error in the value of the Green's function between the two cases calculated as described above. The calculations were made for relative errors ranging from 10^{-5} to 10^{-1}, and the total number of Floquet modes used in each of the truncated doubly infinite series which met the criterion was recorded. Each of these computations was repeated for different values of Δz ranging from 0.001λ to 0.1λ; it was found that the results were relatively insensitive to variations in Δx and Δy. The results in Tables 5.1 and 5.2 below provide an indication of the convergence properties of the spectral and hybrid forms of the periodic Green's function.

Δz	$E_{rel}=10^{-1}$	$E_{rel}=10^{-2}$	$E_{rel}=10^{-3}$	$E_{rel}=10^{-4}$	$E_{rel}=10^{-5}$
0.1 λ	25	49	49	121	169
0.05 λ	25	49	81	225	225
0.03 λ	25	81	225	625	961
0.01 λ	25	361	1,521	3,481	6,241
0.005 λ	49	361	2,401	6,241	14,161
0.001 λ	81	841	4,761	25,281	101,761

Table 5.1 : Number of Floquet modes used to obtain a converged value for the spectral periodic Green's function for a given relative error and vertical displacement of the testing point from the plane of the sources.

Δz	$E_{rel}=10^{-1}$	$E_{rel}=10^{-2}$	$E_{rel}=10^{-3}$	$E_{rel}=10^{-4}$	$E_{rel}=10^{-5}$
0.1 λ	9	25	49	49	121
0.05 λ	9	25	49	49	225
0.03 λ	9	25	49	49	225
0.01 λ	9	25	49	225	729
0.005 λ	9	25	49	289	841
0.0	9	25	49	361	841

Table 5.2 : Number of Floquet modes used to obtain a converged value of the hybrid periodic Green's function for a given relative error and vertical displacement of the testing point from the plane of the sources.

Comparing the data in the Tables 5.1 and 5.2, it is noted that for values of $\Delta z > 0.03\lambda$, both the spectral and hybrid periodic Green's functions generally require a similar number of Floquet modes to achieve a given level of numerical convergence. Therefore, if a testing point is separated by a distance of $\Delta z > 0.03\lambda$ from the sources, the interaction is described

here as satisfying the *off-plane* condition. In this case, convergence acceleration yields only a marginal improvement in computational efficiency and the spectral periodic Green's function is adequate. For values of $\Delta z < 0.001\lambda$, the spectral periodic Green's function series is very slowly convergent, and requires in excess of 100 times as many terms to achieve convergence when compared with the hybrid periodic Green's function series. Hence, if a testing point is spaced by a distance of $\Delta z < 0.001\lambda$ from the sources, the interaction is said to satisfy the *on-plane* condition where the hybrid periodic Green's function is used. Tables 5.1 and 5.2 also show that for values of Δz between the two extremes, convergence of the spectral periodic Green's function series requires typically 3 to 5 times as many terms as the hybrid periodic Green's function series. In this region, convergence acceleration of the spectral periodic Green's function is also considered beneficial, and the interactions are described in this thesis as satisfying the *near on-plane* condition. The conclusions of this section are summarised in Table 5.3 below.

Condition	Interaction Distance	Periodic Green's Function Used
On-plane	$\Delta z < 0.001\ \lambda$	Hybrid
Near on-plane	$0.001\ \lambda \leq \Delta z \leq 0.03\lambda$	Hybrid
Off-plane	$\Delta z > 0.03\lambda$	Spectral

Table 5.3 : Definition of on-plane, near on-plane and off-plane interactions, and the type of generalised periodic Green's function to be used in the analysis for a numerically efficient solution to be obtained.

The conclusions derived here are illustrated below by the modelling of an infinite array of vertical monopoles which has an element geometry in which the mutual coupling between the current sources distributed in the z dimension are characterised by on-plane, near on-plane and off-plane conditions.

5.2.2 Formulation for an Infinite Array of Vertical Monopoles

Figure 5.2 shows an element of an infinite phased array of vertical monopoles above an infinitely large ground plane, being modelled as a thin metal strip of length l and width w, orientated vertically in the yz plane and excited by a Delta-gap voltage at its base. In terms of modelling, the important difference between this element's geometry and that of the horizontal metal strip discussed previously is that the current sources are distributed in the z dimension over more than a single segment so that on-plane, near on-plane and off-plane conditions apply.

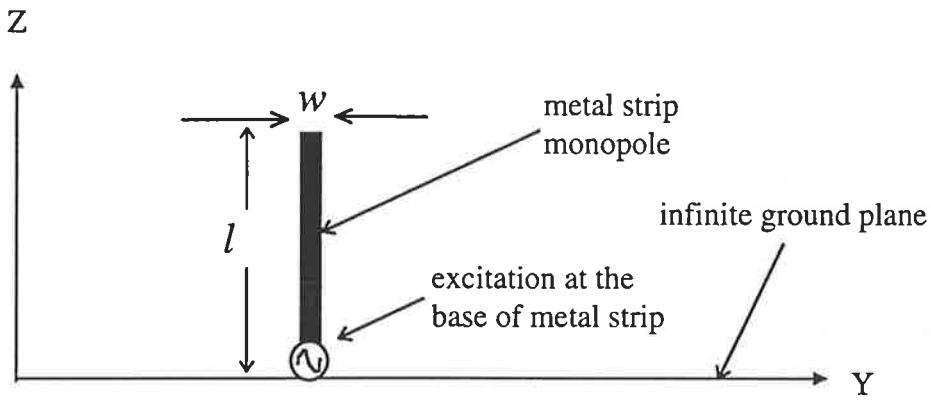

Figure 5.2 : An element of an infinite array of vertical monopoles above an infinite ground plane, modelled as a vertical metal strip.

The vertical metal strip in Figure 5.2 is divided into segments, and the bottom two segments of the metal strip are depicted in Figure 5.3. The lowest segment is in contact with the ground plane, and its image is depicted as a source segment S'_1 . The effect of source points on the three segments at a testing point P_t located at the centre of segment S_1 is being considered next. It is assumed that the height of a segment, $\Delta z = 0.05\lambda$, so that by the definitions given in Section 5.2.1, all of the source points in S_1 are in either the on-plane or near on-plane condition with respect to P_t . Furthermore, some of the source points in both S_2 and S'_1 are also in the near on-plane condition with respect to P_t . It is not expeditious to represent the effect of only the part of S_2 and S'_1 satisfying the near on-

plane condition, by means of a hybrid periodic Green's function. Hence, where parts of adjacent segments have source points which satisfy the near on-plane condition, the hybrid periodic Green's function is used to represent the effect of all the sources from those segments on P_t.

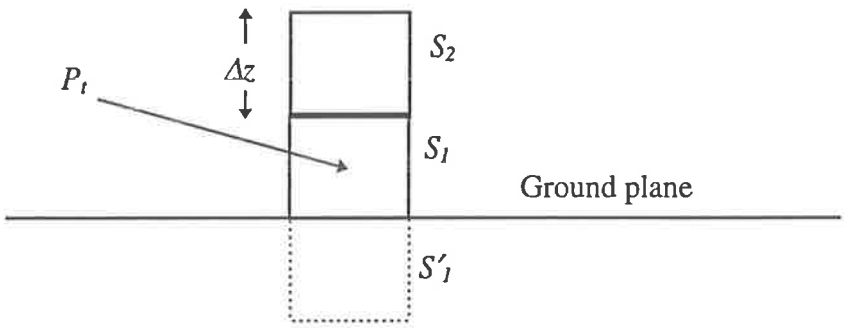

Figure 5.3 : Adjacent segments on the vertical metal strip in which there are on-plane and near on-plane interactions.

A model of the infinite array of vertical monopoles is developed for a rectangular grid lattice as well as a triangular grid lattice. In the latter case, the spectral periodic Green's function for a triangular lattice as derived in Section 3.3.1 is used in the numerical computations. For off-plane interactions, the spectral periodic Green's function is used in the computations. For on-plane and near on-plane interactions, the hybrid periodic Green's function is used. The arrangement of the elements in both lattice structures is shown in Figure 5.4 below. The rectangular grid lattice is represented by the dark ellipses and the triangular grid lattice is represented by the small rectangles. The dimensions and segmentation of the elements, and the lattice spacings for the triangular grid lattice are specified to be identical to those of the monopole array analysed by Schuman [63], so that the results could be compared.

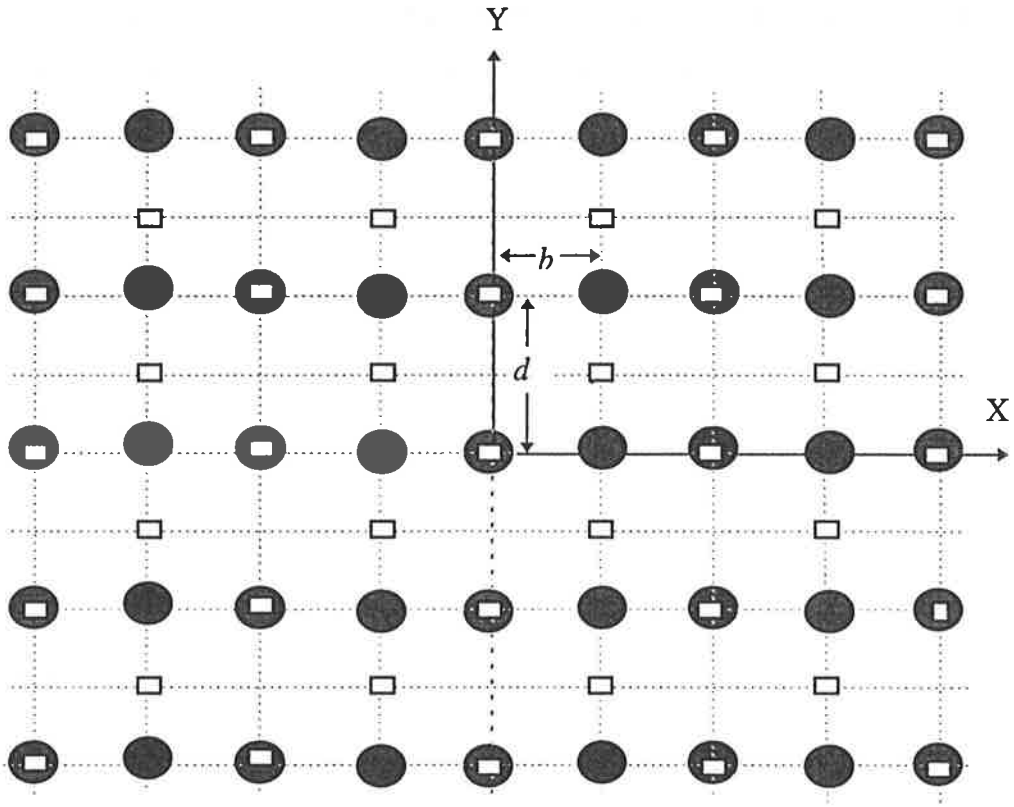

Figure 5.4 : Arrangement of the array elements in rectangular and triangular grid lattices.

Schuman analysed this infinite array structure using a form of the Integral Equation solution known as the Plane Wave Expansion Moment Method (PWEMM), and each element of the array was modelled as a thin wire monopole with axial currents. In this analysis, each monopole is modelled as a vertical metal strip orientated in the yz plane. The width of the metal strip, $w = 0.02\lambda$ is chosen to be 4 times the equivalent radius of the wire used by Schuman. In the case of the rectangular grid lattice, the inter-element spacings are chosen to be $b = 0.5\lambda$ and $d = 0.577\lambda$ respectively, in the x and y directions. For the triangular grid lattice, the distance between columns of elements is $b = 0.5\lambda$ and the distance between elements in the same column is set at $d = 0.577\lambda$. Each metal strip of height $h = 0.3\lambda$ is divided into 4 segments and is excited by a z-directed delta-gap voltage at the bottom segment which is in contact with the ground plane. In this case, it is only necessary to use the hybrid periodic Green's function for self couplings and mutual

couplings between adjacent segments; the spectral periodic Green's function is used to represent all the other sets of interactions. The graph of active impedance variation with scan angle in the *xz* plane for the triangular lattice monopole array is given in Figure 5.5 below.

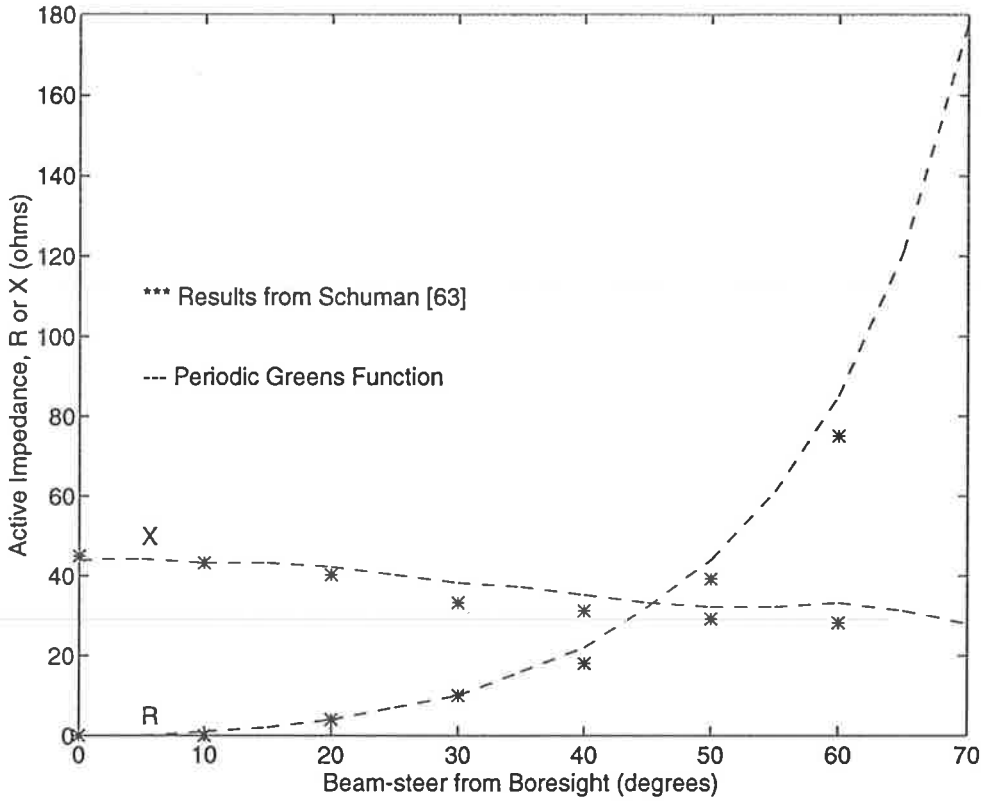

Figure 5.5 : Active impedance as a function of scan angle in the *xz* plane for a *triangular grid lattice* infinite array of vertical monopoles; $h = 0.3\lambda$, $w = 0.02\lambda$, $b = 0.5\lambda$, $d = 0.577\lambda$, $n_z = 4$.

In Figure 5.5, it is apparent that the results obtained using the Generalised Periodic Green's Function technique are in good agreement with Schuman's results for an infinite array of monopoles in a triangular grid lattice. The results for a rectangular grid lattice array with the same element geometry are shown in Figure 5.6. The results for a triangular grid lattice from Figure 5.5 are superimposed for comparison.

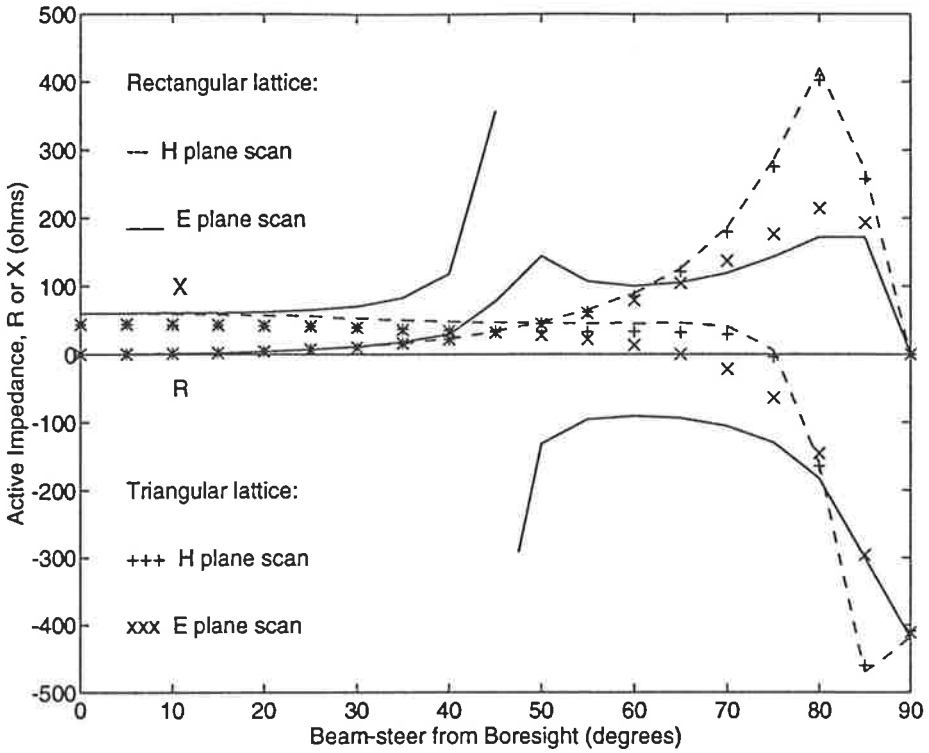

Figure 5.6 : Active impedance variation with scan angle in the principal planes for a *rectangular grid* and *a triangular grid lattice* array of vertical monopoles; $h = 0.3\lambda$, $w = 0.02\lambda$, $b = 0.5\lambda$, $d = 0.577\lambda$, $n_z = 4$.

In the xz plane scan which also the H-plane, the active impedance are similar for the rectangular and triangular grid lattices. However in the yz plane which is the E-plane, there is a grating lobe predicted at 47° scan angle for the rectangular lattice array but not for the triangular lattice array. This observation confirms the expectation in Section 3.4.3 about the superiority of the triangular grid lattice array in avoiding grating lobes.

The numerical efficiency of the Generalised Periodic Green's Function technique for the infinite array of metal strip monopoles in which the element geometry involves both on-plane and near on-plane interactions is shown in Table 5.4 below.

Number of Floquet Modes used in Generalised Periodic Green's Function		Active Impedance at Boresight Scan Angle
xz plane	*yz* plane	(Ω)
1	1	0.0 - j 42.6
3	3	0.0 + j 15.8
5	5	0.0 + j 40.2
7	*7*	*0.0 + j 48.3*
9	9	0.0 + j 50.7
11	11	0.0 + j 51.0
21	21	0.0 + j 51.7

Table 5.4 : Active Impedance at boresight scan for an infinite rectangular grid lattice array of vertical metal strips above an infinite ground plane; $h = 0.3\lambda$, $w = 0.02\lambda$, $b = 0.5\lambda$, $d = 0.577\lambda$, $n_z = 4$.

As shown in Table 5.4, a converged value for the active impedance is reached when the hybrid periodic Green's function series is truncated at $-3 \leq m \leq 3$ and $-3 \leq n \leq 3$. The corresponding CPU time to calculate the active impedance per scan angle is 0.54 seconds.

Having developed the technique to efficiently model metal strips with current sources distributed in the dimension perpendicular to the array plane, the next section extends the analysis to model the junctions between metal strips which may be required for element geometries such as folded dipoles and for inclusion of coplanar strip feedlines into the horizontal metal strips array model.

5.3 Modelling of Metal Strip Junctions

The infinite array analyses for horizontal and vertical metal strip elements using the Generalised Periodic Green's Function technique, have been shown to be numerically efficient so that the typical CPU time required to calculate the active impedance is less than one second per scan angle. The high computational efficiency of the technique makes it possible to include the feedlines into the model, and to model other types of metal strip elements for purposes of impedance matching. Furthermore, it is also highly desirable to be able to model these structures in their entirety with a minimum of idealisations. To do this, it is first necessary to be able to model metal strip junctions. Apart from accuracy, an important consideration in junction modelling is to enforce the current continuity condition at the junction in such a way as to enable a computationally efficient numerical solution to be obtained. A number of different techniques have been developed for junction modelling; three of these methods and their relative merits will be briefly described and assessed in this section. Finally, a simple but sufficiently accurate method of *modelling metal strip junctions* is developed to be used with the Generalised Periodic Green's Function technique.

5.3.1 Survey of Approaches to Junction Modelling

A type of junction model which is commonly encountered is known as the *wire junction model* [60,61,62]. The wire is usually modelled with an equivalent radius, and the axial currents I_1, I_2, and I_3 at the wire junction are expanded using pulse basis functions as shown in Figure 5.7. The charge density distribution is also expanded using pulse basis functions with the same pulse length, but off set from the current pulses by half a pulse. The half-pulses representing the charges protruding beyond the physical ends of the wires are made to overlap at the junction, and the continuity condition is maintained by enforcing the conservation of charge at the end of each wire.

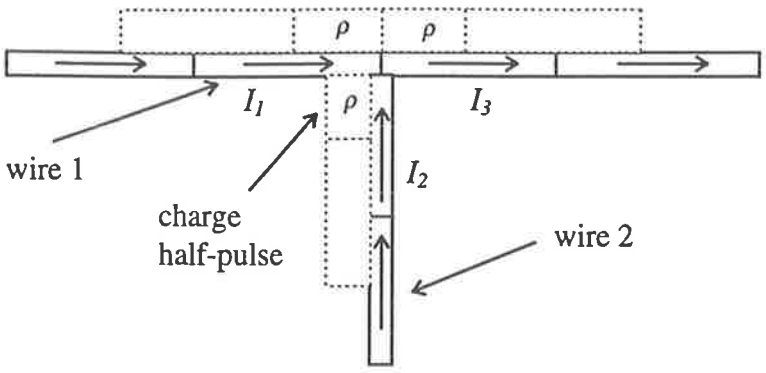

Figure 5.7: A wire junction model showing the junction current and charge density pulses.

This wire junction model is particularly suitable for use with the spatial periodic Green's function where pulse basis functions representing the charges are off-set from those representing the currents, so that the derivatives contained in the dyadic Green's function are taken using the method of central finite difference. It is not as suitable for modelling junctions between metal strips which have two dimensional currents. It is also found to be incompatible for implementation with the spectral periodic Green's function in which the current and charge pulses are not off-set from each other. Hence this technique could not be adopted.

A second junction model was developed by Newman and Pozar [58] for modelling wire-to-surface patch junctions using one-dimensional basis functions for the wires, two-dimensional basis functions for the flat plate surfaces, and overlapped surface patch modes where two plates intersect. This method assumes that in the vicinity of a wire-to-plate junction where the wire lies in a plane orthogonal to the plate, the current may be decomposed into a quasi-radial component flowing from the wire onto the plate over a *generalised frill,* and a slowly varying component distributed over the plate. Such a frill and the basis functions associated with it is referred to as an *attachment mode.* However, if the conducting part of the element geometry consists only of interconnected metal strips with various orientations which lie in the same vertical plane, then a dominant quasi-radial component does not exist, and a simpler method for modelling the junctions between the metal strips is possible.

A third junction model has been developed by Popovic and Kolundzija [64] who adopted entire domain basis functions and a Galerkin approach for solving the integral equations, and employed wires and quadrilaterals to approximate the element geometry. By expressing the entire-domain approximation for the equivalent currents in the same coordinates as the surface elements, they used a procedure for converting any set of basis functions into a new set which automatically satisfies current continuity at all interconnections without the need for attachment modes. This technique, though attractive, cannot be used in this analysis which employs sub-domain basis functions and the point matching method. However, conclusions about the behavior of the currents in the so called *junction domain* in their model, provide useful insights which are applied to the junction model to be described in the next section. The concept of a junction domain is shown in Figure 5.8 below.

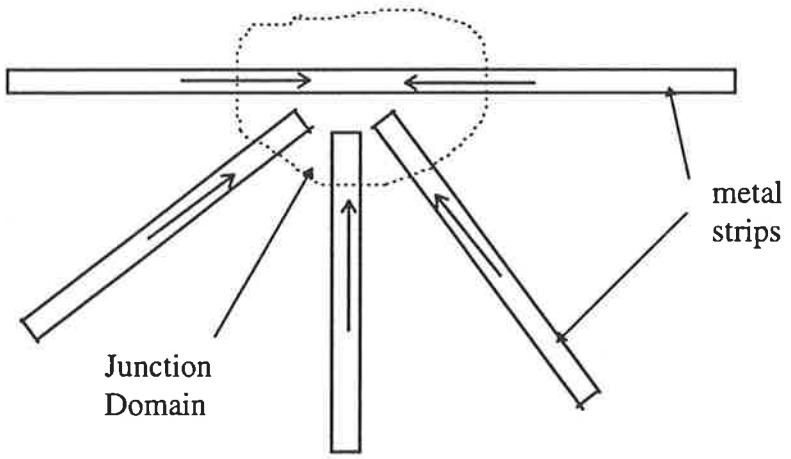

Figure 5.8 : A localised junction model junction showing a junction domain enclosing the ends of the metal strips which are interconnected.

As depicted in Figure 5.8, at the metal strip junction, the ends of the metal strips are assumed to be interconnected by small pieces of metallic wire located in an electrically small region of arbitrary shape known as a *junction domain*. From quasistatic analysis, it can be shown that provided the junction domain is electrically small, the sum of all the currents on the metal strips flowing into this region is zero, and that the currents flowing through the ends of the metal strips are independent of the geometry of the metallic wires

interconnecting them. Therefore a satisfactory analysis of such a junction can be obtained by omitting the interconnecting wires from the geometrical model, provided that the current continuity condition is enforced at the junction.

5.3.2 A New Junction Model for Metal Strips

Based on Popovic's arguments outlined in the previous section, if the junction region between one or more metal strips is electrically small, then the contribution of the currents in the junction domain to the radiated field may be ignored provided that the current continuity condition is obeyed. This principle is used here to derive a new junction model shown in Figure 5.9 below.

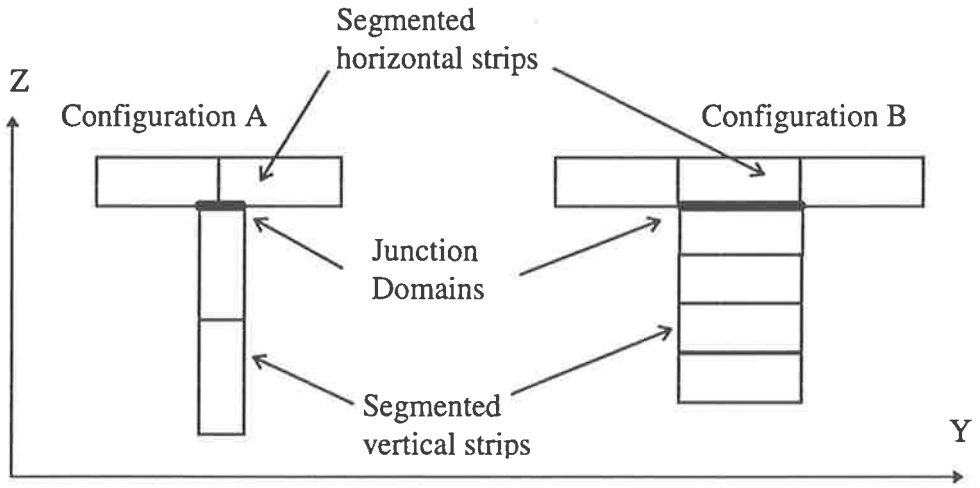

Figure 5.9 : Two configurations of metal strip junctions where the interconnections of metal strip segments at the junction are within a rectangular junction domain.

There are a number of ways of configuring the metal strip junction in relation to the segments used to represent the equivalent currents on the metal strip surfaces. In Figure 5.9, the junction domain is assumed to be an electrically small rectangle which encloses the line where the vertical and horizontal strips come into contact. There are two possible configurations that may be used to model the junction, as shown in Figure 5.9. *Configuration A* enables the segment size for the vertical and horizontal arms to be independently specified. In *Configuration B*, the same segment dimensions are used for

both the vertical and horizontal metal strips which enable the entire structure to placed on a common grid as described in Figure 4.4 so that the spatial component of the hybrid periodic Green's function may be more efficiently computed. Both configurations have been successfully used to model various types of phased array elements in this research. Since the metal strip segments have two dimensional equivalent currents, the current continuity condition is implicitly enforced on the junction segments by the boundary conditions, provided that the interconnections in the junction domain do not contribute to the radiation. This latter condition is met since the junction domain is electrically small.

5.3.3 Convergence Acceleration of the Spectral Periodic Green's Function for Junction Segments

In the spectral periodic Green's function technique, the coefficient of the equivalent current pulse is evaluated at the centre of each segment. The coefficient of the charge pulse which represents the derivative of the current, is also evaluated analytically at the centre of each segment. This procedure of determining the equivalent currents is compatible with the junction model developed in Section 5.3.2. However, in the case where the testing and source points are located on segments which lie just above and below the junction domain, the more rapidly convergent hybrid periodic Green's function is used. This Green's function has a spatial component in which the integration has to be evaluated numerically. The spatial component has a current component and a charge component which is a partial derivative of the current. The derivative is normally evaluated by the method of central finite difference [65]. The evaluation of this derivative needs to be performed with some care in order to preserve the correct contribution of these sources near the junction region.

Figure 5.10a shows how the partial derivatives of the spatial Green's function with respect to z should be taken in the case where the geometry is a continuous metal strip. Figure 5.10b shows the case when the source and testing points are located in segments adjacent to the junction domain. The double partial derivative may be taken with respect to any two dimensions. Because the junction domain can be considered as a thin rectangle cutting

across the ends of the segments immediately above and below it in the yz plane, only the z directed currents can flow into this rectangle. Hence only the partial derivatives with respect to z require special attention.

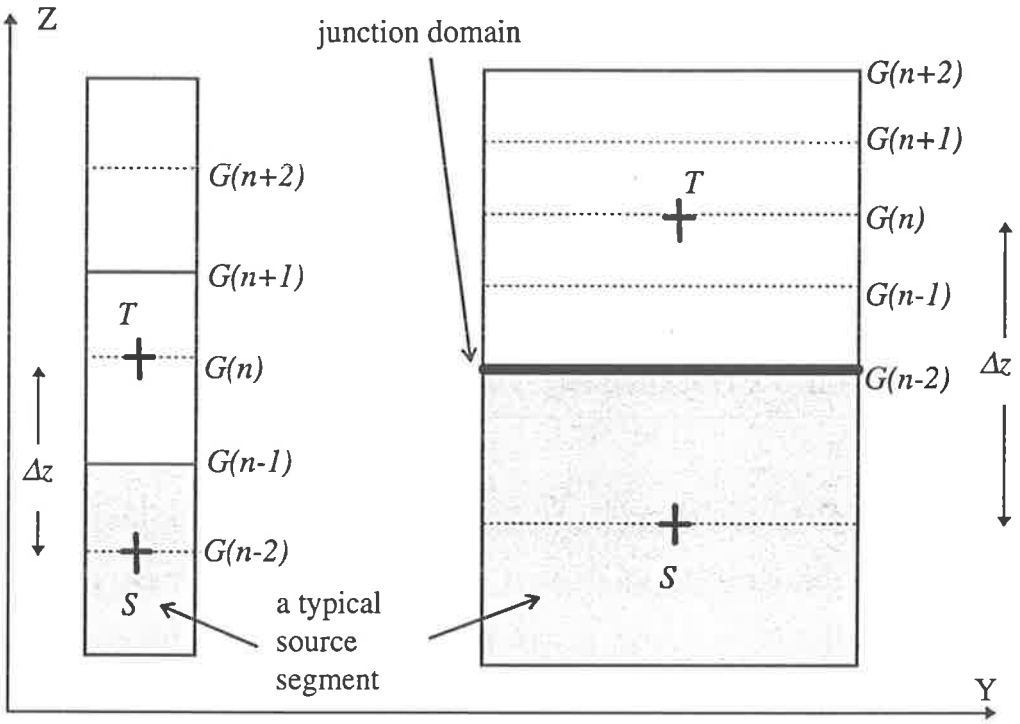

Figure 5.10a : Taking of finite difference for segments on a continuous metal strip

Figure 5.10b : Taking of finite difference for segments adjacent to the metal strip junction

The procedure for taking a double partial derivative with respect to the z direction is first considered for the case of a continuous metal strip shown in Figure 5.10a. The source segment centred at S is shaded, and the current basis function is a two-dimensional pulse of dimensions equal to the segment. If $G(n)$ is the spatial periodic Green's function representing the effect of an infinite array of sources centred at S, on a testing point T, then the double partial derivative of this Green's function with respect to z may be evaluate by central finite difference as:

$$\frac{\partial^2}{\partial z^2} G(n) = \frac{G(n+2) - 2G(n) + G(n-2)}{(\Delta z)^2} \tag{5.1}$$

Equation (5.1) describes how the derivative is numerically evaluated in the case of the continuous metal strip where the Green's function is evaluated at intervals of $\Delta z/2$. This procedure also applies to the case of self interaction, when both the source and testing points are located on the same segment adjacent to the junction domain.

In Figure 5.10b, the location of the source and testing points on different sides of the junction domain needs to be taken into account when determining the interval between the points at which the Green's function is evaluated. If the Green's functions are evaluated at smaller intervals of $\Delta z/4$, the field points used for taking the finite difference do not cross over the junction into the source segment. It was found from numerical experiments that provided this condition is met, the use of even smaller intervals to compute the finite difference did not lead to significant improvements in the evaluation of the partial derivatives. Hence the derivative of the spatial component of the hybrid periodic Green's function for junction segments is given by:

$$\frac{\partial^2}{\partial z^2} G(n) = \frac{G(n+2) - 2G(n) + G(n-2)}{(\Delta z/2)^2} \tag{5.2}$$

In summary, partial derivatives of the spatial component of the hybrid periodic Green's function are evaluated by the method of finite difference. For source and testing points located on different sides of a junction domain, finer intervals must be used when taking the finite differences with respect to the z direction. The interval size must be chosen such that the testing point does not cross over the junction when evaluating the finite difference. The junction modelling technique developed in this section is next illustrated using the analysis of an infinite array of folded dipoles.

5.3.4 Formulation for Infinite Arrays of Folded Dipoles

Figure 5.11 shows how an element of an infinite array of centre-fed folded dipoles may be modelled as two metal strips of length l and width Δz, connected to two individual metal segments of height Δz, at an overall height h above an infinite ground plane. The structure is excited at the centre of the driven arm by a delta-gap voltage, and has a total of 4 junctions connecting the 2 metal strips and 2 thin individual metal segments. The use of the hybrid periodic Green's function for on-plane and near on-plane interactions, and the junction modelling technique described in Section 5.3.2 are applied into the analysis of this structure.

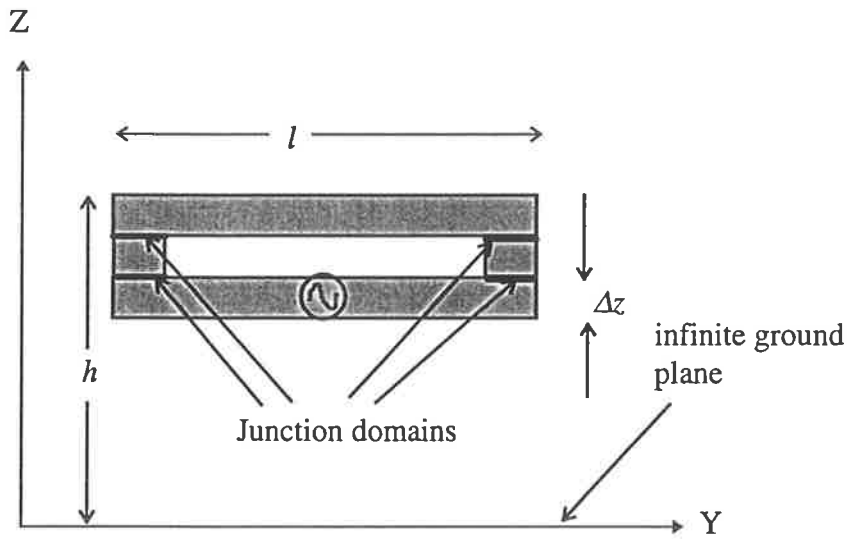

Figure 5.9 : Centre-fed metal strip folded dipole element of an infinite array above an infinite ground plane.

The characteristics of an isolated folded dipole [66,67] and for a two element folded-dipole [68] are documented in the literature. A folded dipole can be modelled by treating its current as being composed of a transmission line mode current and an antenna mode current [69,70,71], provided that its driven and folded arms are electrically thin and closely spaced. Under these conditions, the *Transmission Line model* of the folded dipole provides an insight into the behavior of the folded dipole and a numerically efficient analysis of the problem. It also describes a relationship between the input impedance of the folded dipole

and that of the simple dipole, which can be used to validate the accuracy of the junction modelling technique described in Section 5.3.2. However, it has been found that the transmission line model of the folded dipole is only accurate [72] if the separation between the parallel arms of the folded dipole are electrically close together (a maximum of about 0.01λ) so that the usual transmission line equations apply [73]. If the separation between the two arms is much greater than 0.01λ, the structure behaves more like a narrow rectangular loop antenna. Lampe [69] has developed an expression for the input impedance of a folded dipole based on the Transmission Line model:

$$Z_{in} = \frac{2(1+a)^2 Z_d Z_t}{(1+a)^2 Z_d + 2Z_t} \tag{5.3}$$

where Z_d and Z_t are the impedance of the equivalent dipole and transmission line modes, respectively; $(1+a)^2$ is the impedance step-up ratio and a is the ratio of the currents on the two dipole arms in the antenna mode. It can be shown [72] that if the two arms of the folded dipole are of equal width and the structure is excited near to the frequency of its half-wave resonance, the input impedance of the metal strip folded dipole given in (5.3) is four times that of an equivalent width single metal strip dipole. This result will be used to validate the model for the infinite array of folded dipoles based on the junction model developed in Section 5.3.2.

The model of an infinite array of metal strip dipoles orientated with their faces perpendicular to the array plane described in Section 4.4 is used to predict the variation of active impedance with scan angle. The results for this metal strip dipole array are plotted in Figure 5.12. The results of active impedance as a function of scan angle for the infinite array of metal strip folded dipoles are also plotted on the same graph, but with the active impedance values divided by a factor of 4. The length of the metal strip in both cases is set at $l = 0.485\lambda$ which is the resonant length of the isolated simple dipole in free space [74]. The height of the element above the ground plane in both cases is adjusted so that a resonance condition is achieved, and the combined width of the metal strip folded dipole arms is set equal to the width of the metal strip.

Figure 5.12 shows the variation of active impedance with scan angle in both the principal planes of scan. It is apparent from the graph that the agreement between the metal strip and folded dipole results is almost exact at the boresight scan angle. This result is significant as it shows that the use of the generalised hybrid periodic Green's function for on-plane and near on-plane interactions described in Section 5.2 as well as the metal strip junction model developed in Section 5.3.2 which have been applied to the folded dipole model have correctly predicted the result for a known condition and complex geometry. The agreement between the results of the two models is very close for all scan angles in the E-plane, and for scan angles up to about 50° in the H-plane. The slight deviation in the results for larger angles in the H-plane is probably due to the finite separation between the two arms of the folded dipole and the stronger mutual couplings in the H-plane at large scan angles.

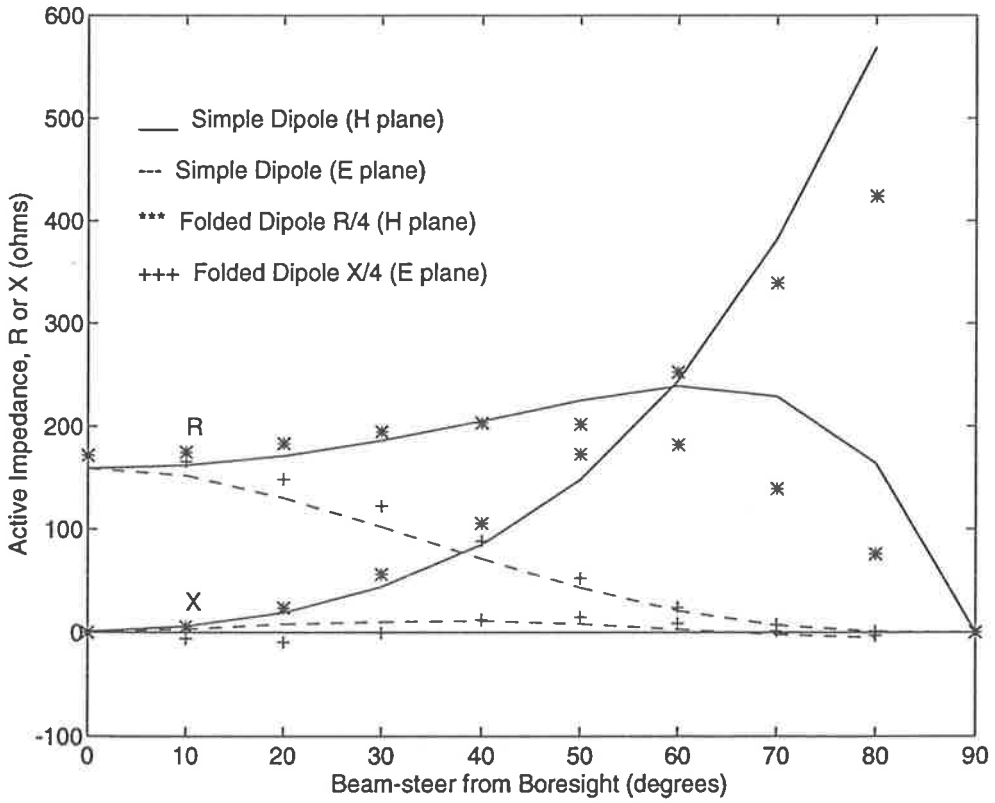

Figure 5.12 : Active impedance as a function of scan angle for infinite arrays of simple dipoles and folded dipoles in the principal planes of scan; $b = d = 0.5\lambda$. For the metal strip, $l = 0.485\lambda$, $w = 0.02\lambda$, $h = 0.226\lambda$. For the folded dipole, $l = 0.485\lambda$, $\Delta z = 0.01\lambda$, $h = 0.2245\lambda$, $n_y = 9$.

The accuracy of the folded dipole model has confirmed the validity of the junction modelling technique employed in the analysis. It is also concluded from the results that provided the folded dipole's arms are sufficiently close together, the Transmission Line model of the folded dipole can be applied to the infinite array environment with good accuracy over all of scan space. The ability to model the full element geometry of the folded dipole without idealisations has been made possible by the high computational efficiency of the Generalised Periodic Green's Function technique.

The numerical efficiency of the technique may be gauged by the number of Floquet modes used in the Hybrid Periodic Green's Function series and the CPU time taken for the calculation of a converged value of the active impedance, as shown in Table 5.5 below.

Floquet Modes Used	Active Impedance (Ω)	CPU Time Taken (Seconds)
1 x 1	450.3 + j 309.0	2.7
3 x 3	474.8 + j 363.5	3.0
5 x 5	*686.0 + j 0.3*	*4.1*
11 x 11	657.5 + j 2.3	12.0
17 x 17	654.5 + j 1.4	23.0

Table 5.5 : Active impedance at boresight scan for an infinite array of centre-fed folded dipoles (rectangular grid lattice) above an infinite ground plane; $b = d = 0.5\lambda$, $l = 0.485\lambda$, $\Delta z = 0.01\lambda$, $h = 0.2245\lambda$, $n_y = 9$.

It is apparent from Table 5.5 that the result is converged for Floquet modes $-2 \leq m \leq 2$ and $-2 \leq n \leq 2$ used in the evaluation of the hybrid periodic Green's function, with a corresponding CPU time of 4.1 seconds used to calculate the active impedance per scan angle. In the next section, the junction modelling technique is used for the analysis of array elements with feedlines.

5.4 Feedline Modelling

Having demonstrated that the metal strip junction modelling technique developed in Section 5.3 is able to accurately and efficiently model the element geometry of a metal strip folded dipole, the technique is now extended to model a coplanar strip feedline for a metal strip dipole. The intention here is to develop the capability to model the feedlines for a microstrip dipole array which is described in Chapter 6. A feed structure that is commonly used for a microstrip dipole antenna is the coplanar strip feedline shown in Figure 5.13. The two feedline-to-radiator junctions can be modelled equally well using either of the Configurations A and B described in Figure 5.9. Configuration A is modelled first so that the results could be validated against the same model analysed by Schuman [29] using the Plane Wave Expansion Moment Method (PWEMM) and by Cooley [75] using a Moment Method with equivalent fin electric currents and aperture magnetic currents. Configuration A also has the advantage that the current segments on the radiating element can be different in dimensions from the those on the feedline.

Configuration A Junction Feedline Model

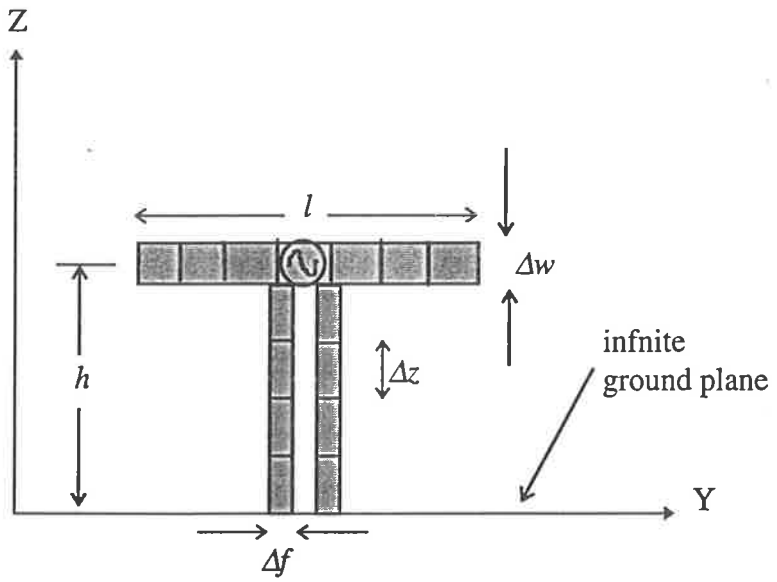

Figure 5.13 : Metal strip array element with coplanar strip feedline. The metal strip - feedline junction is modelled using *Configuration A* junction feedline model.

Using the same segmentation scheme as Schuman, the metal strip of length $l = 0.375\lambda$ is divided into 5 segments, and the coplanar strip feedline of height $h = 0.25\lambda$ is divided into 4 segments. The element is excited by a delta-gap voltage at the centre segment of the horizontal metal strip. In order to relate this model to a practical antenna structure, it is assumed that the active impedance obtained at the feed point of the metal strip can be translated back to the base of the coplanar strip feedline which is connected to a balun structure located below the ground plane. It is also assumed that the impedance at the base of the feedline is terminated with a short circuit at the ground plane. Schuman modelled both the dipole element and feedline as thin wires with the same equivalent radius, $r = 0.0125\lambda$. As the dipole element and feedline are modelled as metal strips in this analysis, the width of each metal strip is set at $w = 4\ r = 0.05\lambda$. The inter-element spacings are set at $b = 0.5\lambda$ and $d = 0.4\lambda$, in the x and y directions, respectively. The results of the model are given in Figure 5.14 below.

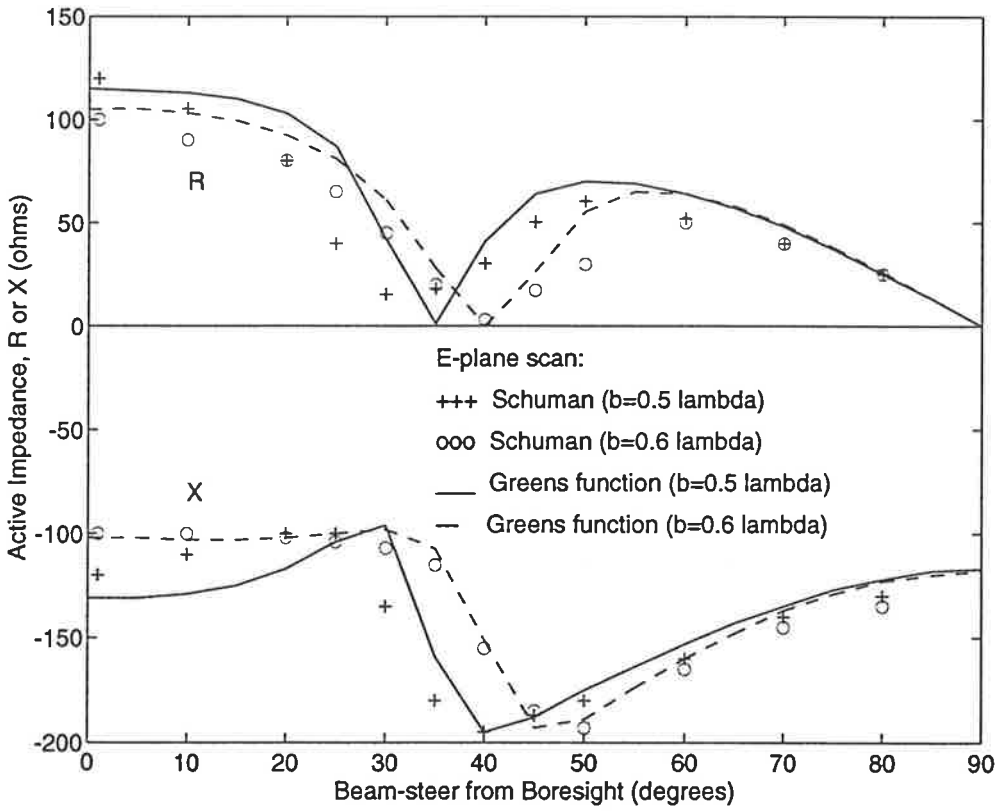

Figure 5.14 : Active impedance as a function of scan angle for an infinite rectangular grid lattice array of metal strips with coplanar strip feedlines in the E-plane; $b = 0.5\lambda$, $d = 0.4\lambda$, $l = 0.375\lambda$, $h = 0.25\lambda$, $\Delta w = \Delta f = 0.05\lambda$, $n_y = 5$, $n_z = 4$.

Figure 5.14 shows the variation of active impedance with scan angle in the E-plane for lattice spacings in the x direction of $b = 0.5\lambda$ and $b = 0.6\lambda$. It can be seen that the results obtained with the generalised periodic Green's function technique and the metal strip junction model developed in this thesis are in very good agreement with Schuman's results. The occurrence of feedline induced scan blindness in infinite dipole arrays is well known [76]. It is apparent that for the $b = 0.6\lambda$ lattice spacing there is a feedline induced scan blindness at about 40° from boresight in the E-plane. When the lattice spacing is reduced to $b = 0.5\lambda$, the scan blindness angle correspondingly reduces to 35° from boresight. Hence the model has confirmed Schuman's findings with regards to the occurrence of scan blindness as well as the effect of the lattice spacings on the scan blindness angle. The computational efficiency of the Generalised Period Green's Function technique and junction modelling technique used for the analysis of this array can be seen in Table 5.6 below.

Floquet Modes Used	Active Impedance (Ω)	CPU Time Taken (Seconds)
1 x 1	52.7 - j 79.5	7.5
3 x 3	52.9 - j 37.8	8.6
5 x 5	71.7 - j 150.0	10.7
7 x 7	130.6 - j 148.9	13.8
9 x 9	*117.1 - j 134.0*	*17.7*
11 x 11	114.7 - j 131.1	22.1
21 x 21	113.2 - j 130.7	62.1

Table 5.6 : Active impedance at boresight scan for an infinite rectangular grid lattice array of centre-fed metal strip dipoles with coplanar strip feedlines (Configuration A junction model used) above an infinite ground plane; $b = 0.5\lambda$, $d = 0.4\lambda$, $l = 0.375\lambda$, $h = 0.225\lambda$, $n_y = 5$, $n_z = 4$.

It is apparent from Table 5.6 that the results are converged for Floquet modes corresponding to $-4 \leq m \leq 4$ and $-4 \leq n \leq 4$ used in the evaluation of the hybrid periodic Green's function, with a corresponding CPU time of 17.7 seconds used to calculate the active impedance per scan angle. In the next section, the Configuration B junction modelling technique is used for the analysis of array elements and their feedlines, and the convergence of the results will be compared with those in Table 5.6.

Configuration B Junction Feedline Model

In Configuration B, the two metal strips of the coplanar strip feedline are aligned directly below one of the segments of the metal strip element. In this configuration, the whole structure can be aligned with a common grid which enables efficient computation of the spatial component of the hybrid periodic Green's function. A disadvantage of this configuration is that the dimensions of the metal strip element and feedline segments cannot be independently specified. However, if the active impedance is required for an exact metal strip length which cannot be conveniently modelled using a grid system, a solution to the problem is to model the array element twice using the grid system for metal strip lengths slightly shorter and longer than the desired length, and to interpolate the results. A feedline model using the Configuration B junction is given in Figure 5.15 below.

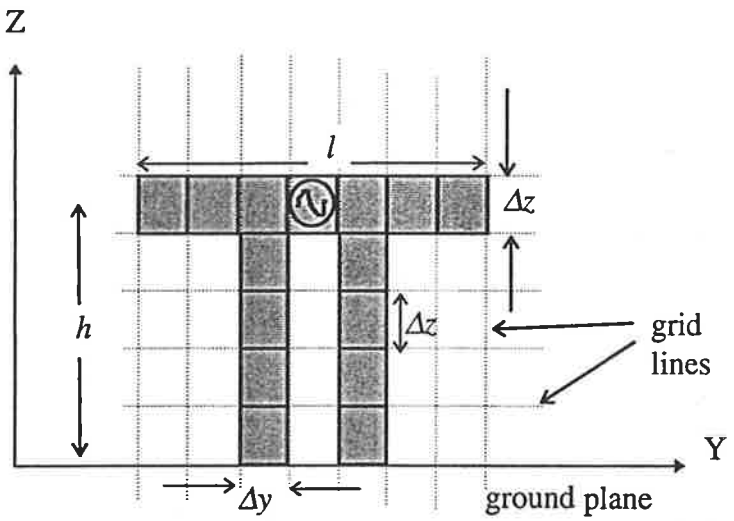

Figure 5.15 : Metal strip array element with coplanar strip feedline. The metal strip - feedline junction is modelled using *Configuration B* junction feedline model.

Apart from the lattice spacing, another parameter which affects the scan blindness angle is the feedline separation. A numerical experiment based on the Configuration B junction model is presented below to demonstrate this effect. As shown in Figure 5.16, a centre-fed horizontal metal strip element of length $l = 0.395\lambda$ is divided into 9 segments and connected to a coplanar strip feedline of height $h = 0.25\lambda$ above the ground plane. The model is first analysed with the feedlines in the AA′ positions when the distance between feedline centres is 6 segment widths apart. The model is then analysed with the feedlines at BB′ (4 segments apart), CC′ (2 segments apart), and DD′ (single strip feedline).

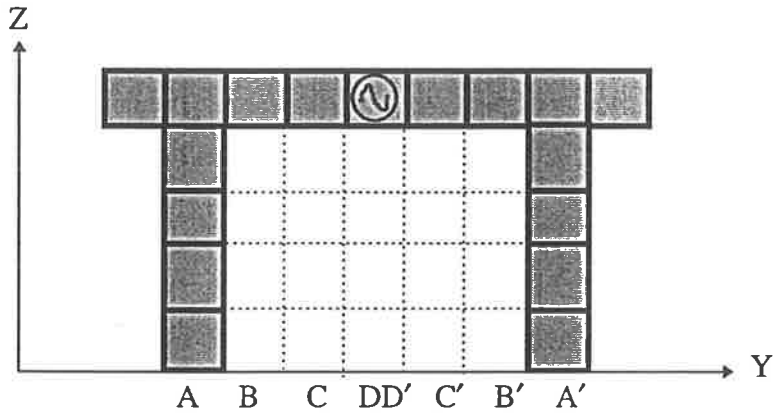

Figure 5.16 : Configuration B junction feedline model for various feedline separations.

The variation of active impedance with scan angle for each of the feedline positions indicated above is plotted in Figure 5.17 to show the effect of the feedline separation on the characteristics of the array. The case of the single strip feedline at position DD′ in fact corresponds to a simplified feedline model [29,77], where the coplanar strip feedlines are sufficiently close together that the balanced (transmission line) mode currents are assumed to have negligible contribution to the radiation characteristics of the array. The analysis of this model is performed by assuming only radiating mode currents on the feedline. A simplified feedline model has been developed and the accuracy of the results have been validated against those obtained by Schuman [29] for a triangular grid lattice infinite array. An outline of the analysis and the results are given in Appendix D. Although in practice,

the feedlines are unlikely to be separated as far apart as positions AA′, the purpose of this numerical experiment is to highlight the effect of feedline separation on the scan blindness condition of the array.

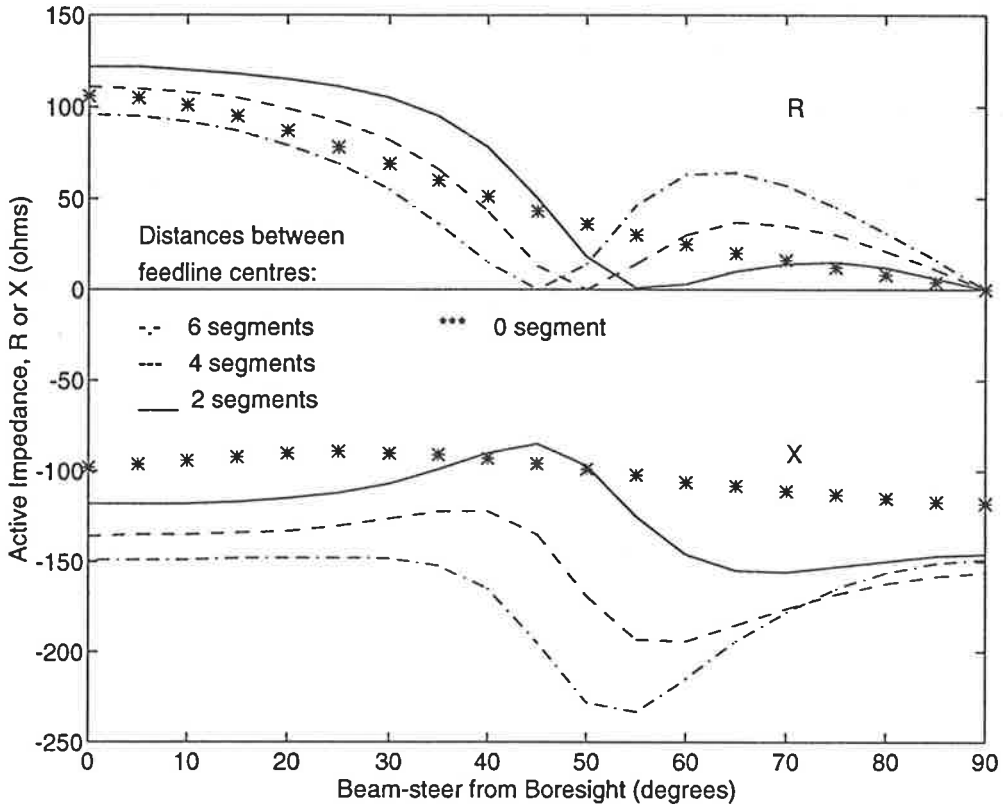

Figure 5.17 : Active impedance as a function of scan angle in the E-plane for the Configuration B junction feedline model with various feedline separations.

As shown in Figure 5.15, except for the single strip feedline case, there is a scan blindness in the E-plane. It is apparent that for close feedline separations, the scan blindness condition occur further away from the boresight angle. The reason is that the feedline induced scan blindness effect is caused by the feedline currents which may be considered as comprising radiating mode currents and transmission line mode currents. For closer feedline separation, the transmission line mode current is smaller, and hence has a less dominant effect. The absence of a scan blindness condition in the results of the single strip feedline model shown in Figure 5.17 cannot be generalised to all cases. It has been found that by using other element and lattice parameters, the radiating mode currents on the

single strip feedline model do cause a scan blindness condition to occur, and the scan blindness is indicated by the results of the model presented in this section.

The computational efficiency of the Generalised Period Green's Function technique and Configuration B junction modelling technique used for the analysis of this array can be seen in Table 5.7 below.

Floquet Modes Used	Active Impedance (Ω)	CPU Time Taken (Seconds)
1 x 1	724.7 + j 1718.3	3.8
3 x 3	124.6 - j 204.8	4.1
5 x 5	*102.4 - j 136.3*	*5.2*
7 x 7	100.4 - j 130.8	5.6
9 x 9	98.6 - j 127.3	6.1
11 x 11	98.0 - j 125.7	6.7
21 x 21	97.4 - j 125.6	16.8

Table 5.7 : Active impedance at boresight scan for an infinite rectangular grid lattice array of centre-fed metal strip dipoles with coplanar strip feedlines (Configuration B junction model) above an infinite ground plane; $b = 0.5\lambda$, $d = 0.4\lambda$, $l = 0.375\lambda$, $h = 0.2\lambda$, $n_y = 5$, $n_z = 4$.

It is apparent from Table 5.7 that the result is converged for Floquet modes corresponding to $-2 \leq m \leq 2$ and $-2 \leq n \leq 2$ used in the evaluation of the generalised periodic Green's function and a CPU time of 5.2 seconds used to calculate the active impedance per scan angle. In comparison with the results in Table 5.6, the results for the Configuration B Junction Model converges with the use of 5 x 5 Floquet modes as against 9 x 9 Floquet modes for the Configuration A Junction Model which requires a CPU time of 17.7 seconds per scan angle. Hence in terms of computational speed in producing converged results, the Configuration B model is three times as fast as Configuration A. Furthermore, the use of a

common grid for evaluation of the spatial component of the hybrid periodic Green's function has enabled the Configuration B model to be more efficiently implemented than Configuration A. This may be observed from Tables 5.6 and 5.7 that for the same number of Floquet modes used in both cases, the Configuration B results take between a quarter to half the CPU time required for the Configuration A results. Therefore, for reasons of greater computational efficiency and comparable rate of convergence of the results, the Configuration B junction model is used for modelling of phased array coplanar strip feedlines in the rest of this thesis.

5.4.1 Formulation for Infinite Arrays of Metal Strip Folded Dipoles with Coplanar Strip Feedlines

In certain types of phased arrays, it may be necessary to design a folded dipole element to improve the impedance match with the feedlines of the structure. The analysis of the folded dipole in Section 5.3.4 and the Configuration B junction feedline model in Section 5.4 are combined here to model an infinite array of folded dipoles with coplanar strip feedlines above an infinite ground plane.

The model of the folded dipole with feedlines is relatively complex, involving a total of six metal strips and six junctions. If the full structure cannot be modelled because of limitations in the analytical tool or computational resources, the problem can be simplified in a number of ways.

- Firstly, the two arms of the folded dipole can be assumed to be very close together so that the Transmission Line Model of the folded dipole applies [72]. If it is further assumed that the dipoles arms are of equal width and that the folded dipole is operated near to its half-wave resonance as is usually the case, then the folded dipole can be assumed to behave like a metal strip dipole of equivalent width but with approximately four times the input impedance of the metal strip dipole. In Section 5.3.4, it was demonstrated using a full analysis of the folded dipole that these

assumptions are reasonable, even when the element is radiating within the environment of an infinite array.

- Secondly, it can be assumed in some cases that the two strips of the feedline are close together and a quarter wavelength long, so that only the radiation mode currents on the feedlines need to be considered.

Under the above two conditions, the geometry of the folded dipole with coplanar strip feedline may be idealised to that of a metal strip dipole with a single strip feedline which is described in Appendix D. However, it is noted that idealisations may lead to errors in the solution, particularly when all the conditions required for making the idealisations are not fully met in the specification of the element geometry's dimensions. The flexibility and high computational efficiency of the Generalised Periodic Green's Function technique is exploited to analyse the full model without the idealisations described above and to implement the solution on a desktop computer. The element geometry is shown in Figure 5.18 below.

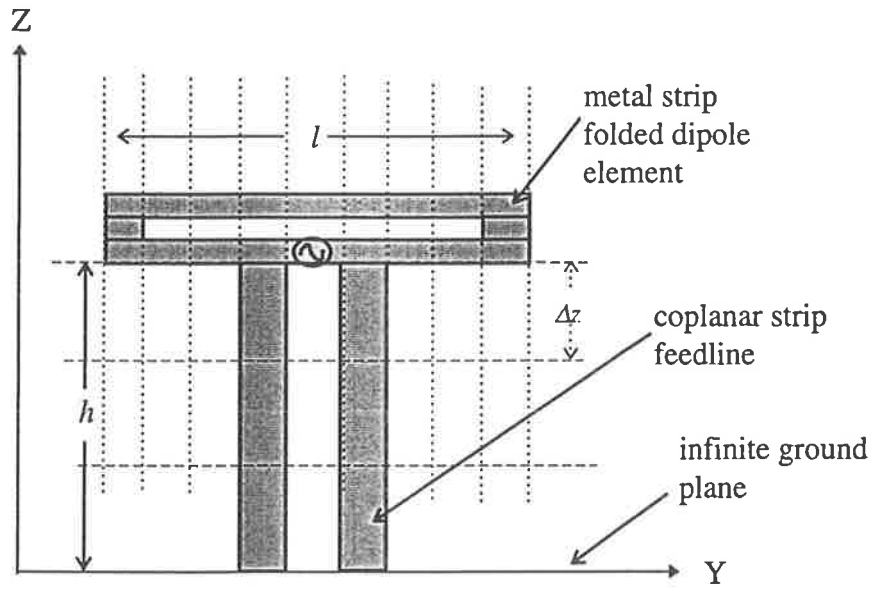

Figure 5.18 : Geometry of a folded dipole element with coplanar strip feedline above an infinite ground plane.

As shown in Figure 5.18, the structure of the folded dipole with feedlines can be modelled as a collection of inter-connected metal strips which are segmented using a grid system. The graph of the active impedance against scan angle for an infinite array of metal strip folded dipoles with coplanar strip feedlines is shown in Figure 5.19. In the graph, the

active impedance of the folded dipole is divided by a factor of 4 and plotted in comparison with that of the metal strip dipole of width equal to the total width of the two arms of the folded dipole. In the H-plane, the active resistance variations are similar, but the reactive component for the folded dipole becomes increasingly capacitive with increasing scan angle. The main difference between the metal strip and folded dipole results lie in the E-plane scan. As compared with the metal strip, the folded dipole has a feedline induced scan blindness in the E-plane at about 40° scan angle from boresight which is evident from the vanishing active resistance and a large reactance shown in the graph. This result is due to the relatively large feedline separation specified in the geometry of the model which has adversely affected the radiation characteristics of the folded dipole.

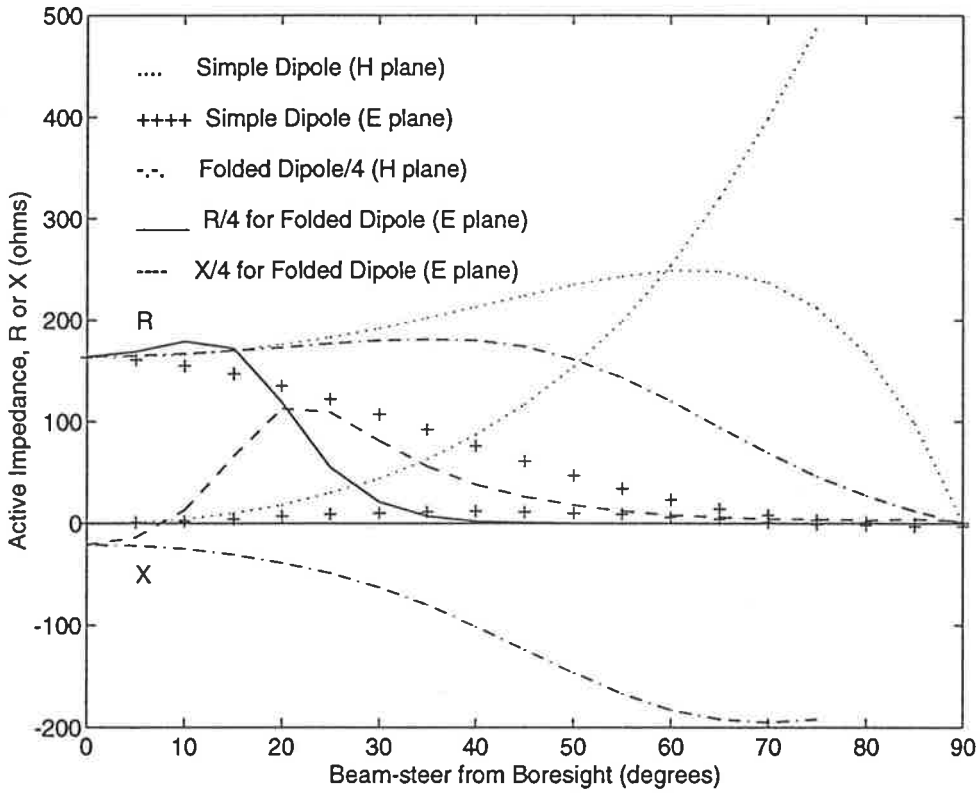

Figure 5.19 : Active impedance as a function of scan angle for an infinite array of folded dipole with coplanar strip feedlines above an infinite ground plane; $b = 0.5\lambda$, $d = 0.5\lambda$, $l = 0.49\lambda$, $h = 0.18\lambda$. The length of the folded dipole is segmented into $n_y = 9$ and the length of the coplanar strip feedline is segmented into $n_z = 7$ segments.

It should be noted that the geometry of the folded dipole with coplanar strip feedline represented by the model has a narrow bandwidth because of the transmission line mode currents from the feedline and the two halves of the folded dipole. Furthermore, the half-wave resonant length of the folded dipole in free space leads to very strong mutual coupling between adjacent elements in the E-plane. This is undesirable for practical use, and some way to shorten the resonant length of the radiating element is required. In Chapter 6, it will be shown that the dielectric substrate causes a shortening of the resonant length which is actually beneficial to the radiation characteristics of the folded dipole.

The computational efficiency of the hybrid period Green's function technique and Configuration B junction modelling technique used for the analysis of this array can be seen in Table 5.8 below.

Floquet Modes Used	Active Impedance (Ω)	CPU Time Taken (Seconds)
1 x 1	63.5 + j 54.4	10.9
3 x 3	657.7 - j 83.9	13.6
5 x 5	*620.6 - j 175.7*	*16.2*
7 x 7	615.3 - j 166.4	22.6

Table 5.8 : Active impedance at boresight scan for an infinite rectangular grid lattice array of folded dipoles with coplanar strip feedlines (Configuration B junction model) above an infinite ground plane; $b = 0.5\lambda$, $d = 0.5\lambda$, $l = 0.49\lambda$, $h = 0.18\lambda$, $n_y = 9$, $n_z = 7$.

It is seen from Table 5.8 that the results are converged for Floquet modes corresponding to $-2 \leq m \leq 2$ and $-2 \leq n \leq 2$ used in the evaluation of the generalised periodic Green's function and a CPU time of 16.2 seconds used to calculate the active impedance per scan angle. The high computational efficiency of the method of analysis has enabled this structure to be model in its entirety with a minimum of idealisations. The advantage of a full analysis such as this is useful for design purposes where a simplified model cannot be

used to investigate the effects of variations in such parameters as feedline separation and dipole-arms separation to the characteristics of the phased array.

5.5 Summary

In this chapter, the Generalised Periodic Green's Function technique has been extended from the analysis of the simple element geometry of a horizontal metal strip to the modelling of array elements with more complex geometries together with their feedlines. To maximise the computational efficiency of the technique, a numerical experiment has been used to demonstrate the need for accelerating the convergence of the spectral periodic Green's function for both the on-plane and near on-plane case. This technique is then applied to the modelling of an infinite array of vertical monopoles.

Three conventional junction modelling techniques are described and found to be incompatible with the Generalised Periodic Green's Function technique of analysis developed in this thesis. A new technique is therefore developed to model metal strip junctions. Mutual coupling of the current segments adjacent to the junction satisfy the near on-plane condition where the hybrid periodic Green's function applies. The calculation of the derivatives of the spatial component of this Green's function is done using the method of finite difference. It is shown that by the use of adequately small intervals for taking the finite difference, the contribution of the currents at the junction is preserved. The metal strip junction modelling technique is applied to the analysis of an infinite array of folded dipoles and extended to the analysis of horizontal metal strips with coplanar strip feedlines. In the latter case, the model is able to identify feedline induced scan blindness which is shown to be a function of lattice spacings and feedline separation. Finally, the techniques developed in this chapter are applied to the modelling of an infinite array of metal strip folded dipoles with coplanar strip feedlines. The techniques developed in this chapter has enabled the analysis to be extended to microstrip dipole arrays which is described in Chapter 6.

The main contributions to research presented in this chapter are as follows:

- A highly efficient Generalised Periodic Green's Function technique has been developed for the analysis of element geometries distributed over three-dimensions by the use of the Hybrid Periodic Green's Function to account for on-plane and near on-plane interactions.

- A new metal strip junction model has been developed which enables the analysis of element geometries such as folded dipoles, and the analysis of the coplanar strip feedlines.

- Numerically efficient models of infinite arrays of vertical metal strip monopoles, metal strip folded dipoles, and horizontal metal strips as well as metal strip folded dipoles with coplanar strip feedlines have been developed and validated against results found in the literature.

CHAPTER 6

Infinite Array Analysis of Microstrip Dipole Antennas

6.1 Introduction and Overview

In the previous three chapters, the Generalised Periodic Green's Function technique was developed and implemented for the analysis of infinite planar arrays of metal strip structures. The flexibility, accuracy and numerical efficiency of the technique was demonstrated through the modelling of a variety of structures such as metal strip dipoles in various orientations, vertical monopoles and folded dipoles, in both rectangular as well as triangular grid lattice infinite arrays. A new technique of junction modelling was also introduced, in which the current continuity condition is implicitly enforced by using a two-dimensional pulse basis function for each source segment. This technique has enabled the efficient modelling of feedlines connected to the radiating elements. It was shown that using a conventional desktop Sparc workstation, the computation time to obtain a well converged active impedance result for a given scan angle ranged from 0.05 seconds for metal strip dipoles to about 16 seconds for

folded dipole elements with feedlines. Having developed the techniques for analysing an infinite array of metal strips in various configurations, it is desirable to extend the analysis to include the substrate, so that each array element has a metallic part as well as a dielectric substrate.

The dielectric substrate itself may be configured in a number of ways in relation to the antenna and its feed network. The basic architecture of microstrip arrays may be grouped into one of two categories [78,79]. The first type is a so called *tile* construction in which all the antenna elements, module electronics (amplifiers, phase shifters, etc) and distribution networks are each integrated onto separate wafers which are orientated parallel to the transverse array aperture and stacked in the longitudinal direction to form the array. This architecture is described in this work as *Transverse Integration and Longitudinal Assembly* (TILA). The second type has been called a *brick* construction in which the antenna element and module electronics are integrated longitudinally to the array aperture on a single chip module, and identical modules are then arranged in the transverse direction to build the array. This architecture is referred to in this thesis as Longitudinal Integration and Transverse Assembly (LITA). The choice of the array architecture will affect not only the electrical characteristics of the array such as its operating bandwidth, scanning performance, radiation pattern and impedance matching characteristics [32], but also other features such as conformity to the surface of the structure on which it is mounted, substrate area availability for power distribution and signal routing, heat removal and maintenance. Therefore, it is desirable to have a method of analysis which is flexible enough to model array elements appropriate for either the TILA or LITA architecture.

A number of techniques have already been developed for the analysis of conventional microstrip arrays. Pozar, Schaubert and others [33,34] have analysed TILA arrays comprising printed dipoles or patches on the top surface of a grounded slab of dielectric substrate which extends continuously across the aperture plane of the array. Because the analysis is based on a spectral domain Green's function for the infinite dielectric slab, it cannot be readily extended to the case where the slab is finite in one or more dimensions.

Bayard, Cooley and others [7] have analysed LITA arrays consisting of printed dipoles on semi-infinite dielectric sheets orthogonal to the ground plane, using a combination of the Green's function Moment Method and a mode matching technique. The technique involves a detailed formulation using both magnetic and electric current sources as well as mode matching. However, in the work reported [80], the two metal strips of the feedline are widely spaced, and because the dielectric sheet is electrically thin, the effect of radiation from the feedline dominates the characteristics of the array. Furthermore, the formulation adopted for semi-infinite dielectric sheets is unsuitable for analysis of substrates which are of finite dimensions and separated from each other.

A third technique developed by Parfitt and others [8,9,10] uses the Integral Equation method and models the metal strip radiating elements using equivalent surface currents and the dielectric substrate using volume polarisation currents. Results have been published for the analysis of infinite arrays of metal strip antennas with feedlines, individually supported on finite size dielectric substrates. In this method of analysis, all the mutual couplings in both the metallic and dielectric parts of the array elements are accounted for by what is identified in this thesis as the Generalised Spatial Periodic Green's Function which is not constrained by the geometry of the array element. The use of a single Green's function in the analysis is desirable because of simplicity in the problem formulation and potential user convenience if the method is developed into a CAD software for general use. Furthermore, since the Green's function is not constrained by the element geometry, the technique can also be used for the analysis of array elements with various novel substrate configurations including inhomogeneous multi-layered substrates and superstrates. However, as pointed out in Sections 3.4.1 and 3.4.2 respectively, the use of the spatial periodic Green's function also implies that the integration of the Green's function over the sources has to be evaluated numerically, and that the results are slowly convergent for large scan angles. Consequently, a supercomputer was required for the implementation of this technique for the analysis of infinite arrays of substrate supported metal strip dipoles, and a large number of terms in the spatial periodic Green's function series had to be used to in order to obtain converged results for large scan angles [10]. It is noted that a numerical solution which requires an extensive amount of computations may also incur inaccuracies due to numerical errors of the computer.

Hence it is concluded that the three techniques described above have a number of limitations in modelling both TILA and LITA microstrip arrays, and that a generalised and more numerically efficient technique of analysis is desirable in order to offer the flexibility of modelling a wide range of array element geometries. In this chapter, the Generalised Periodic Green's Function technique is applied to the analysis of infinite microstrip dipole arrays suitable for both TILA and LITA architectures. In Section 6.2 an analysis of an infinite microstrip array with the conventional infinite dielectric slab is described. The analysis is then extended to the case where the dielectric consists of semi-infinite dielectric sheets and completely finite dielectric substrates in Sections 6.3 and 6.4, respectively. It will also be shown that high computational efficiency can be achieved by the technique, to the extent that a full analysis of array element structures such as folded dipoles with their feedlines mounted on finite-size substrates, is feasible using desktop computing resources.

In the Chapter 5, it was demonstrated that the Generalised Hybrid Periodic Green's function technique is able to accurately predict the feedline induced scan blindness effect in both simple and folded dipole arrays with coplanar strip feedlines radiating in free space. In this chapter, it will be shown that the technique can also accurately predict the occurrence of substrate induced scan blindness in microstrip dipole arrays. For the case where the feedlines are included in the analysis, it will shown that the technique can be used not only to accurately predict the occurrence of a scan blindness, but also predict which of the feedline or substrate causes the scan blindness and thus allow the antenna designer to explore ways of reducing the effect of scan blindness in array performance.

6.2 Formulation for an Infinite Dielectric Slab Structure

Figure 6.1 shows a section of an infinite planar array of metal strip dipoles supported on the top face of a dielectric substrate which extends continuously in the xy plane. Each element is assumed for the purpose of the analysis to be excited by an idealised delta-gap

voltage source at the centre of the metal strip, so that no feedlines are included in this analysis.

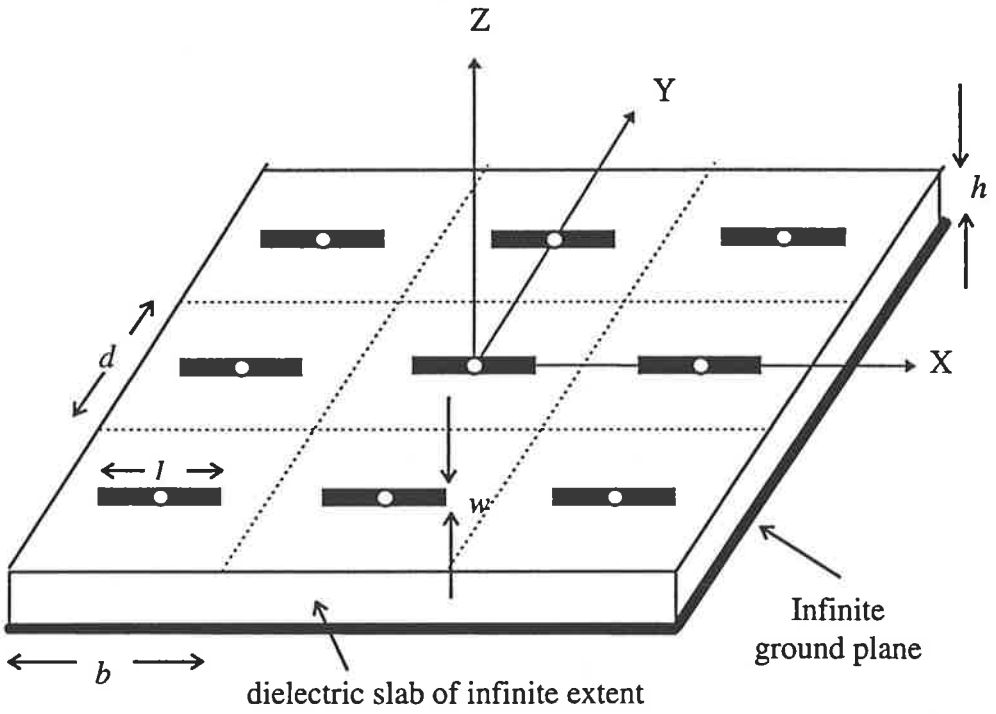

Figure 6.1 : A section of an infinite array of metal strip dipoles supported on the top face of a dielectric substrate of infinite lateral extent.

6.2.1 Integral Equation Formulation

The method of problem formulation employed here is similar to that employed by Sarkar [81] and Parfitt [10]. For the subsequent analysis in this section, primed co-ordinates refer to the position of the sources and unprimed co-ordinates to the position of the field points. The electric field integral equations for this geometry are obtained from the boundary conditions associated with the tangential electric field on the surface of the metal strips and the conditions which determine the total electric field within the dielectric substrate. The boundary condition governing the tangential components of the incident electric field $\left[\vec{E}^i(\vec{r})\right]_{\tan}$ and scattered electric field $\left[\vec{E}^s(\vec{r})\right]_{\tan}$ on the surface of the metal strips at location $\vec{r}$ as given in (4.1), is:

$$\left[\vec{E}^i(\vec{r})\right]_{\tan} + \left[\vec{E}^s(\vec{r})\right]_{\tan} = 0 \qquad \text{for} \quad \vec{r} \in S_c \tag{6.1}$$

where S_c denotes the surface of the metal strips.

The second boundary condition governing the total electric field in the dielectric substrate is given by:

$$\vec{E}^i(\vec{r}) + \vec{E}^s(\vec{r}) = \vec{E}^{total}(\vec{r}) \qquad \text{for} \quad \vec{r} \in V_d \tag{6.2}$$

where V_d denotes the volume of the dielectric substrate.

Using the equivalence principle, the metal strips may be replaced by the equivalent surface current $\vec{J}_c$ and the dielectric substrate by the equivalent volume polarisation currents $\vec{J}_d$, both of which exist in free space. The metal strips are assumed to be infinitesimally thin, so that the equivalent surface current $\vec{J}_c$ represents the total currents on the strips. For this analysis, the width of each metal strip is assumed to be narrow with respect to its length so that the metal strip is represented by a single segment in the dimension perpendicular to its length. However, the technique can also be applied to the analysis of rectangular metal patch radiating elements by using more than one current segment in each dimension on the surface of the patch. With the above representations of the currents, the scattered electric field at a location $\vec{r}$ may be written as:

$$\vec{E}^s(\vec{r}) = L_c\left\{\vec{J}_c\right\} + L_d\left\{\vec{J}_d\right\} \tag{6.3}$$

The expressions for the operators L_c and L_d will be given below. The relationship between the total electric field in the dielectric and the volume polarisation current is given by:

$$\vec{J}_d(\vec{r}') = \vec{E}^{total}(\vec{r}) \; j\omega\varepsilon_0(\varepsilon_r - 1) \tag{6.4}$$

where ω is the angular frequency, ε_0 is the permittivity of free space and ε_r is the relative permittivity of the dielectric slab. For the purpose of this analysis, the dielectric is assumed to be homogeneous and lossless; however both inhomogeneity and losses in the substrate can be readily incorporated in the analysis when required. Substituting the expressions for

the scattered and total electric fields into (6.1) and (6.2), the coupled electric field integral equations can be expressed in terms of the equivalent currents as follows:

$$\left[\vec{E}^i(\vec{r})\right]_{\tan} = -\left[L_c\left\{\vec{J}_c\right\}\right]_{\tan} - \left[L_d\left\{\vec{J}_d\right\}\right]_{\tan} \qquad \text{for} \quad \vec{r} \in S_c \tag{6.5}$$

$$\vec{E}^i(\vec{r}) = \frac{\vec{J}_d(\vec{r}')}{j\omega\varepsilon_0(\varepsilon_r - 1)} - L_c\left\{\vec{J}_c\right\} - L_d\left\{\vec{J}_d\right\} \qquad \text{for} \quad \vec{r} \in V_d \tag{6.6}$$

Omitting for the moment the image component, the operator L_c for the current sources on the metal strip surfaces may be expressed as:

$$\begin{aligned} L_c\left\{\vec{J}_c\right\} &= -j\omega\vec{A}_c - \vec{\nabla}\phi_c \\ &= -j\omega\mu_0 \iint_{S_c} \vec{J}_c(\vec{r}')\, G_\infty dS_c' - \frac{\vec{\nabla}}{\varepsilon_0} \iint_{S_c} \rho_c(\vec{r}')\, G_\infty dS_c' \end{aligned} \tag{6.7}$$

where μ_0 is the permeability of free space, ρ_c is the charge density on the surface of the metal strips, and both the integrals are evaluated over the surface of the metal strip S'_c. As before, the physical interpretation of this equation is that the first term represents the vector potential due to the current sources on the metal strips, and the second term represents the scalar potential due to the charges on the metal strips. The Green's function G_∞ used in the above equation is either the generalised spectral periodic Green's function given by (3.9) for off-plane interactions, or the generalised hybrid periodic Green's function given by (4.15) for on-plane and near on-plane interactions. The charge density ρ_c on the metal strip surface is related to the electric currents on the conductors by the continuity equation:

$$\vec{\nabla}'.\vec{J}_c = -j\omega\rho_c \tag{6.8}$$

Substituting (6.8) into (6.7), the L_c operator can be expressed entirely in terms of the equivalent current and Green's function as follows:

$$L_c\left\{\vec{J}_c\right\} = -j\omega\mu_0 \iint_{S_c} \vec{J}_c(\vec{r}')\, G_\infty dS_c' - \frac{j\vec{\nabla}}{\omega\varepsilon_0} \iint_{S_c} \vec{\nabla}'.\vec{J}_c(\vec{r}')\, G_\infty dS_c' \tag{6.9}$$

where the integration is over the current sources on the surface S_c of the metal strips and over their images formed by the ground plane, and the results are summed together.

In a similar manner, the L_d operator is given by:

$$L_d\{\vec{J}_d\} = -j\omega\mu_0 \iiint_{V_d} \vec{J}_d(\vec{r}\,') G_\infty dV' + \frac{\vec{\nabla}}{j\omega\varepsilon_0} \iiint_{V_d} \vec{\nabla}'.\vec{J}_d(\vec{r}\,') G_\infty dV' \tag{6.10}$$

where the integration is evaluated over the volume polarisation current sources in the dielectric region. However it is known that there is no charge associated with this current in the interior of the dielectric. Hence on the surface of the dielectric, the charge density ρ_d is given by:

$$\rho_d(\vec{r}\,') = -\frac{1}{j\omega}\vec{\nabla}'.\vec{J}_d(\vec{r}\,') = \frac{1}{j\omega}\hat{n}.\vec{J}_d(\vec{r}\,') \qquad \text{for} \quad \vec{r}\,' \in S_d \tag{6.11}$$

Substituting for ρ_d from (6.11), it is seen that the second volume integral in (6.10) is reduced to a surface integral over the charges on the surface S_d of the dielectric substrate:

$$L_d\{\vec{J}_d\} = -j\omega\mu_0 \iiint_{V_d} \vec{J}_d(\vec{r}\,') G_\infty dV' + \frac{j\vec{\nabla}}{\omega\varepsilon_0} \iint_{S_d} \hat{n}.\vec{J}_d(\vec{r}\,') G_\infty dS_d' \tag{6.12}$$

In summary, by enforcing the boundary conditions for the tangential electric field on the surface of the metal strips and the total field in the substrate region, the coupled integral equations are obtained in terms of the equivalent surface currents on metal strips and volume polarisation currents in the dielectric substrate.

6.2.2 Numerical Implementation

Having formulated the problem in terms of the equivalent currents, the coupled integral equations (6.5) and (6.6) are used to solve for the current values J_c and J_d. In order to maximise computational efficiency, the whole structure may be segmented in such a

manner that the segments of the metal strips and dielectric both fall onto a common grid. However for the microstrip dipole analysed, the width of the metal strip Δw is much narrower than the width of the dielectric slab d of a unit cell, as shown in Figure 6.2. Hence it is computationally more efficient to use a smaller segment Δw for the metal strip and larger segments of width Δy for the substrate in the y dimension.

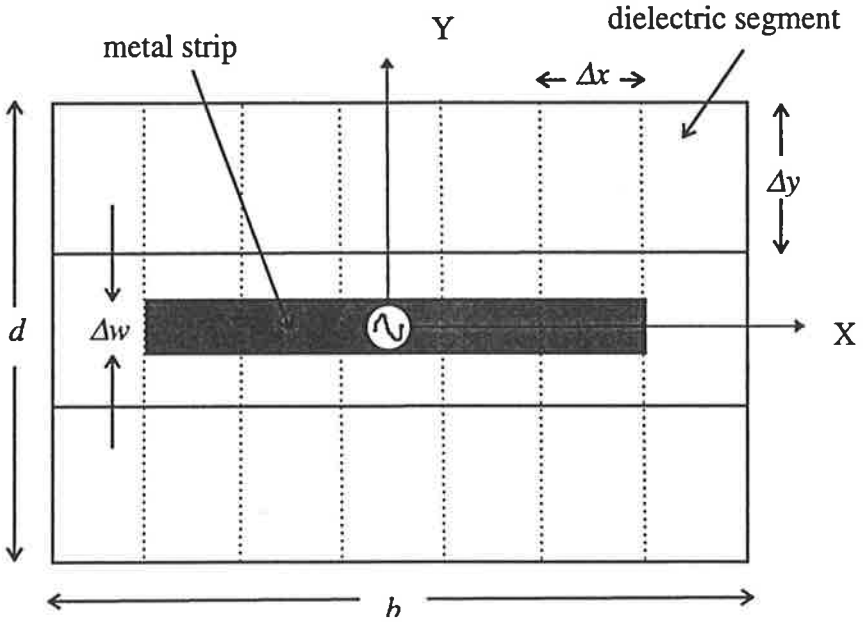

Figure 6.2 : Segmentation scheme for a unit cell of the infinite array

The surface currents on the metal strip are then expanded in terms of N_c two-dimensional pulse basis functions so that:

$$\vec{J}_c(\vec{r}') = \sum_{j=1}^{N_c} P_j(x', y')\left(J_{cxj}\hat{x} + J_{cyj}\hat{y}\right) \tag{6.13}$$

where the two-dimensional pulse functions are given by:

$$P_j(x', y') = \begin{cases} 1, & \text{if } x', y' \in j^{th} \text{ segment} \\ 0, & \text{otherwise} \end{cases} \tag{6.14}$$

and J_{cxj} and J_{cyj} are the unknown metal strip current coefficients to be determined. The volume polarisation currents in the dielectric substrate are expanded in terms of N_d three-dimensional pulse basis functions so that:

$$\vec{J}_d(\vec{r}') = \sum_{j=1}^{N_d} Q_j(x', y', z')\left(J_{dxj}\hat{x} + J_{dyj}\hat{y} + J_{dzj}\hat{z}\right) \tag{6.15}$$

where the three-dimensional pulse functions are given by:

$$Q_j(x', y', z')\} = \begin{cases} 1, & \text{if } x', y', z' \in j^{th} \text{ segment} \\ 0, & \text{otherwise} \end{cases} \tag{6.16}$$

and J_{dxj}, J_{dyj}, *and* J_{dzj} are the unknown dielectric current coefficients to be determined. Hence the metal strip currents have been expanded into $2N_c$ basis functions, and the dielectric currents have been expanded into $3N_d$ basis functions. A point matching Moment Method is applied, and the Moment Matrix equation is represented by:

$$[\mathbf{Z}]\ [\mathbf{J}] = [\mathbf{E}] \tag{6.17}$$

The meaning of each element in the above matrix equation is described below. The moment matrix of $(2N_c+3N_d)^2$ elements is given in (6.18) where each element will be defined later.

$$[\mathbf{Z}] = \begin{bmatrix} [\mathbf{Z}_{cc}] & [\mathbf{Z}_{cd}] \\ [\mathbf{Z}_{dc}] & [\mathbf{Z}_{dd}] \end{bmatrix} + \frac{1}{j\omega\varepsilon_0(\varepsilon_r - 1)} \begin{bmatrix} 0 & 0 \\ 0 & \bar{\mathbf{I}} \end{bmatrix} \tag{6.18}$$

Each element of [**Z**] is determined by the action of a source segment and its image about the ground plane, at the points in space for which the boundary condition equations (6.5) and (6.6) are enforced. In the first matrix on the right hand side of the above equation, each sub-matrix has two subscripts. The first subscript refers to the testing point and the second subscript refers to the source. The symbol *c* denotes the metal strip conductor and *d* denotes the dielectric. Hence Z_{cc} denotes the self-coupling of the metal strip, Z_{dd} refers to the self-coupling of the dielectric, and Z_{cd} and Z_{dc} refer to the cross-coupling effects of the composite structure. Each of the sub-matrices is further sub-divided into blocks of matrix elements denoting the mutual couplings associated with the directions of each pair of testing and source points, and is given by:

$$[\mathbf{Z}_{cc}] = \begin{bmatrix} [Z_{c_x c_x}]_{N_c, N_c} & [Z_{c_x c_y}]_{N_c, N_c} \\ [Z_{c_y c_x}]_{N_c, N_c} & [Z_{c_y c_y}]_{N_c, N_c} \end{bmatrix} \tag{6.18a}$$

$$[\mathbf{Z}_{\mathbf{cd}}]=\begin{bmatrix}[Z_{c_xd_x}]_{N_c,N_d} & [Z_{c_xd_y}]_{N_c,N_d} & [Z_{c_xd_z}]_{N_c,N_d}\\ [Z_{c_yd_x}]_{N_c,N_d} & [Z_{c_yd_y}]_{N_c,N_d} & [Z_{c_yd_z}]_{N_c,N_d}\end{bmatrix} \qquad (6.18b)$$

$$[\mathbf{Z}_{\mathbf{dc}}]=\begin{bmatrix}[Z_{d_xc_x}]_{N_d,N_c} & [Z_{d_xc_y}]_{N_d,N_c}\\ [Z_{d_yc_x}]_{N_d,N_c} & [Z_{d_yc_y}]_{N_d,N_c}\\ [Z_{d_zc_x}]_{N_d,N_c} & [Z_{d_zc_y}]_{N_d,N_c}\end{bmatrix} \qquad (6.18c)$$

$$[\mathbf{Z}_{\mathbf{dd}}]=\begin{bmatrix}[Z_{d_xd_x}]_{N_d,N_d} & [Z_{d_xd_y}]_{N_d,N_d} & [Z_{d_xd_z}]_{N_d,N_d}\\ [Z_{d_yd_x}]_{N_d,N_d} & [Z_{d_yd_y}]_{N_d,N_d} & [Z_{d_yd_y}]_{N_d,N_d}\\ [Z_{d_zd_x}]_{N_d,N_d} & [Z_{d_zd_y}]_{N_d,N_d} & [Z_{d_zd_z}]_{N_d,N_d}\end{bmatrix} \qquad (6.18d)$$

The second matrix on the right hand side of (6.18) refers to the total electric field in the dielectric due to its volume polarisation current, and is the matrix representation of the boundary condition equation (6.6). Each element of the matrix has the same rank as the corresponding element in the first matrix on the right hand side of (6.18); **0** denotes a zero matrix and $\bar{\mathbf{I}}$ denotes an identity matrix. The current vector comprising $(2N_c+3N_d)$ x 1 elements, is given by:

$$[\mathbf{J}]=\begin{bmatrix}\mathbf{J_c}\\ \mathbf{J_d}\end{bmatrix}=\begin{bmatrix}[J_{cx1},\ldots J_{cxN_c},J_{cy1},\ldots J_{cyN_c}]^T\\ [J_{dx1},\ldots J_{dxN_d},J_{dy1},\ldots J_{dyN_d},J_{dz1},\ldots J_{dzN_d}]^T\end{bmatrix} \qquad (6.19)$$

In view of the fact that the metal strip is assumed to be excited by a delta-gap voltage at its centre, and that there is no incident electric field in the dielectric, the excitation vector of $(2N_c+3N_d)$ x 1 elements is given by:

$$[\mathbf{E}]=\begin{bmatrix}[\mathbf{E_c}]\\ [\mathbf{E_d}]\end{bmatrix} \qquad (6.20)$$

where the elements of the sub-vectors $[\mathbf{E_c}]$ and $[\mathbf{E_d}]$ are given by:

$$E_c = \begin{cases} E_0, & \text{at the feedpoint} \\ 0, & \text{otherwise} \end{cases} \tag{6.20a}$$

$$E_d = 0 \tag{6.20b}$$

Substituting (6.13) into (6.9), the operator L_c for a testing point at the k^{th} segment due to the j^{th} current segment becomes:

$$\begin{aligned} L_c\left\{\vec{J}_c\right\}_k = & -j\omega\mu_0 \sum_{j=1}^{N_c} \left(J_{cxj}\hat{x} + J_{cyj}\hat{y}\right) \iint_{S_c} P_j(x',y')\, G_\infty dx'dy' \\ & -\frac{j}{\omega\varepsilon_0}\left(\hat{x}\frac{\partial}{\partial x} + \hat{y}\frac{\partial}{\partial y} + \hat{z}\frac{\partial}{\partial z}\right) \cdot \\ & \left\{\sum_{j=1}^{N_c} \iint_{S_c} \frac{\partial}{\partial x'}\left[J_{cxj} P_j(x',y') G_\infty dx'dy'\right]\right. \\ & \left. + \sum_{j=1}^{N_c} \iint_{S_c} \frac{\partial}{\partial y'}\left[J_{cyj} P_j(x',y') G_\infty dx'dy'\right]\right\} \end{aligned} \tag{6.21}$$

Because the problem is solved by using pulse basis functions and point matching, the source point derivatives in the above equation may be taken outside the integral with no effect on the result. Since the pulse basis functions and testing functions are symmetrical, it is also permissible to compute both derivatives at the field point. For each source point, (6.21) is applied to both the source current and its image, and the results are added. For off-plane interactions between source and testing points, G_∞ in (6.21) is implemented using the Generalised Spectral Periodic Green's Function given in (3.9) where the integration over the sources is evaluated analytically. For on-plane and near on-plane interactions, as described in Section 5.2.1, G_∞ is implemented using the Generalised Hybrid Periodic Green's Function given in (4.15) which has a spectral and a spatial component. The integration of the spectral component over the sources is evaluated analytically, whereas the integration of the spatial component is evaluated numerically. All the methods for maximising computational efficiency of the solution elucidated in Section 4.3 are applied to this analysis.

The numerical implementation of the operator L_d in (6.12) is determined by the geometry of the dielectric substrate. The dielectric slab shown in Figure 6.1 extends to infinity in the x and y directions, and is finite only in the z dimension. Furthermore, as the bottom face of the substrate is in contact with the ground plane, the charges on this surface are cancelled by the image component and need not be considered any further. Therefore, the surface charges exist only on the top face of the substrate and its image, and the operator L_d becomes:

$$\begin{aligned} L_d\left\{\vec{J}_d\right\}_k = &-j\omega\mu_0\sum_{j=1}^{N_d}\left(J_{dxj}\hat{x}+J_{dyj}\hat{y}+J_{dzj}\hat{z}\right)\iiint_{V_d} Q_j(x',y',z')G_\infty dx'dy'dz' \\ &-\frac{j}{\omega\varepsilon_0}\left(\hat{x}\frac{\partial}{\partial x}+\hat{y}\frac{\partial}{\partial y}+\hat{z}\frac{\partial}{\partial z}\right)\sum_{j\in S_{xy}}\alpha J_{dzj}\iint_{S_{xy}} Q_j(x',y',z')G_\infty dx'dy' \end{aligned} \tag{6.22}$$

where S_{xy} refers to the top face of the dielectric slab and its image over which the surface integral is evaluated, and

$$\alpha=\begin{cases} 1, & \text{if } \hat{n}=\hat{z} \\ -1 & \text{if } \hat{n}=-\hat{z} \\ 0, & \text{otherwise} \end{cases} \tag{6.23}$$

where $\hat{n}$ is the outward pointing unit vector, which in this case, is normal to the top face of the dielectric slab and its image.

Equation (6.22) relates the incident electric field at a testing point located at the k^{th} segment to the current sources at the j^{th} segment, and may be interpreted to mean that surface charge is permitted on the surface of every dielectric segment. This interpretation appears to contradict the physical reality that charges do not exist within the dielectric slab, and has led to past criticism of the use of rectangular pulse basis functions to model homogeneous dielectric regions [82]. However, it has been shown [8] that the interpretation of this part of the model does not in fact contradict reality. Firstly, the physical meaning of (6.11) is that within a homogeneous dielectric, $\vec{\nabla}.\vec{J}_d=0$, so that any internal surface charge is fictitious. For the purpose of calculating the surface charge, the polarisation currents in

adjacent dielectric segments should be interpolated at their junction, so that the pulse representation of these currents are effectively smoothened at the junction location. If this were carried out, the resultant averaged surface charge density function would be zero for these surfaces within the dielectric, which is in accordance with physical reality. Now, if the dielectric segment is located at the outer surfaces of the substrate, interpolation is not appropriate as there is a discontinuity in the polarisation current. For these segments, a surface charge does exist and is given by the surface integral in (6.22). In (6.23), the definition of α serves to ensure that surface charges internal to the homogeneous dielectric substrate are not included into the calculation. The procedure is numerically the same as the averaging approach explained above for avoiding internal surface charge within the dielectric.

As before, the use of the generalised spectral periodic Green's function for off-plane interactions enables the integrals to be evaluated analytically. The generalised hybrid periodic Green's function used for computing the on-plane and near on-plane interactions has a spatial component containing both surface and volume integrals which have to be evaluated numerically. At each source point, (6.22) is applied to both the source current and its image, and the results are added together.

6.2.3 Design Examples

The infinite array of metal strip dipoles on an infinite dielectric slab is a type of element suitable for TILA architecture employed in conventional MMIC arrays, and has been extensively studied. The intention here is not to describe the properties of this array in detail, but to demonstrate that the Generalised Periodic Green's Function technique is able to accurately and efficiently model this class of microstrip phased arrays using two of the design examples given in [33]. The design examples also provide a basis for comparison with other novel substrate configurations described later on in this chapter, since the Green's function is unconstrained by the substrate geometry.

Design Example 1

Referring to Figure 6.1, the inter-element spacings for the first design example in [33] are given by $b = d = 0.5\lambda$, and each dipole element has a length $l = 0.39\lambda$ and width $w = 0.002\lambda$. The infinite dielectric slab has a thickness $h = 0.19\lambda$ and a relative permittivity $\varepsilon_r = 2.55$. The dipole is resonant at boresight giving an active impedance $Z_b = 75 + j0\Omega$. All of these parameters are used directly in the analysis developed in Section 6.2, with the exception of the metal strip length l for the following reason. As shown in Figure 6.2, the numerical implementation of the analysis is more efficient if both the substrate and metal strip in each unit cell are divided into segments of the same lengths in the x dimension. However, this implies that the metal strip's length is constrained to be an integral number of segment lengths. Since the substrate is divided into 7 segments in the x dimension and 5 segments in the y dimension, the metal strip is modelled using 5 segments along its length thus giving $l = 0.357\lambda$. The height of the dielectric substrate is divided into 3 segments, resulting in 105 volume segments for the dielectric slab and 5 surface segments for the metal strip. With this scheme of segmentation, a boresight active impedance of $Z_b = 78.7 + j11.7\Omega$ is obtained, and no effort is made to alter any of the other parameters in order to achieve the resonance condition. Bearing in mind the difference in the dipole lengths for the two models, the results are compared in Figure 6.3.

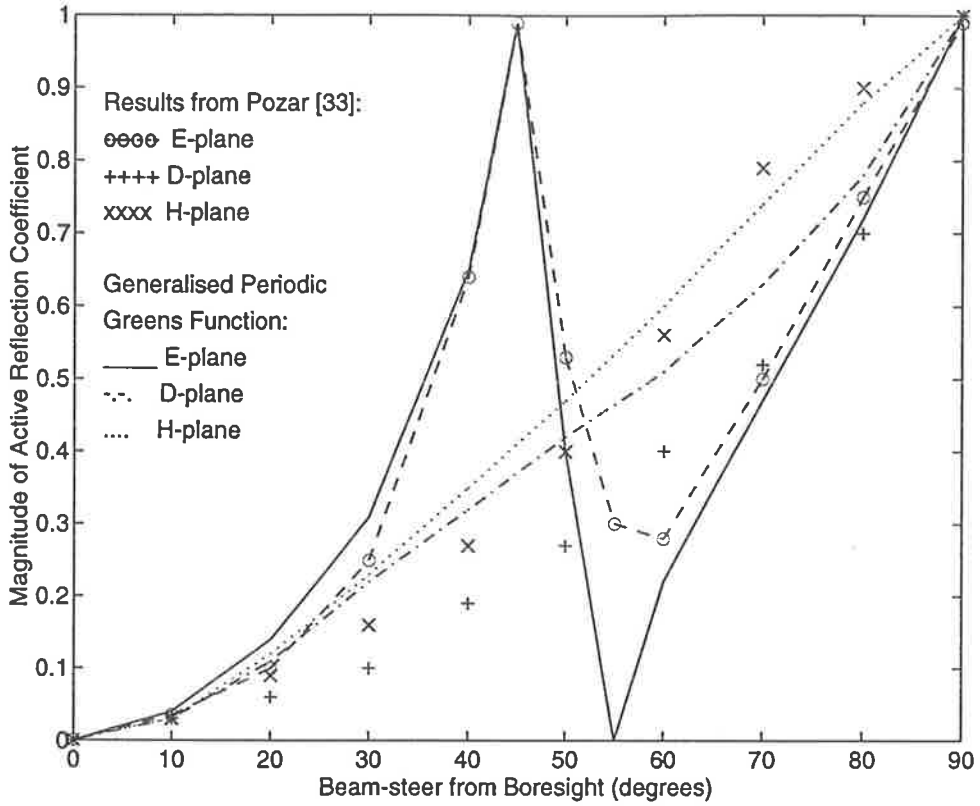

Figure 6.3 : Magnitude of active reflection coefficient for an infinite array of metal strip dipoles on an infinite dielectric slab in the principal and diagonal scan planes; $l = 0.39\lambda$, $b = d = 0.5\lambda$, $h = 0.19\lambda$, $w = 0.002\lambda$, $\varepsilon_0 = 2.55$, $n_x = 7$, $n_y = 5$, $n_z = 3$, $Z_b = 75 + j0\ \Omega$.

Figure 6.3 shows the variation of the magnitude of active reflection coefficient with scan angle in the principal and diagonal scan planes for the Dielectric Slab Green's Function model developed in [33] as well as the Generalised Periodic Green's Function model developed in this chapter. The agreement between the results computed using the two methods is very good, particularly with regard to the prediction of the scan blindness angle which corresponds to a unity magnitude of active reflection coefficient at about 45° scan angle in the E-plane.

The existence of a scan blindness at an angle close to boresight has implications not only on scanning performance but also on the useful frequency bandwidth that can be achieved with this class of arrays. Notwithstanding the availability of a variety of bandwidth enhancing techniques for use with such arrays [83,84,85,86], it is still useful to gauge the

bandwidth achievable with the array in the form shown in Figure 6.1. The numerical model described above is used to compute the magnitude of the active reflection coefficient for a range of frequencies around the resonance condition at a given scan angle. The four scan angles used for purposes of bandwidth calculation are boresight, and a scan angle of 30° in the E, H and D planes. The magnitude of active reflection coefficient is then plotted against the frequency, which is normalised to the resonant frequency at boresight scan angle. The frequency bandwidth achieved by the array for this purpose is defined as the frequency range, centred at the boresight resonant frequency, over which the magnitude of active reflection coefficient satisfies a useful but arbitrary condition of being less than a value of 0.4 for all four scan angles. The graph of these frequency variations is given Figure 6.4.

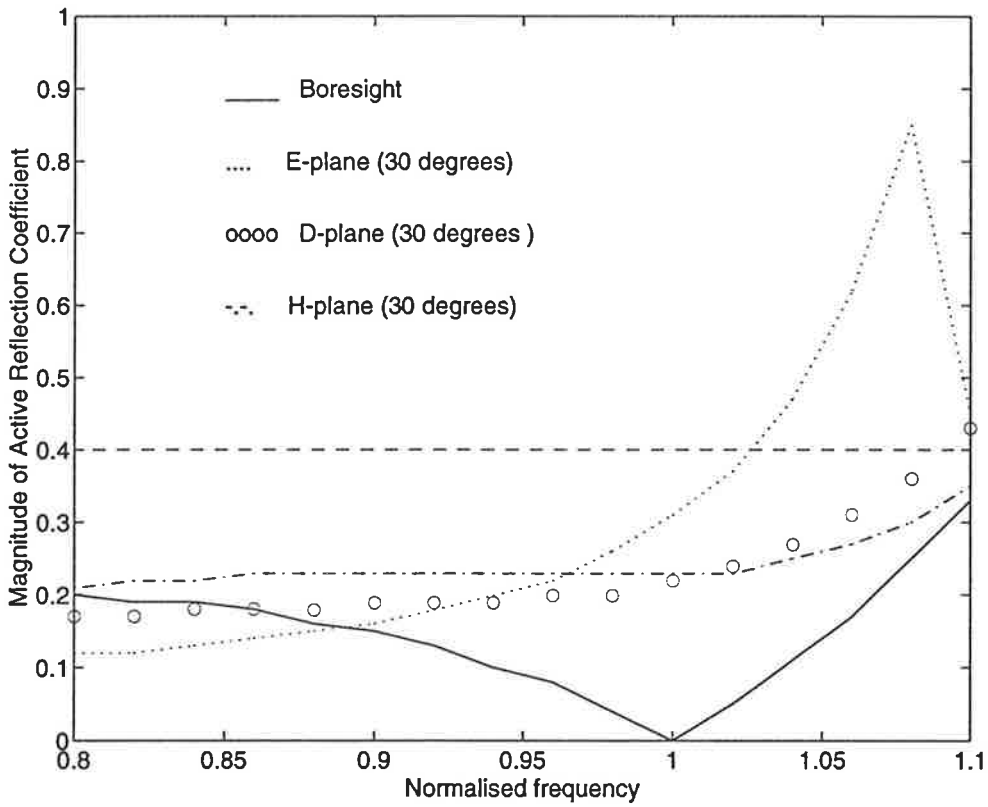

Figure 6.4: Variation of magnitude of active reflection coefficient magnitude with normalised frequency for an infinite array of metal strip dipoles on an infinite slab of dielectric substrate; $l = 0.357\lambda$, $b = d = 0.5\lambda$, $h = 0.19\lambda$, $w = 0.002\lambda$, $\varepsilon_0 = 2.55$, $n_x = 7$, $n_y = 5$, $n_z = 3$, $Z_b = 75 + j0.0\ \Omega$.

It is apparent from Figure 6.4 that a greater mismatch occurs for the higher frequencies. The condition which causes the most severe degradation of the array's bandwidth corresponds to the 30° scan angle in the E-plane. This condition is directly related to the fact that the array has a scan blindness at 45° in the E-plane when operated at the centre frequency. Based on the condition set above, the usable bandwidth for this array is found to be about 4%.

Design Example 2

Another useful feature of the model is the prediction of grating lobes and the variation of the active impedance in the vicinity of a grating lobe, as shown in Figure 6.5 below. Using a second design example from [33], The Generalised Periodic Green's Function technique is used to analyse an array shown in Figure 6.1 and having identical parameters as in Design Example 1 with the exception of the inter-element spacing in the x dimension which is chosen to be $b = 0.5155\lambda$. From the analysis described in Section 3.4.3, an inter-element spacing of more than 0.5λ could enable a grating lobe to emerge in visible space. The variation of the magnitude of active reflection coefficient with scan angle in the principal and Diagonal planes is given in Figure 6.5 for segmentations of $n_x = 7$, $n_y = 5$, and $n_z = 3$.

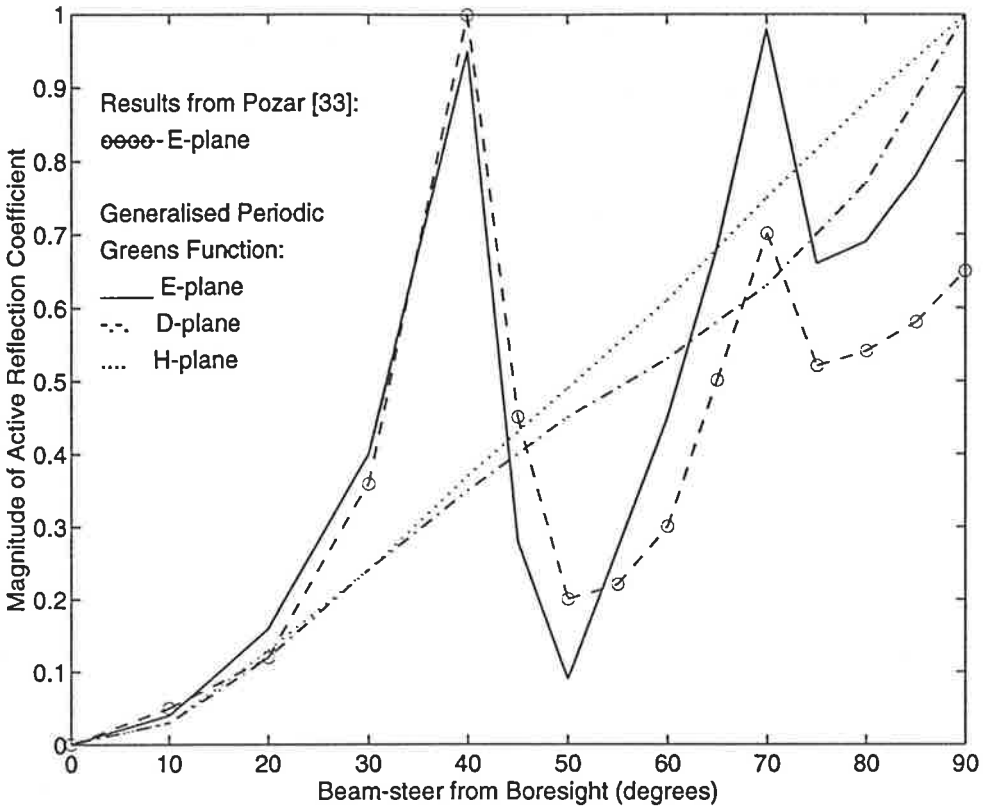

Figure 6.5 : Magnitude of active reflection coefficient for an infinite array of metal strip dipoles on an infinite dielectric slab in the principal and diagonal scan planes; $l = 0.39\lambda$, $b = 0.5155\lambda$, $d = 0.5\lambda$, $h = 0.19\lambda$, $w = 0.002\lambda$, $\varepsilon_0 = 2.55$, $n_x = 7$, $n_y = 5$, $n_z = 3$, $Z_b = 75 + j0\ \Omega$.

It can be seen from Figure 6.5 that in the E-plane, there are two scan angles at which the magnitude of the active reflection coefficient approaches unity. The first instance is associated with a substrate induced scan blindness at about 39°, whilst the second is due to a grating lobe which emerges into visible space when the scan angle is about 70°. Both of these features are also observed in the E-plane scan results of [33] which are shown on the same graph for comparison. The agreement between the E-plane scan results of the Dielectric Slab Green's Function technique and Generalised Periodic Green's Function technique is very good except for a slight discrepancy at the grating lobe angle.

The two design examples provided above have demonstrated the capability of the Generalised Periodic Green's Function technique to accurately model the characteristics of

an infinite array of metal strip dipoles supported on top of an infinite slab of dielectric. The prediction of the active impedance variation with scan angle as well as the angular location of the scan blindness and grating lobes using this method compares very well with Pozar's method using the Dielectric Slab Green's Function technique. The numerical convergence, and consequently the computational efficiency of the technique, can be seen in Table 6.1.

Floquet Modes Used	Active Impedance (Ω)	CPU Time Taken (Seconds)
1 x 1	78.4 - j 1.6	33.4
1 x 3	77.9 - j 1.0	35.8
3 x 1	*79.5 + j 11.1*	*35.8*
3 x 3	78.7 + j 11.7	42.5
5 x 5	78.6 + j 13.1	51.5
7 x 7	78.7 + j 13.5	70.9
11 x 11	78.2 + j 14.8	94.6

Table 6.1 : Active impedance of an infinite array of metal strip dipoles supported on an infinite dielectric slab substrate above an infinite ground plane in the boresight scan angle, analysed using the Generalised Hybrid Periodic Green's Function technique; $l = 0.357\lambda$, $b = d = 0.5\lambda$, $h = 0.19\lambda$, $w = 0.002\lambda$, $\varepsilon_0 = 2.55$, $n_x = 7$, $n_y = 5$, $n_z = 3$.

It can be seen from Table 6.1 that converged results are obtained when the generalised periodic Green's function is evaluated using Floquet modes (m,n) where $-1 \leq m \leq 1$ and $n = 0$. The corresponding CPU time per scan angle is about 36 seconds which is just over twice as long to compute an impedance value for an infinite array of metal strip folded dipoles with coplanar strip feedlines, the latter being the most complex metal strip array without substrate modelled so far using this technique. A total of about 33.5M bytes of

storage and 4.2M bytes of memory are required for the computer to calculate a value of the active impedance.

The computation time required is comparable with the Dielectric Slab Green's Function technique which is reported [32,33] to take about 30 seconds to calculate a value of the active impedance per scan angle. The main difference is that whilst this latter technique requires only 3 to 5 basis functions to model the dipole and no basis functions for the substrate, up to about 120 x 120 Floquet modes are required for converged results to be obtained. For the results shown in Table 6.1, the Generalised Periodic Green's Function Technique requires 110 basis functions to represent the equivalent currents on the metal strip dipole and substrate, but converged results are obtained with only 3 x 1 Floquet modes used in the calculation of the periodic Green's functions. Therefore, it is concluded that while the two techniques have different formulations and relative advantages and disadvantages in numerical implementation, their overall performance in accuracy and computational efficiency is comparable. However, the distinct advantage of the Generalised Periodic Green's Function technique lies in its flexibility for use in the analysis of other substrate configurations. This useful feature of the technique is described in the next two sections.

6.3 Formulation for a Structure with Semi-infinite Dielectric Sheets

Figure 6.6 shows the geometry of an array of metal strip dipoles supported on the front face of semi-infinite dielectric sheets which are perpendicular to the ground plane. Each dielectric sheet is infinitely long in x dimension, and there is an infinite number of rows of these dielectric sheets with supported metal strip dipoles.

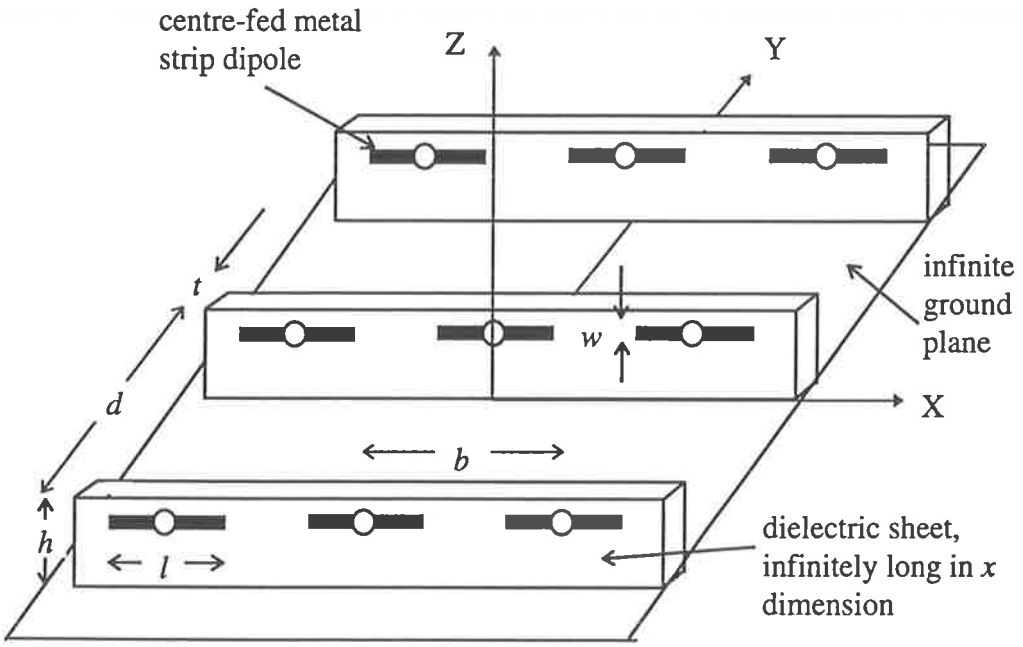

Figure 6.6 : Infinite array of metal strip dipoles supported on semi-infinite dielectric sheets perpendicular to the infinite ground plane.

From an analytical point of view, there are two main differences between this structure and the infinite slab structure analysed in the previous section:

- Firstly, the dielectric slab is finite in the y and z dimensions, and infinite only in the x dimension. There are two important implications to this difference:

- The first implication is that the Dielectric Slab Green's Function technique [32,33] is unsuitable for analysing this structure because the substrate is not an infinite slab of dielectric which is an inherent assumption of that technique. The flexibility of the Generalised Periodic Green's Function technique is suitable for analysing this structure as the Green's function is not constrained by the element geometry.

- The second implication is that charges can exist not only on the top face of the slab as in the previous case, but also on the front and back faces of the slab as well.

- Secondly, each metal strip dipole, instead of being located on the top face of the infinite slab as in the previous case, is positioned on the front face of a semi-infinite dielectric sheet but not necessarily contiguous with the top edge. In this case, a testing point at the centre of a dipole segment could have source points in the dielectric slab located above and below it. The implication is that the direction of Floquet mode propagation in the z direction needs to be explicitly enforced when evaluating the surface and volume integrals of the Green's function over the source points for the purpose of filling the moment matrix elements.

With these two differences accounted for, the procedure of analysis is the same as that described earlier for the infinite slab substrate structure.

6.3.1 Numerical Implementation

The structure in Figure 6.6 is modelled as a metal strip with two dimensional surface currents in the xz plane, and semi-infinite dielectric substrate with three-dimensional volume polarisation currents. As in the previous case, the width of the metal strip is much narrower than the height of the substrate, so that it is computationally more efficient to use a smaller size segment for the metal strip as compared with those for the substrate in the z dimension as shown in Figure 6.7. In the x dimension, the metal strip is divided into segments of the same length as the substrate, although the length l of the metal strip is shorter than the width b of a unit cell.

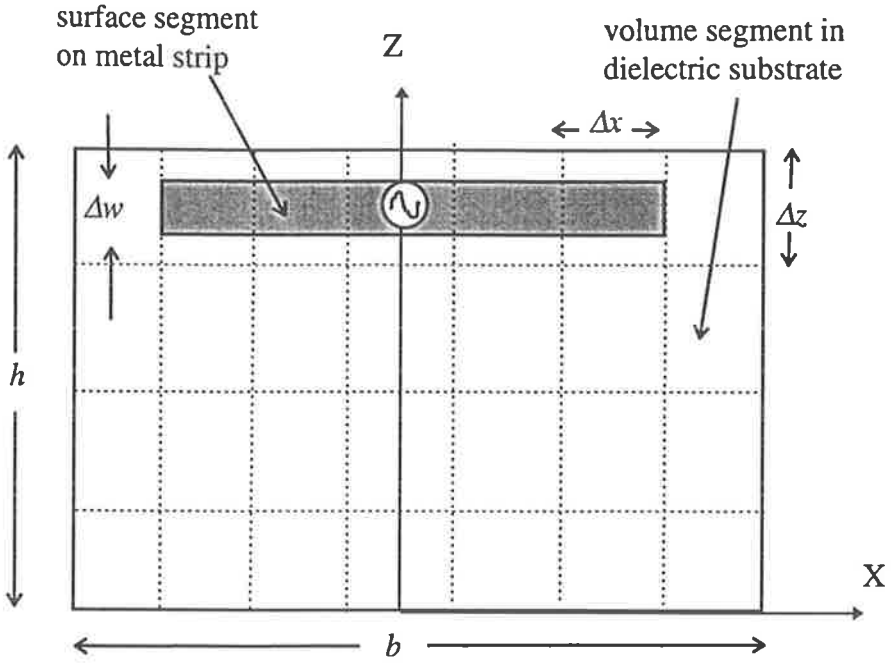

Figure 6.7 : Segmentation scheme for metal strip and dielectric sheet substrate within a unit cell of the infinite array.

Figure 6.7 shows a section of a unit cell of the structure. The substrate and metal strip are both conveniently divided into n_x and n_x -2 segments of width Δx, respectively. As in the previous case, placing both the metal strip and substrate on a common segmentation grid in the x direction results in greater computational efficiency but has the disadvantage is that the length of the metal strip is now constrained by having to be specified in terms of an integral number of segments. However, the interpolation procedure suggested in the previous case also applies here. In the z dimension, the substrate is divided into n_z segments of width Δz, and the metal strip is represented by a segment of width Δw.

The surface currents on the metal strips and their images are expanded in terms of N_c two-dimensional pulse basis functions, and the polarisation currents in the dielectric substrates and their images in terms of N_d three-dimensional pulse basis functions as before, so that:

$$\vec{J}_c(\vec{r}') = \sum_{j=1}^{N_c} P_j(y',z')\left(J_{cyj}\hat{y} + J_{czj}\hat{z}\right) \tag{6.24}$$

and

$$\vec{J}_d(\vec{r}\,') = \sum_{j=1}^{N_d} Q_j(x',y',z')\left(J_{dxj}\hat{x} + J_{dyj}\hat{y} + J_{dzj}\hat{z}\right) \tag{6.25}$$

where

$$P_j(y',z')\} = \begin{cases} 1, & \text{if } x', y', \in j^{th} \text{ segment} \\ 0, & \text{otherwise} \end{cases} \tag{6.26}$$

and $Q_j(x',y',z')$ is given by (6.16). J_{cyj}, J_{czj}, J_{dxj}, J_{dyj}, *and* J_{dzj} are the unknown current coefficients to be determined. The Moment Matrix equation is set up in the same way as for the infinite substrate case given in equations (6.17) to (6.20), except that the two dimensional pulse basis representation of the metal strips is in the *yz* plane rather than in the *xy* plane.

The L_c operator for a testing point at the k^{th} segment due to the j^{th} current segment and its image thus becomes:

$$\begin{aligned} L_c\left\{\vec{J}_c\right\}_k = & -j\omega\mu_0 \sum_{j=1}^{N_c}\left(J_{cyj}\hat{y} + J_{czj}\hat{z}\right)\iint_{S_c} P_j(y',z')\, G_p dy'dz' \\ & -\frac{j}{\omega\varepsilon_0}\left(\hat{x}\frac{\partial}{\partial x} + \hat{y}\frac{\partial}{\partial y} + \hat{z}\frac{\partial}{\partial z}\right) \cdot \\ & \left\{\sum_{j=1}^{N_c}\iint_{S_c}\frac{\partial}{\partial y'}\left[J_{cyj}P_j(y',z')G_p dy'dz'\right]\right. \\ & \left.+\sum_{j=1}^{N_c}\iint_{S_c}\frac{\partial}{\partial z'}\left[J_{czj}P_j(y',z')G_p dy'dz'\right]\right\} \end{aligned} \tag{6.27}$$

Since the surface charges on the substrate exist only on the top, as well as the front and back surfaces of the substrates as well as their respective images, the L_d operator becomes:

$$\begin{aligned} L_d\{\vec{J}_d\}_k = & -j\omega\mu_0 \sum_{j=1}^{N_d} \left(J_{dxj}\hat{x} + J_{dyj}\hat{y} + J_{dzj}\hat{z}\right) \iiint_{V_d} Q_j(x',y',z') G_p dx'dy'dz' \\ & -\frac{j}{\omega\varepsilon_0}\left(\hat{x}\frac{\partial}{\partial x} + \hat{y}\frac{\partial}{\partial y} + \hat{z}\frac{\partial}{\partial z}\right) \cdot \\ & \left\{ \sum_{j\in S_{xy}} \alpha J_{dzj} \iint_{S_{xy}} Q_j(x',y',z') G_p dx'dy' \right. \\ & \left. + \sum_{j\in S_{xz}} \beta J_{dyj} \iint_{S_{xz}} Q_j(x',y',z') G_p dx'dz' \right\} \end{aligned} \tag{6.28}$$

where S_{xy} refers to the summation over the segments on the top face and S_{xz} to the summation over the segments on the front and back faces of the dielectric substrate and their images, and

$$\alpha = \begin{cases} 1, & \text{if } \hat{n} = \hat{z} \\ -1 & \text{if } \hat{n} = -\hat{z} \\ 0, & \text{otherwise} \end{cases} \qquad \beta = \begin{cases} 1, & \text{if } \hat{n} = \hat{y} \\ -1 & \text{if } \hat{n} = -\hat{y} \\ 0, & \text{otherwise} \end{cases} \tag{6.31}$$

where $\hat{n}$ is the outward pointing unit vector normal to the surface and its image.

Apart from the above differences, the rest of the procedure for numerical implementation using the Method of Moments is the same as in the previous section, and will not be repeated here.

6.3.2 Design Examples

The infinite array of printed dipoles on semi-infinite dielectric sheets is useful for application to LITA architectures employed in MMIC arrays, and was studied by Bayard, Cooley and Schaubert [7,80] where results have been presented for electrically thin substrates. It is known that an electrically thick substrate has a more significant effect on

the characteristics of the dipole than a thin substrate [5]. The aim of this section therefore is to demonstrate that the Generalised Periodic Green's Function technique is able to accurately and efficiently model this type of microstrip arrays, and also to extend the analysis to the case of electrically thick substrates as would be applied in MMIC antennas for operation at millimetre wavelengths.

Using the first of the design examples given in [7] and based on the diagram given in Figure 6.6, the array has inter-element spacings $b = d = 0.5\lambda$, where λ is the free-space wavelength. The semi-infinite dielectric sheet has a height $h = 0.373\lambda$ and thickness $t = 0.0084\lambda$. Each metal strip is of length $l = 0.48\lambda$ and width $w = 0.0192\lambda$, and located at a height of 0.263λ which is equivalent to $0.71h$ above the ground plane. With a substrate relative permittivity of $\varepsilon_r = 2.2$, the equivalent electrical thickness is about 4.5 electrical degrees.

The segmentation scheme shown in Figure 6.7, is designed for optimal computation efficiency, but it can only approximately model the metal strip's dimensions given in [7]. As mentioned before, if a given length of the metal strip cannot be conveniently modelled using the grid system, a solution to this problem is to model the element using the grid system for a metal strip length slightly shorter than the required length, and then again with a slightly longer length, and to interpolate the results. However, it has been found that the results are not sensitive to slight differences in the dimensions of the metal strip; hence the grid system is used in this analysis.

In order to model the array given in [7], the substrate within each unit cell is segmented using $n_x = 13$, $n_y = 2$ and $n_z = 4$, thus giving a total of 104 volume segments. A comparison of the array parameters used in [7] and in the model using the Generalised Periodic Green's Function technique is given in Table 6.2 below.

Array Parameters	Dimensions used in [7]	Dimensions used here
b	0.5λ	0.5λ
d	0.5λ	0.5λ
ε_r	2.2	2.2
l	0.48λ	0.423λ
t	0.0084λ	0.0084λ
w	0.0192λ	0.025λ
h	0.373λ	0.373λ
Boresight impedance Z_b	175 + j 0.0 Ω	154 + j 2.0 Ω

Table 6.2 : A comparison of the array dimensions used in [7] and in the model using the Generalised Periodic Green's Function technique. For the Generalised Periodic Green's Function technique, the substrate in a unit cell is divided into $n_x = 13$, $n_y = 2$, $n_z = 4$ segments.

It can be seen from Table 6.2 that the length of the metal strip used in the model is slightly shorter than that in [7]. Consequently, the width of the metal strip is also adjusted slightly in order to obtain a resonance condition. All the other parameters used in the model are the same as in [7]. Figure 6.8 shows the variation of active impedance with scan angle in the E-plane for the array.

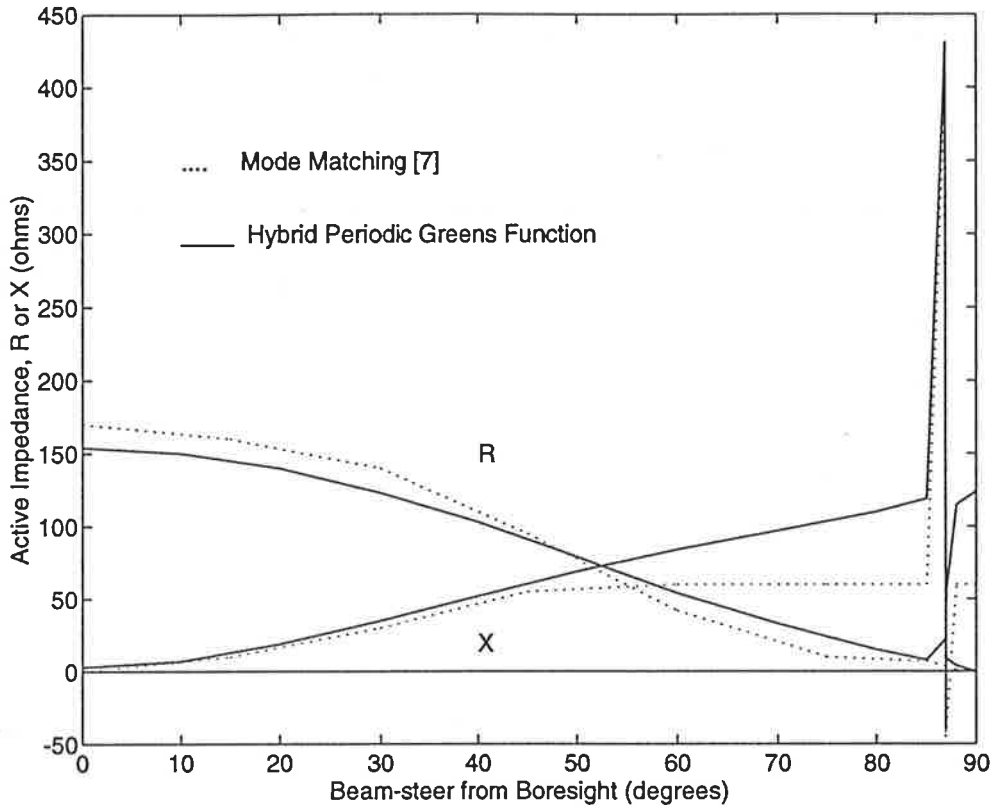

Figure 6.8 : Active impedance as a function of scan angle in the E-plane for an infinite array of metal strip dipoles on semi-infinite dielectric sheets. The array parameters for the Generalised Periodic Green's Function model and for the model in [7] are as given in Table 6.2.

It can be seen in Figure 6.8 that despite the slight difference in the dipole's dimensions, agreement in the results of the two models in terms of variation of the active impedance with scan angle and in the detection of the scan blindness angle, is good. For the Generalised Periodic Green's Function model, the metal strip dipole's half-wave resonance occurs at the boresight scan angle with an active impedance of about 155Ω . As expected, the active resistance becomes zero at the grazing scan angle (θ = 90°) since the inter-element spacings are set to preclude grating lobes. In the E-plane, a scan blindness is detected at 85° scan angle, which is noted to be much further away from boresight than that for the infinite array of metal strip dipoles supported on an infinite dielectric slab. The accuracy of the Generalised Periodic Green's Function technique is therefore validated for a substrate geometry which may be used for LITA architecture arrays.

The results shown in Figure 6.8 are for an array element with an electrically thin substrate. The numerical model developed in this thesis is used to design an array of such antennas with a resonant condition at boresight scan angle using electrically thicker substrates. Denoting the antenna parameters in Table 6.2 as those of Antenna A, two other sets of resonant conditions are computed for the parameters as shown in Table 6.3. The active impedance variation with scan angle for the three antenna arrays is given in Figure 6.9.

Antenna	ε_r	Substrate thickness (t)	Substrate height (h)	Electrical thickness (t_e)	Dipole length (l)
A	2.2	0.0084λ	0.373λ	4.5 degrees	0.423λ
B	4.9	0.01λ	0.24λ	8 degrees	0.318λ
C	10.2	0.015λ	0.1425λ	17.2 degrees	0.269λ

Table 6.3: Array element parameters of an infinite array of metal strip dipoles supported on semi-infinite dielectric sheets for substrate electrical thickness of 4.5, 8 and 17.2 electrical degrees.

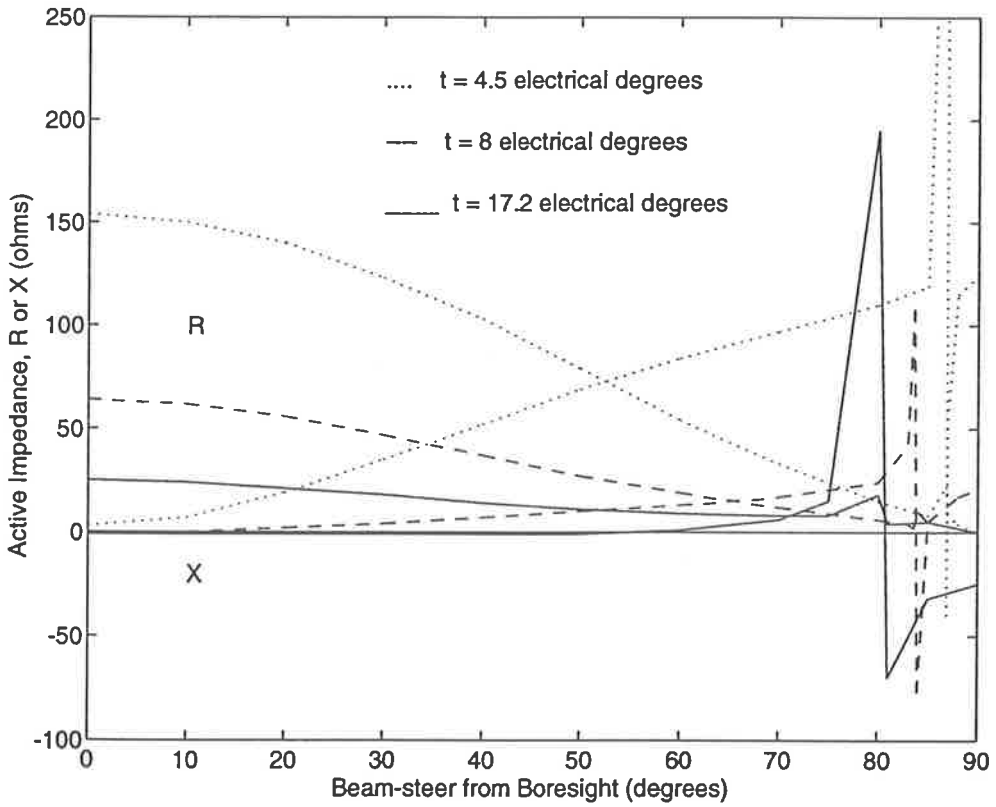

Figure 6.9 : Active impedance as a function of scan angle in the E-plane for an infinite array of metal strip dipoles supported on semi-infinite dielectric sheets, with substrate electrical thickness of 4.5, 8 and 17.5 electrical degrees. Array parameters for the three designs are as given in Table 6.3

It can be seen from Table 6.3 and Figure 6.9 that increasing the electrical thickness of the substrate has two effects on active impedance characteristics of the array:

- Firstly, the half-wave resonant length and active impedance of the dipole are correspondingly reduced. In the particular antenna designs shown above, an increase in the electrical thickness by a factor of 4 has led to a reduction of the dipole's resonant length by a factor of nearly 40% , and a reduction of its active impedance by a factor of 6. An important consequence of this is that with electrically thick substrates such as that for Antenna C, it is difficult to match the impedance of the dipole radiating element to a typical coplanar strip feedline. One method for overcoming the problem of poor impedance matching is to design a resonant folded dipole element in which the higher feed point impedance is better matched to that of the feedline, as will be shown in the case of a slightly different antenna structure in the Section 6.4.3.

- The second effect of increasing the substrate's electrical thickness is that the angular position of the scan blindness in the E-plane is shifted nearer to boresight. Clearly, the capability of the model to accurately predict the scan blindness location for such antennas is important in the design process.

The numerical model for Antenna C is extended to investigate the frequency bandwidth obtained for an array with this particular element geometry. The variation of the magnitude of active reflection coefficient with frequency which is normalised to the resonance frequency for boresight scan, is given in Figure 6.10. Using the same conditions for bandwidth as given in Section 6.2.3, the boresight curve in Figure 6.10 yields a bandwidth of about 10%. However the useful bandwidth is degraded by the E and H-plane curves, giving a resultant bandwidth of about 6% for a substrate thickness of 17.2 electrical degrees. This is slightly better than the 4% achieved using the infinite slab substrate geometry, and suggests that breaking the continuity of the substrate in one or more dimensions leads to the occurrence of a scan blindness condition at a scan angle further away from boresight. The shifted scan blindness is the mechanism for achieving a larger bandwidth for the array.

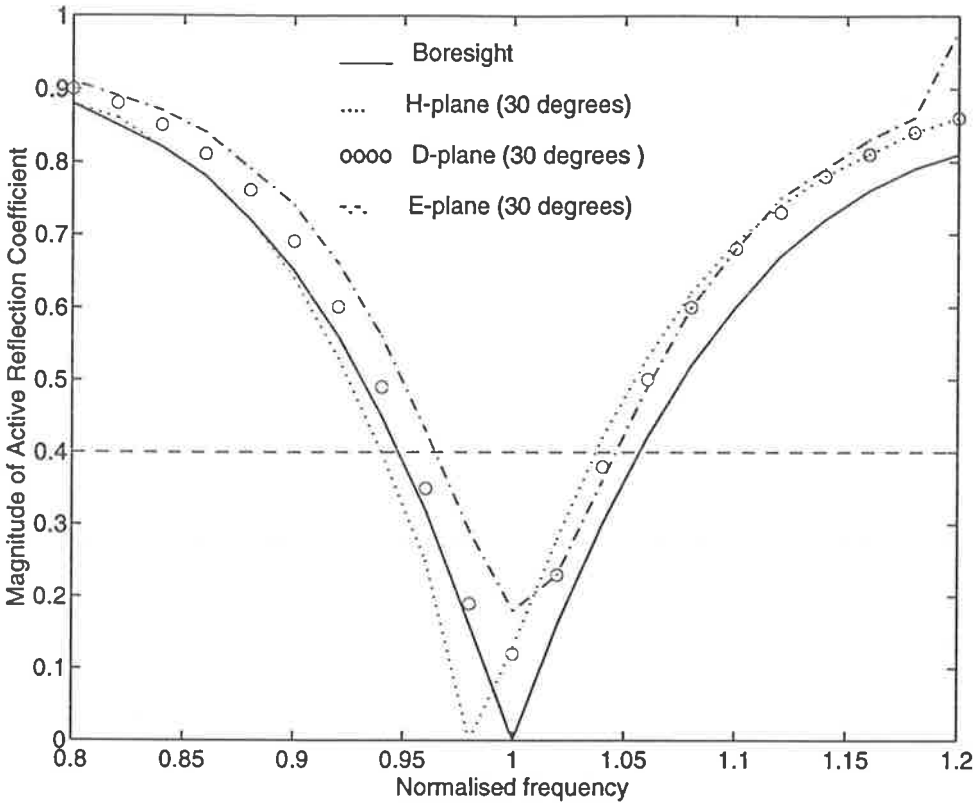

Figure 6.10 : Magnitude of active reflection coefficient as a function of normalised frequency scan for an infinite array of metal strip dipoles supported on semi-infinite dielectric sheets; $\varepsilon_r = 10.2$, $b = d = 0.5\lambda$, $l = 0.269\lambda$, $h = 0.1425\lambda$, $t = 0.015\lambda$, $n_x = 13$, $n_y = 2$, $n_z = 4$.

The numerical convergence and computational efficiency of the Generalised Periodic Green's Function technique can be seen from Table 6.4 below. It can be seen from the table that well converged results are obtained when the generalised periodic Green's function is evaluated using Floquet modes (m,n) where $-1 \leq m \leq 1$ and $-1 \leq n \leq 1$; and the corresponding CPU time per scan angle is about 40 seconds. A total of about 32.8 MBytes of storage and 2.5 MBytes of memory are required for the computer to calculate a value of the active impedance.

Floquet Modes Used	Active Impedance (Ω)	CPU Time Taken (Seconds)
1 x 1	103.3 - j 18.7	28.4
1 x 3	108.3 - j 14.7	31.6
3 x 1	112.0 - j 4.9	31.6
3 x 3	*118.2 - j 1.2*	*39.6*
5 x 5	118.5 + j 0.3	40.6
7 x 7	118.7 + j 0.5	53.8
11 x 11	118.7 + j 0.6	94.9

Table 6.4 : Active impedance of an infinite array of metal strip dipoles supported on semi-infinite dielectric sheets above an infinite ground plane at the boresight scan angle, analysed using the Generalised Periodic Green's Function technique; $l = 0.389\lambda$, $b = d = 0.5\lambda$, $h = 0.45\lambda$, $w = 0.028\lambda$, $t = 0.0217\lambda$, $n_x = 13$, $n_y = 2$, $n_z = 4$, $\varepsilon_0 = 2.2$.

In the next section, a formulation for an infinite microstrip dipole array with completely finite substrates will be presented.

6.4 Formulation for a Structure with Finite Dielectric Substrates

In Sections 6.2 and 6.3, the analyses of infinite arrays of microstrip dipoles were presented based on formulations for an infinite slab and semi-infinite sheets of dielectric substrate, respectively. In this section, the analysis is described for the case when the array element has a substrate which is finite all three dimensions. The analysis of metal strip dipoles with idealised feed is described first, and then extended to include coplanar strip feedlines. Finally, for reasons of impedance matching with the feedlines, the analysis of finite substrate supported metal strip folded dipoles with feedlines will be considered.

6.4.1 Metal Strip Dipoles with Idealised Feed

Figure 6.11 shows a section of an infinite array of metal strip dipoles, each of length l and width w, spaced a distance of b and d apart, respectively in the xy plane. Each metal strip is assumed for the moment to be fed by an indealised delta-gap voltage, and is supported on the front face of a finite-size dielectric substrate of length l, thickness t, and height h above an infinite ground plane. There are two important differences between this structure and the semi-infinite sheet substrate structure analysed in the Section 6.3.

- Firstly, the dielectric substrate is finite in all three dimensions. The implication is that surface charges can exist on all the six faces of the substrate; however because the bottom face is in contact with the ground plane, the charges on this face are cancelled out by the equal and opposite charges of the image and may be discounted in the analysis.

- Secondly, the metal strip is contiguous with the entire top edge of the front face of the substrate; hence the length of the metal strip is equal to the length of the substrate.

Other than accounting for these two differences, the procedure of analysis for this structure is the same as before.

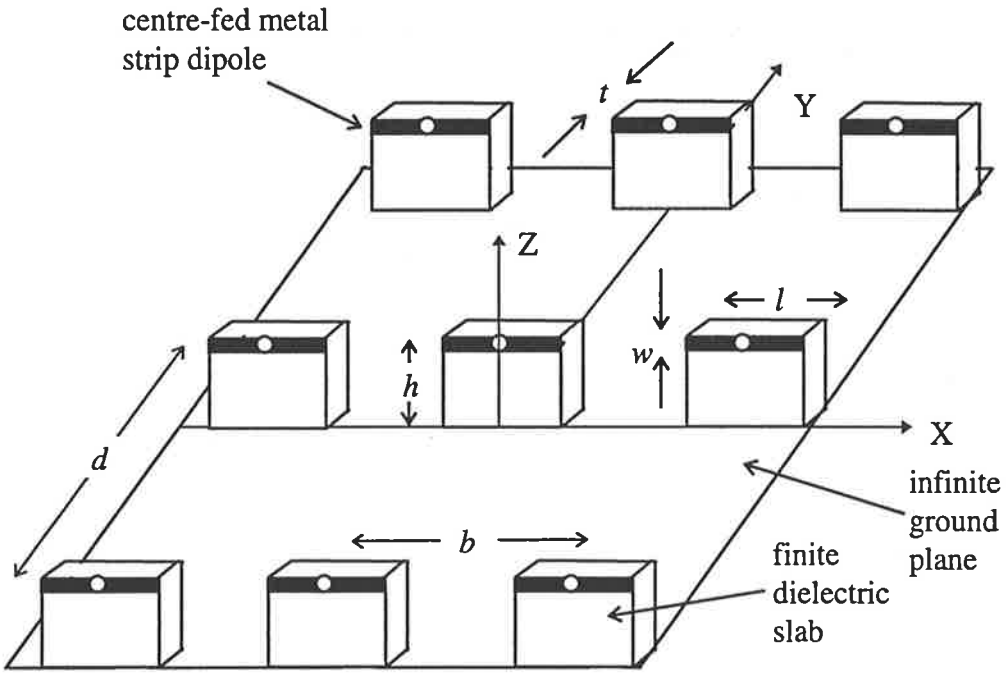

Figure 6.11 : Geometry of an infinite array of metal strip dipoles with idealised feeds supported on finite dielectric substrates

Segmentation and Basis Functions

For each element of the array shown in Figure 6.11 the metal strip is modelled with two-dimensional surface currents in the xz plane, and the dielectric substrate with three-dimensional volume polarisation currents. The simplicity of the element geometry enables both the metal strip and substrate to be placed on a common grid for computational purposes. As shown in Figure 6.12, the substrate is divided into n_x, n_y, and n_z segments of width Δx, Δy, and Δz in the x, y, and z dimensions, respectively. The metal strip segments are aligned with the segments forming the top edge of the substrate. The surface currents on the metal strip are expanded in terms of N_c two-dimensional pulse basis functions, and the volume polarisation currents in the dielectric substrate in terms of N_d three-dimensional pulse basis functions as given in (6.13) to (6.16).

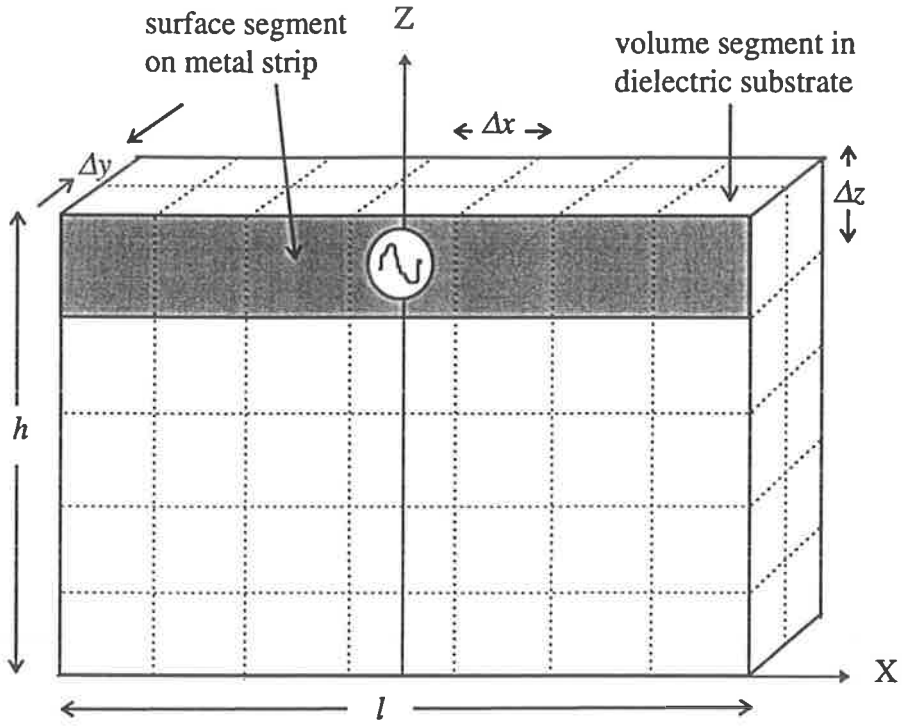

Figure 6.12 : Segmentation scheme for metal strip and finite dielectric substrate

The L_c operator for a testing point at the k^{th} segment due to the j^{th} current segment is the same as that given in (6.21). Since the substrate is finite in all dimensions, surface charges on the substrate exist on all the faces except the bottom face as explained earlier. Hence the L_d operator becomes:

$$
\begin{aligned}
L_d\left\{\bar{J}_d\right\}_k = -j\omega\mu_0 \sum_{j=1}^{N_d}\left(J_{dxj}\hat{x} + J_{dyj}\hat{y} + J_{dzj}\hat{z}\right)\cdot \\
\iiint_{V_d} Q_j(x',y',z')G_p\,dx'dy'dz' - \frac{j}{\omega\varepsilon_0}\left(\hat{x}\frac{\partial}{\partial x} + \hat{y}\frac{\partial}{\partial y} + \hat{z}\frac{\partial}{\partial z}\right)\cdot \\
\left\{\sum_{j\in S_{xy}} \alpha J_{dzj}\iint_{S_{xy}} Q_j(x',y',z')G_p\,dx'dy'\right. \\
+ \sum_{j\in S_{xz}} \beta J_{dyj}\iint_{S_{xz}} Q_j(x',y',z')G_p\,dx'dz' \\
\left. + \sum_{j\in S_{yz}} \gamma J_{dxj}\iint_{S_{yz}} Q_j(x',y',z')G_p\,dy'dz'\right\}
\end{aligned}
\tag{6.30}
$$

where S_{xy} refers to the top face, S_{xz} to the front and back faces, and S_{yz} to the two faces on the side of the dielectric slab over which the surface integrals are evaluated, and

$$\alpha=\begin{cases}1, & \text{if } \hat{n}=\hat{z}\\ -1 & \text{if } \hat{n}=-\hat{z}\\ 0, & \text{otherwise}\end{cases}\quad \beta=\begin{cases}1, & \text{if } \hat{n}=\hat{y}\\ -1 & \text{if } \hat{n}=-\hat{y}\\ 0, & \text{otherwise}\end{cases}\quad \gamma=\begin{cases}1, & \text{if } \hat{n}=\hat{x}\\ -1 & \text{if } \hat{n}=-\hat{x}\\ 0, & \text{otherwise}\end{cases} \tag{6.31}$$

where $\hat{n}$ is the outward pointing unit vector normal to the surfaces. Apart from the differences described above, the numerical implementation procedure is the same as in the previous section and will not be repeated here.

Design Examples

The infinite array of metal strips supported on finite-size dielectric substrates is another example of a microstrip array with LITA architecture, and was first proposed by Parfitt and others [8,9,10]. Their analysis was performed using the spatial form of the periodic Green's function, and both analytical and experimental results have been presented for electrically thick substrates. The design examples are provided below to demonstrate that the Generalised Hybrid Periodic Green's Function technique is able to accurately model this type of microstrip array with significantly better computational efficiency than the spatial domain technique used by Parfitt. The models are also used to investigate the effect of the electrical thickness of the substrate on the scanning performance of the array, as well as the frequency bandwidth achievable for this class of microstrip dipole array.

In the first design example based on [10], the array shown in Figure 6.11 is modelled with inter-element spacings $b = d = 0.5\lambda$. Each metal strip has a length $l = 0.285\lambda$. The substrate has the same length as the metal strip, a height $h = 0.5l$ and a thickness $t = 0.075l$. The substrate is modelled with the relative permittivity of RT Duroid 6010 $\varepsilon_r = 10.2$, thus resulting in an equivalent electrical thickness of 24.5°. Excitation is provided by an idealised delta-gap voltage at the centre of the metal strip. The above dimensions have been experimentally verified [8] to produce a half-wave resonant condition for the isolated element. The substrate is segmented using $n_x = 9$, $n_y = 2$ and $n_z = 5$ thus resulting in 90 volume segments for the substrate and 9 surface segments for the metal strip. The active impedance as a function of scan angle in the H-plane is given in Figure 6.13:

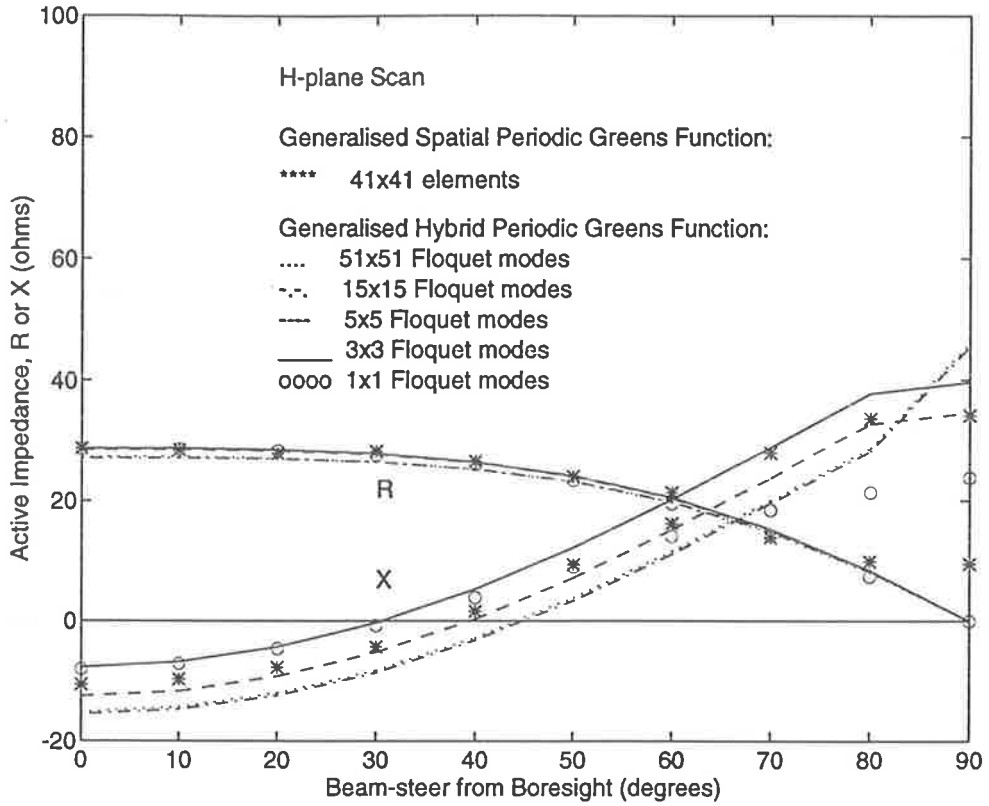

Figure 6.13 : Active impedance as function of scan angle in the H-plane for an infinite array of finite-substrate supported metal strip dipole antennas with idealised feed; $b = d = 0.5\lambda$, $l = 0.285\lambda$, $h = 0.5l$, $t = 0.075l$, $n_x = 9$, $n_y = 2$ $n_z = 5$, $\varepsilon_r = 10.2$.

The results in the H-plane based on the Generalised Spatial [10] and Hybrid Periodic Green's Function techniques are in good agreement except for large scan angles. Since there are no grating lobes, the active resistance should be zero at the grazing angle, as correctly shown by the spectral domain results. In the spatial domain results, the active resistance is about 10Ω at this angle, suggesting that the results are probably not fully converged even after 41 x 41 elements have been included in the spatial summations. Figure 6.14 shows that the E-plane scan results of the Generalised Spatial and Hybrid Periodic Green's Function techniques are in good agreement, including the prediction of a scan blindness at $\theta = 75°$. Once again, the lack of convergence of the generalised spatial periodic Green's function at large scan angles is apparent from the graph. For the Generalised Hybrid Periodic Green's Function technique, use of Floquet mode (0,0) alone is not adequate to predict the scan blindness; but the use of as few as 3 Floquet modes in

each dimension ($-1 \leq m \leq 1$ and $-1 \leq n \leq 1$) is sufficient to reasonably compute accurate active impedance results.

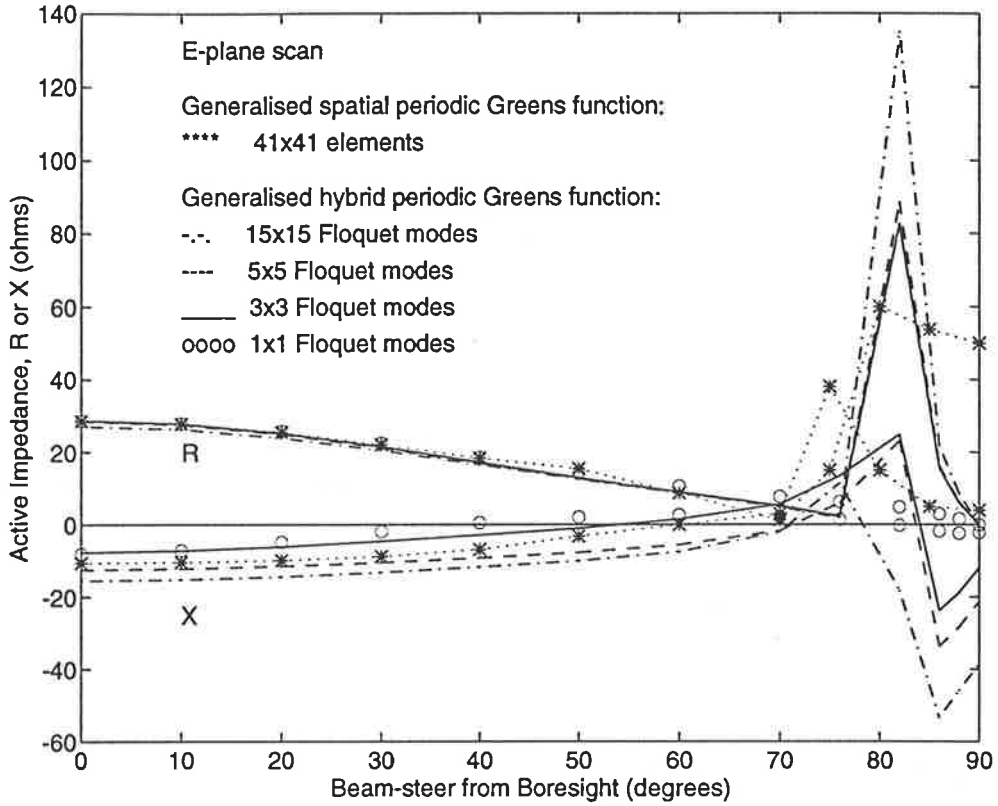

Figure 6.14 : Active impedance as function of scan angle in the E-plane for an infinite array of finite-substrate supported metal strip dipole antennas with idealised feed; $b = d = 0.5\lambda$, $l = 0.285\lambda$, $h = 0.5l$, $t = 0.075l$, $n_x = 9$, $n_y = 2$ $n_z = 5$, $\varepsilon_r = 10.2$.

Table 6.5a shows that the results of the Hybrid Periodic Green's function technique are well converged with segmentation of the metal strip, and Table 6.5b shows a comparison of the numerical efficiency of the two techniques in the analysis of the same structure.

n_x	7	*9*	15
Active impedance	29.19 - j 13.1 Ω	*28.86 - j 6.71 Ω*	28.38 - j 5.60 Ω

Table 6.5a : Active impedance at boresight scan based on array parameters in Figure 6.14, for different segmentations of the length of the metal strip dipole based on the Generalised Hybrid Periodic Green's function technique; $n_y = 2$, $n_z = 5$.

Elements or Floquet Modes	Segmentation			CPU Time Required
	n_x	n_y	n_z	
Generalised Spatial Periodic Green's Function technique				
41 x 41	2	19	10	4 min
Generalised Hybrid Periodic Green's Function technique with convergence acceleration of on-plane points only				
51 x 51	2	9	5	56 min
15 x 15	2	9	5	6.5 min
Generalised Hybrid Periodic Green's Function technique with acceleration of on-plane and near on-plane points				
5 x 5	2	9	5	55 sec
3 x 3	2	9	5	42 sec
1 x 1	2	9	5	35 sec

Table 6.5b : Computational effort needed to obtain converged results for the Generalised Spatial Periodic Green's Function technique using a supercomputer and the Hybrid Periodic Green's Function technique using a desktop computer to analyse an infinite array of substrate supported metal strip antennas; $b = d = 0.5\lambda$, $l = 0.285\lambda$, $h = 0.5l$, $t = 0.075l$, $\varepsilon_r = 10.2$.

In Table 6.5b, the spatial domain results are taken from those reported in [10] and require 4 minutes of CPU time on a VP2200 vector supercomputer per scan angle. The results for the Generalised Hybrid Periodic Green's Function technique are presented for two cases - convergence acceleration of the spectral periodic Green's function for on-plane interactions only, and convergence acceleration for both on-plane and near on-plane interactions. The former case requires nine times as much CPU time (6.5 minutes) to compute a set of converged results as the latter (42 seconds). It is apparent that compared with the Generalised Spatial Periodic Green's Function technique, the computational efficiency achieved by the Generalised Hybrid Periodic Green's Function technique is significantly better. The efficiency gained is due to two main reasons.

- Firstly, the integration over the sources for the spectral component of the hybrid periodic Green's function is evaluated in closed form, thus saving much numerical integration time required by the spatial technique.

- Secondly, the hybrid periodic Green's function has a very rapid rate of convergence with Floquet modes. It has been reported [11] that the Dielectric Slab Green's function requires as many as 120 x 120 Floquet modes to produce a well converged solution. As demonstrated in Figures 6.13 and 6.14, the results of the Generalised Hybrid Periodic Green's function requires only 3 x 3 Floquet modes for convergence. One implication of the computation speed achieved is that this technique should be capable of modelling more complex element geometries such as folded dipoles and feedlines on a desktop computer. This extension will be discussed in the next section. Moreover, accurate calculations over a range of frequencies are feasible in a reasonable time, thus making the technique suitable for extension to frequency domain analysis of wideband structures.

The numerical model developed above is used to design for a resonant condition at boresight scan for substrates with varying electrical thickness. Denoting the antenna parameters in Figure 6.13 as those of Antenna E, three other sets of antenna parameters are specified, with the parameters as shown in Table 6.6 below:

Antenna	ε_r	Substrate thickness (t)	Electrical thickness (t_e)	Dipole length (l)	Active Impedance at Boresight
D	2.55	0.0174λ	10 degrees	0.383λ	99+j0Ω
E	10.2	0.0214λ	24.5 degrees	0.285λ	28.7-j7.7Ω
F	10.2	0.0435λ	50 degrees	0.275λ	27-j1Ω
G	12.8	0.0582λ	75 degrees	0.249λ	20+j0Ω

Table 6.6: Resonant metal strip dipole lengths for various substrate electrical thickness for an infinite array of substrate supported metal strip dipole antennas.

In Table 6.6, Antenna D is designed with the relative permittivity of PTFE, whilst Antenna G is designed for operation with Gallium Arsenide which would be used for monolithically fabricated arrays. It can be seen from the table that the greater the electrical thickness of the substrate, the shorter is the half-wave resonant length of the metal strip, and also the smaller the boresight active impedance of the antenna. The characteristics of active

impedance with scan angle for this array is very similar to that for the semi-infinite dielectric sheet array. The scanning performance of Antennas D, F and G are shown in the Figure 6.15 below.

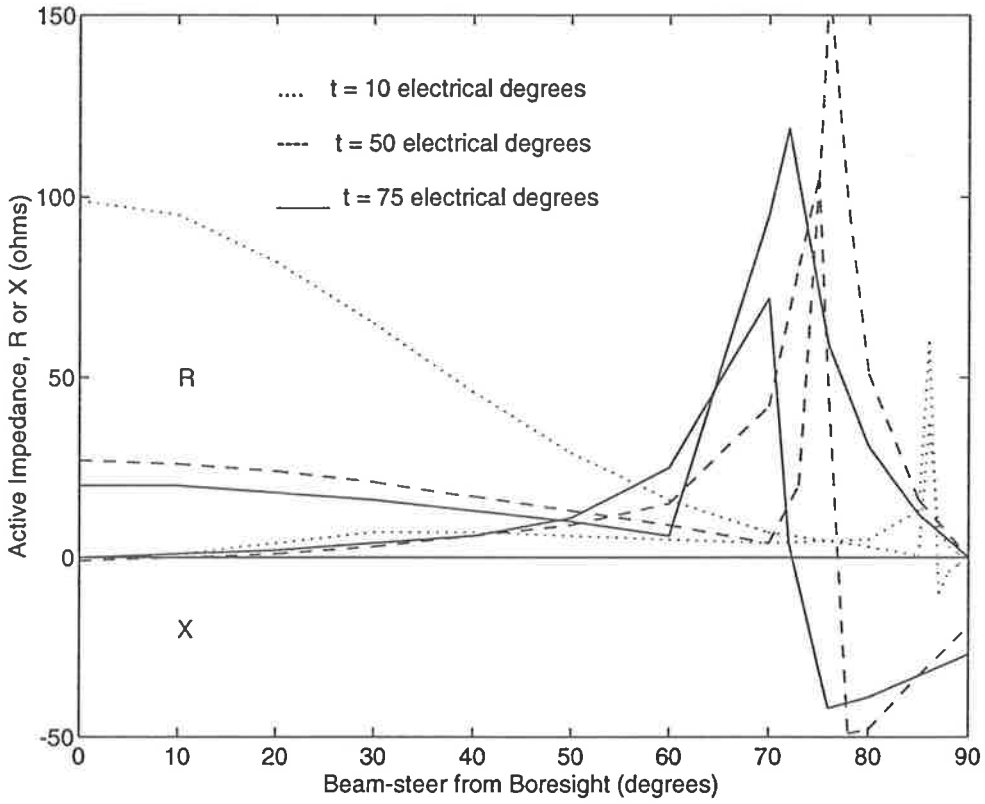

Figure 6.15 : Active impedance as a function of scan angle for an infinite array of finite-substrate supported metal strip dipole antennas with various substrate electrical thicknesses. The dimensions for the geometries are as given in Table 6.6 for antennas D, F and G.

As shown in Figure 6.15, the substrate induced scan blindness conditions in the E-plane occur at approximately 85°, 70°, and 60° scan angles for substrate thicknesses of 10, 50 and 75 electrical degrees, respectively. This illustrates that the effect of an increase in the electrical thickness of the substrate is that the angular position of the substrate induced scan blindness is shifted closer to boresight.

As in the previous two sections, the model is used to investigate the bandwidth for this class of microstrip dipole arrays. Using the same condition as before, the graph of the magnitude of active reflection coefficient as a function of normalised frequency for Antenna E is plotted in Figure 6.16.

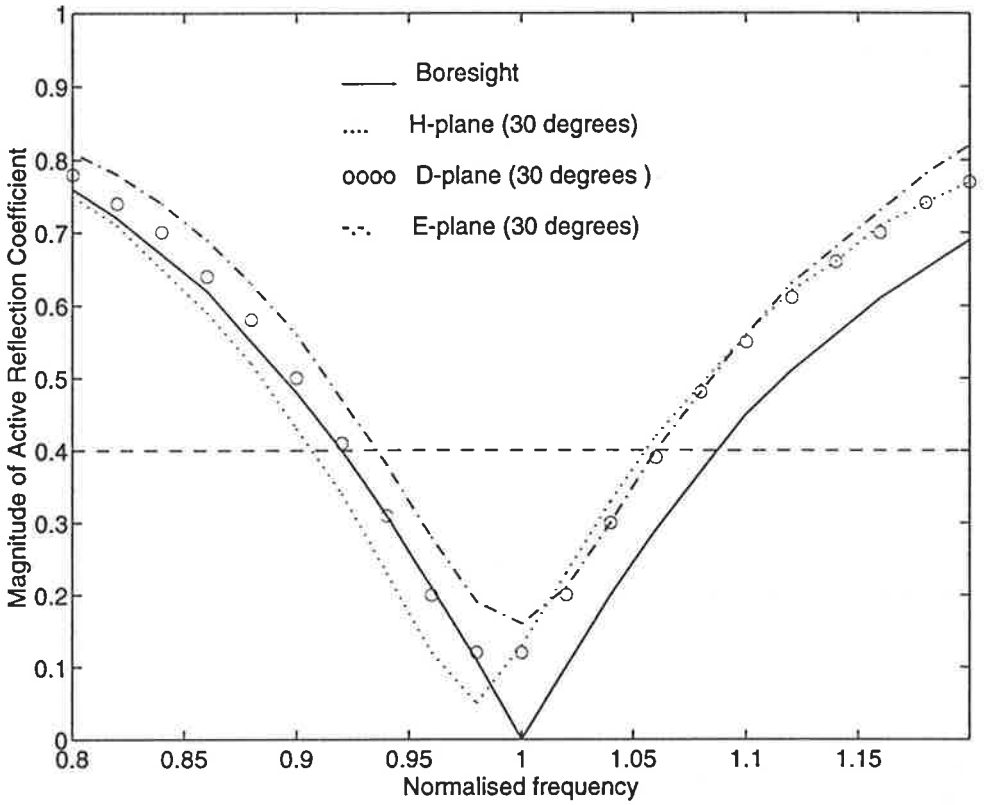

Figure 6.16 : Magnitude of active reflection coefficient as a function of normalised frequency for an infinite array of substrate supported metal strip antennas; $b = d = 0.5\lambda$, $l = 0.285\lambda$, $h = 0.5l$, $t = 0.075l$, $\varepsilon_r = 10.2$.

Figure 6.16 shows that the boresight curve gives a bandwidth of about 17%, but this figure is degraded by the E and H-plane curves, giving an overall bandwidth of about 11% which satisfies all the four conditions. This result is an improvement over the infinite slab and semi-infinite sheet substrate structures analysed in the Sections 6.2 and 6.3 which have bandwidths of 4% and 6%, respectively. Based on the data presented in this chapter, it appears that a break in the continuity of the substrate causes the scan blindness angle to occur further away from boresight, and consequently leads to a greater achievable bandwidth for the array.

6.4.2 Metal Strip Dipoles with Coplanar Strip Feedlines

Having modelled the infinite array of substrate supported metal strip dipoles with idealised feed and analysed the effect of the substrate on the characteristics of the array, the analysis is extended to include a feedline. The geometry of such an array element is shown in Figure 6.17. The analysis follows as described in Section 6.4.1 for the substrate supported metal strip dipole with idealised feed, except that the Configuration B junction feedline model described in Section 5.4 is incorporated into the analysis.

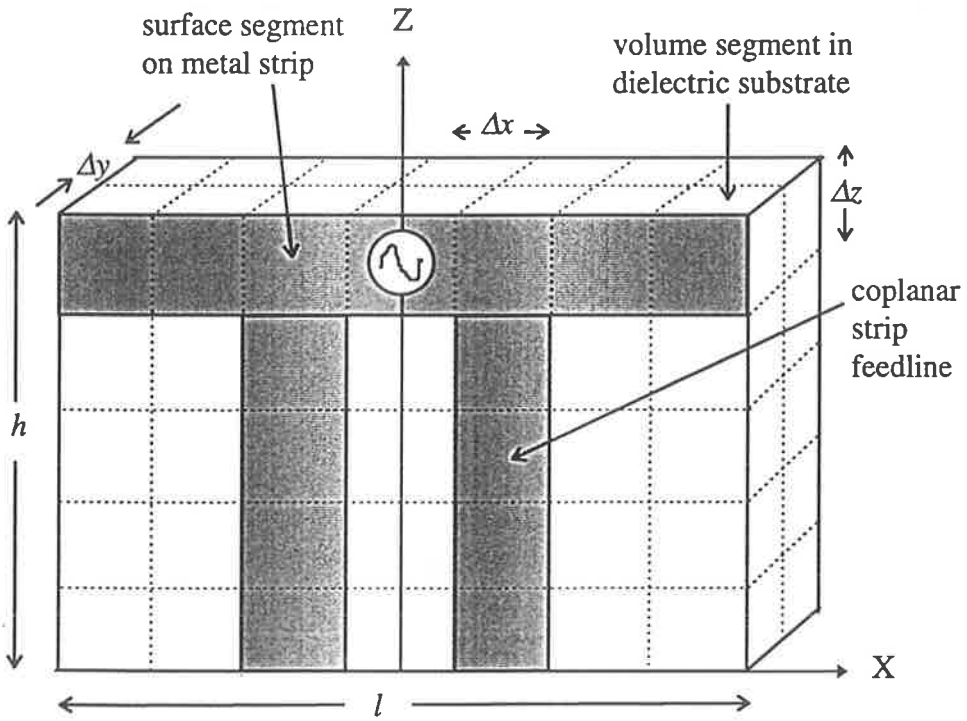

Figure 6.17 : Segmentation scheme for metal strip, coplanar strip feedlines and finite dielectric slab within a unit cell of the infinite array.

Design Examples

It has been shown in Sections 5.4 and 6.1 that both the feedline and substrate can cause a scan blindness condition for the array. In the design examples presented here, results are given for the models of Antennas D and G in the previous section, but with the inclusion of

coplanar strip feedlines. It is noted that Antenna D is configured with a substrate of 10 electrical degrees thickness, and Antenna G has a substrate thickness of 75 electrical degrees. It is intended to demonstrate in this section the application of the analysis to explore the effect of feedline induced scan blindness compared with substrate induced scan blindness for antenna elements with electrically thin and thick substrates.

Antenna D:

Figure 6.18 shows the active impedance variation with scan angle in the E-plane for Antenna D with and without feedlines. In the case of the antenna without feedlines, the array element is resonant at the boresight scan angle. The now familiar substrate induced scan blindness can be seen to occur at a scan angle of 85°. It is noted that both the real and imaginary parts of the active impedance undergo very rapid changes with scan angle in the region of the substrate induced scan blindness.

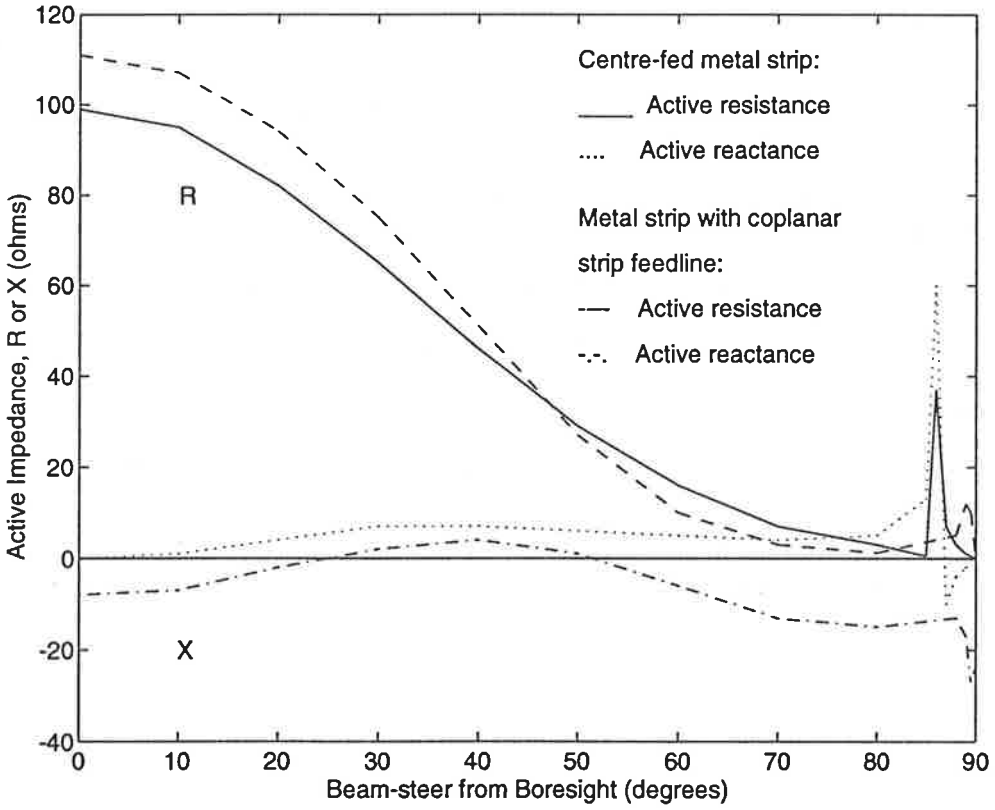

Figure 6.18 : Active impedance as a function of scan angle in the E-plane for an infinite array of metal strip dipoles with and without feedlines supported on electrically thin substrates; $b = d = 0.5\lambda$, $l = 0.383\lambda$, $h = 0.1915\lambda$, $t = 0.0174\lambda$, $\varepsilon_r = 2.55$.

In the case of the structure with feedlines, the metal strip is no longer resonant at the boresight scan angle, implying that the feedline currents have an effect on the radiation characteristics of the array. A scan blindness also occurs at about 80°, but it is apparent from Figure 6.18 that the nature of the impedance variation in the region of the scan blindness is different from the case without feedlines. In this region, the active resistance has its maximum at a much lower value and the active reactance does not undergo rapid variations in a manner observed in the previous case. Furthermore, the pattern of the active impedance variation around the scan blindness region is similar to that described in the previous chapter for metal strip dipoles with feedlines. Accordingly, this is identified as a feedline induced scan blindness. As the antenna substrate is electrically thin (about 10 electrical degrees), it is observed that the feedline induced scan blindness effect is dominant in this case.

Antenna G:

Figure 6.19 shows the active impedance variation with scan angle in the E-plane for Antenna G which has a substrate thickness of 75 electrical degrees. In the case of the antenna modelled without feedline, the active impedance shows a resonance condition at boresight scan angle. A substrate induced scan blindness occurs at about 60° scan angle. In the case of the antenna modelled with the feedline, the antenna is near to a resonance condition at the boresight scan angle. A scan blindness occurs at about 65° scan angle, and the nature and angular location of the rapid variations in active impedance values in this region are very similar to that of the antenna modelled without feedlines. It is therefore concluded that this latter case is also a substrate induced scan blindness, and the only effect of the feedlines is to shift the angular location of the substrate induced scan blindness further away from boresight.

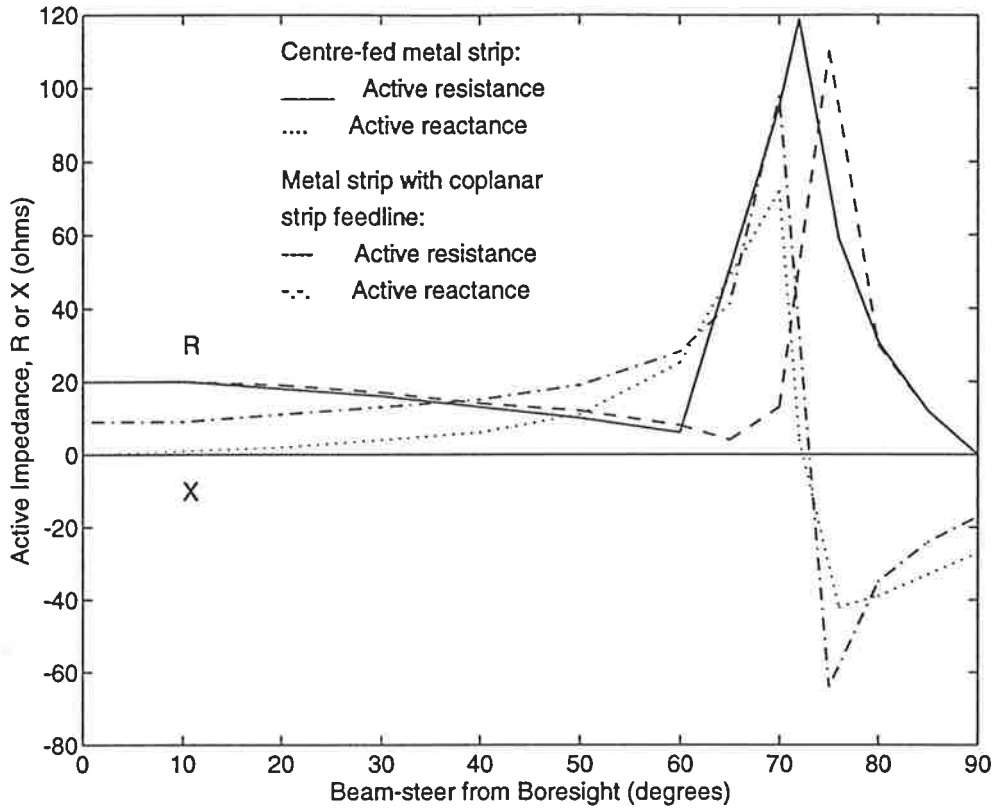

Figure 6.19 : Active impedance as a function of scan angle in the E-plane for an infinite array of metal strip dipoles with and without feedlines supported on electrically thick substrates; $b = d = 0.5\lambda$, $l = 0.249\lambda$, $h = 0.1245\lambda$, $t = 0.0582\lambda$, $\varepsilon_r = 12.8$.

Based on the observations made from the results in Figures 6.18 and 6.19, the effects of the substrate and feedline on the radiation properties of the metal strip dipole array are summarised below:

- For electrically thin substrates, the active impedance characteristics are affected by the feedline currents to the extent that a feedline induced scan blindness condition is observed. As demonstrated by the design examples in Section 5.4, by designing the antenna with the feedlines closer together, the angular location of the scan blindness angle will occur further away from boresight.

- For electrically thick substrates, the polarisation currents in the substrate dominate the active impedance characteristics of the antenna array and cause a substrate induced scan blindness. In this case, the effect of the feedlines is significantly reduced. In the particular example shown, the effect of the feedlines is actually beneficial in that the scan blindness

condition occurs at a scan angle further away from boresight as compared with the case without feedlines. For electrically thick substrates, the occurrence of scan blindness at around 60° scan angle may be a serious limitation to the performance of the array.

An indication of the numerical convergence as well as the computational effort required for the model of the infinite array of substrate supported metal strip dipoles with coplanar strip feedlines can be seen in Table 6.7 where the computations are based on Antenna E with the inclusion of coplanar strip feedlines.

Floquet Modes Used	Active Impedance (Ω)	CPU Time Taken (Seconds)
1 x 1	27.2 - j 9.4	38.3
3 x 3	*27.5 - j 14.9*	*48.3*
5 x 5	27.7 - j 15.9	63.0
7 x 7	27.0 - j 16.2	87.4
9 x 9	26.9 - j 16.3	120.5

Table 6.7 : Active impedance of an infinite array of substrate supported metal strip dipoles with coplanar strip feedlines above an infinite ground plane at the boresight scan angle, analysed using the Generalised Hybrid Periodic Green's Function technique; $\varepsilon_0 = 10.2$, $b = d = 0.5\lambda$, $l = 0.285\lambda$, $h = 0.5l$, $t = 0.075l$, $n_x = 9$, $n_y = 2$, $n_z = 5$.

It can be seen from Table 6.7 that well converged results are obtained when the generalised hybrid periodic Green's function is evaluated using Floquet modes (m,n) where $-1 \leq m \leq 1$ and $-1 \leq n \leq 1$, and the corresponding CPU time per scan angle is about 48.3 seconds. A total of about 34.1 MBytes of storage and 4.5 MBytes of memory are required for the computer to calculate a value of the active impedance.

6.4.3 Metal Strip Folded Dipoles with Coplanar Strip Feedlines

It was shown in Figure 6.15 that for electrically thick substrates, the active impedance of the finite substrate supported metal strip dipole array at resonance is around 28Ω. For the elements with substrates considered so far, typical coplanar strip feedline dimensions result in feedline characteristic impedances of about 100Ω [87]. The low impedance of the substrate supported metal strip dipole is therefore not well matched to the feedline. One way to effect an impedance match is to replace the single metal strip dipole with a *metal strip folded dipole*. As discussed in Section 5.4, at the resonant condition in free space the active impedance of a folded dipole with equal width driven and folded arms is approximately four times that of the single strip with equivalent width. It has been shown experimentally [88] that the same impedance step-up ratio also applies to folded dipole radiating elements mounted on finite-size dielectric substrates. The model described in Section 6.4.2 is extended here to incorporate the metal strip folded dipole into the analysis.

Figure 6.20 shows an infinite array element geometry comprising a finite-size substrate supported *coplanar strip folded dipole* with a coplanar strip feedline. For the radiating element to operate effectively as a resonant folded dipole, the driven and parasitic arms need to be sufficiently close together. The simplest way to achieve this requirement in the numerical implementation is to place the folded dipole on a common grid with the rest of the element in the z dimension, and to divide the whole element structure into a large number of segments in this dimension in order that the folded dipole arms separation is sufficiently close. However, this method of segmentation is computationally inefficient as around 30 segments would be needed in the z dimension in order to achieve a sufficiently close spacing between the two arms of the folded dipole. A computationally more efficient method developed for this analysis is divide the top segment of the substrate into 4 equal sub-segments for convenience, and to make the width of each folded dipole arm equal to one of these sub-segments ($\Delta w = \Delta z/4$). It has been found that by doing this and then dividing the substrate vertically into 9 segments, the separation of the folded dipole arms

are sufficiently close for it to operate effectively in the resonant condition. However, the disadvantage of using different segmentation grids for the folded dipole and substrate is that it also leads to a more complicated analysis in the integration of the Green's function over the sources. Apart from the segmentation method described above, the procedure of analysis is essentially the same as that for the case of the substrate supported metal strip with coplanar strip feedline element.

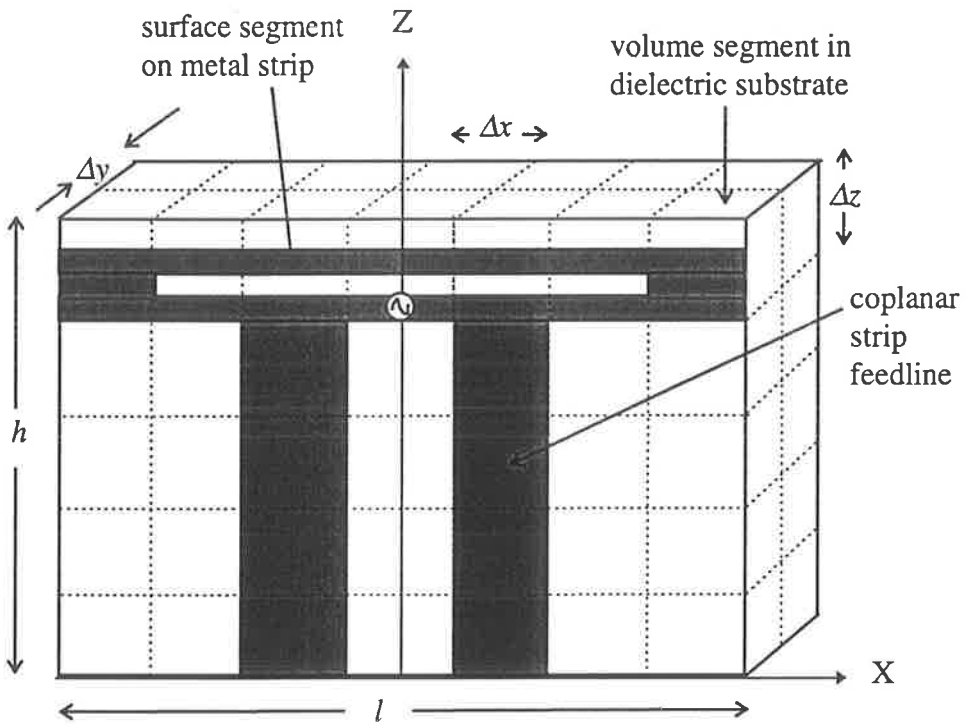

Figure 6.20 : Segmentation scheme for coplanar strip folded dipole, coplanar strip feedlines and finite dielectric slab of the infinite array element.

An infinite array with element geometry shown in Figure 6.20 is modelled as discussed above. The structure was found to be narrow band due to the fact that the feed point of the folded dipole can be considered to be located at the junction of three short-circuited transmission lines formed by the two arms of the folded dipole and the coplanar strip feedline. The thickness of the substrate is chosen to be $t = 0.03\lambda$ where the free space wavelength λ is again used. For a substrate material with $\varepsilon_r = 10.2$, this gives an equivalent electrical thickness of 35 electrical degrees. As before, the inter-element spacing are chosen to be $b = d = 0.5\lambda$ in order to avoid any grating lobes. As shown in Figure 6.21,

the folded dipole is found to have a half-wave resonance with a length of $l = 0.2725\lambda$, for an overall substrate height of $h = 0.11\lambda$.

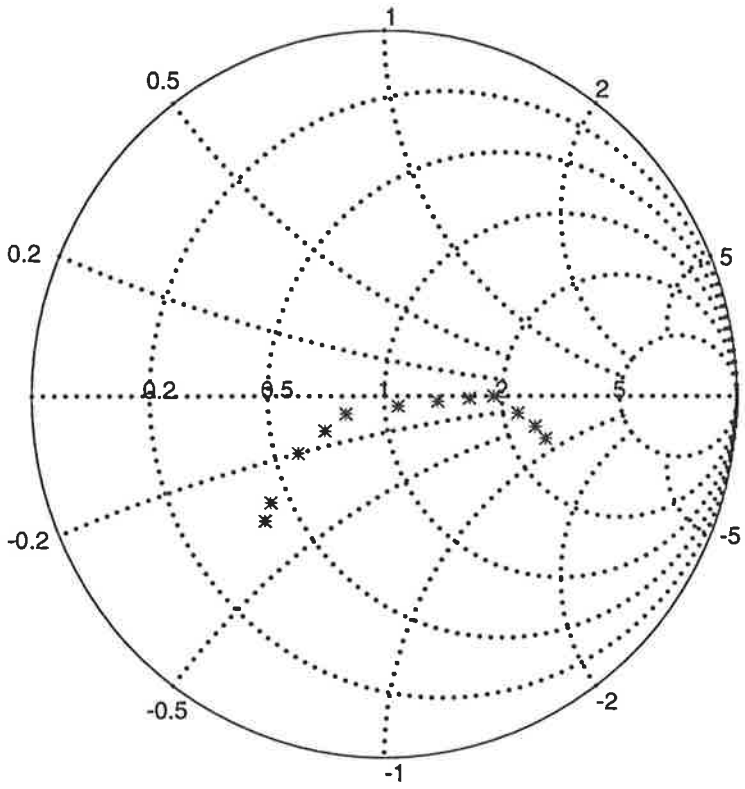

Figure 6.21: Variation of active impedance (normalised to 50Ω) with the ratio l / λ for an infinite array of substrate supported metal strip folded dipoles with coplanar strip feedlines at boresight scan angle; $\varepsilon_r = 10.2$, $b = d = 0.5\lambda$, $h = 0.11\lambda$, $t = 0.03\lambda$, l / λ varies from 0.2625 to 0.2765 with a resonant condition at 0.2725; $n_x = 9$, $n_y = 2$, $n_z = 9$.

The plots of the active impedance as a function of scan angle in the H-plane and E-plane are given in Figures 6.22 and 6.23. Without the substrate, the folded dipole array at resonance has an active resistance of 640Ω at the boresight scan angle with a metal strip length of $l = 0.49\lambda$. With the substrate and at resonance, an active resistance of 95Ω at the boresight scan angle is obtained for the folded dipole array with a metal strip length of $l = 0.2725\lambda$. It can be seen that the presence of the substrate has caused a 6.74 times reduction in the resonant active resistance. For comparison, the active impedance at all scan angles for the folded dipole array without substrate is scaled down by a factor of 6.74 and plotted in Figures 6.22 and 6.23.

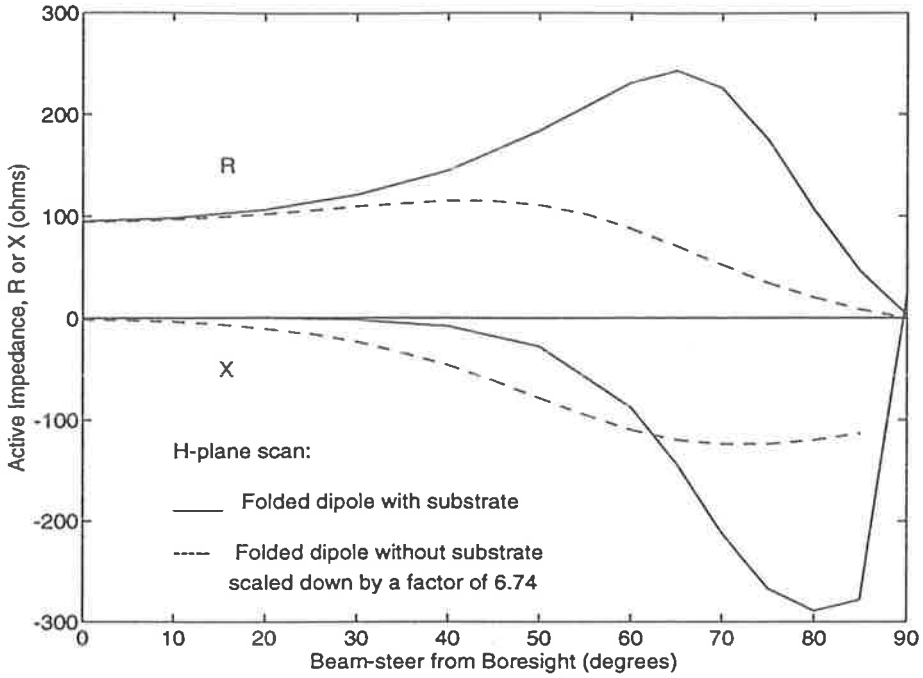

Figure 6.22 : Variation of active impedance with scan angle in the H-plane for an infinite array of substrate supported metal strip folded dipole antennas with coplanar strip feedlines; $\varepsilon_r = 10.2$, $b = d = 0.5\lambda$, $l = 0.2725\lambda$, $h = 0.11\lambda$, $t = 0.03\lambda$, $n_x = 9$, $n_y = 2$, $n_z = 9$.

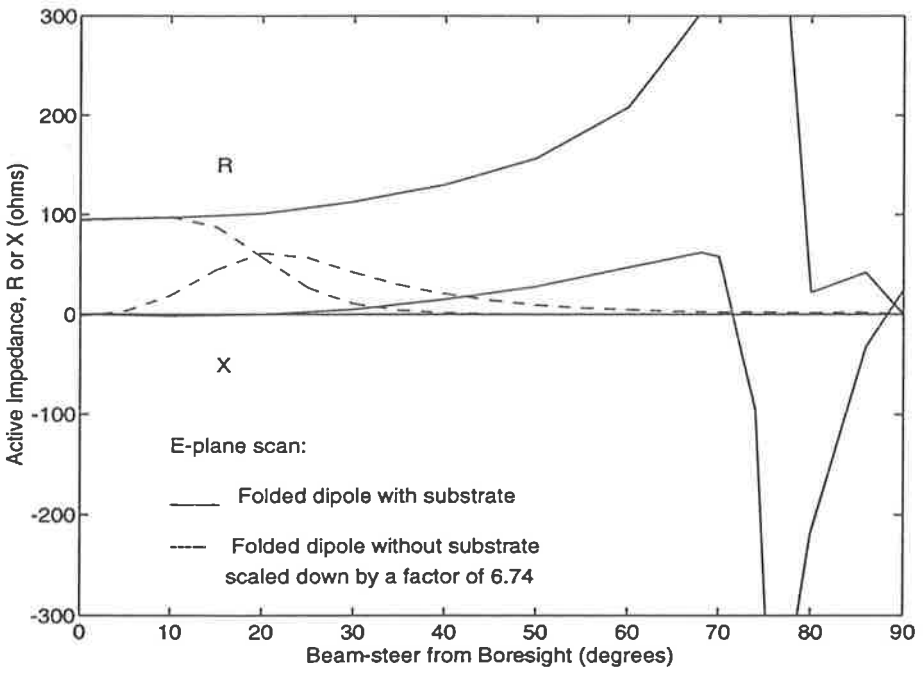

Figure 6.23 : Variation of active impedance with scan angle in the E-plane for an infinite array of substrate supported metal strip folded dipole antennas with coplanar strip feedlines; $\varepsilon_r = 10.2$, $b = d = 0.5\lambda$, $l = 0.2725\lambda$, $h = 0.11\lambda$, $t = 0.03\lambda$, $n_x = 9$, $n_y = 2$, $n_z = 9$.

The effect of the substrate on the active impedance of an infinite array of folded dipoles with coplanar strip feedlines can be clearly seen from Figures 6.22 and 6.23.

- At the boresight scan angle, the resonant active resistance of 95Ω for the substrate supported folded dipole presents an improved match to the characteristic impedance of the coplanar strip feedline than that of the single metal strip dipole illustrated by Antenna E in Table 6.3. Compared with the resonant active resistance of about 28Ω for the case of the single metal strip dipole element, the metal strip folded dipole element's resonant active resistance of 95Ω agrees with the expected impedance step-up ratio of approximately four times.

- In the H-plane scan, the substrate has a beneficial effect on the active impedance characteristics up to about 65° scan angle; at larger scan angles it causes a large reactance component in the active impedance.

- In the E-plane scan, the folded dipole array without substrates has a feedline induced scan blindness at about 40° scan angle which severely degrades the performance of the array. The feedline induced scan blindness effect is absent for the folded dipole array with substrate electrical thickness of 35 electrical degrees. As in the case of the H-plane scan, the substrate has a beneficial effect on the active impedance characteristics up to about 75° scan angle.

Figure 6.24 provides an indication of the useful frequency bandwidth that can be achieved by this array. Using the same conditions for determining the bandwidth as before, an overall bandwidth of about 5.5% is obtained for this array. Although the bandwidth is lower than the 11% obtained for the substrate supported single metal strip with idealised feed, it is noted that this is a more useful model in which a practical feedline has been incorporated into the analysis.

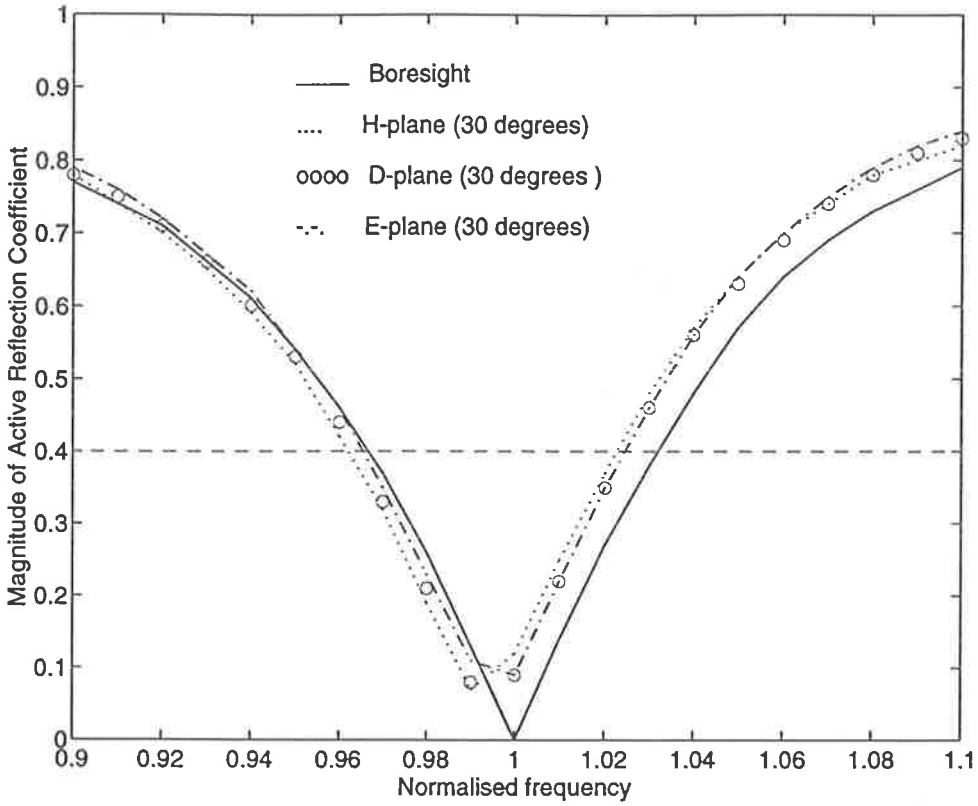

Figure 6.24 : Magnitude of active reflection coefficient as a function of normalised frequency for an infinite array of substrate supported metal strip folded dipoles with coplanar strip feedlines; $\varepsilon_r = 10.2$, $b = d = 0.5\lambda$, $l = 0.2725\lambda$, $h = 0.11\lambda$, $t = 0.03\lambda$.

The numerical convergence as well as the computational effort required to model the infinite array of substrate supported metal strip folded dipole with coplanar strip feedlines is given in Table 6.8 below. It is apparent from the table that well converged results are obtained when the generalised hybrid periodic Green's function is evaluated using Floquet modes (m,n) where $-1 \leq m \leq 1$ and $-1 \leq n \leq 1$; and the corresponding CPU time per scan angle is about 3.75 minutes. A total of about 40.7 MBytes of storage and 14.5 MBytes of memory are required for the computer to calculate a value of the active impedance.

Floquet Modes Used	Active Impedance (Ω)	CPU Time Taken (Seconds)
1 x 1	64.6 - j 0.3	185
3 x 1	85.8 - j 3.9	193
3 x 3	*95.3 - j 0.04*	*224*
5 x 5	93.9 - j 3.1	282
7 x 7	92.9 - j 3.0	369

Table 6.8 : Active impedance of an infinite array of substrate supported metal strip dipoles with coplanar strip feedlines above an infinite ground plane at the boresight scan angle; $\varepsilon_0 = 10.2$, $b = d = 0.5\lambda$, $l = 0.2725\lambda$, $h = 0.11\lambda$, $t = 0.03\lambda$, $n_x = 9$, $n_y = 2$, $n_z = 9$.

6.5 Summary

In this chapter, the Generalised Periodic Green's Function technique which was used in Chapter 5 for the analysis of infinite arrays of metal strip structures, is extended to model microstrip dipole arrays in which the element geometry has a metal part and a dielectric substrate. The integration of the antenna elements with the module electronics and distribution networks in microstrip arrays is described as being of either a TILA and LITA architecture. Three techniques for microstrip array analysis found in the literature are discussed, and it is observed that these techniques have a number of limitations where it is required to efficiently model both TILA and LITA microstrip arrays.

The Generalised Periodic Green's Function technique is shown to be capable of accurately modelling microstrip dipole arrays for both the TILA and LITA architectures with a high degree of computational efficiency. The details of the problem formulation and numerical

implementation of the technique are described in the context of modelling an infinite array of metal strip dipoles with idealised feeds and which are supported on a dielectric substrate extending continuously in the aperture plane of the array. The flexibility of the technique is demonstrated by its application to the cases where the dielectric substrate is discontinuous in either one, or both dimensions in the array plane. Accuracy is validated by the design examples for which results using other methods of analysis are available for comparison. The computational efficiency of the technique is quantified in the tables indicating that converged active impedance results are obtained typically in less than a minute of CPU time per scan angle using a desktop computer.

For the case of finite-size substrates, an analysis is developed which incorporates coplanar strip feedlines into the model. Finally, the issue of improving the impedance match between the metal strip dipoles and the feedlines is addressed by developing a model for an infinite array of substrate supported metal strip folded dipoles in which the active impedance is better matched to the characteristic impedance of the associated coplanar strip feedlines. It is shown that the models are able to detect both feedline induced and substrate induced scan blindness effects in the arrays analysed, and can be used to show how a knowledge of these effects would enable the design of an array with more desirable impedance characteristics.

The contributions made in this chapter are as follows:

- An accurate and computationally efficient method of analysis for microstrip dipole arrays has been developed based on the Generalised Periodic Green's Function technique which has the flexibility of modelling arrays suitable for both TILA and LITA architectures.
- The use of the technique for the analysis of microstrip dipole arrays with and without substrate discontinuities has been demonstrated.

- Highly efficient numerical models have been developed for microstrip dipole arrays with the substrate configured as an infinite dielectric slab, semi-infinite dielectric sheet and as finite-size dielectric substrates.
- Based on the models, an understanding of feedline and substrate induced scan blindness effects, and the conditions under which either of these effects dominate the array's impedance characteristics, is gained.

In summary, this chapter has demonstrated that the Generalised Periodic Green's Function technique is an accurate, flexible and highly efficient method of analysis of infinite microstrip dipole arrays that may be implemented on desktop computers. In practice, an infinite array environment is itself a form of idealisation, and all arrays are finite. In Chapter 7, it will be shown how the method of infinite array analysis developed in this Chapter 3 can be extended to the analysis of finite arrays by means of a spatial Fourier windowing technique.

CHAPTER 7

Generalised Periodic Green's Function - Spectral Widowing Analysis of Finite Arrays

7.1 Introduction and Overview

The Generalised Periodic Green's Function technique developed in Chapter 4 has been shown to be an accurate, flexible and computationally efficient method of analysis for infinite arrays of metal strip structures in Chapter 5 and microstrip dipoles with various substrate configurations in Chapter 6. The technique has been applied to the analysis of array element geometries ranging from the simpler metal strip dipole to the more complex substrate supported metal strip folded dipole with coplanar strip feedline. The corresponding computer CPU time required for the numerical analyses of these two infinite arrays range from 0.05 seconds to 3.75 minutes when implemented on a desktop computer.

The aim of this chapter is to develop and apply a finite array analysis technique which is also suitable for implementation on desktop computers. The accurate analysis of finite arrays using desktop computers presents a formidable challenge, as it is widely recognised that finite arrays of more than a few elements normally require considerably more computational resources to model than either the isolated element or infinite arrays. The reason is because the current distributions of the elements in a finite array differ depending on the location of the element in the array. A full Element-by-Element analysis of a finite microstrip array would normally result in a very large moment matrix which is more conveniently solved using a supercomputer. Pozar [11,12] developed a solution for the N^2 element finite array of printed dipoles and rectangular microstrip patches using an Infinite Dielectric Slab Green's Function technique to model each of the array element, and an Element-by-Element method to model the composite effect of the finite array. While the individual element analysis can be efficiently performed, it was recognised [12] that the use of the Element-by-Element method and the complexity of the array elements place a limit on the size of the array that can be handled. On the other hand, an infinite array analysis such as the one developed in this thesis is useful for predicting the behavior of elements located in the central region of a large size array, but does not enable the element to element variations in the currents to be obtained.

In the last decade, a number of techniques have been developed for numerically efficient analysis of finite array problems based on modifications to the infinite array approach. In most cases, the techniques are designed to avoid the solution of the full Moment Matrix obtained using the Element-by-Element method, by means of simplifying approximations about the current distributions on the elements of the finite array. The approaches taken by these techniques are briefly summarised below.

- A technique attributed to Roederer [89,90] involves a Fourier windowing of the infinite array far-field element pattern to obtain the finite array patterns. However, the technique does not yield any information about the active impedance of the individual elements of the array.

- Ishimaru and others [91] developed a finite periodic structure active impedance for large finite arrays by means of a convolution between the infinite periodic structure

active impedance and the Fourier transform of the aperture current distribution. While the approach demonstrates potential for the analysis of finite microstrip arrays, the method for obtaining the infinite array active impedance was based on a simplified analysis using assumed current distributions. Furthermore, the analysis was only applied to finite arrays of metal strip dipoles in the published work.

- Skrivervik and Mosig [13,14] applied Ishimaru's approach to the analysis of finite phased arrays of microstrip patches; but instead of working with active impedances, Pozar's Dielectric Slab Green's function was used in the analysis. This technique is numerically more efficient that the Element-by-Element method because the computation time is independent of the size of the finite array analysed. However, the disadvantage associated with the use of an infinite dielectric slab Green's function is that the technique cannot be used to analyse finite arrays in which the individual elements are associated with finite-size substrates.

- Parfitt [92] has developed a simple and effective technique to analyse the finite array problem based on a truncated version of the Generalised Spatial Periodic Green's Function for the infinite array given in Section 3.2. The use of a generalised Green's function potentially enables the flexibility of modelling of finite microstrip arrays with various substrate configurations and ground planes. However as discussed in Section 3.4.1 and 3.4.2, the limitations of using the Spatial Periodic Green's Function are the need for time consuming numerical integrations and the poor convergence property of the results for large scan angles.

From the above considerations, this chapter presents a technique for the analysis of finite arrays of metal strip and microstrip dipoles based on a *Generalised Periodic Green's Function for a Finite Array* which has the following features:

- The technique is based on a Green's Function whose advantages for numerical modelling has been demonstrated in the previous chapters.

- The finite array solution is obtained more efficiently than the full Element-by-Element method by using Ishimaru's approach of windowing the infinite array data at various

scan angles with the Fourier transform of the aperture current distribution of the finite array.

In this chapter, the spatial and spectral forms of the Generalised Periodic Green's Function for a finite array are derived using an Element-by-Element approach. The spectral form of the Green's function is developed into a technique for the analysis of the finite array problem, and is applied to the modelling of finite arrays of metal strips with idealised feeds as well as coplanar strip feedlines, and to substrate supported metal strips.

7.2 Generalised Periodic Green's Function for a Finite Array

Figure 7.1 shows the geometry for a finite planar array of M x N periodically spaced point current sources phased to produce a beam in the direction (θ,ϕ).

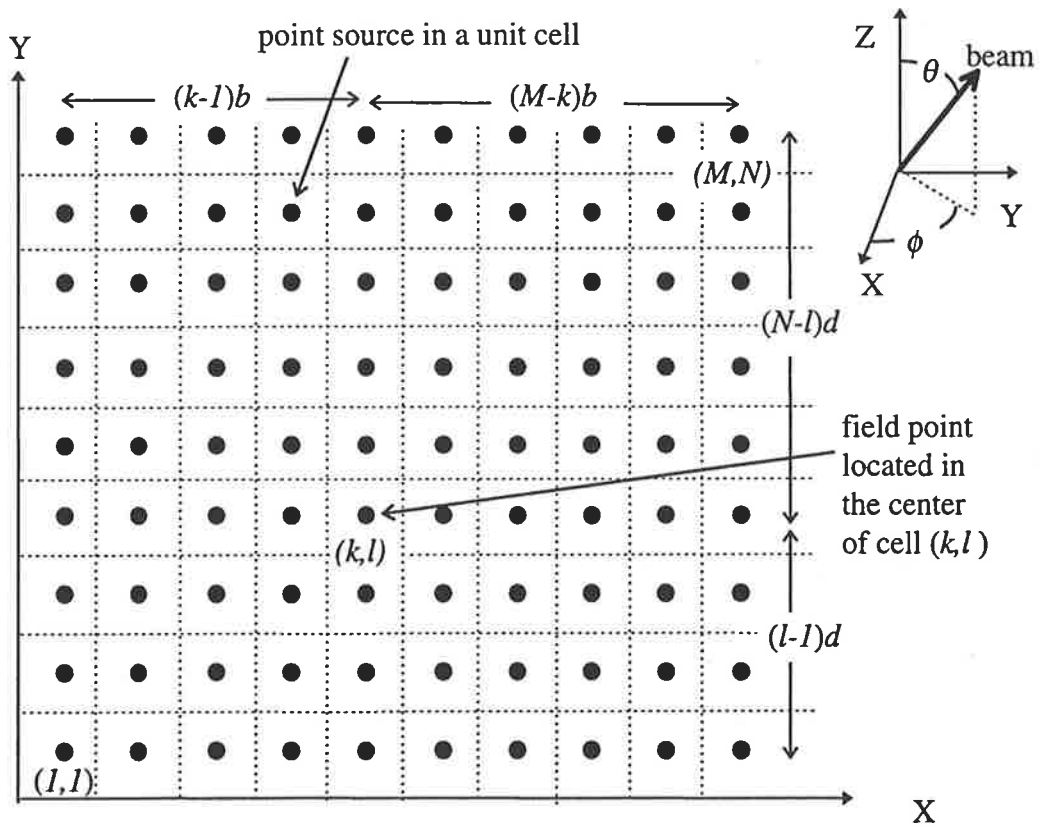

Figure 7.1 : Geometry for a finite array of regularly spaced point current sources.

The point sources are spaced at a distance b and d apart in the x and y dimension, respectively. The array plane is divided into unit cells of identical dimensions so that each unit cell contains a point source element located in the center of the cell. The origin of the co-ordinate axes is located at the bottom left hand corner of the array, so that the unit cells are numbered from (1,1) through to (*M,N*). It is required to obtain an expression for the Green's function at a field point located in the center of cell (*k,l*) due to the mutual coupling from all the elements of the finite array.

7.2.1 Finite Array Spatial Periodic Green's Function

The array of phase shifted sources J may be represented mathematically as:

$$J = \sum_{m=1}^{M}\sum_{n=1}^{N} J_{mn}\delta(x - x' - mb)\delta(y - y' - nd)\delta(z - z')e^{-jk_0 mbT_x}e^{-jk_0 ndT_y} \tag{7.1}$$

where $T_x = sin\theta cos\phi$ and $T_y = sin\theta cos\phi$ are the direction cosines. As before, the Dirac delta functions are used to represent the locations of the sources rather than an infinite value for the sources at those locations.

If the currents in all the cells are normalised to the current in cell (*k,l*), then the representation of the normalised sources becomes:

$$J_{mn,kl} = \sum_{m=1-k}^{M}\sum_{n=1-l}^{N}\frac{J_{mn}}{J_{kl}}\delta(x_k - x'_m - [m-k]b)\,\delta(y_l - y'_n - [n-l]d)\cdot \\ \delta(z - z')\,e^{-jk_0(m-k)bT_x}\,e^{-jk_0(n-l)dT_y} \tag{7.2}$$

The *Finite Array Generalised Spatial Periodic Green's Function* at a field point (*k,l*) due to the sources of an M x N array is then given by the integral of the free space scalar Green's function over the sources of the array:

$$G_{finite}^{kl,MN} = \iiint_{-\infty}^{\infty} \frac{e^{-jk_0 r}}{4\pi r} J_{mn,kl} \quad dxdydz$$
$$= \sum_{m=1-k}^{M-k} \sum_{n=1-l}^{N-l} \frac{J_{mn}}{J_{kl}} G(x,y,z)\, e^{-jk_0(m-k)bT_x}\, e^{-jk_0(n-l)dT_y} \tag{7.3}$$

where $G(x,y,z) = e^{-jk_0 R_{mn,kl}} / 4\pi R_{mn,kl}$ is the spatial Green's function for the array

and $R_{kl,mn} = \sqrt{\left[x_k - x'_m - (m-k)b\right]^2 + \left[y_l - y'_n - (n-l)d\right]^2 + (z-z')^2}$

It is noted that this Green's function representing a finite array has the following features:

- The *periodicity* of the array is expressed in the exponentials, which represent a linear phase shift over the elements with regular inter-element spacings *b* and *d*. However, it is also possible to extend the analysis to irregularly spaced array elements [91,93].
- The *finite nature* of the array is expressed in the limits $m = -(k-1)$ to $(M-k)$ as well as $n = -(l-1)$ to $(N-l)$ of the double summation over the sources in the finite array aperture. The summation limits essentially determines the size of the array.
- The differing effect of *mutual coupling* between the elements is expressed in the current ratios J_{mn} / J_{kl}. In the case of an infinite array, this current ratio takes a value of unity as the element currents are identical except for the imposed phase shift.
- The *edge effect* of the finite array is expressed through the position (k,l) of the field point which uniquely defines each cell, so that a unique Green's function is used to evaluate the current for each element in the finite array.

Special Cases for the Infinite Array and Isolated Element

Equation (7.3) represents the periodic Green's function for a general *M* x *N* phased array of which the infinite array and isolated element Green's functions are special cases. In the case of an infinite array, the field point in cell (k,l) is chosen to be the origin of the co-ordinate axes and also the reference cell, so that $k = l = 0$. In this case, the summation over the current sources extends from $-\infty$ to $+\infty$, and the currents $J_{mn} = J_{kl}$ because of the

infinite array environment. Under these conditions, (7.3) becomes the familiar *Generalised Spatial Periodic Green's Function for an infinite array*:

$$G_{\infty}^{spatial} = \sum_{m=-\infty}^{\infty} \sum_{n=-\infty}^{\infty} \frac{e^{-jk_0 R_{mn}}}{4\pi R_{mn}} e^{-jk_0 mbT_x} e^{-jk_0 ndT_y} \tag{7.4}$$

where $R_{mn} = \sqrt{(x-x'-mb)^2 + (y-y'-nd)^2 + (z-z')^2}$

In the case of the isolated element, the array has only one unit cell, so that the parameters *M, N, k, l, m, n* all assume a value of unity, and equation (7.3) reduces to:

$$G_{isolated}(x,y,z \mid x',y',z') = \frac{1}{4\pi r} e^{-jk_0 r} \tag{7.5}$$

where $r = \sqrt{(x-x')^2 + (y-y')^2 + (z-z')^2}$, which is the well-known *free space Green's function* for a point source.

When applied to the analysis of a finite array of antennas, the method which makes use of equation (7.3) is called the spatial windowing technique, because the spatial periodic Green's function for the infinite array is truncated to a window equal to the size of the finite array, and then applied to the Moment Method to solve for the equivalent currents on each element of the array. Parfitt and Yeo [92,94,95] have successfully employed this technique to obtain reasonably good results for small one- and two-dimensional arrays of monopoles and dipoles. However, the implementation of this spatial domain technique for more complex element geometries like microstrip arrays involves a high computational overhead because of the need for numerical integration, and it is therefore preferable to work in the spectral domain where the integration can be evaluated analytically.

7.2.2 Finite Array Spectral Periodic Green's Function

As described in Section 3.3, it is possible to represent the point sources of the phased array as current sheets located in the aperture plane of the array. This transformation is expressed mathematically using Poisson's sum formula:

$$\sum_{m=1}^{M} f(m) = \sum_{m'=-\infty}^{\infty} \int_0^M f(m)\, e^{-j2\pi n' m} dm \tag{7.6}$$

Applying (7.6) to (7.3), a summation of discrete point sources is transformed into an integration over continuous sources in the aperture of the array as shown below:

$$\begin{aligned} G_{finite}^{kl,MN} &= \sum_{m=1-k}^{M-k} \sum_{n=1-l}^{N-l} \frac{J_{mn}}{J_{kl}} G(x,y,z)\, e^{-jk_0(m-k)bT_x}\, e^{-jk_0(n-l)dT_y} \\ &= \sum_{m'=-\infty}^{\infty} \sum_{n'=-\infty}^{\infty} \int_{-(l-1)}^{N-l} \int_{-(k-1)}^{M-k} \frac{J_{mn}}{J_{kl}} G(x,y,z)\, e^{-jk_0(m-k)bT_x} \\ &\quad e^{-jk_0(n-l)dT_y}\, e^{-j2m'\pi u}\, e^{-j2n'\pi v}\, du\, dv \end{aligned} \tag{7.7}$$

where m,n and u,v are continuous variables, and m',n' take on integer values which will be shown later to be the Floquet modes for the infinite array spectral periodic Green's function. Since the array has regular element spacings, the following spatial displacement relations apply:

$$(x_m' - x_k) = ub = (m-k)b \quad \text{and} \quad (y_n' - y_l) = vd = (n-l)d \tag{7.8}$$

Substituting the relations in (7.8) into (7.7) leads to:

$$\begin{aligned} G_{finite}^{kl,MN} &= \sum_{m'=-\infty}^{\infty} \sum_{n'=-\infty}^{\infty} \int_{-(l-1)d}^{(N-l)d} \int_{-(k-1)b}^{(M-k)b} \frac{J_{mn}}{J_{kl}} \frac{G(x,y,z)}{bd}\, e^{-jk_0T_x(x_m'-x_k)} \\ &\quad e^{-jk_0T_y(y_n'-y_l)}\, e^{-j2m'\pi(x_m'-x_k)/b}\, e^{-j2n'\pi(y_n'-y_l)/d}\, dx\, dy \end{aligned} \tag{7.9}$$

where $x = x_m' - x_k$ and $y = y_n' - y_l$ are the displacements of the source points in the x and y dimensions with respect to the position of the field point. The next step is to convert the spatial Green's function into its spectral form by means of the inverse Fourier transform:

$$G(x,y,z) = \frac{1}{(2\pi)^2} \int_{-\infty}^{\infty} \int_{-\infty}^{\infty} \tilde{G}(\beta_x,\beta_y,z)\, e^{j\beta_x(x_m'-x_k)}\, e^{j\beta_y(x_n'-x_l)}\, d\beta_x\, d\beta_y \tag{7.10}$$

Substituting (7.10) into (7.9), the following is obtained:

$$G_{finite}^{kl,MN} = \sum_{m'=-\infty}^{\infty}\sum_{n'=-\infty}^{\infty}\int_{-(l-1)d}^{(N-l)d}\int_{-(k-1)b}^{(M-k)b}\frac{J_{mn}}{J_{kl}}\frac{1}{4\pi^2 bd}\int_{-\infty}^{\infty}\int_{-\infty}^{\infty}\tilde{G}(\beta_x,\beta_y,z)$$
$$e^{j\beta_x(x'_m-x_k)}\,e^{j\beta_y(y'_n-y_l)}\,d\beta_x\,d\beta_y\,e^{-jk_0T_x(x'_m-x_k)} \qquad (7.11)$$
$$e^{-jk_0T_y(y'_n-y_l)}\,e^{-j2m'\pi(x'_m-x_k)/b}\,e^{-j2n'\pi(y'_n-y_l)/d}\quad dx\,dy$$

A change of variables $\beta_x = 2m'\pi/b+\alpha$ and $\beta_x = 2n'\pi/d+\beta$ is introduced to simplify (7.11) so that the following is obtained:

$$G_{finite}^{kl,MN} = \int_{-\infty}^{\infty}\int_{-\infty}^{\infty}\left[\left\{\sum_{m'=-\infty}^{\infty}\sum_{n'=-\infty}^{\infty}\frac{1}{bd}\tilde{G}\left(\frac{2m'\pi}{b}+\alpha,\frac{2n'\pi}{d}+\beta,z\right)\right\}\right.$$
$$\left.\left\{\frac{1}{4\pi^2}\int_{-(l-1)d}^{(N-l)d}\int_{-(k-1)b}^{(M-k)b}\frac{J_{mn}}{J_{kl}}e^{-j(k_0T_x-\alpha)(x'_m-x_k)}\,e^{-j(k_0T_y-\beta)(y'_n-y_l)}dxdy\right\}\right]d\alpha\,d\beta \qquad (7.12)$$

The integrand in (7.12) contains a product of two terms within the square brackets. The first term involves a double infinite summation over a summand which is a phased shifted Fourier transform of the spatial Green's function *G(x,y,z)* within a unit cell of an array given in (7.3). It has been shown in Appendix B that by means of the Poisson transform, the Fourier integral form of this spatial Green's function is given by:

$$\tilde{G}\left(k_{x_m},k_{y_n},k_{z_{mn}}\right) = \frac{1}{j2k_{z_{mn}}}e^{-jk_{z_{mn}}|z-z'|} \qquad (7.13)$$

Hence it is recognised that the phased shifted function within the first set of braces in (7.12) is the *Generalised Spectral Periodic Green's Function* for the infinite array given by:

$$G_{\infty}^{spectral} = \sum_{m'=-\infty}^{\infty}\sum_{n'=-\infty}^{\infty}\frac{1}{j2k_{z_{mn}}bd}e^{-jk_{x_m}(x-x')}\,e^{-jk_{y_n}(y-y')}\,e^{-jk_{z_{mn}}|z-z'|}$$
$$= \sum_{m'=-\infty}^{\infty}\sum_{n'=-\infty}^{\infty}\frac{1}{bd}\tilde{G}\left(\frac{2m'\pi}{b}+\alpha,\frac{2n'\pi}{d}+\beta,z\right) \qquad (7.14)$$

The expression within the second set of braces in (7.12) is the *spectral window function* which appears as a Fourier transform of the normalised current distribution across the aperture of the array. This window function is characterised by the following parameters:

- The *finite nature* of the array is expressed through the limits of the double integral $-(k-1) \leq m \leq (M-k)$ and $-(l-1) \leq n \leq (N-l)$ across the array aperture.
- The *mutual coupling* between the array sources is expressed in the current ratio J_{mn} / J_{kl}
- The *edge effect* is expressed by the position (k,l) of the field point.

The above characteristics of the window function resemble those of the spatial periodic Green's function for the finite array, except for the periodicity factor which is inherently defined by the infinite array spectral periodic Green's function. Equation (7.12) may be expressed as a convolution:

$$G_{finite}^{kl,MN} = G_{\infty}^{spectral}\left(T_x, T_y\right) * W\left(T_x, T_y\right) \tag{7.15}$$

where * denotes convolution, and the spectral window function is given by:

$$W\left(k_0 T_x - \alpha, k_0 T_y - \beta\right) = \frac{1}{4\pi^2} \int_{-(l-1)d}^{(N-l)d} \int_{-(k-1)b}^{(M-k)b} \frac{J_{mn}}{J_{kl}} e^{-j(k_0 T_x - \alpha)x} e^{-j(k_0 T_y - \beta)y} dxdy \tag{7.16}$$

The physical meaning of (7.15) is that the spectral form of the periodic Green's function for a finite array is given by the convolution of the infinite array spectral periodic Green's function with the Fourier transform of the aperture current distribution. It can be shown that the expression in (7.12) becomes the spectral form of the periodic Green's function for the infinite array under the condition when the size of the array $M \to \infty$ and $N \to \infty$ [91]. Hence, as for the spatial case described in Section 7.2.2, the spectral form of the infinite array periodic Green's function is a special case of (7.12).

7.3 Generalised Periodic Green's Function - Spectral Windowing Technique

The spatial and spectral forms of the Generalised Periodic Green's Function were developed for a finite array. Because of the greater computational efficiency associated with the spectral form of this Green's function over the spatial form in enabling the integration over the sources to be evaluated analytically, the spectral form is chosen to be developed into a technique for the analysis of finite arrays. In this section, the procedure for applying the technique to the analysis of finite arrays is outlined, and illustrated by modelling a finite array of horizontal metal strips with their faces orientated parallel to the ground plane. Each of the main features of the technique is described below in turn.

7.3.1 Modelling of the Ground Plane

In practice, any ground plane associated with a finite array will also be of finite dimensions. In this analysis, it is assumed that the ground plane is truncated sufficiently far away from the edges of the array that image theory can be used to account for the effects of the ground plane. As a second order effect on the radiation pattern, the Geometrical Theory of Diffraction (GTD) or related high frequency techniques [96] could be adopted to allow for edge diffraction. It has been found [92] that such corrections are not necessary for impedance calculations and are therefore neglected here. In certain practical array applications, however, the ground plane is truncated close to the array edge, and GTD cannot be accurately applied for elements near the edge of the array. In this case, the ground plane can be modelled as equivalent currents in each of the unit cells identified in Section 7.2 which are then computed as part of the electric field integral equation. Important issues arising out of the ground plane modelling in this manner are the non-physical discontinuities of the ground plane current distributions at the internal cell boundaries obtained by the analysis and the wedge diffraction effects from the ground plane edges. These issues have been studied in some depth [92] in order to more properly

account for the ground plane truncation in the practical application of small arrays in areas where the need for compact housings preclude the use of extensive ground planes.

7.3.2 Evaluation of the Infinite Array Periodic Green's Function

It is apparent from (7.15) that the finite array Green's function is given by of the convolution of the *Generalised Spectral Periodic Green's Function of the infinite array* with the *Spectral Current Window*. It has been shown in Chapters 3 and 4 that significant computational efficiencies can be achieved by accelerating the convergence of the spectral periodic Green's function in the on-plane and near on-plane cases of interactions. The principle also applies when the infinite array periodic Green's function is to be used in finite array analysis, so that the two forms of the infinite array Green's function that could be used in the convolution process described by (7.15) are as follows:

- The Generalised Spectral Periodic Green's Function given by (3.9) for off-plane interactions.
- The Generalised Hybrid Periodic Green's Function given by (4.15) for on-plane and near on-plane interactions.

7.3.3 Evaluation of the Spectral Window Function

It is noted that because the spectral window function given in (7.16) contains a current ratio term J_{mn} / J_{kl} , the exact numerical evaluation of the spectral window function would require a-priori knowledge of the currents in the elements of the finite array. This problem may be overcome by assuming for the purpose of the convolution that variation of the currents between adjacent elements is small, so that the *current ratio is approximately unity* for all elements. Although a unity current ratio is employed, a unique current window is still obtained for each cell because the integral in the window function given in

(7.16) takes account of the position (k,l) of the field point. In practice, the assumption of a unity current ratio enables reasonably accurate results to be obtained provided that the mutual coupling between elements is not very strong. However if the condition of weak mutual coupling is not met, the effect of the currents is significant in the convolution and leads to inaccuracies in the evaluation of the equivalent currents on the elements of the array. If a unity current ratio is assumed, the window function in (7.16) then becomes:

$$W(\alpha_0-\alpha,\beta_0-\beta)=\frac{1}{4\pi^2}\int_{-(l-1)d}^{(N-l)d} e^{-j(\beta_0-\beta)y}dy \int_{-(k-1)b}^{(M-k)b} e^{-j(\alpha_0-\alpha)x}dx$$
$$=\frac{MNbd}{\pi^2}\,sinc(M_x)\,sinc(M_y)\,e^{jkb(\alpha_0-\alpha)}\,e^{jld(\beta_0-\beta)} \qquad (7.17)$$

where $M_x = Mb(\alpha_0-\alpha)$, $M_y = Nd(\beta_0-\beta)$, and α , β are the convolution variables. The window function thus obtained by assuming a unity current ratio is described as a *Simplified Spectral Window.*

The Simplified Spectral Window is an approximation based on a unity current ratio which assumes no current variation between the elements. However, the effect of the currents can be incorporated into the solution iteratively by obtaining another approximation of the spectral window function for evaluating the equivalent currents in the array elements. The subsequent approximation is presumed to be more accurate because the unity current ratio is no longer assumed and the effect of the currents has been introduced into the spectral window function. The procedure for an iterative solution is given below:

- Step 1: The *Simplified Spectral Window* is used in the finite array technique to obtain the equivalent current in cell (k,l) of a M x N array of sources.

- Step 2: The equivalent currents in all the other cells of the array are similarly obtained by application of the Simplified Spectral Window.

- Step 3: The equivalent currents evaluated for all the cells of the M x N array are used to obtain a second approximation of the window function, which is referred to as a *Refined Spectral Window.* In this case, the integral in (7.16) is evaluated over each individual unit cell instead of over the whole aperture of the array, and the contributions of the integrals are summed over all the unit cells making up the array. For the evaluation of the integral

over each unit cell, the value of the current ratio is the equivalent current of the element in that cell which was obtained in the Step 2. The procedure is expressed mathematically as follows:

$$
\begin{aligned}
&W(\alpha_0-\alpha,\beta_0-\beta)\\
&=\frac{1}{4\pi^2}\sum_{m=1}^{M}\sum_{n=1}^{N}\frac{J_{mn}}{J_{kl}}\int_{(n-l-1/2)d}^{(n-l+1/2)d}e^{-j(\beta_0-\beta)y}dy\int_{(m-k-1/2)b}^{(m-k+1/2)b}e^{-j(\alpha_0-\alpha)x}dx\\
&=\frac{bd}{4\pi^2}bd\ sinc\left(\frac{b(\alpha_0-\alpha)}{2}\right)sinc\left(\frac{d(\beta_0-\beta)}{2}\right)\cdot\\
&\sum_{m=1}^{M}\sum_{n=1}^{N}\frac{J_{mn}}{J_{kl}}e^{-j(\alpha_0-\alpha)(m-k)b}e^{-j(\beta_0-\beta)(n-l)d}
\end{aligned}
\tag{7.18}
$$

- Step 4: The Refined Spectral Window thus obtained can then be used again to re-evaluate the equivalent currents on any selected element of the array by the same process of convolution with the infinite array data.

In the later part of this section, results will be presented for analyses using both the simplified and refined spectral windows. The refined spectral window serves two purposes in the analysis:

- In the case of the infinite array technique, numerical convergence can be achieved using an increasing number of basis functions and Floquet modes in the numerical evaluation to the point where the results show no appreciable difference with further increase of these two parameters. In the case of the finite array technique described here, numerical convergence of the infinite array data can still be achieved in the same manner. However, this alone may not be sufficient to ensure the numerical convergence of the overall solution for the finite array. The iterative use of the Refined Spectral Window is one way of testing if the results have not significantly changed for the finite array analysis.

- In the finite array analysis, the assumption of a unity current ratio is an approximation. By incorporating the effect of the currents into the analysis by the use of a refined spectral window, a better approximation is thereby achieved.

7.3.4 Evaluation of the Convolution

The numerical implementation of the Generalised Periodic Green's Function - Spectral Windowing technique makes use of the Method of Moments to solve for the equivalent currents in a given element of the finite array. Assuming that it is desired to evaluate the currents in element (k,l) of a M x N finite array, the associated Moment Matrix elements Z_{kl}^{MN} and finite array periodic Green's functions $G_{finite}^{kl,MN}$ are related by:

$$\begin{aligned} Z_{kl}^{MN} &= \left(j\omega\mu_0 + \frac{j\nabla\nabla'}{\omega\varepsilon_0} \right) \iint_{S_c} J_c \left\{ G_{finite}^{kl,MN} \right\} dS_c \\ &= \left(j\omega\mu_0 + \frac{j\nabla\nabla'}{\omega\varepsilon_0} \right) \iint_{S_c} J_c \left\{ G_{\infty}^{spectral} * W_{kl}\left(T_x, T_y\right) \right\} dS_c \\ &= \left\{ \left(j\omega\mu_0 + \frac{j\nabla\nabla'}{\omega\varepsilon_0} \right) \iint_{S_c} J_c G_{\infty}^{spectral} dS_c \right\} * W_{kl}\left(T_x, T_y\right) \\ &= Z^{\infty} * W_{kl}\left(T_x, T_y\right) \end{aligned} \tag{7.19}$$

where Z^{∞} represents the elements in the Moment Matrix for the infinite array.

Equation (7.19) shows that the elements of the finite array Moment Matrix may be obtained either by a process involving the convolution of the spectral window function with the infinite array Green's function, or by the convolution of the same window function with the associated infinite array Moment Matrix elements. Because the convolution cannot be readily evaluated analytically in either case, the latter approach is chosen in this analysis for the following reasons:

- The solution to the finite array problem is conveniently divided into two parts. The first part involves the analysis of the infinite array which has identical element and lattice parameters to the finite array. Having obtained the infinite array Moment Matrix, the second part of the solution involves the convolution of each of these Moment Matrix elements with the window function. The second part of the solution is independent of the way in which the first part is solved. Any infinite array technique which enables the

Moment Matrix elements for various scan angles to be obtained, may be used in the first part of the solution.

- A technique of infinite array analysis described in Chapters 3 and 4 has already been developed. The numerical models for the various metal strip and microstrip dipole infinite arrays described in Chapters 5 and 6 can be readily used to obtain the data required for the first part of the solution. In this sense, the finite array technique described in this section is an *add-on technique* which operates on the infinite array data to obtain the solution for the finite array.

Having obtained the elements of the Moment Matrix, the equation to solve for the equivalent currents in element (k,l) of a $M \times N$ array is given by:

$$\left[\mathbf{Z}_{kl}^{MN}\right] \left[\mathbf{I}_{kl}^{MN}\right] = \left[\mathbf{E}_{kl}^{MN}\right] \tag{7.20}$$

The finite array excitation vector is correspondingly given by the convolution of the infinite array excitation vector with the spectral window function.

$$E_{kl}^{MN} = E^{\infty} * W_{kl}\left(T_x, T_y\right) \tag{7.21}$$

The convolution in (7.19) is evaluated numerically by first sampling each element of the Moment Matrix at various angles in scan space and performing a Fast Fourier Transform (FFT) on the sampled data [97]. In the transformed domain, the convolution becomes a product of the two functions at each sampled data point. An inverse FFT is then applied to the product to translate it back into the original domain, and the finite array moment matrix equation in (7.20) is then solved in the usual way for each scan angle used in the sampling. The wave propagation vectors in the xy plane for the spectral periodic Green's function given in (3.7b) may be expressed as:

$$k_{x_m} = \frac{2m\pi}{b} + k_0 T_x \quad \text{and} \quad k_{y_n} = \frac{2n\pi}{d} + k_0 T_y \tag{7.22}$$

It is apparent that k_{x_m} and k_{y_n} are periodic in the *u-v* space with a period of $2\pi/b$ and $2\pi/d$, respectively. This periodicity is also the reciprocal lattice spacings [98] of the grating lobe lattice, and therefore any sampling of a whole rectangle of these dimensions contains all the information available. When sampling with a N_f x N_f grid for performing the FFT where N_f is the number of sample points in each dimension of the grating lobe lattice, N_f should be a product of small prime numbers for maximum computational efficiency, and the discrete values of the FFT variables α_m and β_n are given by:

$$\alpha_m = \frac{m}{N_f}\left(\frac{2\pi}{b}\right) \qquad m = 0, 1, \ldots\ldots N_f - 1$$
$$\beta_n = \frac{n}{N_f}\left(\frac{2\pi}{d}\right) \qquad n = 0, 1, \ldots\ldots N_f - 1 \tag{7.23}$$

7.3.5 Design Examples

The Generalised Periodic Green's Function - Spectral Windowing technique developed in this chapter is illustrated using a number of design examples. For convenience, active impedance results will first be presented for boresight scan angle with various array sizes and lattice spacings so that impedance variations between elements can be readily compared. Following this, results of active impedance as a function of scan angle for elements at various significant locations of a finite array will be presented to show the general characteristics of the array and to identify specific features such as grating lobes which are dependent on the scan angle. In each of the graphs shown below:

- Finite array results using an accurate but computationally demanding Element-by-Element approach implemented using the free space Green's function given in (7.5) are displayed as a reference for comparison. Because of the large computer storage requirement of this technique, a maximum array size is soon attained, which for the desktop computer used in this research is a 9 x 9 array.

- Infinite array results using the Generalised Periodic Green's Function technique are displayed to show the difference in characteristics between the elements in the finite array and infinite array.

- Finite array results from the Generalised Periodic Green's Function - Spectral Windowing technique using both the simplified and refined spectral windows, are displayed to illustrate the technique which has been developed. Although the iterative procedure to obtain the refined spectral window can be applied more than once, it has been found that at the expense of large computational overheads, there are no significant changes in the results obtained by redefining a refined spectral window a second or subsequent time. Therefore the refined spectral window is used only once in obtaining the results presented in this chapter.

Design Example 1: Inter-element spacing of 0.6λ in the E-plane

The first design example is chosen to be a finite array in which each metal strip dipole has length $l = 0.44\lambda$, width $w = 0.05l$ and is located at a height $h = 0.5l$ above an infinite ground plane. The unit cell dimensions are chosen with $b = 0.6\lambda$ and $d = 0.5\lambda$. The metal strip is divided into $n_x = 21$ segments. In the generalised periodic Green's function technique, the infinite array data used for the convolution is converged after truncation of the Floquet modes at $-1 \leq m \leq 1$ and $-1 \leq n \leq 1$. Figures 7.2, 7.3 and 7.4 show the active impedance results for each element at boresight scan angle for a 3 x 3, 5 x 5 and 9 x 9 array with the above element and lattice dimensions. In the case of the 9 x 9 array, to avoid excessive congestion of the points in the graph, results are displayed only for the bottom left quadrant of the array. The position of the array element for which the active impedance is computed is designated by a cell number and cell type along the x axis of each graph, and is shown schematically by a diagram above each of the graphs. The cell types are designated C for a corner element, E for an edge element, I for an interior element and M for the center element.

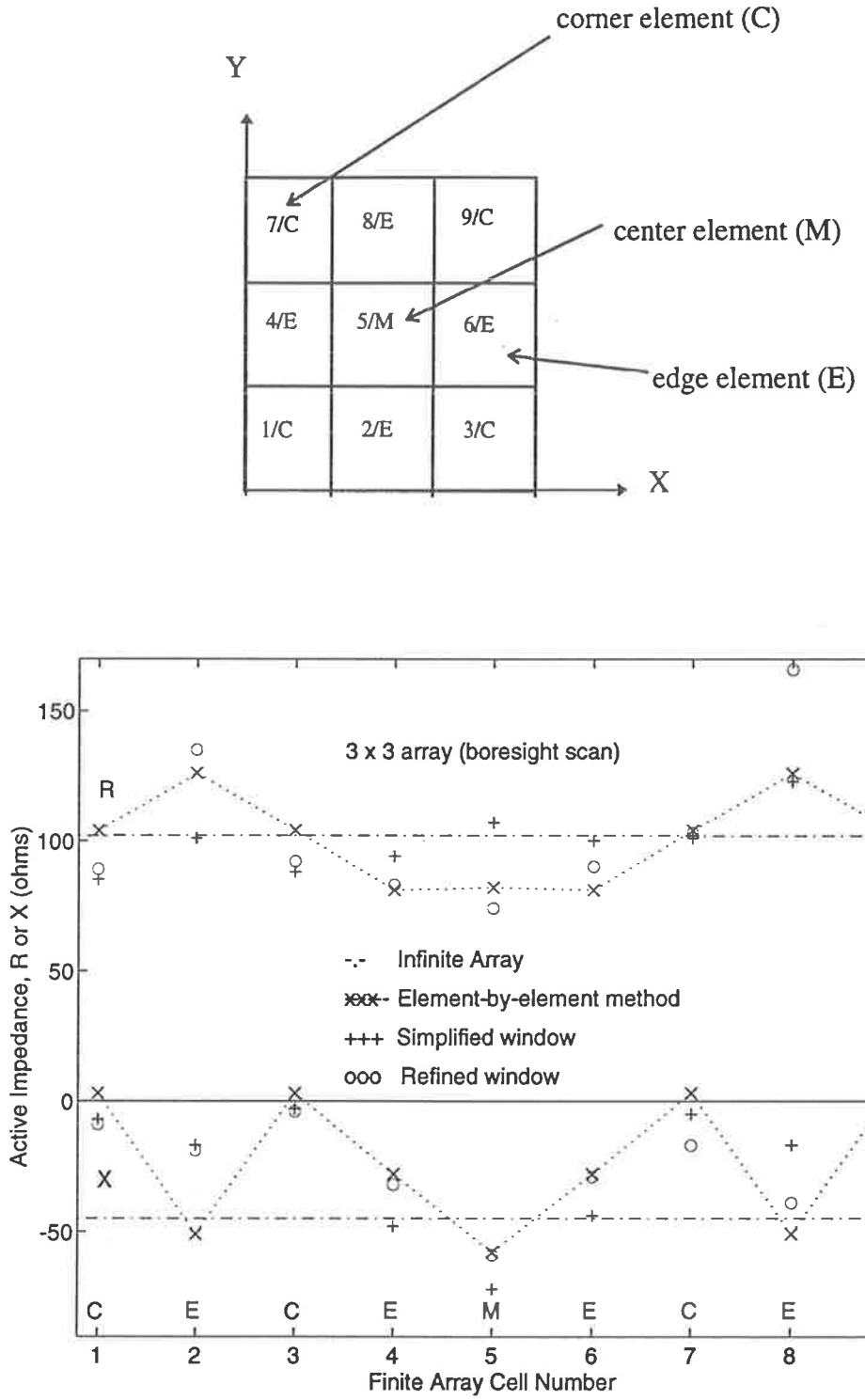

Figure 7.2 : Active impedance of elements in a 3 x 3 array of horizontal metal strips above an infinite ground plane in the boresight scan angle; $b = 0.6\lambda$, $d = 0.5\lambda$, $l = 0.44\lambda$, $w = 0.05l$, $h = 0.5l$, $n_x = 21$ segments.

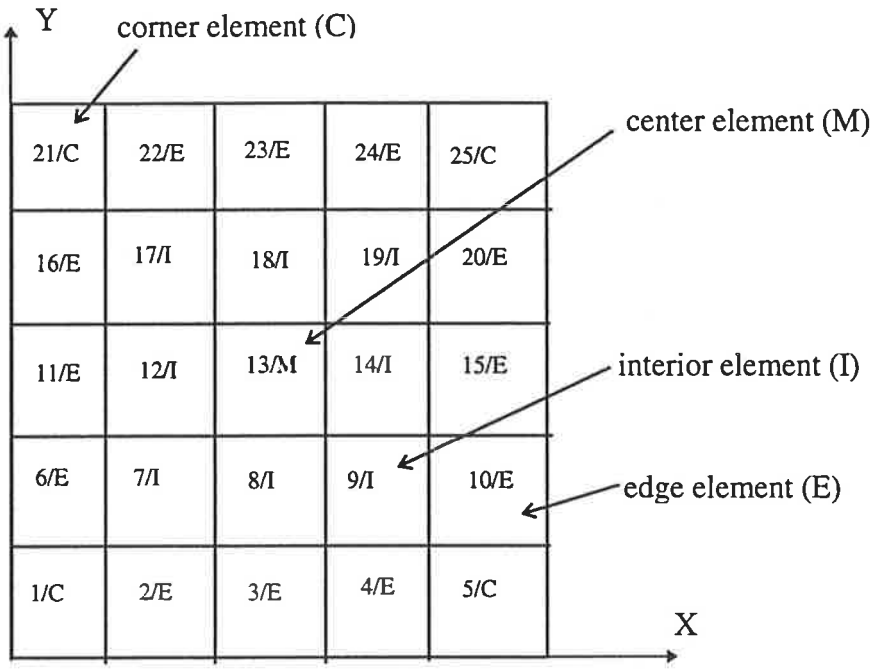

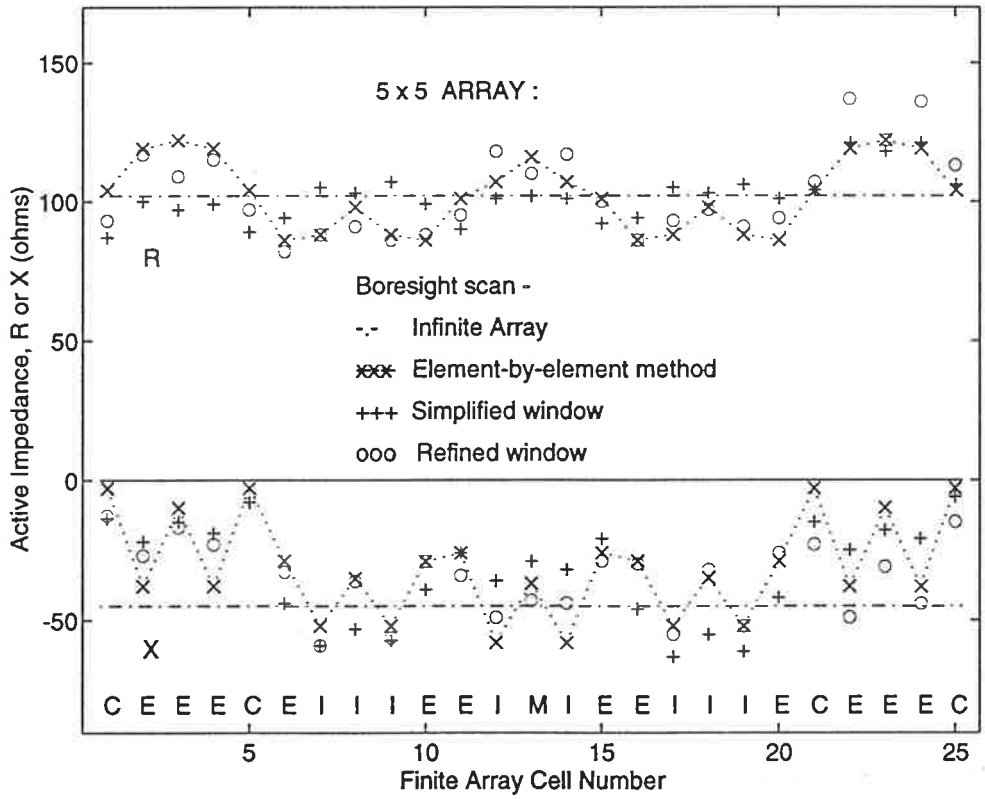

Figure 7.3 : Active impedance of elements in a 5 x 5 array of horizontal metal strips above an infinite ground plane in the boresight scan angle; $b = 0.6\lambda$, $d = 0.5\lambda$, $l = 0.44\lambda$, $w = 0.05l$, $h = 0.5l$, $n_x = 21$ segments.

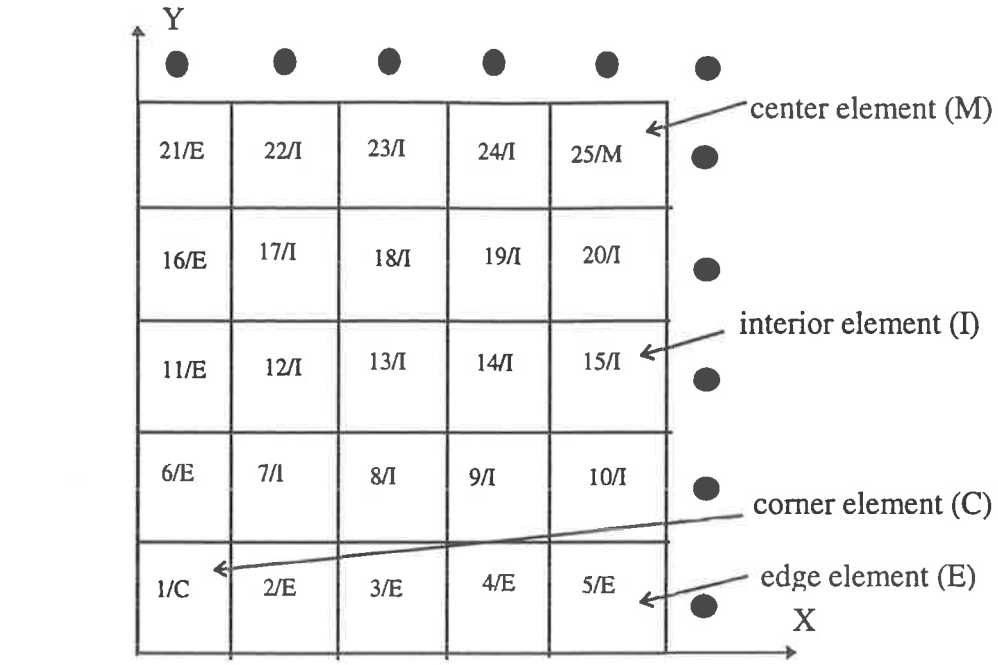

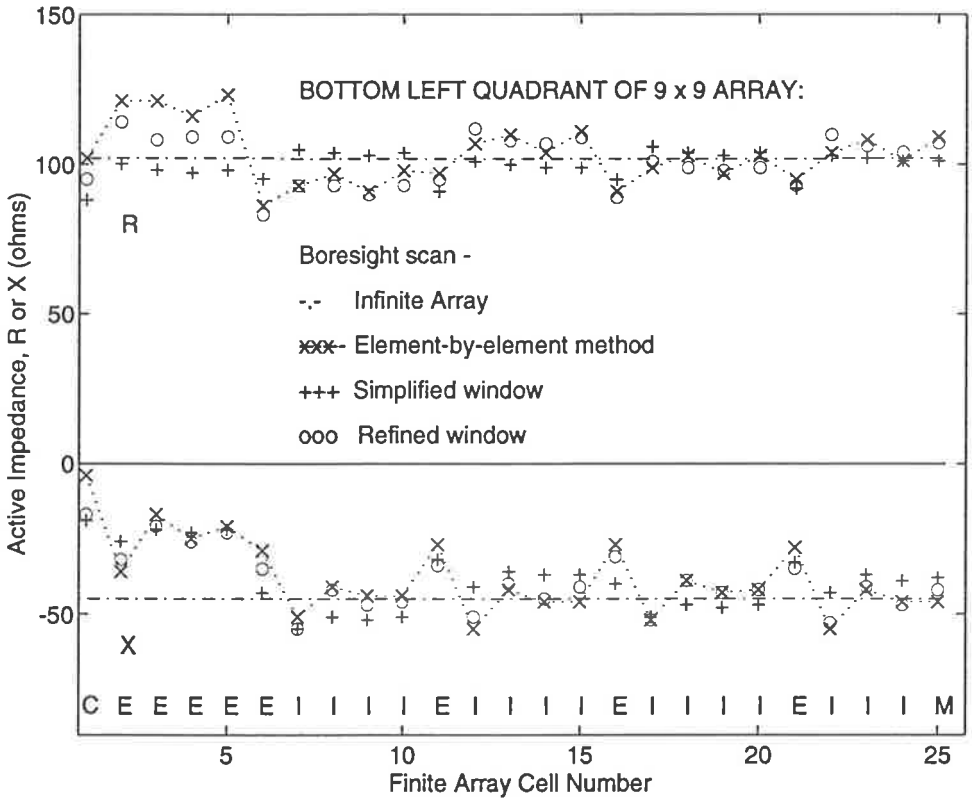

Figure 7.4 : Active impedance of elements in bottom left quadrant of a 9 x 9 array of horizontal metal strips above an infinite ground plane in the boresight scan angle; $b = 0.6\lambda$, $d = 0.5\lambda$, $l = 0.44\lambda$, $w = 0.05l$, $h = 0.5l$, $n_x = 21$ segments.

The following observations can be made from the graphs given in Figures 7.2, 7.3 and 7.4:

- The infinite array model can only provide a uniform active impedance value for all elements and so is shown to be unsatisfactory in many instances.

- The Element-by-Element results reveal that the values of element active impedances fall about the infinite array value. These results are used to test the windowing technique.

- The results obtained with the Generalised Periodic Green's Function - Spectral Windowing technique using the simplified and refined spectral windows are both in good agreement with those of obtained using the Element-by-Element method. In almost all cases, the differences in values between the data points of the two methods do not exceed 10% of absolute values of the data. In particular, the following more detailed observations can also be made from the graphs:

    - It is noted that for about 50% of the data points, the refined spectral window results show a closer agreement with the Element-by-Element results than those obtained with the simplified spectral window. Conversely, the simplified spectral window results are in closer agreement with the Element-by-Element results for less than 10% of the data points. For the remainder of the data points, there is no appreciable difference between the simplified and refined spectral window results. It can be concluded that the results obtained with the Generalised Periodic Green's Function - Spectral Windowing technique exhibit a degree of convergence with the use of a refined spectral window to incorporate the effect of the currents into the analysis.

    - The size of the array analysed does not appear to affect the accuracy of the results obtained using the Generalised Periodic Green's Function - Spectral Windowing technique. However it is noted that for a small array such as a 3 x 3 array, the width of the main beam is too broad for the array to be useful in practice.

    - It appears that the results obtained using the Generalised Periodic Green's Function - Spectral Windowing technique are generally more accurate for the elements in the central region of the finite array and less accurate for the elements at the periphery.

Design Example 2: Inter-element spacing of 0.5λ in E-plane

The second design example is a 5 x 5 element metal strip dipole array with inter-element spacings of $b = 0.5\lambda$ and $d = 0.5\lambda$. Two cases are analysed for a metal strip dipole at a height $h = 0.25\lambda$ above the ground plane: a length of $l = 0.375\lambda$ and $l = 0.44\lambda$. The latter case has a stronger mutual coupling between the elements than the former case. Each metal strip of the array is of width $w = 0.05l$. The cell number and cell type designations are the same as those given in Figure 7.3. Figures 7.5 and 7.6 show the active impedance results at boresight scan angle.

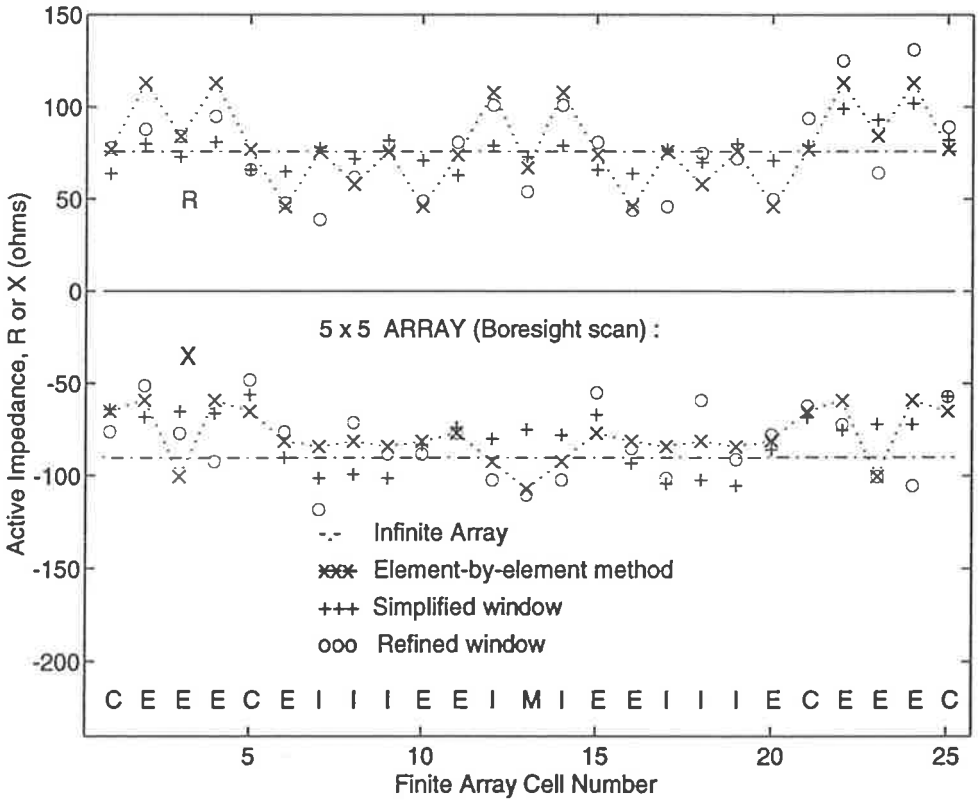

Figure 7.5 : Active impedance of elements in bottom left quadrant of a 5 x 5 array of horizontal metal strips above an infinite ground plane in the boresight scan angle; $b = 0.5\lambda$, $d = 0.5\lambda$, $l = 0.375\lambda$, $w = 0.05l$, $h = 0.25\lambda$, $n_x = 21$ segments.

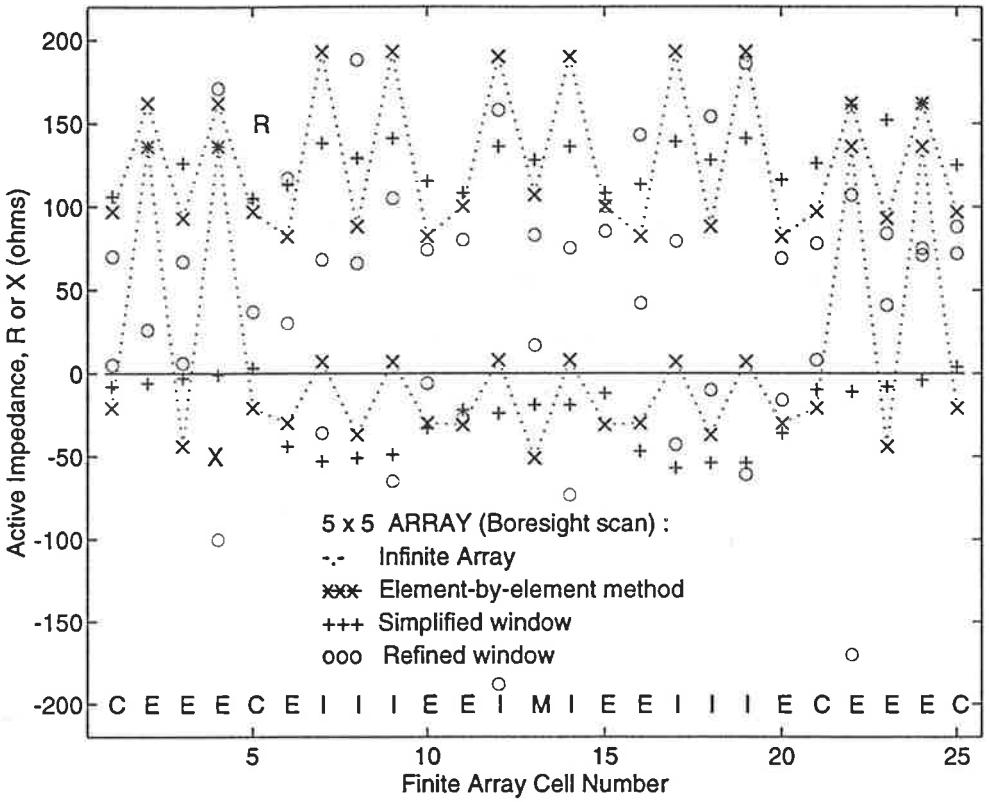

Figure 7.6 : Active impedance of elements in bottom left quadrant of a 5 x 5 array of horizontal metal strips above an infinite ground plane in the boresight scan angle; $b = 0.5\lambda$, $d = 0.5\lambda$, $l = 0.44\lambda$, $w = 0.05l$, $h = 0.5l$, $n_x = 21$ segments.

For the example at hand, the inter-element spacing $b = 0.5\lambda$, whereas in Design Example 1 the spacing is $b = 0.6\lambda$. A closer inter-element spacing potentially increases the mutual coupling between the elements. Of the two cases considered in this design example, Figure 7.5 shows that the results using the Generalised Periodic Green's Function - Spectral Windowing technique for the shorter metal strip length $l = 0.375\lambda$ are in good agreement with those using the Element-by-Element method. In the case of stronger mutual coupling between elements caused by a longer metal strip length $l = 0.44\lambda$, the results show poor agreement with those of the Element-by-Element method. Therefore, it is noted that the Generalised Periodic Green's Function - Spectral Windowing technique may produce inaccurate results for finite arrays in which there is strong mutual coupling between elements.

Design Example 3: Variation of active impedance with scan angle for significant elements

Having seen the accuracy of the Generalised Periodic Green's Function - Spectral Windowing technique for two design examples in which the results are presented only at the boresight scan angle, an analysis of the active impedance variation of a finite array as a function of scan angle is considered next. It has been found that the accuracy of the technique at various scan angles is not sensitive to the size of the array considered. Therefore, indicative results are presented in Figures 7.7 to 7.11 for the E- and H-plane scans of the center element, a corner element and an edge element of a 9 x 9 array of horizontal metal strips having the same element and lattice dimensions as for Design Example 1.

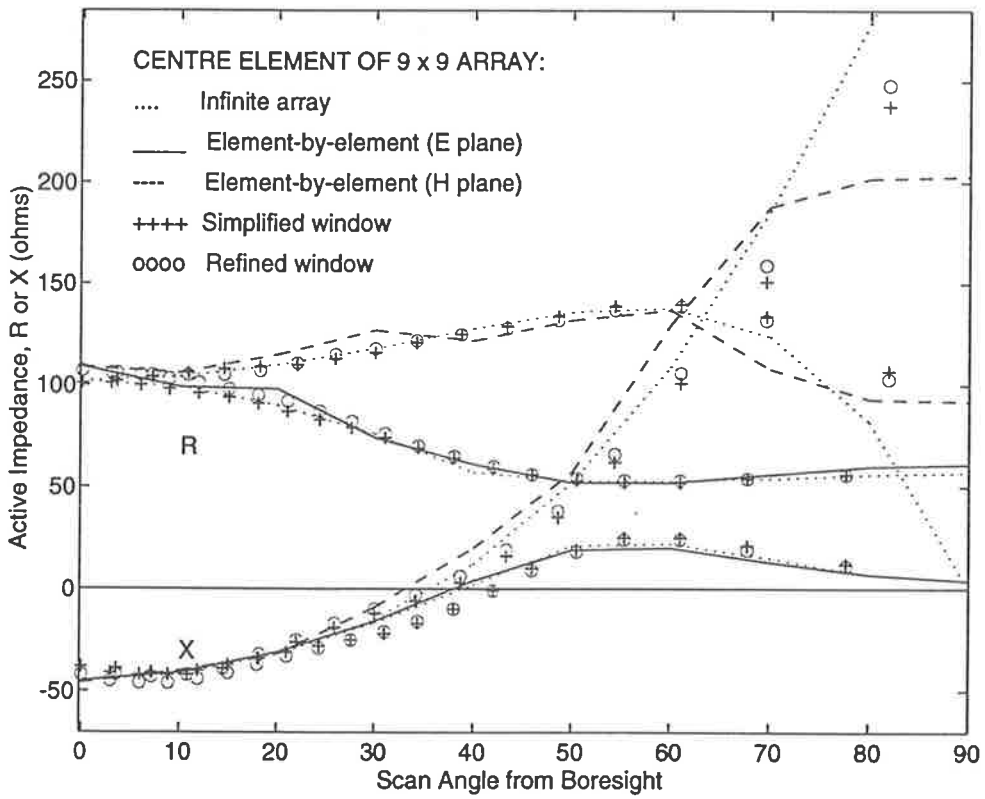

Figure 7.7 : Active impedance as a function of scan angle in the E- and H-plane for the centre element of a 9 x 9 array of horizontal metal strips above an infinite ground plane; $b = 0.6\lambda$, $d = 0.5\lambda$, $l = 0.44\lambda$, $w = 0.05l$, $h = 0.5l$, $n_x = 21$ segments.

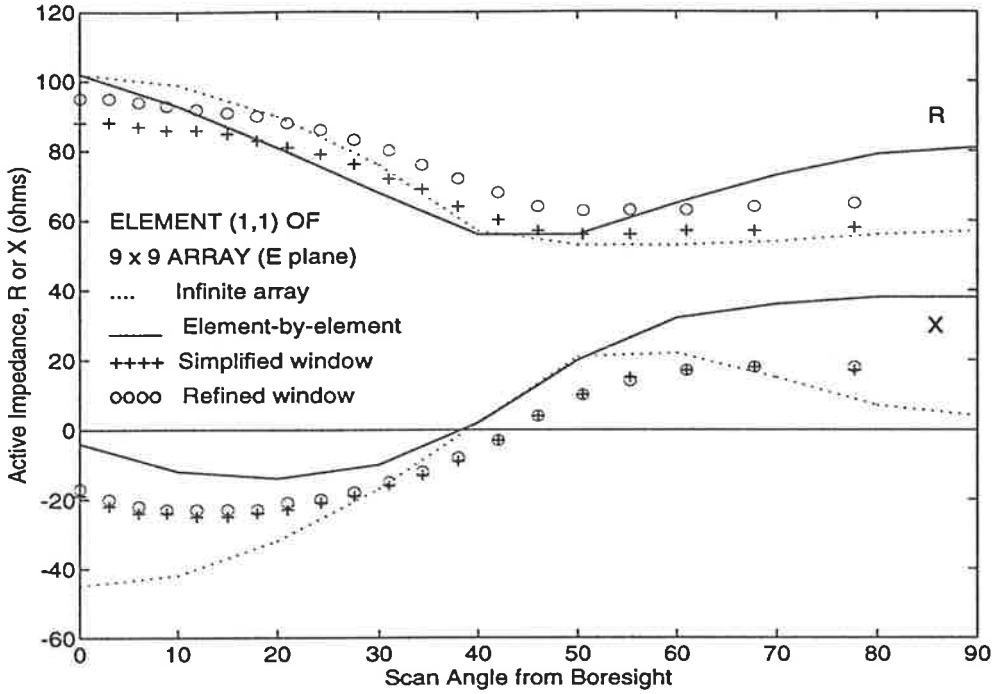

Figure 7.8 : Active impedance as a function of scan angle in the E-plane for a corner element of a 9 x 9 array of horizontal metal strips above an infinite ground plane; $b = 0.6\lambda$, $d = 0.5\lambda$, $l = 0.44\lambda$, $w = 0.05l$, $h = 0.5l$, $n_x = 21$ segments.

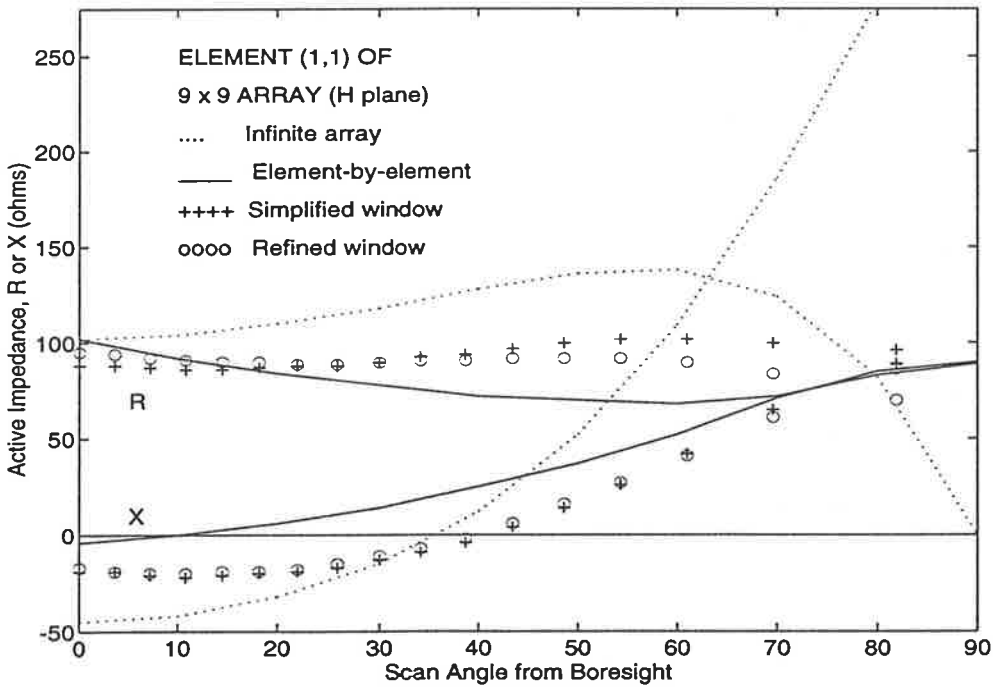

Figure 7.9 : Active impedance as a function of scan angle in the H-plane for a corner element of a 9 x 9 array of horizontal metal strips above an infinite ground plane; $b = 0.6\lambda$, $d = 0.5\lambda$, $l = 0.44\lambda$, $w = 0.05l$, $h = 0.5l$, $n_x = 21$ segments.

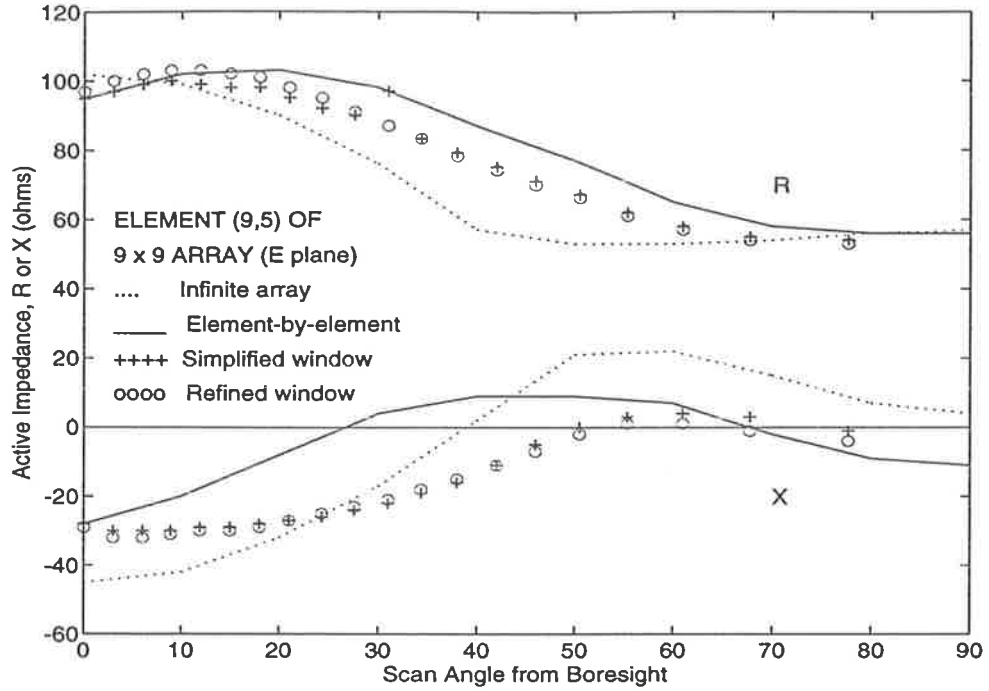

Figure 7.10 : Active impedance as a function of scan angle in the E-plane for an edge element of a 9 x 9 array of horizontal metal strips above an infinite ground plane; $b = 0.6\lambda$, $d = 0.5\lambda$, $l = 0.44\lambda$, $w = 0.05l$, $h = 0.5l$, $n_x = 21$ segments.

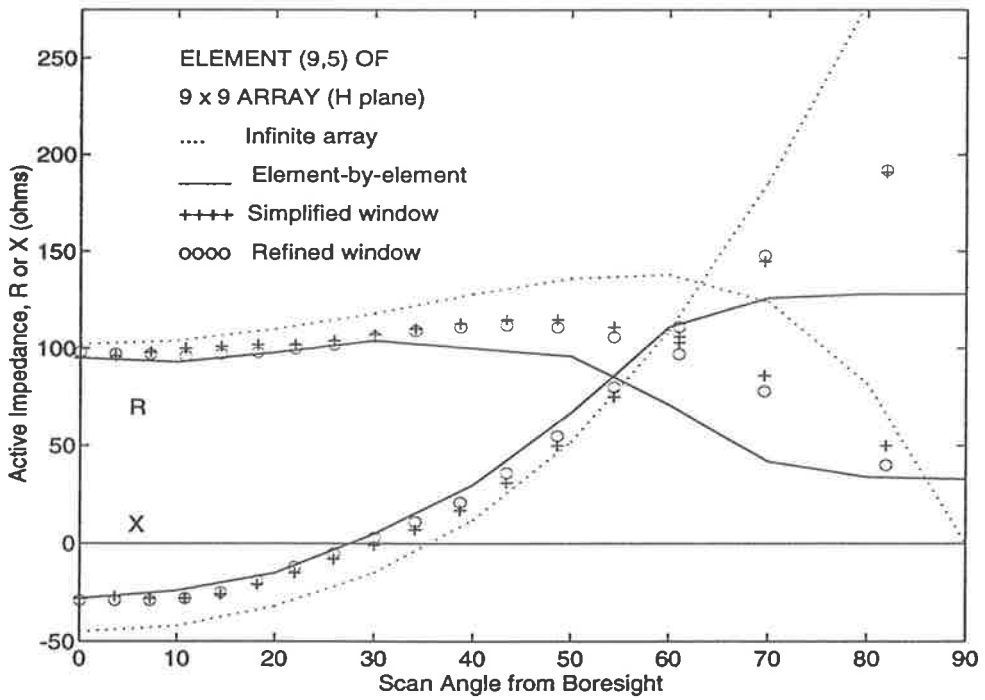

Figure 7.11 : Active impedance as a function of scan angle in the H-plane for an edge element of a 9 x 9 array of horizontal metal strips above an infinite ground plane; $b = 0.6\lambda$, $d = 0.5\lambda$, $l = 0.44\lambda$, $w = 0.05l$, $h = 0.5l$, $n_x = 21$ segments.

Based on the graphs in Figures 7.7 to 7.11, the following observations can be made:

- The infinite array curves, which convey no position dependent information, indicate the presence of a grating lobe in the E-plane, as the active resistance does not become zero at the grazing scan angle. The grating lobe has been calculated to emerge into visible space for a scan angle of 42°. In the H-plane, there are no grating lobes so that the active resistance becomes zero and the active reactance has a large value at the grazing scan angle.

- The Element-by-Element method results show that for the centre element of the 9 x 9 array, the variation of active impedance with scan angle is similar to that of the infinite array except at large scan angles in the H-plane. The variations are significantly different for the corner and edge elements, especially for the active reactance term. The active resistance obtained using the Element-by-Element method does not become zero at the grazing scan angle even when there is no grating lobe emerging in the corresponding scan plane. Although this information may not be of significant practical use, it shows that power can be propagated away from a finite array at the grazing scan angle.

- The results obtained using the Generalised Periodic Green's Function - Spectral Windowing technique are in good agreement with those obtained using the Element-by-Element method, with the exception of the active reactance for the corner element. However, even with this exception, the trend of the curves is similar to those obtained by the Element-by-Element method.

In summary, the graphs in Figures 7.7 to 7.11 show that the Generalised Periodic Green's Function - Spectral Windowing technique is able to predict with good accuracy the active impedance variation with scan angle for a finite metal strip dipole array. The results suggest that this technique is suitable for application to engineering design and overall performance assessment of finite arrays. The numerical efficiency of the technique is evident from the computational resources used to obtain the data presented above compared with the resources required by the Element-by-Element method, as shown in Table 7.1. In comparing the computation time taken by the two methods, it should be noted that in the case of the Element-by-Element method, the active impedance for all the

elements of the finite array are simultaneously calculated by the computer program for each scan angle. In the case of the Generalised Periodic Green's Function - Spectral Windowing technique, the active impedance for a range of scan angles are simultaneously calculated by the computer program for each element of the finite array at a time. Hence an average CPU time per scan angle for each element is used as a basis for the comparison.

Method Used	Array Size	Computer Storage Used	Computer Memory Used	CPU Time Used
Simplified Spectral Window	Any size	21.2 MBytes	1.2 MBytes	17sec for 1 element at 11 scan angles (1.5sec / element / scan angle)
Refined Spectral Window	9 x 9	21.2 MBytes	1.9 MBytes	90.5sec for 9 elements at 11 scan angles (0.9sec / element / scan angle)
Element-by-Element Method	3 x 3	137 MBytes	1.7 MBytes	12sec for 9 elements at 1 scan angle (1.3sec / element / scan angle)
Element-by-Element Method	5 x 5	141 MBytes	9.3 MBytes	145sec for 25 elements at 1 scan angle (5.8sec / element / scan angle)
Element-by-Element Method	9 x 9	183 MBytes	58.8 MBytes	31min for 81 elements at 1 scan angle (23sec / element / scan angle)

Table 7.1 : Comparison of computational resources required by the Generalised Periodic Green's Function - Spectral Windowing technique with Simplified and Refined Spectral Window, and the Element-by-Element method in calculating the active impedances for a finite array.

It is apparent from Table 7.1 that even for a simple element geometry of a horizontal metal strip, the computational resources required by the Element-by-Element method for the analysis of large finite arrays makes it inconvenient for implementation on desktop

computers. For a more complicated element geometry involving metallic and substrate parts, the same computational resources described in Table 7.1 would probably enable the analysis of an array with no more than a few elements using this method. In comparison, the computational resources required by the Generalised Periodic Green's Function - Spectral Windowing technique using the Simplified Spectral Window are relatively more manageable on desktop computer implementation, and more importantly, are independent of the array size. If the Refined Spectral Window is used with the technique, the results for all the elements are made available simultaneously because the currents for all the elements are calculated using the simplified spectral window in the first iteration in order to obtain the refined spectral window.

In summary, the Generalised Periodic Green's Function - Spectral Windowing technique has been described using as an example the analysis of a finite array of horizontal metal strips. It has been shown that except when mutual coupling between the elements is very strong, the accuracy of the technique though not comparable to the Element-by-Element method, is adequate to enable general trends in the element to element impedance characteristics of the finite array to be observed. The use of the Refined Spectral Window does not result in a significant improvement in the accuracy of the technique. However, it does demonstrate a degree of convergence of the results even when the effect of the currents are incorporated into the analysis by means of the refined spectral window. In this sense, use of the Refined Spectral Window provides an additional basis for confidence to be placed in the reliability of the technique.

In the next two sections, the Generalised Periodic Green's Function - Spectral Windowing technique is extended to the analysis of finite arrays of metal strips with coplanar strip feedlines, and to finite arrays of metal strips supported on a dielectric substrate. These two structures are known to exhibit feedline and substrate induced blindness conditions respectively, at certain scan angles in the infinite array environment. In addition to demonstrating the applicability of the technique in modelling finite arrays of such structures, the technique is used to investigate the impedance characteristics of the finite array in the vicinity of the scan blindness angles.

7.4 Finite Arrays of Metal Strip Dipoles with Coplanar Strip Feedlines

In Section 7.3, the Generalised Periodic Green's Function - Spectral Windowing technique for obtaining finite array characteristics from infinite array data was illustrated using a formulation for a metal strip dipole element. In this section, the technique is implemented for a finite array of metal strip dipoles with coplanar strip feedlines. The geometry of the metal strip dipole element with coplanar strip feedline operating within an infinite array environment was presented in Section 5.4. It was shown in that analysis that this structure has a feedline induced scan blindness in the E-plane. The objective of this section is to describe the behavior of the structure operating in a finite array environment, especially at scan angles in the vicinity of the infinite array scan blindness angle. Table 7.2 below places this section's discussion into context in relation to the analyses of similar geometries which have been presented in the earlier sections of this thesis.

Infinite array of metal strip dipoles without feedlines: • Presented in Section 4.2 • No scan blindness • Tested against Chang's results [59]	*Finite array of metal strip dipoles without feedlines:* • Presented in Section 7.3 • No scan blindness • Tested against the Element-by-element method evaluation
Infinite array of metal strip dipoles with feedlines: • Presented in Section 5.4 • Feedline induced scan blindness • Tested against Schuman's results [29]	*Finite array of metal strip dipoles with feedlines:* • To be presented in this section • Behavior in vicinity of scan blindness angle to be discussed here

Table 7.2 : Configurations of the metal strip dipole element and array structure analysed in this thesis.

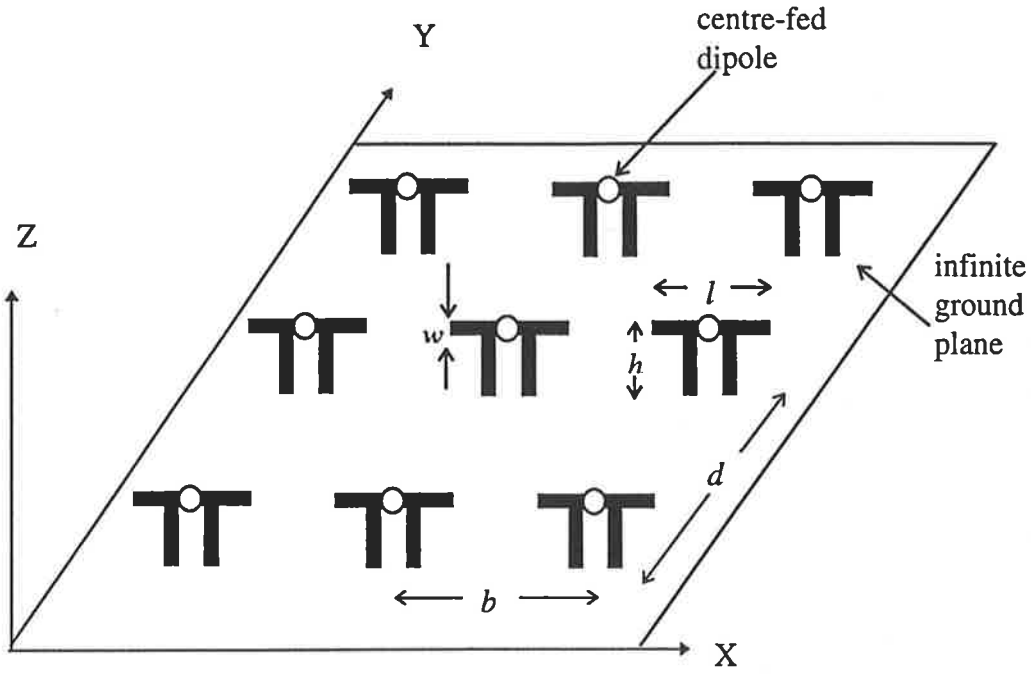

Figure 7.12 : Geometry for a finite array of centre-fed metal strip dipoles with coplanar strip feedline above an infinite ground plane.

Figure 7.12 shows the geometry of a finite array of metal strip dipoles extending above an infinite ground plane. Each metal strip is fed by a coplanar stripline, and the excitation of the source at the base of the feedline is translated to the feed point of the metal strip and modelled as delta-gap voltage. A structure having this geometry is analysed for a metal strip length $l = 0.375\lambda$ and width $w = 0.055\lambda$, positioned at a height of $h = 0.25\lambda$ above the ground plane. The inter-element spacings of the array in both the x and y dimensions are chosen to be $b = d = 0.5\lambda$ so as to preclude the emergence of a grating lobe into visible space for all scan angles. The variation of active impedance with scan angle is given Figure 7.13 for the infinite array, and the centre element of 25 x 25, 15 x 15 and 5 x 5 arrays. No attempt was made to analyse this structure using the Element-by-Element method as the resultant size of the Moment Matrix would be too large for implementation on the desktop computer used in this research.

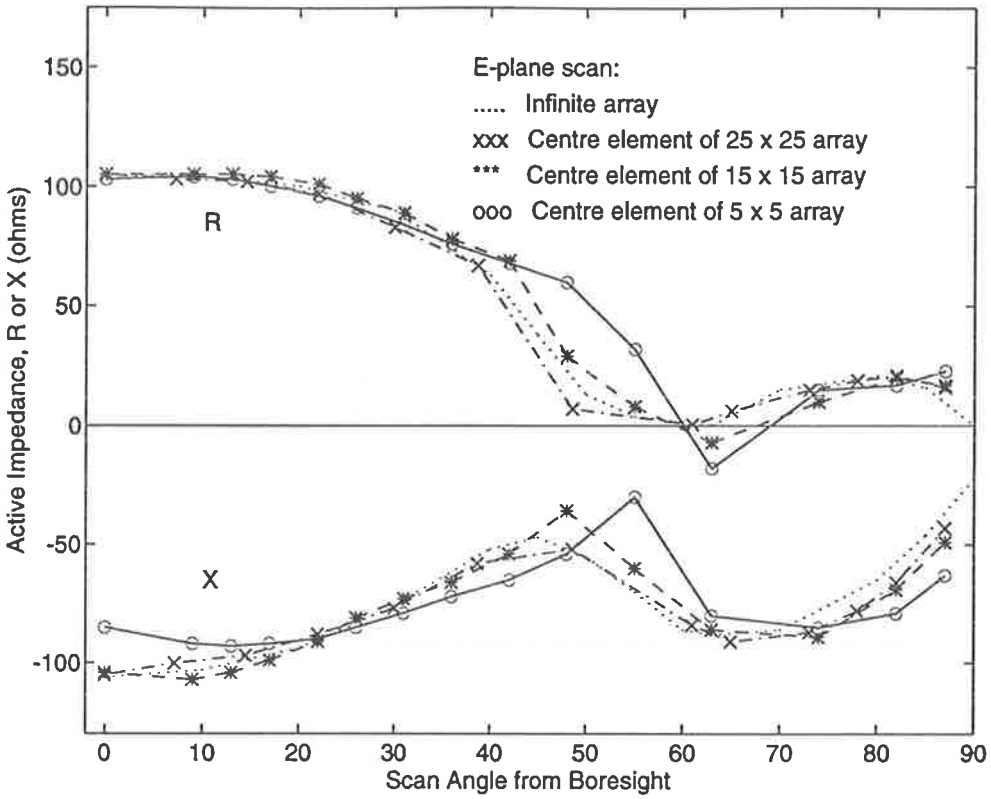

Figure 7.13 : Active impedance as a function of scan angle in the E-plane for infinite and finite arrays of metal strip dipoles with coplanar strip feedlines; $l = 0.375\lambda$, $w = 0.055\lambda$, $h = 0.25\lambda$ and inter-element spacings $b = d = 0.5\lambda$, $n_x = 5$, $n_z = 4$.

As shown in Figure 7.13, the active impedance for the infinite array indicates a feedline induced scan blindness at about 63° in the E-plane. The variation of active impedance with scan angle for the centre element of a 25 x 25 array is almost identical to that of the infinite array, except for scan angles in the vicinity of the grazing angle. In the case of the infinite array, the active resistance becomes zero at the grazing scan angle. This does not occur for the finite array, since some power is propagated away from array at the grazing scan angle. In the case of the 15 x 15 array, for angles up to about 50° from boresight, the variation of active impedance with scan angle is again similar to that for the infinite array. For larger angles, a deviation from the infinite array curve is noticed. Furthermore, a negative active resistance is observed close to the feedline induced scan blindness angle for the infinite array. This implies that near the scan blindness angle, the centre metal strip of the 15 x 15 array is actually delivering power back to its generator. Since the total power is conserved, power is being transferred from other radiating elements of the array into this centre metal

strip at a scan angle of about 63°. Again, the active resistance is non-zero at the grazing scan angle. For the centre element of the 5 x 5 array, the same phenomenon leading to a negative resistance near to the infinite array scan blindness angle and non-zero active resistance at the grazing angle are observed.

So far, the discussion has focussed only on the centre element of the finite array. Figure 7.14 shows the magnitudes of the active reflection coefficients across the centre row of elements.

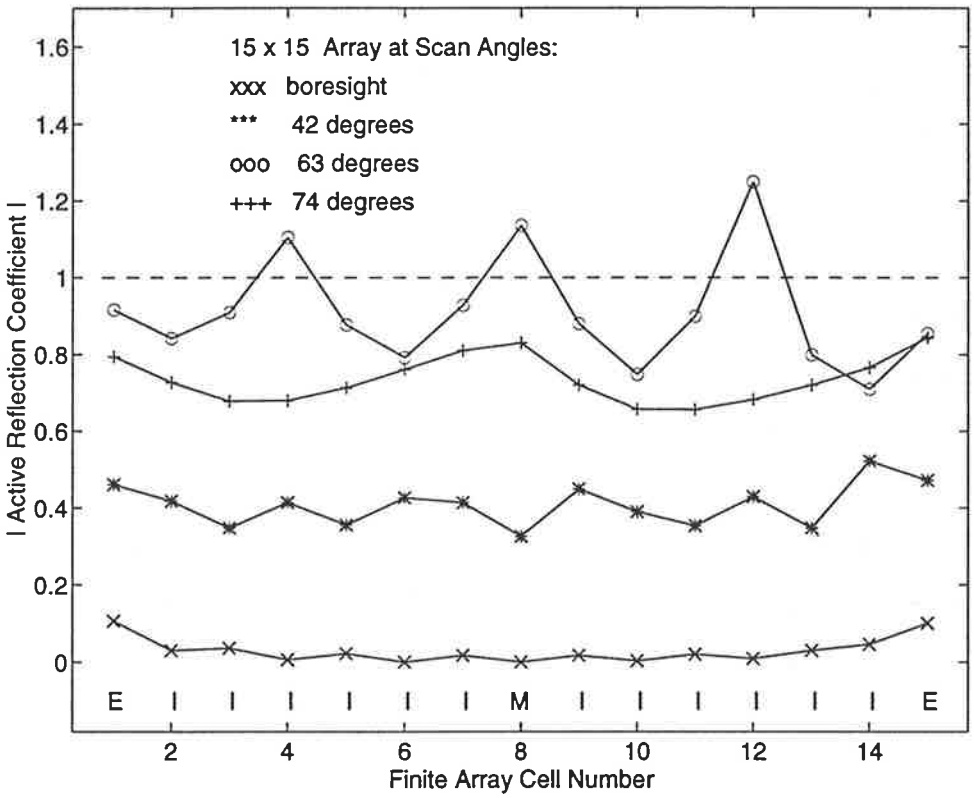

Figure 7.14 : Magnitude of active reflection coefficient for elements in the centre row of a 15 x 15 array of metal strip dipoles with coplanar strip feedlines, at various scan angles in the E-plane; $l = 0.375\lambda$, $w = 0.055\lambda$, $h = 0.25\lambda$ and inter-element spacings $b = d = 0.5\lambda$.

In Figure 7.14, it is noted that the centre element in the centre row is also the centre element of the entire finite array. Each element is designated in Figure 7.14 as either an edge (E), interior (I) or centre (M) element of the array. The magnitudes of the active reflection coefficients are normalised to the centre element of the array which is assumed to be conjugate matched at boresight scan. At the boresight scan angle, the values of the

active reflection coefficients are symmetrical about the centre element and small, suggesting a well-matched condition for the centre element, but a slightly mismatched condition for the other elements. Near the scan blindness angle for the infinite array which is predicted to be 63°, the active reflection coefficient values are near unity and in some cases greater than unity. At this scan angle, the elements with less than unity reflection coefficients are transferring power to those elements with greater than unity reflection coefficients. Under these conditions, the antenna array is expected to be ineffective. At the other scan angles (42° and 74°), the active reflection coefficients are still high, but remain less than unity.

In summary, the graphs in Figures 7.13 and 7.14 indicate that irrespective of the size of the finite array, the variation of active impedance with scan angle up to 30° from boresight at the centre element is similar to that of the infinite array. At larger scan angles for the centre element and at all scan angles for elements located on the periphery of the finite array, the active impedance variation with scan angle shows a deviation from that of the infinite array case. The technique developed in this chapter can be used to predict these deviations. The results also indicate the necessity to predict element active impedances of the finite array in the vicinity of the infinite array's feedline induced scan blindness angle, where power being transferred between elements of the finite array is likely to degrade the performance of the array. The numerical model developed for this analysis requires 34.9 Mbytes of computer storage, 3.1 Mbytes of computer memory and 37 seconds to calculate the active impedance for 10 scan angles on a desktop computer, indicating a high computational efficiency for the algorithm developed here.

7.5 Finite Arrays of Metal Strip Dipoles Supported on a Dielectric Substrate

In Sections 7.3 and 7.4, the Generalised Periodic Green's Function - Spectral Windowing technique was used to analyse a finite array of metal strip dipoles with idealised feeds and

with coplanar strip feedlines. In this section, the technique is extended to the analysis of a finite array metal strip dipoles supported on a dielectric substrate which is the structure shown in Figure 6.1 but truncated to a finite size in the lateral dimensions except for the ground plane. This structure is analysed here because comparative results exist. Before the results of the model for this structure are compared with data available in [32], it is noted that there are differences in the technique of analysis used in [32] and in this research. These differences are given in Table 7.3.

Model Characteristics	Dielectric Slab Green's Function and Element-by-Element Method [32]	Generalised Periodic Green's Function - Spectral Windowing Technique
Unit cell model	Single current element on an infinite slab dielectric substrate	Collection of surface conduction and volume polarisation current elements within the unit cell
Unit cell Green's function	Spectral Green's function specific to the infinite dielectric slab	Same Generalised Hybrid Periodic Green's function for metal strip and substrate
Model of dipole	Wire with axial currents only	Metal strip with two-dimensional currents
Basis functions	Piecewise sinusoid	Pulse
Testing functions	Galerkin method	Point testing
Finite array obtained by:	Element-by-Element method	Simplified spectral window
Finite array structure representation	Finite array of printed dipoles on an infinite slab dielectric substrate, above an infinite ground plane	Finite array of printed dipoles on a finite slab of dielectric substrate defined by the boundary of the unit cells, above an infinite ground plane

Table 7.3 : Differences between the modelling technique employed in [32] and the method used in this analysis.

Of the differences listed in Table 7.3, the most important is the finite array structure represented by the two models. In [31], the substrate is not modelled using basis functions but as an infinite dielectric slab environment. Hence the finite nature of the array is confined to only the dipoles; both the dielectric substrate and ground plane are still infinite in extent. For the technique developed in this chapter, both the metal strips and substrate are modelled using basis functions, but the ground plane is not. Therefore the Fourier windowing procedure results in truncation of both the size of the metal strip array and the size of the substrate, leaving only the ground plane as infinite. As mentioned in Section 7.1, the ground plane in this analysis is assumed to be infinite so that image theory applies. However, a finite ground plane can be incorporated into the analysis if desired [92], though at the cost of additional computational overheads.

The element and lattice dimensions used in this analysis are the same as those used in Design Example 1 in Section 6.2.3. The elements of the infinite array Moment Matrix obtained in Section 6.2.3 are used in the convolution with the simplified spectral window to obtain the finite array data. Based on the infinite array boresight active impedance of Z_b = 78.7 + j11.7Ω, the magnitudes of the active reflection coefficients for the centre element of a 19 x 19 array at various scan angles are obtained and plotted in Figure 7.15 below. The graph shows that the infinite array has a substrate induced scan blindness at about 47° scan angle, as indicated by the near unity magnitude of the active reflection coefficient.

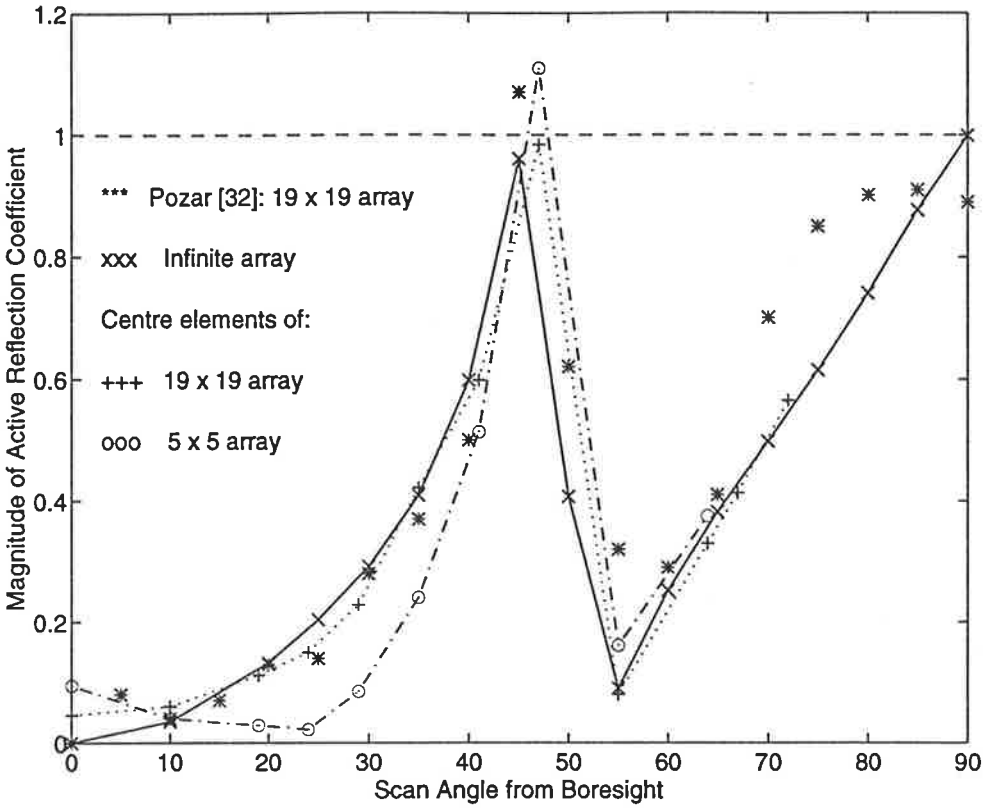

Figure 7.15 : Magnitude of active reflection coefficient as a function of scan angle in the E-plane for the infinite array and centre element of finite arrays of metal strip dipoles supported on a single slab dielectric substrate; $l = 0.39\lambda$, $b = d = 0.5\lambda$, $h = 0.19\lambda$, $w = 0.02\lambda$, $\varepsilon_0 = 2.55$, $n_x = 7$, $n_y = 5$, $n_z = 3$, $Z_b = 78.7 + j11.7\Omega$.

For the centre element of the 19 x 19 array, the active reflection coefficient indicates a slight mismatch to that of the infinite array at boresight scan; otherwise, the curve is similar to that of the infinite array. Noting the difference in the two techniques of analysis, Pozar's results [32] for a 19 x 19 array shows a greater than unity active reflection coefficient for the centre element. Using the technique developed in this chapter, the condition of greater than unity active reflection coefficient is observed for the centre element of the 5 x 5 array but not for the 19 x 19 array. As for the model in Section 7.3, this suggests that in the vicinity of the substrate induced scan blindness angle of the infinite array, power is being transferred between elements of the finite array.

The active impedance of elements across the centre row of the 19 x 19 array at different scan angles is given in Figure 7.16 below.

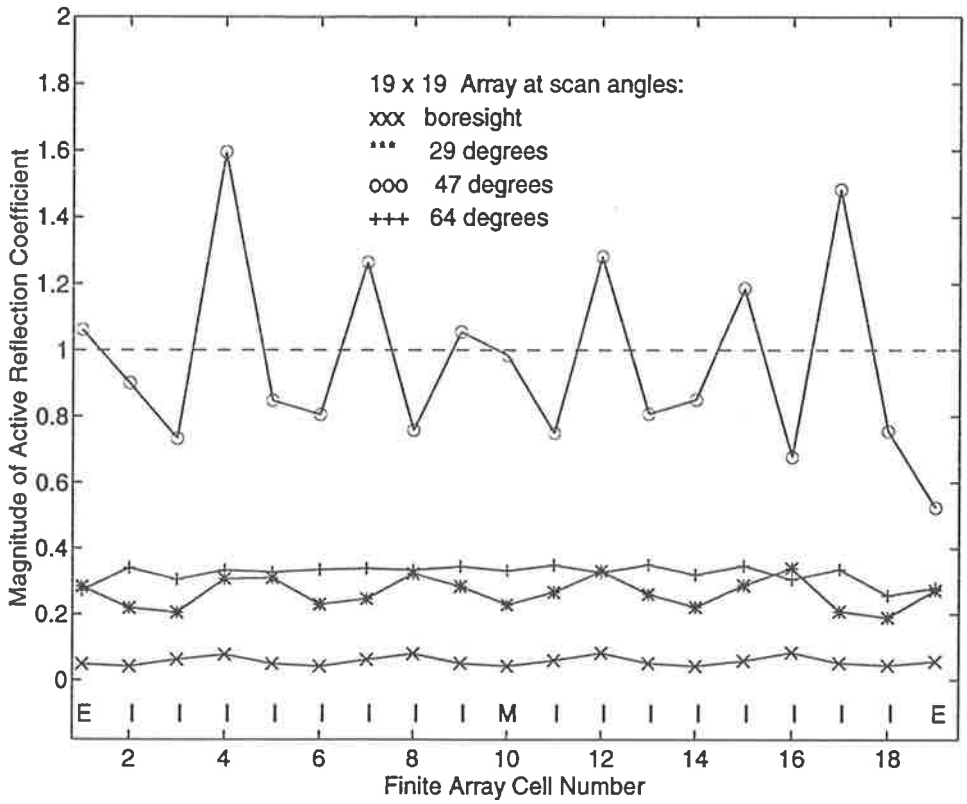

Figure 7.16 : Magnitude of active reflection coefficient for elements along the centre row of a 19 x 19 array of metal strip dipoles supported on a finite slab dielectric substrate, for different scan angles in the E-plane; $l = 0.39\lambda$, $b = d = 0.5\lambda$, $h = 0.19\lambda$, $w = 0.02\lambda$, $\varepsilon_0 = 2.55$, $n_x = 7$, $n_y = 5$, $n_z = 3$, $Z_b = 78.7 + j11.7\Omega$.

As indicated by the symbols above the x axis of the graph, all the elements along the centre row are interior elements (I) except for elements 1 and 19 which are edge elements (E) and element 10 which is the centre element of the row (M) and also the centre element of the entire array. At the boresight scan angle, the reflection coefficient values are near zero and symmetrical about the centre element, indicating a well-matched condition. The small variation between the reflection coefficient values of adjacent elements at the boresight scan angle is in contrast to that for the finite array of metal strip dipoles analysed in Section

7.3. This indicates that the relatively higher Q of the structure with substrate results in small variations in active impedance between the elements of the array. At 47° scan angle, which corresponds to the substrate induced scan blindness condition for the infinite array, the active reflection coefficient values are highly asymmetrical about the centre element and close to unity, indicating a highly mismatched condition. A number of elements are observed to have a greater than unity active reflection coefficient, indicating that power is being transferred between elements of the array at this scan angle. Hence the finite array is not expected to perform effectively at this scan angle. At other scan angles away from 47°, the active reflection coefficient values are lower and exhibit smaller variations between adjacent elements, thus indicating a better matched condition than at 47° scan angle.

As indicated in Section 7.1, the analysis of finite arrays is computationally more demanding than infinite array analysis. The computer resources required by the finite array model developed in this section, as compared to those for solving the associated infinite array problem, are given in Table 7.4.

Technique	Computer Storage	Computer Memory	Computer CPU Time
Infinite array	33.5 MBytes	4.2 MBytes	42.5 s / scan angle
Finite array	120.2 MBytes	44 MBytes	10.5 min for 12 scan angles (52 s / scan angle)

Table 7.4 : Comparison of computational resources required for the Generalised Hybrid Periodic Green's Function technique for analysis of infinite arrays, against the same technique with Fourier Windowing for analysis of finite arrays.

It is apparent from Table 7.4 that the finite array technique based on the Generalised Hybrid Periodic Green's Function technique coupled with Fourier Windowing requires about four times as much computer storage and ten times as much computer memory as the corresponding infinite array technique of analysis. However, it has been demonstrated that the computational resources required for both the finite and infinite array techniques can be

adequately accommodated on a typical desktop computer in use today. Hence there is scope for developing this technique into a numerically efficient computer software for the analysis and engineering design of typical microstrip antenna arrays on desktop computers.

7.6 Summary

The numerical analysis of finite arrays is computationally more demanding than that for infinite arrays because the current distributions on the elements are not identical. The Element-by-Element approach of modelling a finite array is potentially accurate, but normally results in a very large Moment Matrix which makes implementation on a desktop computer inconvenient except in the case of small arrays with simple element geometries. In the last decade, a number of advances have been made in analysing a finite array using an infinite array approach. Of the techniques considered in this chapter, Ishimaru's spectral windowing approach appears to be the most promising for the analysis of finite microstrip arrays and has been chosen to be developed into the Generalised Periodic Green's Function - Spectral Windowing technique described in this thesis. The uniqueness of the technique is that it is based on a generalised periodic Green's function which is not constrained by the element geometry.

In this chapter, the spatial and spectral forms of the Generalised Periodic Green's Function for a finite array are derived using an Element-by-Element approach. In the case of the spectral form, it is shown that the Green's function is a convolution of the Generalised Spectral Periodic Green's Function for the infinite array with a Spectral Window Function which is the Fourier transform of the aperture current distribution of the finite array. In both forms, the expression for the Green's function takes account of the periodicity, finite nature, mutual coupling between elements and edge effects of the finite array. Based on an insight of the properties of the generalised periodic Green's function described in Sections 3.4 and 4.3.2, a numerically more efficient hybrid form of the periodic Green's function is chosen to be developed into a technique of analysis of finite arrays.

A Simplified Spectral Window function is used for the convolution by assuming similar values of the element currents. However, a new iterative procedure is developed in which the equivalent currents of the elements obtained using the simplified spectral window are used to redefine a Refined Spectral Window. Using a numerical example, it is shown that the use of the refined spectral window can be used to provide confidence that the finite array results are accurate. It is shown that the elements of the finite array Moment Matrix are conveniently evaluated by means of a convolution of the spectral window function with the elements of the infinite array Moment Matrix. The convolution process is efficiently carried out by sampling the infinite array results at scan angles within a periodic rectangle of the grating lobe lattice and evaluating the convolution using a Fast Fourier Transform.

Design examples are given to illustrate the modelling procedure and the results indicate that the technique is sufficiently accurate in predicting the active impedance characteristics of the elements of a finite array at various scan angles provided that the mutual coupling between the elements is not too strong. A comparison indicates that the Element-by-Element method requires on average nearly ten times as much computer storage as well as fifty times as much computer memory, and takes twenty times as long as the Generalised Periodic Green's Function - Spectral Windowing technique to calculate a set of active impedance results for a 9 x 9 array of horizontal metal strip dipoles. The relative computational efficiency of the technique developed in this chapter is even more significant when applied to the analysis of finite microstrip arrays.

The Generalised Periodic Green's Function - Spectral Windowing technique is also applied to the analysis of finite arrays of metal strips with coplanar strip feedlines and substrate supported metal strips. In both cases, the analysis is able to predict the active impedance of the finite array's elements at various scan angles and offers new insight into the behavior of the finite array in the vicinity of the scan blindness angle for the corresponding infinite array, which is not available using an infinite array analysis. Information on computational resources used indicates that the analysis of finite microstrip arrays, though more computationally demanding than that of infinite arrays of simple dipoles, is well within the

capabilities of desktop computers currently available. Therefore the main significance of this chapter is in extending the infinite array technique into a reasonably accurate, flexible and numerically efficient finite array technique which is potentially applicable to the analysis and design of most types of microstrip antenna arrays.

The contributions to research presented in this chapter are:

- The spatial and spectral forms of a Generalised Periodic Green's Function have been derived using the Element-by-Element approach for a finite planar phased array of regularly spaced point sources arranged in a rectangular grid lattice.
- A new Generalised Periodic Green's Function - Spectral Windowing technique has been developed for the analysis of finite arrays of metal strips and microstrip dipoles. The novelty of this technique is that its kernel is the accurate, flexible and numerically efficient Generalised Hybrid Periodic Green's Function.
- An iterative procedure has been developed leading to the evaluation of a Refined Spectral Window used for the convolution, which incorporates the effect of the element currents into the analysis.
- Design examples have been used to illustrate the applicability of the technique for the analysis of finite arrays of metal strip dipoles and microstrip arrays.

CHAPTER 8

Conclusions and Recommendations

8.1 Conclusions

In recent years, the rapid advances in radar and communications systems have resulted in considerable current interest in the development of microstrip phased array antennas of greater complexity to meet modern system specifications. The motivation for the research described in this thesis is the need to be able to accurately evaluate the performance of a wide variety of practical microstrip phased array antennas in an efficient and insightful manner for purposes of engineering design. A numerical technique suitable for the analysis of microstrip arrays should desirably have the capability of predicting the characteristics of the array elements with adequate accuracy for purposes of engineering analysis and design, flexibility to model a variety of array lattice arrangements and element geometries, and computational efficiency to enable its implementation on desktop computers for antennas with realistic detail. Having reviewed some of the common techniques currently available for the analysis of individual microstrip antennas as well as antennas operating in an array environment, it is concluded that although each of the

methods surveyed has certain unique advantages, few are able to fully satisfy all the desirable characteristics described above. A new technique is identified to cater for all the above requirements. The technique makes use of Electric Field Integral Equations for formulating the problem, a Generalised Periodic Green's Function which accounts for the mutual coupling between the array elements but which is unconstrained by the element geometry, and the Method of Moments for its numerical implementation. The technique essentially solves the infinite array problem as a first step and then transforms the infinite array data into a solution of the finite array problem as a subsequent step.

The kernel of the new technique is the Generalised Periodic Green's Function which may be represented in two ways. In the first representation, the periodic Green's function is the vector potential response due to an infinite array of regularly spaced, phase-shifted point sources. Arising out of this approach, the spatial form of the Generalised Periodic Green's Function is derived for both a rectangular and a triangular grid lattice. By representing the phased array of point sources as a current sheet located at the aperture plane of the array, the spectral form of the Generalised Periodic Green's Function is also derived for both a rectangular and a triangular grid lattice. It is recognised that the two forms of the Generalised Periodic Green's Function have uniquely different properties, and these properties have been described in relation to the efficient modelling of antenna arrays. An advantage of the spectral form of the Generalised Periodic Green's function is that it enables closed form evaluation of the integrals whereas for the spatial form, the integration normally has to be evaluated numerically. The spectral form of the generalised periodic Green's function has poor numerical convergence for on-plane interactions whereas the spatial form is poorly convergent for large scan angles. Two other properties of the Generalised Spectral Periodic Green's Function related to prediction of grating lobes and the grazing scan angle condition are also described. The first two properties described above are critical to the computational efficiency of the technique developed in this thesis, and are discussed in detail.

The procedure of analysis using the Generalised Periodic Green's Function technique is illustrated by modelling an infinite array of horizontal metal strip dipoles. In order for a

numerically efficient solution to be obtained, a number of areas in the solution procedure are identified in which the computational load may be reduced. By choosing to use the spectral form of the Generalised Periodic Green's Function in the problem formulation, the integration over the sources is evaluated analytically, and the poor numerical convergence associated with the spatial form at large scan angles is avoided. To overcome the poor numerical convergence of the Generalised Spectral Periodic Green's Function for on-plane interactions, a technique is used to accelerate its convergence thus resulting in a Generalised Hybrid Periodic Green's Function having a spatial and a spectral component both of which are rapidly convergent. In the numerical implementation of the technique, computational overheads are reduced by avoiding repeated calculations in the evaluation procedure. This is achieved by the use of a grid system for segmenting the structure to minimise the number of numerical integrations for the spatial component of the Generalised Hybrid Periodic Green's Function, exploitation of the Toeplitz-like symmetries to avoid repeated calculations of elements in the Moment Matrix which have identical values, and the use of look-up tables. As a result of applying the above techniques to improve numerical efficiencies, the computational speed using the Hybrid Periodic Green's Function is found to be at least 40 times faster than obtained by use of either of the Spatial or Spectral Periodic Green's Functions.

Having developed an efficient technique of analysis for infinite arrays in which the elements are distributed in the plane of the array, the technique is extended to three-dimensional element geometries. For sources distributed perpendicular to the array plane, further improvement in computational efficiency is gained by the use of the generalised hybrid periodic Green's function for interactions which satisfy both the on-plane and near on-plane conditions. This concept is used to develop a model for an infinite array of vertical metal strip monopoles in which the results are validated against those found in the literature. In order to be able to model feedlines and metal strip elements in which the input impedance is more suitably matched to the characteristic impedance of the feedline, a new metal strip junction model is developed. Using this model, an analysis of an infinite array of centre-fed folded dipoles with equal width driven and folded arms is developed and validated at a known resonant condition. The numerical efficiency associated with the

technique is attested to by computation times of between half a second and a few seconds required to obtain a set of active impedance result for the models developed.

The metal strip junction model is used to analyse an element geometry of a metal strip dipole with coplanar strip feedline and validated against results found in the literature using another method of analysis. An important feature in practice is the feedline induced scan blindness effect which exists for such antenna arrays. Of relevance to engineering design is the conclusion that occurrence of the scan blindness condition at an angle further away from boresight can be achieved by designing the array with closer feedline separation or with larger inter-element spacings in the dimension corresponding to the vertical plane of the scan blindness angle. In preparation for the analysis of folded dipole elements with feedlines on substrates, the model for an infinite array of metal strip folded dipoles with coplanar strip feedlines is also developed. The high numerical efficiency of the technique in modelling array elements with feedlines is indicated by computation times of 5 seconds and 16 seconds to compute an active impedance value for the metal strip dipole element with coplanar strip feedline and metal strip folded dipole with coplanar strip feedline, respectively.

The Generalised Periodic Green's Function technique is next applied to the analysis of microstrip dipole arrays. It is noted that the conventional method of analysis for such structures found in the literature is applicable to TILA structures having an infinite dielectric slab, and is unsuitable for analysis of LITA structures having finite substrate configurations. The flexibility of the technique described in this thesis is demonstrated by its use to model an infinite array of centre-fed metal strip dipoles with three practical alternative substrate configurations. For each substrate configuration, the accuracy of the model is validated using results found in the literature which are obtained by another method of analysis. In every case, good agreement in the results is found both for the active impedance variation with scan angle as well as in the detection of substrate induced scan blindness conditions for the arrays. The computation times of less than a minute for obtaining an active impedance result in the models indicate that it can reasonably be developed into a microstrip array CAD design software for implementation on desktop

computers. From the model results, it is found that for the case of the semi-infinite sheet and finite substrate configurations, an increase in the electrical thickness of the substrate results in the occurrence of a substrate induced scan blindness at an angle nearer to boresight. It is also found that in general, a larger useable bandwidth is obtained for LITA structures having discontinuous substrates as compared with TILA structures with a single slab substrate configuration. Hence important design information of the array element can be readily obtained from the model.

Following this, the finite-substrate element configuration is extended to the analysis of infinite arrays of metal strip dipoles and metal strip folded dipoles with coplanar strip feedlines. These two element geometries represent practical antenna structures in which all the important features are modelled with a minimum of idealisations. In the case of the metal strip dipole element, it is found that the feedline induced scan blindness condition prevails for electrically thin substrates, whereas the substrate induced scan blindness condition dominates the characteristics for electrically thick substrates. This finding is of considerable importance for purposes of engineering design as trade-offs can be made by varying the substrate electrical thickness parameters. Finally, in order to be suitably matched to the characteristic impedance of the coplanar strip feedline of about 100Ω for typical dimensions used in such geometries, a metal strip folded dipole array element is analysed and found to have a active resistance of 95Ω at resonance in the boresight scan. The model has shown that the substrate parameters actually has a beneficial effect on the scanning performance of the array. Despite the complexity of the element geometry modelled, the computation time for a value of active impedance per scan angle taken is 48.3 seconds and 3.75 minutes for the substrate supported metal strip dipole and folded dipole case, respectively. The computational efficiency afforded by the technique to model the radiating element, substrate and feedline as an entire structure with a minimum of idealisations is thus of significance for engineering analysis and design.

The concepts developed for infinite array analysis are then extended to the analysis of finite arrays. An accurate and efficient analysis of finite arrays using a desktop computer is more challenging than for infinite arrays because the current distribution on the elements of the

finite array are not identical as assumed in the infinite array case. The traditional Element-by-Element method can provide accurate results for finite array analysis, but places a high demand on computational resources. Having reviewed a number of techniques for finite array analysis using the infinite array approach, a spectral windowing procedure is chosen to be developed into a technique making use of the numerically efficient Generalised Hybrid Periodic Green's Function which forms the core of this research. Using an Element-by-Element approach, the spatial and spectral forms of a Generalised Periodic Green's Function for a finite array are derived. In both forms, the Green's function developed takes account of the periodicity, finite array size, mutual coupling between elements and edge effects of the finite array.

For the same reason of computational efficiency as described in the infinite array case, the spectral form of the periodic Green's function is developed for the analysis of finite arrays. The process involves a convolution of the data in the Moment Matrix elements of the infinite array problem with a spectral window function. To evaluate the Moment Matrix elements, the numerically efficient Generalised Hybrid Periodic Green's Function for an infinite array is used. A Simplified Window Function is developed by intially assuming similar element currents in the finite array. In addition, an iterative procedure is developed in which the equivalent currents obtained using the Simplified Spectral Window are used to define a Refined Spectral Window which is again applied to the solution procedure to provide an improved set of current results. The convolution process is carried out by sampling the infinite array results at chosen scan angles within a periodic rectangle of the grating lobe lattice and evaluating the convolution discretely using a Fast Fourier Transform.

For illustration purposes, and also to enable comparison of results with those obtained using a full Element-by-Element analysis, a finite array of horizontal metal strip dipoles is modelled. The results show good agreement between the Generalised Periodic Green's Function - Spectral Windowing technique and the Element-by-Element method in predicting the element active impedance of the finite array, provided the mutual coupling between the elements is not too strong. This is expected since the initial assumption of

uniform currents has to provide a good starting point. Furthermore, results obtained using the Refined Spectral Window are similar to those using the Simplified Spectral Window, thus providing a measure of confidence in the accuracy of the solution. The technique is applied to the analysis of a finite array of horizontal metal strip dipoles with coplanar strip feedlines in one case, and with a substrate in a second case. It is noted that the corresponding infinite array has a feedline induced scan blindness in the first case, and a substrate induced scan blindness in the second. In both situations, the analysis shows that in the vicinity of the corresponding infinite array's scan blindness angle, electrical power being transferred between the elements would degrade the effective performance of the array as an antenna. Therefore, an ability to predict the variation of the active impedance of the finite array elements under these conditions is useful for purposes of engineering analysis and design. Based on the computational resources required by the models, it is concluded that an analysis of finite microstrip arrays using the Generalised Periodic Green's Function - Spectral Windowing technique is well within the capabilities of desktop computers.

In summary, this thesis presents an accurate, flexible and numerically efficient technique for the analysis of antenna elements located in the central region as well as the periphery of a finite array in which a three-dimensional element geometry comprising a metal part with feed mechanism and a dielectric part in various configurations may be modelled using a desktop computer. The original contribution of this research is outlined at the end of each chapter, but the broader achievements of the work described here are:

- An review of the methods for microstrip antenna and array analysis found in the literature has been made with a view to understand their relative merits and disadvantages.
- An in-depth analysis and description of the spatial and spectral forms of the Generalised Periodic Green's Function for both the infinite and finite array has been presented in relation to the modelling of antenna arrays.

- An accurate, flexible and numerically efficient technique for the analysis of infinite and finite arrays of metal strip and microstrip dipole structures has been developed which can be conveniently implemented on a desktop computer.
- An extensive number of numerical models of typical infinite and finite arrays have been developed and used to illustrate the capabilities of the technique as well to study the effects of feedline and substrate configurations on the impedance characteristics of the metal strip and microstrip dipole arrays.

The research presented has therefore been able to make a significant contribution to the methods for analysis and design of microstrip phased arrays by offering an alternative technique of analysis that warrants further development into a computer aided design software tool for general usage, especially when unconventional substrate geometries are required.

8.2 Recommendations for Future Work

The research presented in this thesis is intended to demonstrate the capabilities of the Generalised Periodic Green's Function - Spectral Windowing technique in the analysis of infinite and finite metal strip and microstrip arrays. Arising from the development of this technique, a number of areas for future work are identified:

- The choice of basis and testing functions which can further enhance the computational efficiency of the technique is a possible area for further research. The pulse basis functions - point matching method is employed in this analysis primarily because of their simplicity and general applicability to both the metal and dielectric parts of the antenna structure. However, numerical models using entire domain or sub-sectional basis functions in which a smaller number of such basis functions is required to obtain well converged solutions may result in even lower computational demands than the models developed in this thesis.

- The general applicability of the technique to other antenna array structures not described in this thesis opens up many possibilities for future work. One possibility is to develop an analysis for arrays of probe-fed microstrip patches with various substrate or superstrate configurations, so as to allow more conventional antennas to be modelled in the same package. Before this analysis can be successfully carried out, the applicability of the metal strip junction modelling technique to the probe-to-patch junction needs to be verified. Another possibility is to use this technique for the modelling of quasi-periodic and broad-band antenna arrays in which efficiency of multi-frequency computations is important.

- Development of a numerical code for the analysis of microstrip phased arrays based on this technique for general usage is a third area of interest. Although the codes written in this research are modular in design and relatively easy to understand, automation of the data input is an area of improvement. Automation in segmentation of the element geometry, setting out and filling of the Moment Matrix for arbitrary strip and substrate configuration, and determination of numerical convergence can also be built into the codes. Furthermore, a software using this technique could be developed for integration with an overall communication system design software package implemented on desktop computers. The ultimate objective in such efforts is to enable the engineer to solve a variety of different element geometries and lattice arrangements without the need for reformulation of the problem or tedious manipulation of the input parameters in using the software tool.

As microstrip antenna technology matures and the demand for more complex arrays increases, the technique for the analysis of such antennas must also increase in sophistication and become more widespread. The areas suggested above provide the starting point for further stimulating research that can be done.

APPENDIX A

Specifications of Computer Used in this Thesis

All the numerical results presented in this thesis are obtained using the same desktop computer with the following specifications given below:

- Maker : Sun Microsystems, Inc.
- Model : Sparc 4/50 GX-16-P40 workstation
- Speed : 60 Mhz
- Memory : 64 MBytes
- Swap space : 250 MBytes

APPENDIX B

Transformation from the Spatial to the Spectral Form of the Periodic Green's Function

The spatial and spectral forms of the Generalised Periodic Green's Function are a Fourier transform pair, sampled using two phase shifted comb functions. Before embarking on the derivation, it is first necessary to set down the spatial Fourier transform of a two dimensional comb function. Let *c(x)* be a one dimensional phase-shifted comb function defined as:

$$c(x) = \sum_{m=-\infty}^{\infty} \delta(x - mb)\, e^{-jk_x mb} \qquad \text{(B.1)}$$

The spatial Fourier transform of this function, applying the frequency shift rule, is given by:

$$\tilde{C}(\beta_x) = \frac{2\pi}{b} \sum_{m=-\infty}^{\infty} \delta(\beta_x - \frac{2\pi m}{b} + k_x) \qquad \text{(B.2)}$$

Similarly, a two dimensional phased-shifted comb function given by:

$$c(x,y) = \sum_{m=-\infty}^{\infty} \sum_{n=-\infty}^{\infty} \delta(x - mb)\, \delta(y - nd)\, e^{-jk_x mb}\, e^{-jk_y nd} \qquad (B.3)$$

has a Fourier transform given by:

$$\tilde{C}(\beta_x, \beta_y) = \frac{(2\pi)^2}{bd} \sum_{m=-\infty}^{\infty} \sum_{n=-\infty}^{\infty} \delta(\beta_x - \frac{2\pi m}{b} + k_x)\, \delta(\beta_y - \frac{2\pi n}{d} + k_y) \qquad (B.4)$$

Next, it is necessary to establish the Fourier transform of a doubly periodic function. A two dimensional periodic function $f_p(x,y)$ may be viewed as the same function truncated to one period b and d in each of the two dimensions within a unit cell, which is then convolved with a two dimensional phase-shifted comb function in space.

$$f_p(x,y) = f_e(x,y) * c(x,y) \qquad (B.5)$$

where $f_e(x,y) = f_p(x,y)$ *for* $-b/2 \le x \le b/2$ and $-d/2 \le y \le d/2$, and zero everyhwere else, * represents a convolution operations, and $c(x,y)$ is given by (B.3).

The Fourier transform of $f_p(x,y)$ is then given by the product of the transforms as follows:

$$\begin{aligned} \tilde{F}_p(\beta_x, \beta_y) &= \tilde{F}_e(\beta_x, \beta_y)\ \ \tilde{C}(\beta_x, \beta_y) \\ &= \tilde{F}_e(\beta_x, \beta_y) \frac{(2\pi)^2}{bd} \sum_{m=-\infty}^{\infty} \sum_{n=-\infty}^{\infty} \delta(\beta_x - \frac{2\pi m}{b} + k_x)\, \delta(\beta_y - \frac{2\pi n}{d} + k_y) \end{aligned} \qquad (B.6)$$

Taking the inverse Fourier transform of (B.6) gives:

$$\begin{aligned} f_p(x,y) &= \frac{1}{(2\pi)^2} \int_{-\infty}^{\infty} \int_{-\infty}^{\infty} \tilde{F}_p(\beta_x, \beta_y)\, e^{+j(\beta_x x + \beta_y)}\, d\beta_x\, d\beta_y \\ &= \frac{1}{bd} \sum_{m=-\infty}^{\infty} \sum_{n=-\infty}^{\infty} \tilde{F}_e(k_{x_m}, k_{y_n}) e^{j\beta_{x_m} x} e^{j\beta_{y_n} y} \end{aligned} \qquad (B.7)$$

where $\beta_{x_m} = \frac{2\pi m}{b} - k_x$ and $\beta_{y_n} = \frac{2\pi n}{d} - k_y$.

Because the double summations are from -∞ to +∞, and the function is symmetrical in m and n, (B.7) can also be expressed in its more commonly known form as follows:

$$f_p(x,y) = \frac{1}{bd} \sum_{m=-\infty}^{\infty} \sum_{n=-\infty}^{\infty} \tilde{F}_e(k_{x_m}, k_{y_n})\, e^{-jk_{x_m}x}\, e^{-jk_{y_n}y} \qquad (B.8)$$

where $k_{x_m} = \frac{2\pi m}{b} + k_x$ and $k_{y_n} = \frac{2\pi n}{d} + k_y$.

The analysis derived above can now be used to transform the spatial form of the periodic Green's Function $G_p(r,r')$ which is doubly periodic in the xy plane with a reference source located at a point (x',y',z') within the unit cell containing the origin, so that:

$$G_p(\vec{r},\vec{r}') = \sum_{m=-\infty}^{\infty} \sum_{n=-\infty}^{\infty} \frac{e^{-jk_0 r_{mn}}}{4\pi r_{mn}}\, e^{-jk_x mb}\, e^{-jk_y nd} \qquad (B.9)$$

where $r_{mn} = \sqrt{(x-x'-mb)^2 + (y-y'-nd)^2 + (z-z')^2}$, $k_x = k_0 \sin\theta\cos\phi$ and $k_y = k_0 \sin\theta\sin\phi$.

We can express this function as the same function truncated to one period (the unit cell), convolved with the appropriate two dimensional phase-shifted comb function in space:

$$G_p(\vec{r},\vec{r}') = G_u(x,y,z;x',y',z') \; * \sum_{m=-\infty}^{\infty} \delta(x-x'-mb)\, e^{-jk_x mb} * \sum_{n=-\infty}^{\infty} \delta(y-y'-nd)\, e^{-jk_y nd} \qquad (B.10)$$

where $G_u(x,y,z;x',y',z')$ is the Green's Function for an isolated unit cell given by $G_u(x,y,z;x',y',z') = e^{-jk_0 r}/4\pi r$ where, $r = \sqrt{(x-x')^2 + (y-y')^2 + (z-z')^2}$ for $-b/2 \le x-x' \le b/2$ and $-d/2 \le y-y' \le d/2$; and $G_u(x,y,z;x',y',z') = 0$ everywhere else.

If it is further assumed that b and d are of the order of a wavelength and (z-z') range from -∞ to +∞, then the radiation from the point source within the unit cell is essentially in the z direction. In this case, $G_u(x,y,z;x',y',z')$ can be treated as a one-dimensional Green's Function whose spectral, or Fourier integral, form is given by:

$$\tilde{G}_u(k_{x_m}, k_{y_n}, k_{z_{mn}}) = \frac{1}{2jk_{z_{mn}}} e^{-jk_{z_{mn}}|z-z'|} \qquad \text{(B.11)}$$

Therefore, if the form of (B.10) is equated with the form of (B.5), then (B.10) can also be expressed in its spectral form similar to (B.8) with the spectral form of the unit cell Green's function given by (B.11). Hence the overall spectral periodic Green's Function is now given by:

$$\begin{aligned} G_p(\vec{r}, \vec{r}') &= \frac{1}{bd} \sum_{m=-\infty}^{\infty} \sum_{n=-\infty}^{\infty} \tilde{G}_u(k_{x_m}, k_{y_n}, k_{z_{mn}})\, e^{-jk_{x_m}(x-x')} e^{-jk_{y_n}(y-y')} e^{-jk_{z_{mn}}|z-z'|} \\ &= \frac{1}{bd} \sum_{m=-\infty}^{\infty} \sum_{n=-\infty}^{\infty} \frac{1}{2jk_{z_{mn}}} e^{-jk_{x_m}(x-x')}\, e^{-jk_{y_n}(y-y')}\, e^{-jk_{z_{mn}}|z-z'|} \end{aligned} \qquad \text{(B.12)}$$

where $k_{x_m} = \frac{2\pi m}{b} + k_x$ and $k_{y_n} = \frac{2\pi n}{d} + k_y$, and in order to satisfy the radiation condition, $k_{zmn} = \sqrt{k_0^2 - k_{xm}^2 - k_{yn}^2}$ for the propagating wave condition $k_0^2 \geq k_{xm}^2 + k_{yn}^2$, and $k_{zmn} = -j\sqrt{k_{xm}^2 + k_{yn}^2 - k_0^2}$ for the evanescent wave condition $k_0^2 < k_{xm}^2 + k_{yn}^2$; and the integers m and n representing the $(m,n)^{th}$ Floquet mode in the xy plane.

APPENDIX C

Convergence Acceleration of the Spectral Form of the Periodic Green's Function

INTRODUCTION

In Singh's technique [38] to accelerate the convergence of the spectral form of the periodic Green's function, the asymptotic part of the Green's function is transformed into the spatial domain to be evaluated numerically. To begin with, it is useful to restate the two forms of the periodic Green's function in the equations below. The spatial form is given by:

$$G_p(\vec{r},\vec{r}') = \sum_{m=-\infty}^{\infty}\sum_{n=-\infty}^{\infty} \frac{e^{-jk_0 r_{mn}}}{4\pi r_{mn}} e^{jk_x mb}\, e^{jk_y nd} \qquad (C.1)$$

where,

$r_{mn} = \sqrt{(x-x'-mb)^2 + (y-y'-nd)^2 + (z-z')^2}$, $k_x = k_0 \sin\theta \cos\phi$ and $k_y = k_0 \sin\theta \sin\phi$.

The spectral form is given by:

$$G_p(\vec{r},\vec{r}') = \frac{1}{2bd} \sum_{m=-\infty}^{\infty} \sum_{n=-\infty}^{\infty} e^{-jk_{x_m}(x-x')} e^{-jk_{y_n}(y-y')} \left[\frac{e^{-jk_{z_{mn}}|z-z'|}}{jk_{z_{mn}}} \right] \qquad (C.2)$$

where $k_{x_m} = 2\pi m/b + k_x$ and $k_{y_n} = 2\pi n/d + k_y$, and in order to satisfy the radiation condition, $k_{z_{mn}} = \sqrt{k_0^2 - k_{x_m}^2 - k_{y_n}^2}$ for the propagating wave condition $k_0^2 \geq k_{x_m}^2 + k_{y_n}^2$, and $k_{z_{mn}} = -j\sqrt{k_{x_m}^2 + k_{y_n}^2 - k_0^2}$ for the evanescent wave condition $k_0^2 < k_{x_m}^2 + k_{y_n}^2$; the integers m and n represent the Floquet modes in the xy plane. It should be noted that the expression within the square brackets contains the asymptotic part of the Green's function, and causes it to become slowly convergent in the 'on-plane' case where $z = z'$.

The two representations of the periodic Green's function given above will ideally produce the same result in an accurate numerical evaluation, but they have quite different convergence properties. It is known that the spectral form of the Green's function given in (C.2) is rapidly convergent everywhere except in the 'on-plane' case, when the testing point lies on or near to the aperture plane of the sources. Hence it is required in this case, to be able to transfer the evaluation of the Green's function to the spatial domain, where it converges exponentially. This can be done in two steps, making use of the Kummer and Poisson transforms as described below.

KUMMER'S TRANSFORM

Assuming that a sum S is given by the following doubly infinite series:

$$S = \sum_{m=-\infty}^{\infty} \sum_{n=-\infty}^{\infty} f(m,n) \qquad (C.3)$$

where the rate of convergence of the series is governed by the asymptotic form of $f(m,n)$ which tends to $f_1(m,n)$ as $m \to \infty$ and $n \to \infty$, such that $f_1(m,n)$ is defined for all integers m,n.

Kummer's transformation is given by:

$$\sum_{m=-\infty}^{\infty}\sum_{n=-\infty}^{\infty} f(m,n) = \sum_{m=-\infty}^{\infty}\sum_{n=-\infty}^{\infty}\left[f(m,n) - f_1(m,n)\right] + \sum_{m=-\infty}^{\infty}\sum_{n=-\infty}^{\infty} f_1(m,n) \qquad (C.4)$$

In this case, the asymptotic part has been subtracted from the original sum, and then added back as another infinite sum so that the value of the original function is retained. Applying Kummer's transformation to the spectral periodic Green's function in (B.2), allows us to remove the asymptotic part that causes the slow convergence from the Green's function so that it becomes rapidly convergent.

The next step is to identify the asymptotic part of the spectral periodic Green's function that needs to be removed. Since the aperture plane is the *xy* plane, a testing point is considered 'off-plane' when it is located away from the *xy* plane in the *z* dimension. The asymptotic part of the Green's function therefore involves the variables in the *z* dimension and is given by:

$$A(m,n) = \frac{e^{-jk_{z_{mn}}|z-z'|}}{k_{z_{mn}}} \qquad (C.5)$$

In the 'on-plane' case, it is desired to transfer either a part, or all of the above expression into the spatial domain. To do this, we introduce a real variable k_{mn} such that:

$$k_{mn} = \sqrt{k_{x_m}^2 + k_{y_n}^2 + u^2} \qquad (C.6)$$

where u is a finite, real variable which is called the *smoothing parameter*. We can now express the *z* directed wave propagation vector in terms of this new variable as follows:

$$k_{z_{mn}} = -j\sqrt{k_{x_m}^2 + k_{y_n}^2 - k_0^2} = -j\sqrt{k_{mn}^2 - \left(k_0^2 + u^2\right)} \qquad (C.7)$$

Substituting (C.7) into (C.5), and for large values of m and n:

$$A(m,n) = \frac{e^{-jk_{z_{mn}}|z-z'|}}{k_{z_{mn}}} \xrightarrow{m,n\to\infty} \frac{e^{-jk_{mn}|z-z'|}}{k_{mn}} \qquad (C.8)$$

Using the asymptotic expression for *A(m,n)* and applying Kummer's transform, the spectral periodic Green's function can be split into two parts as follows:

$$G_p(\vec{r},\vec{r}') = \frac{1}{2bd}\sum_{m=-\infty}^{\infty}\sum_{n=-\infty}^{\infty} e^{-jk_{x_m}(x-x')}\, e^{-jk_{y_n}(y-y')}\left[\frac{e^{-jk_{z_{mn}}|z-z'|}}{jk_{z_{mn}}} - \frac{e^{-k_{mn}|z-z'|}}{k_{mn}}\right] + \frac{1}{2bd}\sum_{m=-\infty}^{\infty}\sum_{n=-\infty}^{\infty} e^{-jk_{x_m}(x-x')}\, e^{-jk_{y_n}(y-y')}\,\frac{e^{-k_{mn}|z-z'|}}{k_{mn}} \qquad (C.9)$$

The second part in (C.9) is slowly convergent in its present form. However, it is possible to transform this second part into a form which is more rapidly convergent by means of the Poisson transform.

POISSON TRANSFORM

The procedure for applying the Poisson transform to a function consists of sampling the function with a comb function, and then applying the Fourier transform to the result. The steps for doing this are given by equations (B.1) to (B.6) in Appendix B, and will not be repeated here. By application of the Poisson transform, the second sum on the right hand side of equation (C.9) is transformed into the spatial domain. This is done recognising the equivalence of (C.1) and (C.2), and substituting *-ju* for k_0 in (C.1), so that finally:

$$G_p(\vec{r},\vec{r}') = \frac{1}{2bd}\sum_{m=-\infty}^{\infty}\sum_{n=-\infty}^{\infty} e^{-jk_{x_m}(x-x')}\, e^{-jk_{y_n}(y-y')}\left[\frac{e^{-jk_{z_{mn}}|z-z'|}}{jk_{z_{mn}}} - \frac{e^{-k_{mn}|z-z'|}}{k_{mn}}\right] + \sum_{m=-\infty}^{\infty}\sum_{n=-\infty}^{\infty} e^{jk_x mb}\, e^{jk_y nd}\,\frac{e^{-ur_{mn}}}{4\pi r_{mn}} \qquad (C.10)$$

The choice of the parameter u merits some discussion at this stage. One simple choice for u is to let $u = jk_0$, by which (C.7) reduces to $k_{z_{mn}} = -jk_{mn}$ for all values of m and n. In this case, the term within the square brackets in (C.10) is zero and the second sum on the right hand side of the equation is similar to equation (C.1). The implication of this is that by choosing $u = jk_0$ for the 'on-plane' case, the whole of the Green's function is transferred from the spectral to the spatial domain. Hence in the Moment Method solution,

the spectral Green's function is employed for the 'off-plane' interactions, and the spatial Green's function is used for all the 'on-plane' interactions. The advantage of this choice in the value of u is the simplicity of the implementation. However its disadvantage is that as the scan angle approaches 90°, the spatial sum itself becomes slowly convergent. Hence implementation of the acceleration technique using $u = jk_0$ is feasible in all cases except for cases close to the grazing scan angle.

A better choice is to let u be a finite, real number so that for large values of m and n, the term within the square brackets in (C.10) becomes zero. Physically, this means the contribution of the evanescent modes to the spectral periodic Green's function, which are slowly convergent in the 'on-plane' case, are transferred to the spatial domain. However, it is expected that this component will be slowly converging for large scan angles. Assuming the absence of grating lobes, the propagation Floquet mode (0,0) as described in Section 3.4.3 is not completely transferred to the spatial domain, so that as $\theta \rightarrow 90°$, $k_{z_{00}} \rightarrow 0$ and by (C.5), $A(0,0) \rightarrow -j\infty$. Hence at the grazing scan angle, the dominant effect of the propagation Floquet mode (0,0) forces the real part of the active impedance to zero so that the value of the entire periodic Green's function in (C.10) is converged. Hence, this is a better choice for the value of u which ensures rapid convergence for all scan angles.

From equation (C.10), it is seen that u causes the exponential decay of the spatial sum, and ideally, should be as large as possible to accelerate its convergence. However, a larger value of u also means that a smaller proportion of the slowly convergent spectral sum has been transferred into the spatial domain. In view of the opposite effect of u on the Green's function in the two domains, Shubair [55] has pointed out that the choice of the specific value of u is not very critical. However, an extreme choice of u would not be optimal as it would make one of the two components of the periodic Green's function very slowly convergent. Hence the choice of $u \approx b/2$, ie half the inter-element spacing, appears to be a good compromise, and is adopted for all the numerical implementations in this research.

APPENDIX D

Simplified Feedline Model

In Chapter 5, the effect of the coplanar strip feedline on the active impedance of a metal strip dipole element of an infinite array was discussed. When the separation of the two strips of the feedline is very close, it has been shown [29,77] that the transmission line mode currents on the feedline can be assumed to have negligible contribution to the radiation characteristics of the element. Under this condition, a *Simplified Feedline Model* can be used in the analysis. An application of this model to the analysis of an infinite array of metal strip dipoles with coplanar strip feedlines is given in this Appendix. The intention is to demonstrate that the Configuration A Junction Feedline Model developed in Section 5.4 can be applied to the case of a single strip feedline.

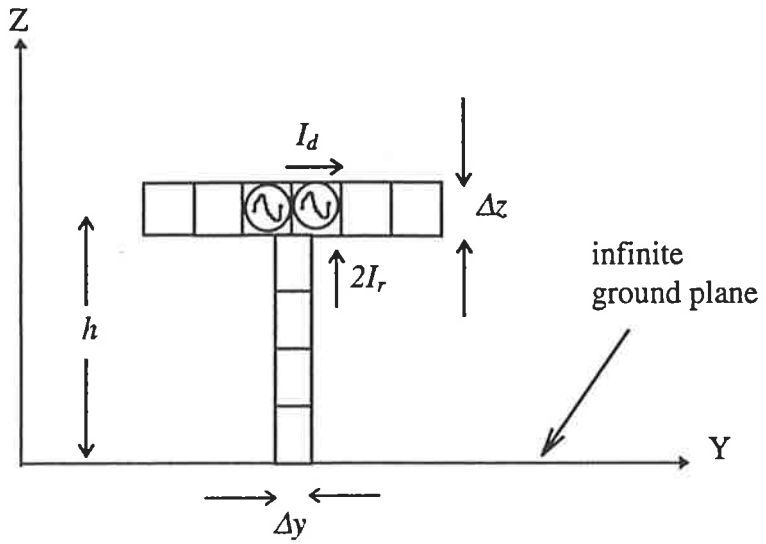

Figure D.1 : Geometry of the simplified feedline model.

As shown in Figure D.1, the geometry of an array element with the simplified feedline model may be represented by a metal strip connected to a single strip feedline. It has been found [29] that for a for a *metal strip with coplanar strip feedline*, the active impedance is given by:

$$Z_{act} = \frac{1}{\left[\left(\frac{I_d - I_r}{V}\right) - \left(\frac{I_t}{V}\right)\right]} \tag{D.1}$$

where I_d is the current on the metal strip dipole, and I_r and I_t are the radiation mode current and transmission line mode currents on the two strips of the coplanar strip feedline, respectively. If the separation between the two strips of the feedline is close, the equal and opposite transmission line mode currents are expected to have minimal radiative coupling to the rest of the structure. If a further condition were imposed that the transmission line mode admittances were zero, as would be the case if the metal strip dipole is located at $\lambda/4$ above the ground plane, then the transmission line mode current $I_t = 0$ and the active impedance is determined by the radiation problem alone. A numerical model was developed based on this simplified feedline modelling technique, and the results are given in Figure D.1 below.

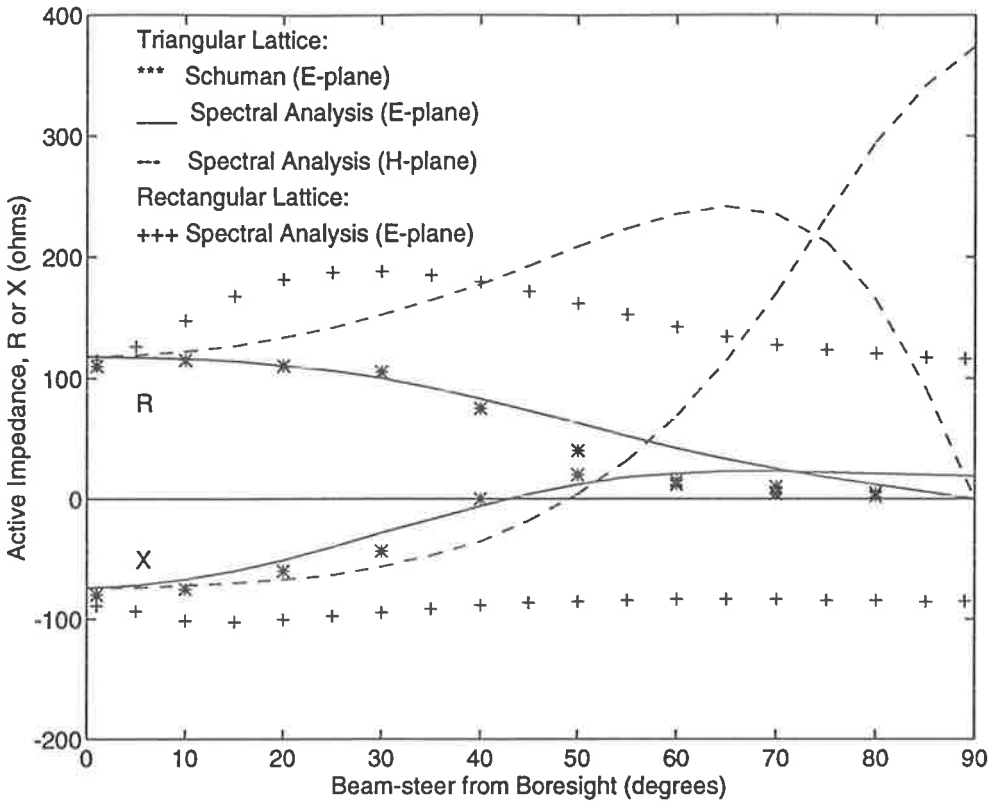

Figure D.2 : Active impedance as a function of scan angle for an infinite array of metal strip dipoles with simplified feedline model in both the triangular and rectangular grid lattices; $l = 0.4375\lambda$, $h = 0.25\lambda$, $n_y = 6$, $n_z = 5$.

As shown in Figure D.2, the variation of active impedance with scan angle in the E-plane is first plotted for the triangular grid lattice and the results compared with those given by Schuman [29]. The agreement between the results using the two different techniques is found to be good. The results for the H-plane scan are also computed and plotted onto the graph. It is noted that for the specified inter-element spacings in the triangular grid lattice, no grating lobe has entered the visible space. The scan results in the E-plane for an array with a rectangular grid lattice and identical lattice spacings are also plotted for comparison. It is noted that in the results for the rectangular grid, the active resistance at the grazing scan angle is not zero, implying the emergence of a grating lobe.

Bibliography

1. J.R. James, What's new in antennas, IEEE Antennas and Propagation Magazine, pp. 6-18, Feb 1990.

2. J. Huang, Microstrip antennas for commercial applications, Chapter 8 of Microstrip Antennas, edited by D.M. Pozar and D.H. Schaubert, IEEE Press, pp. 371-379, 1995.

3. D.M. Pozar, Microstrip Antennas, Proceedings of the IEEE, Vol 80, No. 1, pp. 79-91, Jan 1992.

4. N.G. Alexopoulos, P.B. Katehi and D.B. Rutledge, Substrate optimization for integrated circuit antennas, IEEE Transactions on Microwave Theory and Techniques, Vol. 31, pp. 550-557, July 1983.

5. D.B. Rutledge, D.P. Niekirk and D.P. Kasilingam, Integrated circuit antennas, Vol. 10 of Infrared and Millimetre Waves, Chapter 1, New York: Academic Press, pp. 1-90, 1983.

6. D.M. Pozar, Considerations for millimetre wave printed antennas, IEEE Transactions on Antennas and Propagation, Vol. 31, pp. 740-747, Sep 1983.

7. J.R. Bayard, M.E. Cooley and D.H. Schaubert, Analysis of infinite arrays of printed dipoles on dielectric sheets perpendicular to a ground plane, IEEE Transactions on Antennas and Propagation, Vol. 39, pp. 1722-1732, Dec 1991.

8. A.J. Parfitt, D.W. Griffin and P.H. Cole, On the modelling of metal strip antennas contiguous with the edge of finite size, electrically thick dielectric substrates, IEEE Transactions on Antennas and Propagation, Vol. 40, pp. 134-140, Feb 1992.

9. A.J. Parfitt, D.W. Griffin and P.H. Cole, Mutual coupling between metal strip dipole antennas on electrically thick, finite size dielectric substrates, IEEE Transactions on Antennas and Propagation, Vol. 41, pp. 108-115, Jan 1993.

10. A.J. Parfitt, D.W. Griffin and P.H. Cole, Analysis of infinite arrays of substrate-supported metal strip antennas, IEEE Transactions on Antennas and Propagation, Vol. 41, pp. 191-199, Feb 1993.

11. D.M. Pozar, Analysis of finite phased arrays of printed dipoles, IEEE Transactions on Antennas and Propagation, Vol. 33, pp. 1045-1053, Oct 1985.

12. D.M. Pozar, Finite phased arrays of rectangular microstrip patches, IEEE Transactions on Antennas and Propagation, Vol. 34, pp. 658-665, May 1986.

13. A.K. Skrivervik and J.R. Mosig, Finite phased arrays of microstrip patch antennas: the infinite array approach, IEEE Transactions on Antennas and Propagation, Vol. 40, pp. 579-582, May 1992.

14. A.K. Skrivervik and J.R. Mosig, Analysis of finite phase arrays of microstrip patches, IEEE Transactions on Antennas and Propagation, Vol. 41, pp. 1105-1114, Aug 1993.

15. D.M. Pozar, Scanning characteristics of infinite arrays of printed antenna subarrays, IEEE Transactions on Antennas and Propagation, Vol. 40, pp. 666-674, June 1992.

16. G.A. Deschamp, Microstrip microwave antennas, Proceedings of the 1953 Antenna Applications Symposium, Sep 1953.

17. H. Gutton and G. Baissinot, Flat aerial for ultra high frequencies, French patent No. 703113, 1955.

18. D.M. Pozar and J.R. James, A review of CAD for microstrip antennas and arrays, in Chapter 1 of Microstrip Antennas, IEEE Press, New York, pp. 51-56, 1995.

19. K.R. Carver and J.W. Mink, Microstrip antenna technology, IEEE Transactions on Antennas and Propagation, Vol. 29, pp. 2-24, Jan 1981.

20. H. Pues and A.Van de Capelle, Accurate transmission-line model for the rectangular microstrip antenna, Proceedings of IEE, Vol. 131, pp. 334-340, Dec 1984.

21. M. Himdi, J.P. Daniel and C. Terret, Analysis of aperture-coupled microstrip antenna using cavity method, Electronic Letters, Vol. 25, pp. 391-392, Mar 1989.

22. D. Thouroude, M. Himdi and J.P. Daniel, CAD-oriented cavity model for rectangular patches, Electronic Letters, Vol. 26, pp. 842-844, Jun 1990.

23. V. Palanisamy and R. Garg, Analysis of arbitrarily shaped microstrip patch antennas using segmentation technique and cavity model, IEEE Transactions on Antennas and Propagation, Vol. 34, pp. 1208-1213, Oct 1986.

24. N. Morita, N. Kumagai and J.R. Mautz, Integral equation methods for electromagnetics, English translation, Morikita Shuppan Co., Ltd., 1990.

25. X. Yuan, D. Lynch and J. Strobehn, Coupling of finite element and moment methods for electromagnetic scattering from inhomogeneous objects, IEEE Transactions on Antennas and Propagation, Vol. 38, pp. 386-394, Mar 1990.

26. T. Cwik, C. Zuffada and V. Jamnejad, Modelling three-dimensional scatterers using a coupled finite element - integral equation formulation, IEEE Transactions on Antennas and Propagation, Vol. 44, pp. 453-459, Apr 1966.

27. C. Wu, K.L. Wu, Z.Q. Bi, and J. Litva, Accurate characterization of planar printed antennas using finite-difference time-domain method, IEEE Transactions on Antennas and Propagation, Vol. 40, pp. 526-534, May 1992.

28. B.A. Munk and G.A. Burrell, Plane wave expansion for arrays of arbitrarily oriented piecewise linear elements and its application to determining the impedance of a single linear antenna in a lossy half-space, IEEE Transactions on Antennas and Propagation, Vol. 27, pp. 331-343, May 1979.

29. H.K. Schuman, D.R. Pflug and L.D. Thomson, Infinite planar arrays of arbitrarily bent thin wire radiators, IEEE Transaction on Antennas and Propagation, Vol. 32, pp. 364-377, Apr 1984.

30. A.A. Oliner and R.G. Malech, Mutual coupling in infinite scanning arrays, Chapter 3 of Microwave scanning antennas, Volume II - Array theory and practice, edited by R.C. Hansen, Academic Press, New York and London, pp. 195-336, 1966.

31. D.M. Pozar, Input impedance and mutual coupling of rectangular microstrip antennas, IEEE Transcations on Antennas and Propagation, Vol. 30, pp. 1191-1196, Nov 1982.

32. D.M. Pozar, Analysis and design considerations of printed array antennas, Vol. 1 of Handbook of Microstrip Antennas, Chapter 12, London: Peter Perigrinus, pp. 693-753, 1989.

33. D.M. Pozar and D.H. Schaubert, Scan blindness in infinite phased arrays of printed dipoles, IEEE Transactions on Antennas and Propagation, Vol. 32, pp. 602-610, June 1984.

34. D.M. Pozar and D.H. Schaubert, Analysis of an infinite array of rectangular microstrip patches with idealized probe feeds, IEEE Transactions on Antenna and Propagation, Vol. 32, pp. 1101-1107, Oct 1984.

35. K.E. Jordan, G.R. Richter and P. Sheng, An efficient numerical evaluation of the Green's function for the Helmholtz operator on periodic structures, Journal of Computational Physics, Vol. 63, pp. 222-235, 1986.

36. R. Lampe, P. Klock and P. Mayes, Integral transforms useful for the accelerated summation of periodic, free-space Green's functions, IEEE Transactions on Microwave Theory and Techniques, Vol. 33, pp. 734-736, Aug 1985.

37. R.E. Jorgenson and R Mittra, Efficient calculation of the free-space periodic Green's function, IEEE Transactions on Antennas and Propagation, Vol. 38, pp. 633-642, May 1990.

38. S. Singh, W.F. Richards, H.R. Zinecka and D.R. Wilton, Accelerating the convergence of series representing the free-space periodic Green's function, IEEE Transactions on Antennas and Propagation, Vol 38, pp. 1958-1962, Dec 1990.

39. R. Mittra, C.H. Chan and T. Cwik, Techniques for analyzing frequency selective surfaces - a review, Proceedings of the IEEE, Vol. 76, pp. 1593-1615, Dec 1988.

40. E.D. Sharp, A triangular arrangement of planar-array elements that reduces the number needed, IRE Transactions on Antennas and Propagation, pp. 126-129, Mar 1961.

41. H.A. Wheeler, The radiation resistance of an antenna in an infinite array or waveguide, Proc. IRE, Vol. 36, pp. 478-488, Apr 1948.

42. H.A. Wheeler, Simple relations derived from a phased-array antenna made of an infinite current sheet, IEEE Transactions on Antennas and Propagation, Vol. 13, pp. 506-514, May 1965.

43. H.A. Wheeler, The grating-lobe series for the impedance variation in a planar phased-array antenna, IEEE Transactions on Antennas and Propagation, Vol. 14, pp. 707-714, Nov 1966.

44. A. Sommerfeld, Partial differential equations in physics, Academic Press Inc., pp. 182-194, New York, 1949.

45. J.L. Allen, Gain and impedance variation in scanned dipole arrays, IRE Transactions on Antennas and Propagation, pp. 566-572, Sep 1962.

46. W.H. Kummer, Basic array theory, Proceedings of the IEEE, Vol. 80, pp. 127-140, Jan 1992.

47. C.A. Balanis, Integral equations and the Moment Method, Chapter 12 of Advanced Engineering Electromagnetics, p.722, New York, John Wiley and Sons, 1981.

48. L. Stark, Radiation impedance of a dipole in an infinite planar phased array, Radio Science, Vol. 1, pp. 361-377, Mar 1966.

49. B.L. Diamond, A generalized approach to the analysis of infinite planar array antennas, Proceedings of the IEEE, Vol. 56, pp. 1837-1851, Nov 1968.

50. K.J. Webb, P.W. Grounds and R. Mittra, Convergence in the spectral domain formulation of waveguide and scattering problems, IEEE Transactions on Antennas and Propagation, Vol. 38, pp. 869-877, June 1990.

51. R.F. Harrington, Field computation by Moment Methods, The Macmillan Company, New York, 1968.

52. R.E. Collin, The role of analysis in an age of computers: view from the analytical side, IEEE Antennas and Propagation Magazine, pp. 27-32 Aug 1990.

53. M.I. Aksun and R. Mittra, Choices of expansion and testing functions for the Method of Moments applied to a class of electromagnetic problems, IEEE Transactions on Microwave Theory and Techniques, Vol.41, pp. 503-509, Mar 1993.

54. A.F. Peterson, D.R. Wilton and R.E. Jorgenson, Variational nature of Galerkin and non-Galerkin Moment Method solutions, IEEE Transactions on Antennas and Propagation, Vol. 44, pp. 500-503, Apr 1996.

55. M. Shubair and Y.L. Chow, Efficient computation of the periodic Green's function in layered dielectric media, IEEE Transactions on Antennas and Propagation, Vol. 41, pp. 498-502, Mar 1993.

56. IMSL Inc., Houston, Texas, IMSL math/library: Users Manual, 1987.

57. A. D. Yaghjian, Electric dyadic Green's functions in the source region, Proceedings of the IEEE, Vol. 68, pp. 248-263, Feb 1980.

58. E.H. Newman and D.M. Pozar, Considerations for efficient wire / surface modelling, IEEE Transactions on Antennas and Propagation, Vol. 28, pp. 121-125, Jan 1980.

59. V.W.H. Chang, Infinite phased dipole array, Proceedings of IEEE, Vol. 56, pp. 1892-1900, Nov 1968.

60. Numerical Electromagnetics Code (NEC), Naval Postgraduate School, Code 62 AB, Monterey, California 93943.

61. J.L. Pages, Numerical modelling of feed points at wire junctions, Journal of Electrical and Electronics Engineering, Australia, Vol. 7, pp. 257-260, Dec 1987.

62. A.J. Parfitt, Substrate supported metal strip antennas for monolithically fabricated millimetre wavelength arrays - Appendix C: numerical modelling of wire junctions, a PhD thesis submitted at the University of Adelaide, Nov 1992.

63. H.K. Schuman, D.R. Pflug and L.D. Thomson, Infinite arrays of arbitrarily bent thin wire radiators, IEEE Transactions on Antennas and Propagation, Vol. 32, pp. 364-377, Apr 1984.

64. B.D. Popovic and B.M. Kolundzija, Analysis of metallic antennas and scatterers, The Institution of Electrical Engineers, Michael Faraday House, United Kingdom, 1994.

65. M. Abramowitz and I. Stegun, Handbook of mathematical functions, New York: Dover, 1965.

66. W.L. Weeks, Wire antennas and related forms, Chapter 4 of Antenna Engineering, McGraw-Hill Inc., pp. 136-198, 1968.

67. T. Tsukiji, On polygonal loop antennas, IEEE Transactions on Antennas and Propagation, Vol. 28, pp. 571-575, Jul 1980.

68. C.W. Harrison and R.W. P. King, Folded dipoles and loops, IRE Transactions on Antennas and Propagation, pp. 171-187, Mar 1961.

69. R.W. Lampe, Design formulas for an asymmetric coplanar strip folded dipole, IEEE Transactions on Antennas and Propagation, Vol. 33, pp. 1028-1031, Sep 1985.

70. W.H. Hayt, Engineering electromagnetics, McGraw-Hill Inc., 1989.

71. H. Fooks and R.A. Zakarevicius, Microwave engineering using microstrip circuits, Prentice Hall, 1990.

72. G.A. Thiele, E.P. Ekelman and L.W. Henderson, On the accuracy of the transmission line model of the folded dipole, IEEE Transactions on Antennas and Propagation, Vol. 28, pp. 700-703, Sep 1980.

73. W.L. Stutzman and G.A. Thiele, Antenna theory and design, New York: Wiley, 1980.

74. A.A. Oliner and R.G. Malech, Radiating elements and mutual coupling, Chapter 2 of Microwave Scanning Antennas, Volume II - Array theory and practice, edited by R.C. Hansen, Academic Press, New York and London, pp. 71-194, 1966.

75. M.E. Cooley, D.H. Schaubert, N.E. Buris and E.A. Urbanik, Radiation and scattering analysis of infinite arrays of endfire slot antennas with a ground plane, IEEE Transactions on Antennas and Propagation, Vol. 39, pp. 1615-1625, Nov 1991.

76. E.D. Mayer and A. Hessel, Feed region modes in dipole phased arrays, IEEE Transactions on Antennas and Propagation, Vol. 30, pp. 66-75, Jan 1982.

77. H.K. Schuman, Modelling folded dipoles and feedlines for radiation and scattering, IEEE Transactions on Antennas and Propagation, Vol. 38, pp. 30-39, Jan 1990.

78. R.J. Mailloux, Antenna array architecture, Proceedings of the IEEE, Vol. 80, pp. 163-172, January 1992.

79. A.J. Parfitt, Monolithic integrated array architectures, Chapter 2 of PhD thesis: Substrate supported metal strip antennas for monolithically fabricated millimetre wavelength arrays, pp. 12-36, 1992.

80. J.P.R. Bayard, M.E. Cooley and D.H. Schaubert, A general method for treating infinite arrays of antennas printed on protruding dielectric substrates, IEEE Antennas and Propagation Symposium, (London, Ontario), pp. 600-603, Jun 1991.

81. T.K. Sarkar and E. Arvas, An integral equation approach to the analysis of finite microstrip antennas: volume / surface formulation, IEEE Transactions on Antennas and Propagation, Vol. 38, pp. 305-312, Mar 1990.

82. R.A. York, R.C. Compton and B.J. Rubin, Experimental verification of the 2-D rooftop approach for modelling microstrip patch antennas, IEEE Transactions on antennas and propagation, Vol. 39, pp. 690-694, May 1991.

83. D.M. Pozar and B. Kaufman, Increasing the bandwidth of a microstrip antenna by proximity coupling, Electronic Letters, Vol. 23, pp. 368-369, Apr 1987.

84. H.F. Pues and A.R. Van De Capelle, An impedance-matching technique for increasing the bandwidth of microstrip antennas, IEEE Transactions on Antennas and Propagation, Vol. 37, pp. 1345-1354, Nov 1989.

85. F. Croq and D.M. Pozar, Millimetre-wave design of wide-band aperture-coupled stacked microstrip antennas, IEEE Transactions on Antennas and Propagation, Vol. 39, pp. 1770-1776, Dec 1991.

86. D.M. Pozar, A review of bandwidth enhancement techniques for microstrip antennas, a review paper in Chapter 4 of Microstrip Antennas, edited by D.M. Pozar and D.H. Schaubert, pp.157-166, IEEE Inc., New York, 1995.

87. K.C. Gupta, R. Garg and I.J. Bahl, Coplanar lines, Chapter 7 of Microstrip Lines and Slotlines, pp. 257-301, Artech House Inc., 1979.

88. A.J. Parfitt, Aspects of practical element design and analysis, Chapter 4 of Substrate supported metal strip antennas for monolithically fabricated millimetre wavelength arrays, PhD thesis, University of Adelaide, Nov 1992.

89. A. Roederer, Etude des reseaux finis de guides rectangulaires a parois epaisses, L'onde Electrique, Vol. 51, fasc. 10, pp. 854-861, Nov 1971.

90. A.J. Roscoe and R.A. Perrot, Large finite array analysis using infinite array data, IEEE Transactions on Antennas and Propagation, Vol. 42, pp. 983-992, Jul 1994.

91. A. Ishimaru, R.J. Coe, G.E. Miller and W.P. Geren, Finite periodic structure approach to large scanning array problems, IEEE Transactions on Antenna and Propagation, Vol. 33, pp. 1213-1220, Nov 1985.

92. A.J. Parfitt, Analysis of small arrays above ground plane of finite extent, paper presented at the 1995 IEEE International Antennas and Propagation Symposium in Newport Beach, CA, June 1995.

93. A. Ishimaru, Theory of unequally-spaced arrays, IRE Transactions on Antennas and Propagation, pp. 691-702, Nov 1962.

94. K.N. Yeo and A.J. Parfitt, Numerical analysis of arrays of finite latera extent, paper present at the Workshop on Antennas and Radio Science, Canberra, June 1995.

95. A.J. Parfitt, Finite array analysis using a spatially windowed infinite array, paper presented at the 5th Australian Symposium on Antennas, Sydney, Feb 1996.

96. G.A. Thiele, Overview of selected hybrid methods in radiating system analysis, Proceedings of the IEEE, Vol. 80, pp. 66-78, Jan 1992.

97. W.D. Stanley, Basic properties of discrete and fast Fourier transforms, Chapter 9 of Digital Signal Processing, pp. 239-274, Prentice Hall, 1975.

98. C. Kittel, Crystal diffraction and the reciprocal lattice, Chapter 2 of Solid State Physics, pp. 47-53, John Wily & Sons Inc., 1976.

ERRATA / ADDENDUM

1. On page xiv, "∇" should read "$\nabla\cdot$".

2. In the second last line of Section 4.2.1 on page 55, "... voltage over ..." should read "... voltage caused by the incident (or impressed) field over ...".

3. In the sentence above equation 4.5 on page 57, "... method, the testing functions ..." should read "... method [51], in the sense that the testing functions used to reduce the continuous equations to matrix form ...".

4. Equation 4.11a on page 58 should read:

$$Z_{xx} = \left\langle W_i \hat{x}, E_x^i \hat{x} \right\rangle$$
$$= \left(j\omega\mu_0 + \frac{j}{\omega\varepsilon_0}\frac{\partial^2}{\partial x_i^2} \right) \int_{-\infty}^{\infty}\int_{-\infty}^{\infty}\int_{-\infty}^{\infty}\int_{-\infty}^{\infty}\int_{-\infty}^{\infty}\int_{-\infty}^{\infty} W_{xi} J_{xj} G_\infty \, dx\, dy\, dz\, dx'\, dy'\, dz'$$

Similarly, for equations 4.11b to 4.11d found on page 59, the limits of integration for all the six integrals should be from $-\infty$ to ∞.

5. In Tables 4.1, 4.2, 4.3 and Figures 4.3, 4.5 found on pages 62-73, a metal strip of width $w = 0.05l$ was used for the computations.

6. The following should be included at the end of the first paragraph on page 66: " ... not pursued. Nevertheless, it is accepted that the use of certain higher order functions could well lead to a fewer number of basis functions being required to achieve numerical convergence of the results, though at the cost of additional computations in the implementation of a common segmentation grid and look-up table as shown in Figure 4.4 and described in Section 4.3.4, respectively".

7. In the second last line of page 78, "separation of variables" should be replaced by "with respect to the separate variables".

8. In the line above equation 4.28 on page 79, "performed by parts" should read "performed in the same manner as that described above over the range of the integration".

9. In the last line of page 79, the phrase "by parts" should be deleted.

10. In the line above equation 4.29 on page 80, "integration by parts" should read "integrating in the same manner described in Section 4.4.1".

11. In the first line of Section 5.2.1 on page 87, "Figure 4.1" should read "Figure 5.1"

12. In the last line of page 123, " inaccuracies due to numerical errors of the computer" should read "round-off errors".

13. The following should be included at the bottom of page 199: "It is noted that the plots of the refined spectral window results are not symmetrical about the points corresponding to the center element owing to errors in the repeated numerical evaluation of the convolutions using the FFT. However, the numerical errors can be reduced by using a larger sample size for each FFT operation, though at a cost of longer computation time".

14. The right hand side of equation C.8 on page 237 should read "$e^{-k_{mn}|z-z'|}/k_{mn}$".